# NEW TRENDS IN HIGH-ENERGY PHYSICS

*Budva, Becici, Montenegro*
*2–8 October 2016*

*Proceedings of the Conference*

JOINT INSTITUTE FOR NUCLEAR RESEARCH

# NEW TRENDS IN HIGH-ENERGY PHYSICS

## Conference

*Budva, Becici, Montenegro*
*2–8 October 2016*

*Proceedings of the Conference*

Dubna 2018

The contributions are reproduced directly from the originals.

The Conference on New Trends in High-Energy Physics organized by the Joint Institute for Nuclear Research, Dubna, and Bogolyubov Institute for Theoretical Physics, National Academy of Sciences of Ukraine, was held at the Hotel Splendid, Conference Hall, Budva, Becici, Montenegro, on 2–8 October 2016.

The present Proceedings contain direct reproductions of authors' originals (reviews and short communications) that arrived at the Organizing Committee and are grouped somewhat loosely. We have united a number of sections. The contributions within each section are ordered according to the conference program. More conference information and pictures can be found on our site: http://indico-new.jinr.ru/event/ntihep2016.

Конференция «Новые тенденции в физике высоких энергий», организованная Объединенным институтом ядерных исследований (Дубна) и Институтом теоретической физики им. Н.Н. Боголюбова НАН Украины (Киев), проходила в конференц-зале гостиницы «Splendid» (Черногория, Будва, Бечичи) 2–8 октября 2016 г.

Данный сборник содержит материалы (обзоры и короткие сообщения), присланные авторами в оргкомитет, сгруппированные в свободном порядке. Мы объединили ряд разделов. Статьи в каждом разделе упорядочены в соответствии с программой конференции. Более подробную информацию о конференции, а также фотографии можно найти на сайте: http://indico-new.jinr.ru/event/ntihep2016.

# CONTENTS

## SECTION "NEUTRINO, ASTROPARTICLE PHYSICS, STANDARD MODEL AND BEYOND"

## SECTION "ADVANCES IN THEORETICAL PHYSICS"

## SECTION "NEW COLLIDERS, FACILITIES, DETECTORS, COMPUTING AND DATA ANALYSES TECHNIQUES"

# CONFERENCE PROGRAM

## 3 October 2016

**09:00 - 10:30**  **INTRODUCTION**
Chair: V. Bednyakov

09:00    N. Russakovich. **Opening Talk**
09:20    S. Bilenky. **Neutrino in the Standard Model and beyond**
09:55    D. Kazakov. **High energy behavior of maximally supersymmetric gauge theories**

**10:30-10:50**    **Coffee break**

**10:50-12:30 SECTION: "STANDARD MODEL AND BEYOND"**
Chair: V. Glagolev

10:50    G. Prodi. **The gravitational wave observatory and its first discoveries**
11:30    A. Krolak. **First detection of gravitational wave signals**
12:00    S. Dubnicka. **Prediction of $\Lambda$-hyperon magnetic FF and ratio $|G_E^\Lambda/G_M^\Lambda|$ in time-like region**

**12:30-14:30**    **Lunch time**

**14:30-16:00 SECTION: "ADVANCES IN THEORETICAL PHYSICS"**
Chair: D. Kazakov

14:30    A. Gladyshev. **Search for supersymmetry: the present status**
15:00    M. Krivoruchenko. **Longitudinal vector form factor in the pion-beta decay**
15:30    O.V. Nitescu. **New phase space calculations for $\beta^+$ and EC decay modes**

**16:00-16:20**    **Coffee break**

**16:20-17:20 SECTION: "ADVANCES IN THEORETICAL PHYSICS"**
Chair: A. Gladyshev

16:20    P. Matak. **Left-left squarks mixing in $K^+\to\pi^+\nu\nu$ decay**
16:50    N. Gromov. **Particles evolution in the early universe**

14:30-16:00  **PARALLEL   SECTION:   "STANDARD   MODEL   AND BEYOND"**
Chair: S. Dubnicka

14:30   N. Raicevic. **HERA Results on proton structure and hard QCD**
15:00   L. Adamczyk. **Diffractions at HERA**
15:30   M. Pesek. **Polarized Drell-Yan measurement at COMPASS**

16:00-16:20     **Coffee break**

16:20-17:50 **PARALLEL SECTION: "NEW FACILITIES, DETECTORS, COMPUTING AND DATA ANALYSES TECHNIQUES"**
Chair: N. Atanov

16:20   V. Baranov. **Particle tracking in the PEN experiment**
16:50   A. Simonenko. **The increase of the light collection from scintillation strip with hole for WLS fiber using various types of fillers**
17:20   Yu. Usov. **$^3$He-$^4$He dilution refrigerators, results, traditions, 50 years anniversary**

09:00 - 10:30 **SECTION "NEUTRINO AND ASTROPARTICLE PHYSICS"**
Chair: R. Bernabei

09:00    Z. Djurcic. **Deep underground neutrino experiment: status and prospects**
09:30    D. Naumov. **Latest results from the Daya Bay reactor neutrino experiment**
10:00    Z. Djurcic. **Physics results from NOvA neutrino oscillation experiment**

10:30-10:50    **Coffee break**

10:50 - 12:30 **SECTION "NEUTRINO AND ASTROPARTICLE PHYSICS"**
Chair: D. Naumov

10:50    R. Bernabei. **Dark matter particles in the galactic halo**
11:30    I. Tkachev. **Axions as dark matter**
12:00    J.K. Hwang. **Elementary particles, dark candidate and new extended Standard Model**

12:30-14:30    **Lunch time**

14:30-16:00 **SECTION "NEUTRINO AND ASTROPARTICLE PHYSICS"**
Chair: I. Tkachev

14:30    T. Yano. **The recent results from Super-K**
15:00    V. Paolone. **Overview of recent results from the T2K experiment**
15:30    D. Svirida. **DANSS reactor antineutrino project: status and proof of principle**

16:00-16:20    **Coffee break**

16:20-17:50 **SECTION: "ADVANCES IN THEORETICAL PHYSICS"**
Chair: G. Lykasov

16:20    M. Ivanov. **Heavy quark physics and XYZ states in covariant quark model**

16:50    A. Liptaj. **Rare decay of heavy mesons in covariant confined quark model**

17:20    A. Afanasiev. **How to differentiate function based on integration operation**

<div align="center">12:30-14:30     **Lunch time**</div>

14:30-16:00  **PARALLEL SECTION: "STANDARD MODEL AND BEYOND"**
Chair: M. Ivanov

14:30    D. Madigozhin. **Searches for lepton number violation and resonances in the $K^+ \to \pi\mu\mu$ decays at the NA48/2 experiment**

15:00    M. Mirra. **Neutral pion form factor measurement by the NA62 experiment**

15:30    J. Pinzinno. **Search for $K^+ \to \pi^+ \nu\nu$ at NA62**

<div align="center">16:00-16:20     **Coffee break**</div>

16:20-18:20 **PARALLEL SECTION: "NEW FACILITIES, DETECTORS, COMPUTING AND DATA ANALYSES TECHNIQUES"**
Chair: B. Sabirov

16:20    A. Volkov. **New type straws: properties and quality**

16:50    N. Khomutov. **Using the cathode surface of straw tube for measuring the track coordinate along the wire and increasing rate capability**

17:20    P. Zarubin. **Diffraction dissociation of relativistic nuclei in nuclear track emulsion**

17:50    I. Zarubina. **Recent applications of the technique of nuclear track emulsion**

09:00 - 10:30    **SECTION "STANDARD MODEL AND BEYOND"**
Chair: G. Mitselmakher

09:00    A. Ivanov. **Search for new physics with CMS**
09:30    I. Yeletskikh. **Search for new physics at TeV scale in dilepton final states at ATLAS experiment**
10:00    G. Lykasov. **Heavy quark distributions in nucleon: collider tests**

10:30-10:50    **Coffee break**

10:50 - 12:30    **SECTION "STANDARD MODEL AND BEYOND"**
Chair: B. Kopeliovich

10:50    O. Igonkina. **Search for new exotic phenomena with the ATLAS detector at the LHC**
11:30    I. Tsukerman. **Review of Higgs results from the ATLAS experiment**
12:00    G. Mitselmakher. **Review of Higgs results from the CMS experiment**

12:30-14:30    **Lunch time**

09:00 - 10:30    **PARALLEL SECTION "NEUTRINO AND ASTROPARTICLE PHYSICS"**
Chair: V. Paolone

09:00    J. Kisiel. **ICARUS experiment: status and perspectives**
09:30    V. Pantuev. **Direct search of keV sterile neutrino in tritium beta decay by 'Troitsk v-mass" experiment**
10:00    A. Babic. **Neutrinoless double-beta decay with emission of single electron**

10:30-10:50    **Coffee break**

**EXCURSION**

09:00 - 10:30     SECTION "STANDARD MODEL AND BEYOND"
Chair: V. Glagolev

09:00     F. Happacher. **The Mu2e experiment at Fermilab**
09:30     I. Logashenko. **A new measurement of the anomalous magnetic moment of muon at Fermilab**
10:00     A. Dubnickova. **Reduction of total precise error of Muon g-2 anomaly and QED $\alpha(M^2_Z)$ by unitary&analytic model description of pseudoscalas meson nonet EM structure**

10:30-10:50     **Coffee break**

10:50 - 12:30     SECTION "STANDARD MODEL AND BEYOND"
Chair: R. Tsenov

10:50     R. Shicker. **ALISE results in pp, pA and AA collisions at the LHC**
11:30     Yu. Kulchitsky. **Two-particle Bose-Einstein correlations in pp collisions at 0.9 and 7 TeV measured with the ATLAS detector**
12:00     N. Pukhaeva. **Bose-Einstein correlation and color reconnection in particle physics**

12:30-14:30     **Lunch time**

14:30-16:00     SECTION "STANDARD MODEL AND BEYOND"
Chair: A. Dubnickova

14:30     D. Pocanic. **PEN and Nab: new precision tests of lepton and quark-lepton universality**
15:00     G. Rutar. **In search of μ→eγ: final result of the MEG experiment**
15:30     R. Tsenov. **A very intense neutrino super beam experiment for leptonic CP violation discovery based on the European spallation source linac**

16:00-16:20     **Coffee break**

16:20-17:50 SECTION: "ADVANCES IN THEORETICAL PHYSICS"
Chair: V. Melezhik

16:20     B. Kopeliovich. **Breakdown of QCD factorization in hard hadronic diffraction**

16:50 L. Csernai. **Shear, turbulence and its observable consequences in heavy ion reactions**

17:20 M. Nardi. **Heavy flavors in nucleus-nucleus and proton-nucleus collisions**

<div align="center">10:30-10:50  **Coffee break**</div>

10:50 - 12:30 **PARALLEL SECTION "ADVANCES IN THEORETICAL PHYSICS"**
Chair: M. Hnatic

10:50 L. Jenkovszky. **Alastic and inelastic diffraction at the LHC**

11:30 C. Adamuscin. **Numerical values of $f^F$, $f^D$, $f^S$ coupling constants in SU(3) invariant interaction lagrangian of vector-meson nonet with $1/2^+$ octet baryons**

12:00 E. Bartos. **Proton charge padius and its consistency with the experiments**

<div align="center">12:30-14:30  **Lunch time**</div>

14:30-16:00 **PARALLEL SECTION: " ADVANCES IN THEORETICAL PHYSICS "**
Chair: L. Jenkovszky

14:30 M. Hnatic. **Quantum field theory methods in classical physics**

15:00 O. Solovtsova. **Twenty years of the analytic perturbation theory in QCD**

15:30 V. Melezhik. **Quantum simulations with sold atoms^ from solid state to high energy physics and cosmology**

<div align="center">16:00-16:20  **Coffee break**</div>

16:20-17:50 **PARALLEL SECTION: "NEW FACILITIES, DETECTORS, COMPUTING AND DATA ANALYSES TECHNIQUES"**
Chair: N. Khomutov

16:20 B. Sabirov. **New technology application to modernization of Electron-positron linear collider (ILC)**

16:50 N. Atanov. **Solar-blind photodetectors with AlGaN photocathodes for light registration in UVC range**

17:20 A. Zaitsev. **Manifestation of the unstable nuclei in relativistic dissociation of the $^{10}$B and $^{11}$C nuclei**

09:00 - 10:30   **SECTION "NEW COLLIDERS FOR BARYONIC MATTER STUDY"**
Chair: S. Dubnicka

09:00    R. Tsenov. **Status of the NICA project**
09:30    M. Pandurovich. **The CLIC physics potential**
10:00    V. Ryabov. **Recent results from PHENIX experiment at RHIC**

10:30-10:50     **Coffee break**

10:50 – 11:50   **SECTION "NEW COLLIDERS FOR BARYONIC MATTER STUDY"**
Chair: L. Jenkovszky

10:50    D. Kotov. **PHENIX results on leading particles and jets measured in Cu+Au collisions at RHIC**
11:30    L. Jenkovszky. **Closing**

**EXCURSION**

20:00   **FAREWELL PARTY**

# SECTION "NEUTRINO, ASTROPARTICLE PHYSICS, STANDARD MODEL AND BEYOND"

Prediction of Λ-hyperon magnetic FF and ratio
$|G_E^\Lambda(t)|/|G_M^\Lambda(t)|$ in time-like region

# Overview of neutrino masses and mixing

S. M. Bilenky

*Joint Institute for Nuclear Research, Dubna, R-141980, Russia*

### Abstract

The status of neutrino oscillations is presented. The Standard Model and the Weinberg effective Lagrangian mechanism of the neutrino mass generation are discussed from the point of view of economy and simplicity.

# 1   Introduction

Idea of neutrino masses, mixing and oscillations was proposed by B. Pontecorvo in 1958 in Dubna [1]. This idea was further developed in the seventies by B. Pontecorvo, V. Gribov and myself [2, 3]. Different experiments on the search for neutrino oscillations were proposed at that time.

It took about thirty years of heroic efforts of many people to discover neutrino oscillations, first in the atmospheric Super-Kamiokande experiment [4] then in the solar SNO experiment [5] and in the reactor KamLAND experiment [6]. Strong indications in favor of neutrino transitions in the sun were found earlier in the pioneer Davis solar neutrino experiment [7] and in the solar neutrino experiments Kamiokande [8], GALLEX [9] and SAGE [10]. Discovery of neutrino oscillations was confirmed by the K2K [11], MINOS [12], T2K [13] and NOvA [14] accelerator neutrino experiments, by the Daya Bay [15], RENO [16] and Double Chooz [17] reactor neutrino experiments and by the solar neutrino experiment BOREXINO [18].

Discovery of the neutrino oscillations is the major recent discovery in the particle physics. In spite the full understanding of the origin of small neutrino masses and peculiar neutrino mixing requires new experimental data and, apparently, new theoretical ideas it is a common belief that small neutrino masses is a first beyond the Standard Model phenomenon found in the particle physics. In 2015 for the discovery of the neutrino oscillations T. Kajita and A. McDonald were awarded by the Nobel Prize.

In this talk I will consider

1. Present status of neutrino oscillations.

2. Role of neutrino in the Standard Model.

3. The most plausible (and the simplest) beyond the Standard Model mechanism of the generation of small neutrino masses.

# 2  Status of neutrino oscillations

Analysis of neutrino oscillation data is based on the assumption that neutrino interaction is the SM charged current and neutral current interaction given by the Lagrangians

$$\mathcal{L}_I^{CC}(x) = -\frac{g}{2\sqrt{2}} j_\alpha^{CC}(x) W^\alpha(x) + \text{h.c.}, \quad j_\alpha^{CC}(x) = 2 \sum_{l=e,\mu,\tau} \bar{\nu}_{lL}(x)\gamma_\alpha l_L(x) \tag{1}$$

and

$$\mathcal{L}_I^{NC}(x) = -\frac{g}{2\cos\theta_W} j_\alpha^{NC}(x) Z^\alpha(x), \quad j_\alpha^{NC}(x) = \sum_{l=e,\mu,\tau} \bar{\nu}_{lL}(x)\gamma_\alpha \nu_{lL}(x). \tag{2}$$

In the case of the neutrino mixing we have (see, for example, the review [19])

$$\nu_{lL}(x) = \sum_{i=1}^{3} U_{li}\, \nu_{iL}(x), \quad l = e, \mu, \tau \tag{3}$$

Here $U$ is the unitary Pontecorvo-MNS [1, 20] mixing matrix and $\nu_i(x)$ is the field of the neutrino with mass $m_i$.

If the total lepton number $L$ is conserved, $\nu_i$ are Dirac particles ($L(\nu_i) = -L(\bar{\nu}_i) = 1$). In this case the PNMS mixing matrix $U^D$ is characterized by three mixing angles $\theta_{12}, \theta_{23}, \theta_{13}$ and one $CP$ phase $\delta$. If there are no conserved lepton numbers, $\nu_i$ are Majorana particles. The $3 \times 3$ mixing matrix has in this case the form

$$U^{Mj} = U^D\, S(\bar{\alpha})\,, \tag{4}$$

where $S(\bar{\alpha})$ is the phase matrix which is characterized by additional two Majorana phases: $S_{ik}(\bar{\alpha}) = S_i \delta_{ik}$, $S_1 = 1$, $S_{2,3} = e^{i\bar{\alpha}_{2,3}}$.

The CC Lagrangian (1) determines the notion of the *flavor neutrinos* $\nu_e, \nu_\mu, \nu_\tau$. Flavor muon neutrino $\nu_\mu$ is a particle which is produced together with $\mu^+$ in the decay $\pi^+ \to \mu^+ + \nu_\mu$ or induces the reaction $\nu_\mu + N \to \mu^- + X$ etc. The state of the flavor neutrino $\nu_l$ with momentum $\vec{p}$ is given by *a coherent superposition of the states of neutrinos with definite masses*

$$|\nu_l\rangle = \sum_{i=1}^{3} U_{li}^* |\nu_i\rangle\,. \tag{5}$$

Here $|\nu_i\rangle$ is the state of neutrino with mass $m_i$, momentum $\vec{p}$ and energy $E_i = \sqrt{p^2 + m_i^2} \simeq E + \frac{m_i^2}{2E}$ ($p^2 \gg m_i^2$). This relation is a consequence of

the Heisenberg uncertainty relation. The relation (5) means that we can not resolve production of ultrarelativistic neutrinos with different masses in weak decays and neutrino reactions.

Small neutrino mass-squared differences can be resolved in special experiments with a large distance between neutrino source and neutrino detector. A possibility to resolve neutrino mass-squared differences is based on the time-energy uncertainty relation [21]

$$\Delta E \ \Delta t \geq 1 \ . \tag{6}$$

In the neutrino case

$$\Delta E = |E_i - E_k| \simeq \frac{|\Delta m_{ki}^2|}{2E}, \quad \Delta t = t \simeq L. \tag{7}$$

Here $\Delta m_{ki}^2 = m_i^2 - m_k^2$ and $L$ is the distance between neutrino source and detector. From (6) we obtain the following condition

$$\frac{|\Delta m_{ki}^2|}{2E} \ L \geq 1 \ . \tag{8}$$

Thus in order to reveal the production of neutrinos with energy difference $|E_i - E_k|$ we need to perform an experiment at a source-detector distance $L$ which satisfy the inequality (8).

If at the time $t = 0$ the flavor neutrino $\nu_l$ is produced at the time $t > 0$ the neutrino state is given by

$$|\nu_l\rangle_t = e^{-iHt} \ |\nu_l\rangle = \sum_i |\nu_i\rangle \ e^{-iE_i t} \ U_{li}^* = \sum_{l'} |\nu_{l'}\rangle \ \left(\sum_i U_{l'i} \ e^{-iE_i t} \ U_{li}^*\right) . \tag{9}$$

Here $H$ is the free Hamiltonian. From (9) for the probability of the $\nu_l \to \nu_{l'}$ transition we find the following expression

$$P(\nu_l \to \nu_{l'}) = |\sum_i U_{l'i} \ e^{-2i\Delta_{pi}} \ U_{li}^*|^2 = |\delta_{l'l} - 2i \sum_{i \neq p} U_{l'i} \ e^{-i\Delta_{pi}} \sin \Delta_{pi} \ U_{li}^*|^2 ,\tag{10}$$

where $p$ is an arbitrary fixed index and $\Delta_{pi} = \frac{\Delta m_{pi}^2 L}{4E}$.

For the probability of $\bar\nu_l \to \bar\nu_{l'}$ transition we have

$$P(\bar\nu_l \to \bar\nu_{l'}) = |\delta_{l'l} - 2i \sum_{i \neq p} U_{l'i}^* \ e^{-i\Delta_{pi}} \sin \Delta_{pi} \ U_{li}|^2 \tag{11}$$

From (4) follows that

$$U_{l'i}^{Mj} U_{li}^{Mj*} = U_{l'i}^D U_{li}^{D*} \ . \tag{12}$$

We conclude from (10), (11) and (12) that the study of neutrino oscillations does not allow to reveal the nature of neutrinos with definite masses (Dirac or Majorana?) [22].

It follows from (10) and (11) that $\nu_l \to \nu_{l'}$ ($\bar{\nu}_l \to \bar{\nu}_{l'}$) transition probability is given by the following expression

$$P(\nu_l \to \nu_{l'})(P(\bar{\nu}_l \to \bar{\nu}_{l'})) = \delta_{l'l} - 4 \sum_i |U_{li}|^2 (\delta_{l'l} - |U_{l'i}|^2) \, \sin^2 \Delta_{pi}$$

$$+8 \sum_{i>k} [\text{Re} \, (U_{l'i} U_{li}^* U_{l'k}^* U_{lk}) \, \cos(\Delta_{pi} - \Delta_{pk})$$

$$\pm \, \text{Im} \, (U_{l'i} U_{li}^* U_{l'k}^* U_{lk}) \, \sin(\Delta_{pi} - \Delta_{pk})] \, \sin \Delta_{pi} \sin \Delta_{pk}. \tag{13}$$

Usually neutrino masses are labeled in such a way that

$$m_2 > m_1, \qquad \Delta m_{12}^2 = \Delta m_S^2 > 0 \,, \tag{14}$$

where $\Delta m_S^2$ is called the solar mass-squared difference. From analysis of the neutrino oscillation data it was found that another neutrino mass-squared difference $\Delta m_A^2$, which is called atmospheric, is about 30 times larger than the solar one. There are two possibilities for the third mass $m_3$ and, correspondingly, for the neutrino mass spectrum

1. Normal ordering (NO) $m_3 > m_2 > m_1$, $\quad \Delta m_{23}^2 = \Delta m_A^2$.

2. Inverted ordering (IO) $m_2 > m_1 > m_3$, $\quad |\Delta m_{13}^2| = \Delta m_A^2$.

Determination of the character of the neutrino mass spectrum is one of the major problem of the present and future neutrino oscillation experiments. Future reactor neutrino experiments JUNO [23] and RENO-50 [24], in which a distance between reactors and the detector will be about 60 km, are planned to solve this problem. From (13) for the probability of the reactor $\bar{\nu}_e$'s to survive in the case of the normal and inverted neutrino mass spectrum we find the following expressions

$$P^{NO}(\bar{\nu}_e \to \bar{\nu}_e) = 1 - \sin^2 2\theta_{13} \sin^2 \Delta_A$$
$$-(\cos^4 \theta_{13} \sin^2 2\theta_{12} + \cos^2 \theta_{12} \sin^2 2\theta_{13}) \sin^2 \Delta_S$$
$$-2 \sin^2 2\theta_{13} \cos^2 \theta_{12} \cos(\Delta_A + \Delta_S) \sin \Delta_A \sin \Delta_S. \tag{15}$$

and

$$P^{IO}(\bar{\nu}_e \to \bar{\nu}_e) = 1 - \sin^2 2\theta_{13} \sin^2 \Delta_A$$
$$-(\cos^4 \theta_{13} \sin^2 2\theta_{12} + \sin^2 \theta_{12} \sin^2 2\theta_{13}) \sin^2 \Delta_S$$
$$-2 \sin^2 2\theta_{13} \sin^2 \theta_{12} \cos(\Delta_A + \Delta_S) \sin \Delta_A \sin \Delta_S. \tag{16}$$

The values of the neutrino oscillation parameters obtained from the global analysis of existing neutrino oscillation data are presented in the Table I.

Table I. The values of the neutrino oscillation parameters [25]

| Parameter | Normal Ordering | Inverted Ordering |
|---|---|---|
| $\sin^2\theta_{12}$ | $0.306^{+0.012}_{-0.012}$ | $0.306^{+0.012}_{-0.012}$ |
| $\sin^2\theta_{23}$ | $0.441^{+0.027}_{-0.021}$ | $0.587^{+0.020}_{-0.024}$ |
| $\sin^2\theta_{13}$ | $0.02166^{+0.00075}_{-0.00075}$ | $0.02179^{+0.00076}_{-0.00076}$ |
| $\delta$ (in $^\circ$) | $(261^{+51}_{-59})$ | $(277^{+40}_{-46})$ |
| $\Delta m^2_S$ | $(7.50^{+0.19}_{-0.17}) \cdot 10^{-5}$ eV$^2$ | $(7.50^{+0.19}_{-0.17}) \cdot 10^{-5}$ eV$^2$ |
| $\Delta m^2_A$ | $(2.524^{+0.039}_{-0.040}) \cdot 10^{-3}$ eV$^2$ | $(2.514^{+0.038}_{-0.041}) \cdot 10^{-3}$ eV$^2$ |

Thus existing data do not allow to distinguish the normal and inverted neutrino mass ordering and we see from Table I that

1. Neutrino oscillations parameters are known with accuracies (3 -10)%.

2. The $CP$ phase $\delta$ is practically unknown.

The major aims of future neutrino oscillation experiments are

- to determine neutrino oscillation parameters with 1% accuracy,

- to establish the neutrino mass ordering,

- to measure the $CP$ phase $\delta$.

Apparently, future neutrino experiments could reveal a true mechanism of generation of small neutrino masses and peculiar neutrino mixing which is very different from the quark mixing. In the last part of this brief overview we will discuss the plausible mechanism of the generation of small (Majorana) neutrino masses.

## 3   Neutrino in the Standard Model

I will start with a few historical remarks. In 1928 Dirac proposed the four-component equation for a relativistic spin 1/2 particle. Now we know the origin of four components: the four-component Dirac field $\psi(x)$ (in the framework of QFT) is *the field of particles and antiparticles.*

In 1929 Weyl put the following question: can we find for a relativistic spin 1/2 particle a two-component equation? Weyl introduced the two-component spinors

$$\psi_L(x) = \frac{1}{2}(1 - \gamma_5)\psi(x), \quad \psi_R(x) = \frac{1}{2}(1 - \gamma_5)\psi(x). \tag{17}$$

and showed that $\psi_L(x)$ and $\psi_R(x)$ satisfy the following two-component equations (which are called Weyl equations)

$$i\gamma^\alpha \partial_\alpha \psi_L(x) = 0, \quad i\gamma^\alpha \partial_\alpha \psi_R(x) = 0 \tag{18}$$

The Weyl equations, however, are not invariant under the space inversion

$$'_{L,R}(x') = \eta\gamma^0 \psi_{L,R}(x), \tag{19}$$

where $x' = (x^0, -\vec{x})$ and $\eta$ is a phase factor.

In the thirties (and many years later) there was a common belief that the conservation of the parity is a law of nature. This was the reason why the Weyl equations were rejected.

After discovery of the parity violation in weak decays it was assumed that neutrino is a massless, Weyl particle and neutrino field is $\nu_L(x)$ or $\nu_R(x)$ (the two-component neutrino theory by Landau [26], Lee and Yang [27] and Salam [28]).

From the two-component theory followed that

1. the large violation of parity in the $\beta$-decay and other weak processes had to be observed,

2. the helicity of neutrino (antineutrino) had to be equal to -1 (+1) in the case of $\nu_L(x)$ and +1 (-1) in the case of $\nu_R(x)$.

The crucial test of the two-component neutrino theory was performed by the classical Goldhaber et al experiment[29] in which the neutrino helicity was measured. The authors of the experiment concluded: "our result is compatible with 100 % negative helicity of neutrino" (neutrino field is $\nu_L(x)$).

The field $\nu_L(x)$ is the field of left-handed Dirac neutrino ($L = 1, \quad h = -1$) and right-handed Dirac antineutrino ($L = -1, \quad h = 1$). However, theories with massless Dirac and Majorana neutrinos are equivalent. Thus $\nu_L(x)$ can be considered as a field of left-handed ($h = -1$) and right-handed ($h = 1$) Majorana neutrino. Let us stress that *the two-component neutrino is the most economical possibility: two degrees of freedom*. In the general Dirac case there are four degrees of freedom.

The Standard Model started with the theory of the two-component, massless, left-handed neutrino. It is based on the following principles

1. The local gauge $SU_L(2) \times U_Y(1)$ invariance of massless fields.

2. The unification of the weak and electromagnetic interactions.

3. The Brout-Englert-Higgs mechanism of mass generation.

The Standard Model is in a perfect agreement with experiment: its most impressive prediction, existence of the scalar Higgs boson, was confirmed by recent LHC experiments. We will present some arguments that the Standard Model teach us that *the simplest, most economical possibilities are likely to be correct.*

Neutrinos are produced in weak decays together with leptons. $SU_L(2)$ is *the simplest symmetry* which allows to unify leptons and neutrinos (and up and down quarks). The fields of left-handed, massless, Weyl fields of neutrinos and leptons are components of doublets

$$
\begin{matrix} lep \\ eL \end{matrix} = \begin{pmatrix} \nu'_{eL} \\ e'_L \end{pmatrix}, \quad \begin{matrix} lep \\ \mu L \end{matrix} = \begin{pmatrix} \nu'_{\mu L} \\ \mu'_L \end{pmatrix}, \quad \begin{matrix} lep \\ \tau L \end{matrix} = \begin{pmatrix} \nu'_{eL} \\ e'_L \end{pmatrix}. \tag{20}
$$

The leptonic electromagnetic current is given by the expression

$$
j_\alpha^{EM} = -\left( \sum_{l=e,\mu,\tau} \bar{l}'_L \gamma_\alpha l'_L + \sum_{l=e,\mu,\tau} \bar{l}'_R \gamma_\alpha l'_R \right) \tag{21}
$$

in which left-handed *and right-handed* lepton fields enter. Thus in order to include the electromagnetic interaction we have to enlarge the symmetry group. The *minimal enlargement* is $SU(2)_L \times U_Y(1)$ group, where $U_Y(1)$ is the group of the hypercharge $Y$ determined by the Gell-Mann-Nishijima relation

$$
Q = T_3 + \frac{1}{2}Y, \tag{22}
$$

where $Q$ is the charge and $T_3$ is the third projection of the isospin.

From the requirements of the local $SU(2)_L \times U_Y(1)$ invariance follow that gauge vector fields must exist. The standard electroweak interaction of fermions and vector gauge $W^\pm, Z^0$ bosons and $\gamma$-quanta

$$
\mathcal{L}_I = \left( -\frac{g}{2\sqrt{2}} j_\alpha^{CC} W^\alpha + \text{h.c} \right) - \frac{g}{2\cos\theta_W} j_\alpha^{NC} Z^\alpha - j_\alpha^{EM} A^\alpha \tag{23}
$$

is the *minimal* (compatible with the local gauge invariance) interaction.

The Standard Model mechanism of mass generation is the Brout-Englert-Higgs mechanism of the spontaneous symmetry breaking [30, 31]. It is based on the assumption of the existence of scalar Higgs fields. In order to generate masses of $W^\pm$ and $Z^0$ vector bosons three Goldsone degrees of freedom are needed. Thus *a minimal possibility* is a doublet of complex Higgs fields (four degrees of freedom). In such a theory it is predicted that *one neutral scalar Higgs boson* must exist. This prediction was perfectly confirmed by the LHC experiments.

Lepton (and quark) masses and mixing are generated by the $SU_L(2) \times U_Y(1)$ invariant Yukawa interaction. For leptons we have

$$\mathcal{L}_Y^{lep} = -\sqrt{2} \sum_{l_1,l_2} \bar{\psi}_{l_1 L}^{lep} Y_{l_1 l_2} l'_{2R} \ \phi + \text{h.c.} \tag{24}$$

Here

$$\phi = \left( \begin{array}{c} \phi_+ \\ \phi_0 \end{array} \right) \tag{25}$$

is the Higgs doublet and $Y$ is a complex $3 \times 3$ Yukawa matrix. If we choose

$$\phi = \left( \begin{array}{c} 0 \\ \frac{v+H}{\sqrt{2}} \end{array} \right) \tag{26}$$

where $v = (\sqrt{2} G_F)^{-1/2} \simeq 246$ GeV is the vacuum expectation value (vev) of the Higgs field and $H$ is the field of the Higgs boson, the electroweak symmetry will be spontaneously broken and Yukawa interaction (24) generates the Dirac mass term

$$\mathcal{L}^D = - \sum_{l_1,l_2} \bar{l}'_{1L} \ Y_{l_1 l_2} \ l'_{2R} \ v + \text{h.c} = - \sum_{l=e,\mu,\tau} \text{m}_l \ \bar{l} \ l, \tag{27}$$

where

$$m_l = y_l \ v. \tag{28}$$

Here $m_l$ is the lepton mass, and the Yukawa coupling $y_l$ is the eigenvalue of the matrix $Y$.

The characteristic feature of the Brout-Englert-Higgs mechanism of the mass generation is a *proportionality of the lepton masses to the vacuum expectation value v* (masses of quarks, $W^{\pm}$ and $Z^0$ bosons are also proportional to $v$).

The Unification of the weak and electromagnetic interactions requires that in the Standard Model Lagrangian enter left-handed and right-handed fields of charged fermions. Thus for the generation of the Dirac lepton (and quark) masses via the Yukawa interaction we do not need additional degrees of freedom.

Neutrino have no direct electromagnetic interaction. In order to generate neutrino masses via the standard mechanism of the spontaneous symmetry breaking we need to assume that in Standard Model Lagrangian enter not only left-handed neutrino fields but also right-handed fields (additional degrees of freedom). On the basis of general arguments of economy and simplicity it is natural to assume that *neutrinos in the Standard Model are*

*massless, two-component, left-handed Weyl particles.*[1] In order to generate neutrino masses and mixing we need a new beyond the Standard Model mechanism.

# 4 The most economical beyond the Standard Model mechanism of neutrino mass generation

A neutrino mass term is a Lorenz-invariant product of left-handed and right-handed components of neutrino fields. Can we build a neutrino mass term if we use only left-handed fields $\nu_{lL}$? The answer to this question was given many years ago by Gribov and Pontecorvo [2]. It is possible to built a neutrino mass term in which only flavor fields $\nu_{lL}$ enter, *if we assume that the total lepton number L is not conserved.* In fact, in this case we can built the following mass term

$$\mathcal{L}^{\mathrm{M}} = -\frac{1}{2} \sum_{l',l} \bar{\nu}_{l'L} \, M_{l'l} (\nu_{lL})^c + \text{h.c.}. \tag{29}$$

Here the conjugated field $(\nu_{lL})^c = C(\bar{\nu}_{lL})^T$ is *right-handed component* ($C$ is the matrix of the charge conjugation) and $M$ is a $3 \times 3$ symmetrical matrix.

The Lagrangian (29) is not invariant under the global phase transformations (does not conserve the total lepton number $L$). As a result, after the diagonalization of the mass matrix

$$M = U \, m \, U^T, \quad U^\dagger U = 1, \quad m_{ik} = m_i \delta_{ik}, \quad m_i > 0 \tag{30}$$

we come to the standard Majorana mass term

$$\mathcal{L}^{\mathrm{Mj}} = -\frac{1}{2} \sum_{i=1}^{3} m_i \, \bar{\nu}_i \nu_i \tag{31}$$

Here

$$\nu_i = \nu_i^c = C\bar{\nu}_i^T \tag{32}$$

---

[1] If we assume that neutrino masses are generated by the Higgs mechanism, in this case we have $m_i = y_i^\nu \, v$. Absolute values of neutrino masses at present are not known. From existing upper bounds on neutrino masses and from neutrino oscillation data we can conclude that the heaviest neutrino mass $m_3$ is in the range ($5 \cdot 10^{-2} \leq m_3 \leq 1$ eV) and the Yukawa constant $y_3^\nu$ is in the range ($2 \cdot 10^{-13} \leq y_3^\nu \leq 4 \cdot 10^{-12}$). For other particles of the third family we have $y_t \simeq 0.7$, $y_b \simeq 1.7 \cdot 10^{-2}$, $y_\tau \simeq 0.7 \cdot 10^{-2}$. Thus, the neutrino Yukawa coupling $y_3^\nu$ is more than nine orders of magnitude smaller than Yukawa couplings of other particles of the third family. It is very unlikely that neutrino masses are of the same origin as masses of lepton and quarks.

is the field of the Majorana neutrino with the mass $m_i$. The flavor field $\nu_{lL}$ is given by the mixture of the fields of the Majorana neutrinos with definite masses

$$\nu_{lL} = \sum_{i=1}^{3} U_{li} \ \nu_{iL}, \quad l = e, \mu, \tau. \tag{33}$$

The approach to the neutrino masses and mixing, we have considered, is purely phenomenological one. Neutrino masses $m_i$ and elements of the mixing matrix $U$ are *parameters* which must be determined from experiments. The relation (33) gives a framework which allow us to analyze the data of neutrino oscillation experiments, experiments on the search for neutrinoless double $\beta$-decay etc. We have no any explanation of the smallness of neutrino masses.

However, it is important to stress that *the Majorana mass term (29) is only possible mass term which can be built with the help of left-handed neutrino fields $\nu_{lL}$.*

We will consider now the effective Lagrangian approach [32] which allow us

- to obtain the Majorana mass term for neutrinos,

- to find some explanation of the smallness of neutrino masses,

- to predict existence of heavy Majorana fermions.

The method of the effective Lagrangian is a powerful, general method which allows to describe effects of a beyond the Standard Model physics. The effective Lagrangian is a nonrenormalizable dimension five or more operator invariant under the $SU_L(2) \times U_Y(1)$ transformations and built from the Standard Model fields. In order to generate the neutrino mass term we need to built an effective Lagrangian which is quadratic in the neutrino fields.

Let us consider the $SU_L(2) \times U_Y(1)$ invariant product

$$(\bar{\psi}_{lL}^{lep} \ \tilde{\phi}) \ , \tag{34}$$

where $\psi_{lL}^{lep}$ is the lepton doublet (see (20) ) and $\tilde{\phi} = i\tau_2 \phi^*$ is the conjugated Higgs doublet. After the spontaneous breaking of the electroweak symmetry we have

$$(\bar{\psi}_{lL}^{lep} \ \tilde{\phi}) = \frac{v + H}{\sqrt{2}} \bar{\nu}_{lL}' \ . \tag{35}$$

From this expression it is obvious that the $SU_L(2) \times U_Y(1)$ invariant effective Lagrangian [32]

$$\mathcal{L}_I^{\text{eff}} = -\frac{1}{\Lambda} \sum_{l_1, l_2} (\bar{\psi}_{l_1 L}^{lep} \tilde{\phi}) \, X_{l_1 l_2}' \, C \, (\bar{\psi}_{l_2 L}^{lep} \tilde{\phi})^T + \text{h.c.} \tag{36}$$

generates a neutrino mass term. The operator in Eq. (36) has a dimension five. Thus $\Lambda$ has a dimension of a mass and $X'$ is a dimensionless $3 \times 3$ symmetrical matrix. Let us stress the following

1. The Lagrangian (36) is the only possible dimension five effective Lagrangian which can generate a neutrino mass term.

2. The effective Lagrangian (36) does not conserve the total lepton number $L$.

3. The constant $\Lambda$ characterizes a scale of a beyond the Standard Model physics.

After the spontaneous symmetry breaking the Lagrangian (36) generates the Majorana mass term

$$\mathcal{L}^{\text{M}} = -\frac{1}{2} \frac{v^2}{\Lambda} \sum_{l_1, l_2} \bar{\nu}_{l_1 L} X_{l_1 l_2} (\nu_{l_2 L})^c + \text{h.c..} \tag{37}$$

The symmetrical matrix $X$ can be presented in the diagonal form

$$X = U \, x \, U^T, \quad U^\dagger \, U = 1, \quad x_{ik} = x_i \delta_{ik}, \quad x_i > 0. \tag{38}$$

From (37) and (38) we have

$$\mathcal{L}^{\text{M}} = -\frac{1}{2} \sum_{i=1}^{3} m_i \, \bar{\nu}_i \nu_i, \quad \nu_{lL} = \sum_{i=1}^{3} U_{li} \, \nu_{iL} \tag{39}$$

Here

$$\nu_i = \nu_i^c = C \, \bar{\nu}_i^T \tag{40}$$

is the field of the neutrino Majorana with the mass

$$m_i = \frac{v^2}{\Lambda} \, x_i \, , \tag{41}$$

where $x_i$ is the eigenvalue of the matrix $X$.

As we discussed before, the Standard Model masses are proportional to $v \simeq 246$ GeV with dimensionless coefficients. Standard Model neutrino

masses can be small only if coefficients of proportionality are extremely small.

Majorana neutrino masses generated by the effective Lagrangian (36) are proportional to $\frac{v}{\Lambda} v$. We have in this case an additional factor

$$\frac{v}{\Lambda} = \frac{\text{scale of SM}}{\text{scale of a new physics}}. \tag{42}$$

Smallness of neutrino masses can be ensured if we assume that a scale $\Lambda$ of a new lepton number violating physics is much larger than the electroweak scale $v$. This is a natural assumption, no fine-tuning is required.

Uncertainties connected with the factors $x_i$ do not allow to determine the scale of a new physics $\Lambda$ in a model independent way. Nevertheless $\Lambda \gg v$ apparently is the most plausible possibility. In fact, let us assume hierarchy of neutrino masses ($m_1 \ll m_2 \ll m_3$). In this case for the third family we find

$$\Lambda \simeq x_3 \frac{v^2}{m_3} \simeq x_3 \frac{v^2}{\sqrt{\Delta m_A^2}}. \tag{43}$$

From this relation we have

$$\Lambda \simeq 1.2 \cdot 10^{15} \, x_3 \text{ GeV}. \tag{44}$$

If we assume that $\Lambda \simeq$ TeV in this case $x_3 \simeq 10^{-12}$ (too small, fine tuning). If $x_3 \simeq 1$ in this case $\Lambda \simeq 10^{15}$ GeV (GUT scale).

The effective Lagrangian (36) could be a result of an exchange of virtual heavy Majorana leptons between lepton-Higgs pairs.[2] In fact, let us assume that exist heavy Majorana leptons $N_i$ ($i = 1, 2, ...n$), singlets of $SU_L(2) \times U_Y(1)$ group, which have the following $SU_L(2) \times U_Y(1)$ invariant Yukawa interaction

$$\mathcal{L}_I^Y = -\sqrt{2} \sum_{l,i} \bar{\psi}_{lL}^{lep} \, \tilde{\phi} \, y'_{li} \, N_{iR} + \text{h.c.} \, . \tag{45}$$

Here $y'_{li}$ are dimensionless Yukawa coupling constants and $N_i = N_i^c$ is the field of Majorana leptons with mass $M_i$.

In the second order of the perturbation theory at $Q^2 \ll M_i^2$ ($Q$ is the momentum of the virtual $N_i$) we obtain effective Lagrangian

$$\mathcal{L}^{\text{eff}} = -\sum_{l_1,l_2} (\bar{\psi}_{l_1L}^{lep} \, \tilde{\phi}) \, (\sum_i y'_{l_1i} \frac{1}{M_i} y'_{l_2i}) \, (\tilde{\phi}^T \, (\, {}_{l_2L}^{lep})^c) + \text{h.c.}. \tag{46}$$

---

[2]The classical example of an effective Lagrangian is the Fermi Lagrangian of the $\beta$-decay. As we know today, this Lagrangian is generated by the exchange of the virtual charged $W^\pm$-bosons between $e - \nu$ and $p - n$ pairs. It is a product of the Fermi constant which has dimension $M^{-2}$ and the dimension six four-fermion operator.

This Lagrangian coincides with the Weinberg effective Lagrangian (36). The matrix $\frac{1}{\Lambda} X'$ is given by the relation

$$\frac{1}{\Lambda} X'_{l_1 l_2} = \sum_i y'_{l_1 i} \frac{1}{M_i} y'_{l_2 i} \tag{47}$$

After the spontaneous symmetry breaking from (46) we find the following Majorana mass term

$$\mathcal{L}^{\mathrm{M}} = -\frac{1}{2} \sum_{l_1, l_2} \bar{\nu}_{l_1 L} \left( \sum_i y_{l_1 i} \frac{v^2}{M_i} y_{l_2 i} \right) (\nu_{l_2 L})^c + \mathrm{h.c.}. \tag{48}$$

Here $y = V_L^\dagger y'$ where the matrix $V_L$ connects flavor and primed neutrino fields $(\nu'_L = V_L \nu_L)$.

It follows from (48) that the scale of a new lepton-number violating physics is determined by masses of heavy Majorana leptons. In spite for uncertainties connected with Yukawa coupling constants $y_{li}$, it is natural to assume that $M_i \gg v$. Let us notice that the mechanism of the generation of neutrino masses, we have considered, is equivalent to the standard seesaw mechanism [33].

The effective Lagrangian (seesaw) mechanism of the neutrino mass generation imply that

1. neutrinos with definite masses $\nu_i$ are Majorana particles. Investigation of the neutrinoless double $\beta$-decay of some even-even nuclei is the most sensitive way of determination of the nature of neutrinos with definite masses. The probability of this process is proportional to the effective Majorana mass $m_{\beta\beta} = \sum_{i=1}^{3} U_{ei}^2 m_i$. From existing data it follows that $|m_{\beta\beta}| \leq (1.4 - 4.5) \; 10^{-1}$ eV. In future experiments the sensitivity $|m_{\beta\beta}| \simeq$ a few $10^{-2}$ eV will be reached (see review [34])

2. the number of neutrinos with definite masses must be equal to the number of the flavor neutrinos (three), i.e. no transitions of flavor neutrinos into sterile states are allowed. Indications in favor of such transitions were obtained in several short baseline experiments: LSND ($\bar{\nu}_\mu \to \bar{\nu}_e$), MiniBooNE ($\nu_\mu \to \nu_e$, $\bar{\nu}_\mu \to \bar{\nu}_e$), reactor ($\bar{\nu}_e \to \bar{\nu}_e$) and source ($\nu_e \to \nu_e$). However, in the recent experiments (MINOS, DayaBay, IceCube) no indications in favor of transitions into sterile states were found and strong tension with old data were obtained. More than 20 new accelerator, reactor and source experiments on the search for sterile neutrinos are in preparation at present (see [35, 36]).

3. heavy Majorana leptons with masses much larger than $v$ must exist. Such leptons can be produced in the early Universe. Their $CP$ violating decays is one of the most attractive explanation of the barion asymmetry of the Universe (see review [37]).

# 5   Conclusion

We reviewed here briefly the status of neutrino mixing and oscillations.

We stressed that from the success of the Standard Model we can conclude that in the framework of general principles, the Standard Model is based on, Nature chooses the simplest possibilities. Massless, two-component, Weyl particle is the simplest possibility for the Standard Model neutrino.

There is one possible lepton number violating effective Lagrangian which (after spontaneous symmetry breaking) generates the Majorana neutrino mass term, the only possible neutrino mass term in the case of the left-handed neutrino fields. Neutrino masses in the effective Lagrangian approach are naturally small because a new, lepton-number violating scale $\Lambda$ is much larger than the electroweak scale $v$. The effective Lagrangian which generate the neutrino mass term is the only effective Lagrangian of the dimension five (proportional to $\frac{1}{\Lambda}$). This means that *neutrino masses are the most sensitive probe of a new physics at a scale which is much larger than the electroweak scale.*

# References

[1] B. Pontecorvo, J.Exptl. Theoret. Phys. **33**, 549(1957) [Sov. Phys. JETP **6**, 429(1958)]; J.Exptl. Theoret. Phys. **34**, 247(1958) [Sov. Phys. JETP **7**, 172(1958)].

[2] V. Gribov and B. Pontecorvo, Phys. Lett. **B28**, 493 (1969).

[3] S.M. Bilenky and B. Pontecorvo, Phys. Rep. **41**, 225 (1978).

[4] Y. Fukuda *et al.*, Super-Kamiokande Collaboration , Phys. Rev.Lett. **81**, 1562 (1998).

[5] Q. R. Ahmad *et al.* , SNO Collaboration, Phys. Rev. Lett. **89**, 011301 (2002).

[6] T. Araki *et al.* ,KamLAND Collaboration, Phys. Rev. Lett.**94**, 081801 (2005).

[7] B. T. Cleveland *et al.*, Astrophys. J. **496**, 505 (1998).

[8] Y. Fukuda *et al.*, Kamiokande, Phys. Rev. Lett. **77** , 1683 (1996).

[9] M. Altmann*et al.*, GNO Collaboration, Phys. Lett. **B616**, 174 (2005).

[10] J. N. Abdurashitov *et al.*, SAGE Collaboration, J. Exp. Theor.Phys. **95**, 181 (2002).

[11] M. H. Ahn *et al.*, K2K Collaboration, Phys. Rev. **D74**, 072003 (2006).

[12] P. Adamson *et al.*, MINOS Collaboration, Phys. Rev. Lett. **110**, 251801, (2013).

[13] K. Abe *et al.*, T2K Collaboration, Phys. Rev. Lett. **112**, 18180 (2014).

[14] P. Adamson *et al.*, NOvA Collaboration, arXiv:1701.05891.

[15] F. An *et al.*, Daya Bay Collaboration, Phys. Rev. Lett. **112**, 061801, (2014).

[16] S. B. Kim *et al.*, RENO Collaboration, Phys. Rev. Lett. **108**, 191802, (2012).

[17] Y. Abe *et al.*, Double Chooz Collaboration, Phys. Lett. **B723**, 66 (2013).

[18] G. Bellini *et al.*, BOREXINO Collaboration, Nature. **512**, 383 (2014).

[19] S. M. Bilenky and S.T. Petcov, Rev.Mod.Phys. **59**, 671 (1987).

[20] Z. Maki, M. Nakagava and S. Sakata, Prog. Theor. Phys. **28**, 870 (1962).

[21] S. M. Bilenky, F. von Feilitzsch and W. Potzel, J. Phys. **G 38**, 115002 (2011).

[22] S. M. Bilenky, J. Hosek and S.T. Petcov, Phys. Lett. **94**, 495 (1980).

[23] F. An *et al.*,JUNO Collaboration, J. Phys. G **43** no.3, 030401 (2016), arXiv:1507.05613.

[24] S. B. Kim, Nucl. Part. Phys. Proc. **265-266**, 93 (2015), arXiv:1412.2199.

[25] I. Esteban, M. C. Gonzalez-Garcia, M. Maltoni, I. Martinez-Soler and T. Schwetz, JHEP **1701**, 087 (2017), arXiv:1611.01514.

[26] L. D. Landau, Nucl. Phys. **3** , 127 (1957).

[27] T. D. Lee and C. N. Yang, Phys. Rev. **105**, 1671 (1957).

[28] A. Salam, Nuovo Cim. **5** , 299 (1957).

[29] M. Goldhaber, L. Grodzins and A. W. Sunyar, Phys. Rev. **109**, 1015 (1958).

[30] F. Englert, R. Brout, Phys. Rev. Lett. **13**, 321 (1964).

[31] P. W. Higgs, Phys. Lett. **12**, 132 (1964).

[32] S. Weinberg, Phys. Rev. Lett. **19**, 1264 (1967).

[33] P. Minkowski, Phys. Lett. **B 67**, 421(1977); M. Gell-Mann, P. Ramond and R. Slansky, in *Supergravity*, p. 315, edited by F. van Nieuwenhuizen and D. Freedman, North Holland, Amsterdam, (1979); T. Yanagida, Proc. of the *Workshop on Unified Theory and the Baryon Number of the Universe*, KEK, Japan, (1979); S.L. Glashow, NATO Adv.Study Inst. Ser. B Phys. **59**, 687 (1979); R.N. Mohapatra and G. Senjanović, Phys. Rev. **D23**, 165 (1981).

[34] S. M. Bilenky and C. Giunti, Int. J. Mod. Phys. A **30** no.04n05, 1530001 (2015), arXiv:1411.4791.

[35] C. Giunti, M. Laveder, Y.F. Li, H.W. Long, Phys.Rev. **D88**, 073008 (2013), arXiv:1308.5288.

[36] J. Kopp, P. A. N. Machado, M. Maltoni, T. Schwetz, JHEP **1305**, 050 (2013), arXiv:1303.3011.

[37] S. Davidson , E. Nardi, Y. Nir, Phys. Rept. **466**, 105 (2008), arXiv:0802.2962.

# Dark Matter Particles in the Galactic Halo

R. Bernabei[a,b,1], P. Belli[a,b], A. Di Marco[a,b], V. Merlo[a,b], F. Montecchia[b,2], F. Cappella[c,d], A. d'Angelo[c,d], A. Incicchitti[c,d], V. Caracciolo[e], R. Cerulli[e], C.J. Dai[f], H.L. He[f], H.H. Kuang[f], X.H. Ma[f], X.D. Sheng[f], R.G. Wang[f], Z.P. Ye[f,g]

[a]*Dipartimento di Fisica, Università di Roma "Tor Vergata", I-00133 Rome, Italy*

[b]*INFN – Tor Vergata, I-00133 Rome, Italy*

[c]*Dipartimento di Fisica, Università di Roma "La Sapienza", I-00185 Rome, Italy*

[d]*INFN – Roma, I-00185 Rome, Italy*

[e]*INFN, Laboratori Nazionali del Gran Sasso, I-67010 Assergi AQ, Italy*

[f]*Key Laboratory of Particle Astrophysics, IHEP, 100049 Beijing, P. R. China*

[g]*University of Jing Gangshan, Ji'an, Jiangxi, China*

**Abstract**

Many experimental observations and theoretical arguments have pointed out that a large fraction of the Universe is composed by Dark Matter (DM) particles. Many possibilities are open on the nature and interaction types of such relic particles. Here main results, obtained by exploiting the model independent DM annual modulation signature for the presence of DM particles in the galactic halo by DAMA, are summarized. Some other recent efforts and results on DM investigation are mentioned as well.

[1]rita.bernabei@roma2.infn.it

[2]also Dip. di Ingegneria Civile e Ingegneria Informatica, Università di Roma "Tor Vergata", I-00133 Rome, Italy

# 1 Introduction

Experimental observations and theoretical arguments pointed out that most of the matter in the Universe has a non baryonic nature and is in form of DM particles. Many candidates, having different nature and with different and various interaction types, have been proposed as DM particles in theories beyond the Standard Model of particle physics. Depending on the DM candidate, the interaction processes can be various. Moreover, many experimental and theoretical uncertainties exist and must be properly considered in a suitable interpretation and comparison among experiments aiming the direct detection of DM particles.

Large efforts are dedicated all over the world to investigate the DM with different strategies and techniques that can give complementary information. In particular, the DM indirect search – that is the study of possible products either of decay or of annihilation in the galactic halo or in celestial body of some DM candidate – is performed as by-product of experiments located underground, under-water, under-ice, or in space. The interpretation of such a study is strongly dependent on the chosen assumptions for the modeling of the background and is restricted to some DM candidates with peculiar features and within some particular scenario. On the other hand, experiments at accelerators may prove – when they can state a solid model independent result – the existence of some possible DM candidates, but they could never credit by themselves that a certain particle is a/the only solution for DM particle(s). Moreover, DM candidate particles and scenarios (even e.g. in the case of the neutralino candidate) exist which cannot be investigated at accelerators.

In order to pursue a widely sensitive direct detection of DM particles in the galactic halo, a model independent approach, a ultra-low-background suitable target material, a very large exposure and the full control of running conditions are strictly necessary.

# 2 DM model independent signature

To obtain a reliable signature for the presence of DM particles in the galactic halo, it is necessary to exploit a suitable model independent signature: with the present technology, one feasible and able to test a large range of cross sections and of DM particle halo densities, is the so-called DM annual modulation signature [1]. The annual modulation of the signal rate originates from the Earth revolution around the Sun. In fact, as a consequence of its annual revolution around the Sun, which is moving in the Galaxy traveling with respect to the Local Standard of Rest towards the star Vega

near the constellation of Hercules, the Earth should be crossed by a larger flux of DM particles around ∼2 June (when the Earth orbital velocity is summed to the one of the solar system with respect to the Galaxy) and by a smaller one around ∼2 December (when the two velocities are subtracted). Thus, this signature has a different origin and peculiarities than effects correlated with seasons (consider the expected value of the phase as well as the other requirements listed below). This DM annual modulation signature is very distinctive since the effect induced by DM particles must simultaneously satisfy all the following requirements: (1) the rate must contain a component modulated according to a cosine function; (2) with one year period; (3) with a phase that peaks roughly around ∼ 2nd June; (4) this modulation must be present only in a well-defined low energy range, where DM particles can induce signals; (5) it must be present only in those events where just a single detector, among all the available ones in the used set-up, actually "fires" (*single-hit* events), since the probability that DM particles experience multiple interactions is negligible; (6) the modulation amplitude in the region of maximal sensitivity has to be $\lesssim 7\%$ in case of usually adopted halo distributions, but it may be significantly larger in case of some particular scenarios such as e.g. those in Ref. [2, 3]. This signature is model independent and might be mimicked only by systematic effects or side reactions able to simultaneously satisfy all the requirements given above; no one is available. At present status of technology it is the only DM model independent signature available in direct DM investigation that can be effectively exploited.

# 3 DAMA DM annual modulation results with highly radiopure NaI(Tl)

The DM annual modulation signature has been exploited with large exposure – using highly radiopure NaI(Tl) as target material – by the former DAMA/NaI ($\simeq$ 100 kg sensitive mass) experiment [4, 5, 6, 7, 8, 9, 10, 11, 12, 13], and by the currently running DAMA/LIBRA ($\simeq$ 250 kg sensitive mass) [14, 15, 16, 17, 18, 19, 20, 21, 22, 23, 24, 25, 26, 27, 28, 29, 30], within the DAMA project. The DAMA project is dedicated to the development and use of low background scintillators for underground physics.

In particular, the experimental observable in DAMA experiments is the modulated component of the signal in NaI(Tl) target and not the constant part of it, as done in the other approaches.

The full description of the DAMA/LIBRA set-up and performances during the phase1 and phase2 (presently running) and other related arguments

have been discussed in details in Refs. [14, 15, 16, 17, 19, 20, 26, 21, 30] and references therein. Here we just remind that the sensitive part of this set-up is made of 25 highly radiopure NaI(Tl) crystal scintillators (5-rows by 5-columns matrix) having 9.70 kg mass each one. In each detector two 10 cm long UV light guides (made of Suprasil B quartz) act also as optical windows on the two end faces of the crystal, and are coupled to two low background photomultipliers (PMTs) working in coincidence at single photoelectron level. The low background 9265-B53/FL and 9302-A/FL PMTs, developed by EMI-Electron Tubes with dedicated R&Ds, were used in the phase1; for details see Ref. [14, 8, 10, 30] and references therein. The detectors are housed in a sealed low-radioactive copper box installed in the center of a low-radioactive Cu/Pb/Cd-foils/polyethylene/paraffin shield; moreover, about 1 m concrete (made from the Gran Sasso rock material) almost fully surrounds (mostly outside the barrack) this passive shield, acting as a further neutron moderator. A threefold-levels sealing system prevents the detectors to be in contact with the environmental air of the underground laboratory [14]. The light response of the detectors during phase1 typically ranges from 5.5 to 7.5 photoelectrons/keV, depending on the detector. The hardware threshold of each PMT is at single photoelectron, while a software energy threshold of 2 keV electron equivalent (hereafter keV) is used [14, 8]. Energy calibration with X-rays/$\gamma$ sources are regularly carried out in the same running condition down to few keV [14]; in particular, double coincidences due to internal X-rays from $^{40}$K (which is at ppt levels in the crystals) provide (when summing the data over long periods) a calibration point at 3.2 keV close to the software energy threshold (for details see Ref. [14]). The radiopurity, the procedures and details are discussed in Ref. [14, 15, 16, 17, 21, 30] and references therein.

The data of DAMA/LIBRA–phase1 correspond to 1.04 ton × yr collected in 7 annual cycles; when including also the data of the DAMA/NaI experiment the total exposure is 1.33 ton × yr collected in 14 annual cycles. In order to investigate the presence of an annual modulation with proper features in the data, many analyses have been carried out. All these analyses point out the presence of an annual modulation satisfying all the requirements of the signature [15, 16, 17, 21, 30]. In Fig. 1, as example, it is plotted the time behaviour of the experimental residual rate of the *single-hit* scintillation events for DAMA/LIBRA–phase1 in the (2–6) keV energy interval. When fitting the *single-hit* residual rate of DAMA/LIBRA–phase1 together with the DAMA/NaI ones, with the function: $A \cos \omega(t - t_0)$, considering a period $T = \frac{2\pi}{\omega} = 1$ yr and a phase $t_0 = 152.5$ day (June $2^{nd}$) as expected by the DM annual modulation signature, the following modulation amplitude is obtained: $A = (0.0110 \pm 0.0012)$ cpd/kg/keV, corresponding
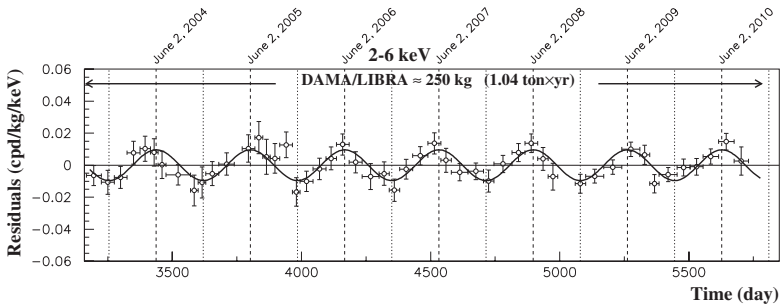
Figure 1: Experimental residual rate of the *single-hit* scintillation events measured by DAMA/LIBRA–phase1 in the (2–6) keV energy interval as a function of the time. The superimposed curve is the cosinusoidal function behaviour $A \cos \omega (t - t_0)$ with a period $T = \frac{2\pi}{\omega} = 1$ yr, a phase $t_0 = 152.5$ day (June $2^{nd}$) and modulation amplitude, $A$, equal to the central values obtained by best fit on the data points of the entire DAMA/LIBRA–phase1. The dashed vertical lines correspond to the maximum expected for the DM signal (June $2^{nd}$), while the dotted vertical lines correspond to the minimum.

to 9.2 $\sigma$ C.L..

When the period, and the phase are kept free in the fitting procedure, the modulation amplitude is $(0.0112 \pm 0.0012)$ cpd/kg/keV (9.3 $\sigma$ C.L.), the period $T = (0.998 \pm 0.002)$ year and the phase $t_0 = (144 \pm 7)$ day, values well in agreement with expectations for a DM annual modulation signal. In particular, the phase is consistent with about June $2^{nd}$ and is fully consistent with the value independently determined by Maximum Likelihood analysis [17].

For completeness, we recall that a slight energy dependence of the phase could be expected in case of possible contributions of non-thermalized DM components to the galactic halo, such as e.g. the SagDEG stream [12, 31, 32] and the caustics [33]. For more details see Ref. [17].

The modulation amplitudes singularly calculated for each annual cycle of DAMA/NaI and DAMA/LIBRA–phase1 are compatible among them and are normally fluctuating around their best fit values [15, 16, 17, 21, 30].

The DAMA/LIBRA–phase1 *single-hit* residuals of Fig. 1 and those of DAMA/NaI have also been investigated by a Fourier analysis. The data analysis procedure has been described in details in Ref. [21]. A clear peak corresponding to a period of 1 year is evident for the (2–6) keV energy interval; the same analysis in the (6–14) keV energy region shows only aliasing peaks instead. Neither other structure at different frequencies has been observed (see also Ref. [21]).

35

Absence of any other significant background modulation in the energy spectrum has been verified in energy regions not of interest for DM; e.g. the measured rate integrated above 90 keV, $R_{90}$, as a function of the time has been analysed [17]. Similar result is obtained in other energy intervals. It is worth noting that the obtained results account of whatever kind of background and, in addition, no background process able to mimic the DM annual modulation signature (that is able to simultaneously satisfy all the peculiarities of the signature and to account for the measured modulation amplitude) is available (see also discussions e.g. in Ref. [14, 15, 16, 17, 20, 21, 25, 34, 35, 36, 37, 38, 39, 40]).
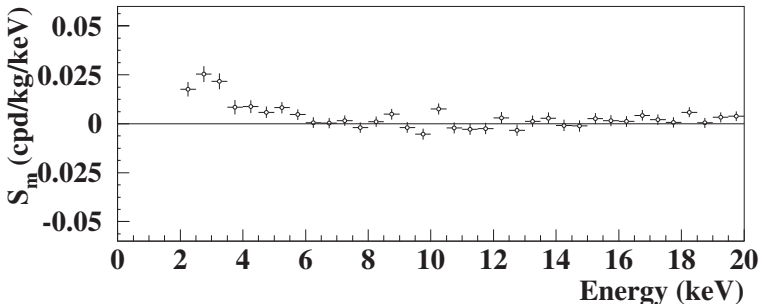


Figure 2: Energy distribution of the $S_m$ variable for the total cumulative exposure 1.33 ton×yr. The energy bin is 0.5 keV. A clear modulation is present in the lowest energy region, while $S_m$ values compatible with zero are present just above. In fact, the $S_m$ values in the (6–20) keV energy interval have random fluctuations around zero with $\chi^2$ equal to 35.8 for 28 degrees of freedom (upper tail probability of 15%).

A further relevant investigation in the DAMA/LIBRA–phase1 data has been performed by applying the same hardware and software procedures, used to acquire and to analyse the *single-hit* residual rate, to the *multiple-hit* one. In fact, since the probability that a DM particle interacts in more than one detector is negligible, a DM signal can be present just in the *single-hit* residual rate. Thus, the comparison of the results of the *single-hit* events with those of the *multiple-hit* ones corresponds practically to compare between them the cases of DM particles beam-on and beam-off. This procedure also allows an additional test of the background behaviour in the same energy interval where the positive effect is observed. In particular, while a clear modulation, satisfying all the peculiarities of the DM annual modulation signature, is present in the *single-hit* events, the fitted modulation amplitude for the *multiple-hit* residual rate is well compatible with zero:

$-(0.0005 \pm 0.0004)$ cpd/kg/keV in the energy region (2–6) keV [17]. Thus, again evidence of annual modulation with the features required by the DM annual modulation signature is present in the *single-hit* residuals (events class to which the DM particle induced events belong), while it is absent in the *multiple-hit* residual rate (event class to which only background events belong). Similar results were also obtained for the last two annual cycles of the DAMA/NaI experiment [11]. Since the same identical hardware and the same identical software procedures have been used to analyse the two classes of events, the obtained result offers an additional strong support for the presence of a DM particle component in the galactic halo.

The annual modulation present at low energy can also be pointed out by depicting – as a function of the energy – the modulation amplitude, $S_{m,k}$, obtained by maximum likelihood method considering $T = 1$ yr and $t_0 = 152.5$ day. For such purpose the likelihood function of the *single-hit* experimental data in the $k-$th energy bin is defined as: $\mathbf{L_k} = \mathbf{\Pi}_{ij} e^{-\mu_{ijk}} \frac{\mu_{ijk}^{N_{ijk}}}{N_{ijk}!}$, where $N_{ijk}$ is the number of events collected in the $i$-th time interval (hereafter 1 day), by the $j$-th detector and in the $k$-th energy bin. $N_{ijk}$ follows a Poisson's distribution with expectation value $\mu_{ijk} = [b_{jk} + S_{ik}] M_j \Delta t_i \Delta E \epsilon_{jk}$. The $b_{jk}$ are the background contributions, $M_j$ is the mass of the $j-$th detector, $\Delta t_i$ is the detector running time during the $i$-th time interval, $\Delta E$ is the chosen energy bin, $\epsilon_{jk}$ is the overall efficiency. Moreover, the signal can be written as $S_{ik} = S_{0,k} + S_{m,k} \cdot \cos \omega (t_i - t_0)$, where $S_{0,k}$ is the constant part of the signal and $S_{m,k}$ is the modulation amplitude. The usual procedure is to minimize the function $y_k = -2ln(\mathbf{L_k}) - const$ for each energy bin; the free parameters of the fit are the $(b_{jk} + S_{0,k})$ contributions and the $S_{m,k}$ parameter. Hereafter, the index $k$ is omitted for simplicity.

In Fig. 2 the obtained $S_m$ are shown in each considered energy bin (there $\Delta E = 0.5$ keV) when the data of DAMA/NaI and DAMA/LIBRA–phase1 are considered. It can be inferred that positive signal is present in the (2–6) keV energy interval, while $S_m$ values compatible with zero are present just above. In fact, the $S_m$ values in the (6–20) keV energy interval have random fluctuations around zero with $\chi^2$ equal to 35.8 for 28 degrees of freedom (upper tail probability of 15%). All this confirms the previous analyses.

As described in Ref. [15, 16, 17, 21, 30], the observed annual modulation effect is well distributed in all the 25 detectors at 95% C.L.

Among further additional tests, the analysis of the modulation amplitudes as a function of the energy separately for the nine inner detectors and the remaining external ones has been carried out for the entire DAMA/LIBRA–phase1. The obtained values are fully in agreement; in
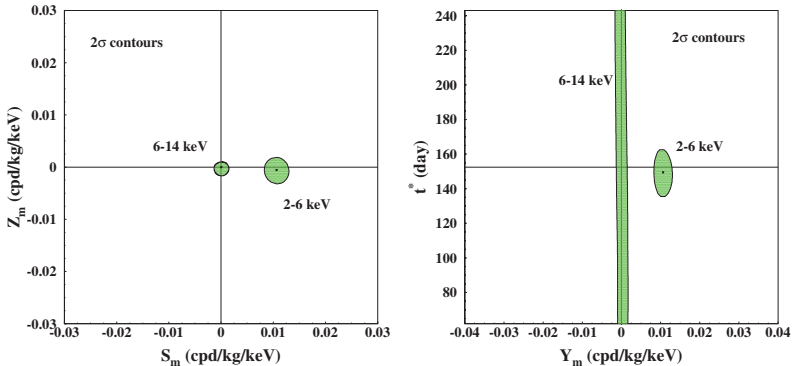
Figure 3: $2\sigma$ contours in the plane $(S_m, Z_m)$ (*left*) and in the plane $(Y_m, t^*)$ (*right*) for the (2–6) keV and (6–14) keV energy intervals. The contours have been obtained by the maximum likelihood method, considering the cumulative exposure of DAMA/NaI and DAMA/LIBRA–phase1. A modulation amplitude is present in the lower energy intervals and the phase agrees with that expected for DM induced signals. See text.

fact, the hypothesis that the two sets of modulation amplitudes as a function of the energy belong to same distribution has been verified by $\chi^2$ test, obtaining: $\chi^2/d.o.f. = 3.9/4$ and $8.9/8$ for the energy intervals (2–4) and (2–6) keV, respectively ($\Delta E = 0.5$ keV). This shows that the effect is also well shared between inner and outer detectors.

Let us, finally, release the assumption of a phase $t_0 = 152.5$ day in the procedure to evaluate the modulation amplitudes. In this case the signal can be written as:

$$
\begin{aligned}
S_{ik} &= S_{0,k} + S_{m,k}\cos\omega(t_i - t_0) + Z_{m,k}\sin\omega(t_i - t_0) \qquad (1)\\
&= S_{0,k} + Y_{m,k}\cos\omega(t_i - t^*).
\end{aligned}
$$

For signals induced by DM particles one should expect: i) $Z_{m,k} \sim 0$ (because of the orthogonality between the cosine and the sine functions); ii) $S_{m,k} \simeq Y_{m,k}$; iii) $t^* \simeq t_0 = 152.5$ day. In fact, these conditions hold for most of the dark halo models; however, as mentioned above, slight differences can be expected in case of possible contributions from non-thermalized DM components, such as e.g. the SagDEG stream [12, 31, 32] and the caustics [33].

Considering cumulatively the data of DAMA/NaI and DAMA/LIBRA–phase1 the obtained $2\sigma$ contours in the plane $(S_m, Z_m)$ for the (2–6) keV and (6–14) keV energy intervals are shown in Fig. 3–*left* while in Fig. 3–*right*

the obtained $2\sigma$ contours in the plane $(Y_m, t^*)$ are depicted.

Finally, setting $S_m$ in eq. (1) to zero, the $Z_m$ values as function of the energy have also been determined by using the same procedure. The values of $Z_m$ are well compatible with zero, as expected [15, 16, 17].

No modulation has been found in any possible source of systematics or side reactions; thus, cautious upper limits on possible contributions to the DAMA/LIBRA–phase1 measured modulation amplitude have been obtained (see Refs. [15, 16, 17, 9, 10, 11, 20, 26]). It is worth noting that they do not quantitatively account for the measured modulation amplitudes, and also are not able to simultaneously satisfy all the many requirements of the signature. Similar analyses have also been performed for the DAMA/NaI data [10, 11].

Table 1: Summary of the contributions to the total neutron flux at LNGS; the value, $\Phi_{0,k}^{(n)}$, the relative modulation amplitude, $\eta_k$, and the phase, $t_k$, of each component is reported. It is also reported the counting rate, $R_{0,k}$, in DAMA/LIBRA for *single-hit* events, in the $(2-6)$ keV energy region induced by neutrons, muons and solar neutrinos, detailed for each component. The modulation amplitudes, $A_k$, are reported as well, while the last column shows the relative contribution to the annual modulation amplitude observed by DAMA/LIBRA, $S_m^{exp} \simeq 0.0112$ cpd/kg/keV [17]. For details see Ref. [26] and references therein.

| | Source | $\Phi_{0,k}^{(n)}$ (neutrons cm$^{-2}$ s$^{-1}$) | $\eta_k$ | $t_k$ | $R_{0,k}$ (cpd/kg/keV) | $A_k = R_{0,k}\eta_k$ (cpd/kg/keV) | $A_k/S_m^{exp}$ |
|---|---|---|---|---|---|---|---|
| SLOW neutrons | thermal n ($10^{-2}-10^{-1}$ eV) | $1.08 \times 10^{-6}$ | $\simeq 0$ however $\ll 0.1$ | – | $< 8 \times 10^{-6}$ | $\ll 8 \times 10^{-7}$ | $\ll 7 \times 10^{-5}$ |
| | epithermal n (eV-keV) | $2 \times 10^{-6}$ | $\simeq 0$ however $\ll 0.1$ | – | $< 3 \times 10^{-3}$ | $\ll 3 \times 10^{-4}$ | $\ll 0.03$ |
| | fission, $(\alpha,n) \to$ n (1-10 MeV) | $\simeq 0.9 \times 10^{-7}$ | $\simeq 0$ however $\ll 0.1$ | – | $< 6 \times 10^{-4}$ | $\ll 6 \times 10^{-5}$ | $\ll 5 \times 10^{-3}$ |
| FAST neutrons | $\mu \to$ n from rock ($> 10$ MeV) | $\simeq 3 \times 10^{-9}$ | 0.0129 | end of June | $\ll 7 \times 10^{-4}$ | $\ll 9 \times 10^{-6}$ | $\ll 8 \times 10^{-4}$ |
| | $\mu \to$ n from Pb shield ($> 10$ MeV) | $\simeq 6 \times 10^{-9}$ | 0.0129 | end of June | $\ll 1.4 \times 10^{-3}$ | $\ll 2 \times 10^{-5}$ | $\ll 1.6 \times 10^{-3}$ |
| | $\nu \to$ n (few MeV) | $\simeq 3 \times 10^{-10}$ | 0.03342* | Jan. 4th* | $\ll 7 \times 10^{-5}$ | $\ll 2 \times 10^{-6}$ | $\ll 2 \times 10^{-4}$ |
| | direct $\mu$ | $\Phi_0^{(\mu)} \simeq 20\ \mu$ m$^{-2}$d$^{-1}$ | 0.0129 | end of June | $\simeq 10^{-7}$ | $\simeq 10^{-9}$ | $\simeq 10^{-7}$ |
| | direct $\nu$ | $\Phi_0^{(\nu)} \simeq 6 \times 10^{10}\ \nu$ cm$^{-2}$s$^{-1}$ | 0.03342* | Jan. 4th* | $\simeq 10^{-5}$ | $3 \times 10^{-7}$ | $3 \times 10^{-5}$ |

* The annual modulation of solar neutrino is due to the different Sun-Earth distance along the year; so the relative modulation amplitude is twice the eccentricity of the Earth orbit and the phase is given by the perihelion.

Sometimes naive statements were put forward as the fact that in nature several phenomena may show some kind of periodicity. It is worth noting that the point is whether they might mimic the annual modulation signature in DAMA/NaI and in DAMA/LIBRA, i.e. whether they might be not

only quantitatively able to account for the observed modulation amplitude but also able to contemporaneously satisfy all the requirements of the DM annual modulation signature. The same is for side reactions too. This has already been deeply investigated and discussed in DAMA literature.

In particular, in Refs. [20, 26] a quantitative evaluation why the neutrons, the muons and the solar neutrinos cannot give any significant contribution to the DAMA annual modulation results and cannot mimic this signature is outlined. Table 1 summarizes the safety upper limits on the contributions to the observed modulation amplitude due to the total neutron flux at LNGS, either from $(\alpha, n)$ reactions, from fissions and from muons' and solar-neutrinos' interactions in the rocks and in the lead around the experimental set-up; the direct contributions of muons and solar neutrinos are reported there too.

No systematic effects or side reactions able to account for the whole observed modulation amplitude and to simultaneously satisfy all the requirements of the exploited DM signature have been found. A detailed discussion about all the related arguments can be found in Refs. [14, 15, 16, 17, 20, 21, 25, 9, 10, 11, 26, 30].

# 4    Implications and comparisons

The long-standing annual-modulation evidence measured in DAMA experiments is model-independent, i.e. without any a-priori assumption of theoretical interpretations of the identity of DM and specifics of its interactions. It can be related to a variety of interaction mechanisms of DM particles with the detector materials and is compatible with a wide set of scenarios regarding the nature of the DM candidate and related astrophysical, nuclear and particle physics. For example, some of the scenarios available in literature and the different parameters are discussed in Refs. [10, 11, 7, 12, 4, 13, 6, 5, 15, 21, 30] and references therein, and recently e.g. in Refs. [41, 28] . Further large literature is available on the topics (see for example in Ref. [21]) and many possibilities are open.

It is worth noting that no other experiment exists, whose result can be – at least in principle – directly compared in a model-independent way with those by DAMA/NaI and DAMA/LIBRA. Some activities claim model-dependent exclusion under many largely arbitrary assumptions (see for example discussions in Ref. [10, 15, 11, 42, 43, 44]). Moreover, often some critical points exist in their experimental aspects, as mentioned above, and the existing experimental and theoretical uncertainties are generally not considered in their presented single model dependent result; moreover, implications of the DAMA results are often presented in incor-

rect/partial/unupdated way. Both the accounting of the existing uncertainties and the existence of alternative scenarios (see literature) allow one to note that model dependent results by indirect and direct experiments actually are not in conflict with the DAMA model independent result.

The model independent annual modulation effect observed by the DAMA experiments has been investigated in terms of many DM candidates. Here we just recall the recent case of a mirror-type dark matter candidates in some scenarios [28, 29].
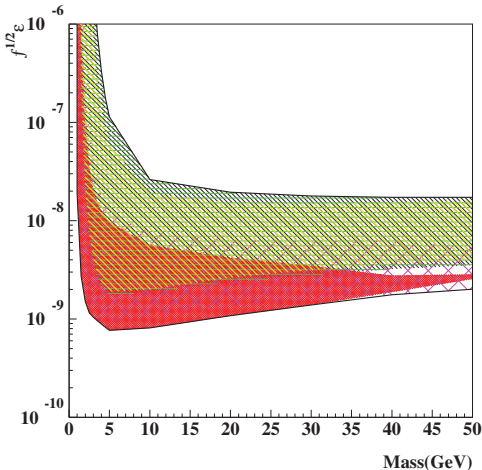


Figure 4: Allowed regions for the $\sqrt{f}\epsilon$ parameter as function of mirror hydrogen mass, obtained by marginalizing all the models for each considered scenario. The allowed intervals identify the $\sqrt{f}\epsilon$ values corresponding to C.L. larger than $5\sigma$ from the *null hypothesis*, that is $\sqrt{f}\epsilon = 0$. The allowed regions corresponding to five different scenarios are depicted in different hatching; the black line is the overall boundary; for details see Ref. [28].

In particular, in the framework of asymmetric mirror matter, the DM originates from hidden (or shadow) gauge sectors which have particles and interaction content similar to that of ordinary particles. It is assumed that the mirror parity is spontaneously broken and the electroweak symmetry breaking scale $v'$ in the mirror sector is much larger than that in the Standard Model, $v = 174$ GeV. In this case, the mirror world becomes a heavier and deformed copy of our world, with mirror particle masses scaled in different ways with respect to the masses of the ordinary particles. Then, in this scenario dark matter would exist in the form of mirror hydrogen composed of mirror proton and electron, with mass of about 5 GeV which is a rather

interesting mass range for dark matter particles.

The data analysis in the Mirror DM model framework allows the determination of the $\sqrt{f}\epsilon$ parameter (where $f$ is the fraction of DM in the Galaxy in form of mirror atoms and $\epsilon$ is the coupling constant). In the analysis several uncertainties on the astrophysical, particle physics and nuclear physics models have been taken into account in the calculation. The obtained values of the $\sqrt{f}\epsilon$ parameter in the case of mirror hydrogen atom ranges between $7.7 \times 10^{-10}$ to $1.1 \times 10^{-7}$; they are well compatible with cosmological bounds [28].

In addition, releasing the assumption $M_{A'} \simeq 5m_p$, the allowed regions for the $\sqrt{f}\epsilon$ parameter as function of $M_{A'}$, mirror hydrogen mass, obtained by marginalizing all the models for each considered scenario, are shown in Fig. 4.

# 5 Diurnal modulation

The results obtained by investigating the presence of possible diurnal variation in the low-energy *single-hit* scintillation events collected by DAMA/LIBRA–phase1 (1.04 ton × year exposure) have been analysed in terms of a DM second order model-independent effect due to the Earth diurnal rotation around its axis [25]. In particular, the data were analysed using the sidereal time referred to Greenwich, often called GMST.

This daily modulation of the rate on the sidereal time, expected when taking into account the contribution of the Earth rotation velocity, has several requirements as the DM annual modulation effect does. The interest in this signature is that the ratio $R_{dy}$ of this diurnal modulation amplitude over the annual modulation amplitude is a model independent constant at given latitude; considering the LNGS latitude one has $R_{dy} = \frac{S_d}{S_m} \simeq 0.016$.

Taking into account $R_{dy}$ and the DM annual modulation effect pointed out by DAMA/LIBRA–phase1 for *single-hit* events in the low energy region, it is possible to derive the diurnal modulation amplitude expected for the same data. In particular, when considering the (2–6) keV energy interval, the observed annual modulation amplitude in DAMA/LIBRA–phase1 is: $(0.0097 \pm 0.0013)$ cpd/kg/keV [17] and the expected value of the diurnal modulation amplitude is $\simeq 1.5 \times 10^{-4}$ cpd/kg/keV.

Fig. 5 shows the time and energy behaviour of the experimental residual rates of *single-hit* events both as a function of solar (*left*) and of sidereal (*right*) time, in the (2–6) keV interval. The used time bin is 1 (either solar or sidereal) hour.

The null hypothesis (absence of residual rate diurnal variation) has been tested by a $\chi^2$ test and run test [25]. Thus, the presence of any significant
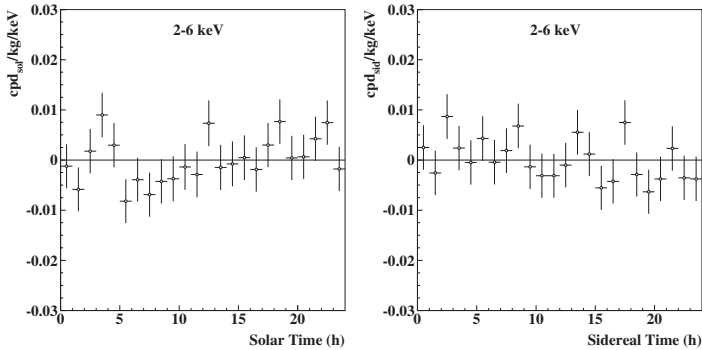
Figure 5: Experimental model-independent diurnal residual rate of the *single-hit* scintillation events, measured by DAMA/LIBRA–phase1 in the (2–6) keV energy interval as a function of the hour of the solar (*left*) and sidereal (*right*) day. The experimental points present the errors as vertical bars and the associated time bin width (1 hour) as horizontal bars. The cumulative exposure is 1.04 ton × yr. See Ref. [25] for details.

diurnal variation and of time structures can be excluded at the reached level of sensitivity (see Fig. 5).

In order to compare the experimental data with the DM diurnal effect due to the Earth rotation around its axis, the sidereal diurnal modulation amplitude of the (2–6) keV energy interval is taken into account: $A_d^{exp} = -(1.0 \pm 1.3) \times 10^{-3}$ cpd/kg/keV. Following the Feldman-Cousins procedure an upper limit can be obtained for the measured diurnal modulation amplitude: $A_d^{exp} < 1.2 \times 10^{-3}$ cpd/kg/keV (90% C.L.); thus, the effect of DM diurnal modulation (expected amplitude $\simeq 1.5 \times 10^{-4}$ cpd/kg/keV) is out the present sensitivity [25].

In conclusion, at that level of sensitivity of DAMA/LIBRA–phase1 the presence of a significant diurnal variation and of diurnal time structures in the data can be excluded for both the cases of solar and sidereal time. In particular, the sidereal diurnal modulation amplitude – expected on the basis of the DAMA DM annual modulation results and because of the Earth diurnal motion – cannot be investigated at the present sensitivity; DAMA/LIBRA–phase2, presently running, with a lower software energy threshold [19] can also offer the possibility to increase sensitivity to such an effect.

# 6 Daily effect on the sidereal time due to the shadow of the Earth

The results obtained in the investigation of possible diurnal effects for low-energy *single-hit* scintillation events of DAMA/LIBRA–phase1 have been analysed in terms of Earth Shadow Effect, a model-dependent effect that is expected for DM candidates inducing only nuclear recoils and having high cross-section ($\sigma_n$) with ordinary matter [27].

In fact a diurnal variation of the low energy rate could be expected for these specific candidates, because of the different thickness of the shield due to the Earth during the sidereal day, eclipsing the wind of DM particles. The induced effect should be a daily variation of their velocity distribution, and therefore of the signal rate measured deep underground. However, this effect is very small and would be appreciable only in case of high cross-section spin independent coupled candidates. Such candidates must constitute a little fraction ($\xi$) of the Galactic dark halo in order to fulfil the positive DAMA result on annual modulation. By the fact, this analysis decouples $\xi$ from $\sigma_n$. Considering the measured DM annual modulation effect and the absence – at the present level of sensitivity – of diurnal effects, the analysis selects allowed regions in the three-dimensional space: $\xi$, $\sigma_n$ and DM particle mass in some model scenarios; for details see Ref. [27].

# 7 ZnWO$_4$ anisotropic scintillator for Dark Matter investigation with the directionality technique

An independent evidence can be obtained by pursuing a different approach, but effective only for those DM candidate particles able to induce just nuclear recoils: the directionality [45]. This strategy is based on the correlation between the arrival direction of the DM particles (and thus of the induced nuclear recoils) and the Earth motion in the Galactic rest frame. Because of the rotation of the Milky Way, the Galactic disc passes through the halo of DM and the Earth is crossed by a wind of DM particles apparently flowing along a direction opposite to that of solar motion. Since the Earth rotates around its axis, the average direction of DM particles with respect to an observer fixed on the Earth changes during the sidereal day. Thus, the directions of the induced nuclear recoils are expected to be strongly correlated with the impinging direction of the considered DM candidates while the background events are not.

In principle, an experiment able to measure the nuclear track might be suitable to investigate the directionality. One possibility is to use low pressure gas detector (such as Time Projection Chambers, TPC) where the range of recoiling nuclei is of the order of mm. However, a realistic experiment with low pressure TPC can be limited e.g. by the necessity of an extreme operational stability, of large detector size and of a great spatial resolution in order to reach a significant sensitivity. The limitations affecting experiments aiming to measure recoil tracks, can be overcome by using the anisotropic scintillation detectors [46, 47]. In this case there is no necessity of a track detection and recognition (in solid detectors the range of recoiling nuclei is typically of order of $\mu$m). In these detectors the quenching for heavy particles and the scintillation pulse shape depend on the incoming direction of the heavy particles relatively to the crystal axes and the information on the presence of DM induced recoils is given by a peculiar variation of the measured counting rate during the sidereal day [48].

## 7.1 The main features of the ZnWO$_4$ anisotropic scintillator

Recently, measurements and R&D works have shown that the ZnWO$_4$ scintillators can offer suitable features for a DM experiment based on the directionality. In this crystal scintillator the light output for heavy particles ($p$, $\alpha$, nuclear recoils) depends on the direction of such particles with respect to the crystal axes while the response to $\gamma/\beta$ radiation is isotropic; the scintillation decay time also shows the same property. In addition to the anisotropy, the recently developed ZnWO$_4$ scintillators have very good level of radiopurity [49], and can work at energy threshold of few keV [50]. The ZnWO$_4$ offers also a high atomic weight and the possibility to realize crystals with masses of some kg [51]. Moreover, three target nuclei with very different masses are present in this detector (Zn, W and O), giving sensitivity to both small and large mass for the considered DM candidates.

Recently, radiopurity and double beta decay processes of zinc and tungsten have been further studied at LNGS using new developed ZnWO$_4$ detectors with masses $0.1 - 0.7$ kg [49, 50, 52, 53]. The growth of the crystals, the scintillation properties, the pulse shape discrimination capability, the anisotropic properties, the residual radioactive contamination and the possible applications have been deeply studied [49, 54, 55, 51, 52, 53, 56, 57]. The obtained results are very promising and an R&D to produce ZnWO$_4$ crystals having higher radiopurity is ongoing. In particular, an R&D to improve ZnWO$_4$ crystals radiopurity by re-crystallization (recently demon-

strated for CdWO$_4$ crystal [56]) is in progress.

In the measured ZnWO$_4$ scintillators the radioactive contamination is: $< 0.002$ mBq/kg for $^{228}$Th and $^{226}$Ra ($\sim 0.5$ ppt for $^{232}$Th and $\sim 0.2$ ppt for $^{238}$U, assuming the secular equilibrium of the $^{232}$Th and $^{238}$U chains), $< 0.02$ mBq/kg for $^{40}$K; the total $\alpha$ activity is 0.18 mBq/kg [49].

As previously mentioned, the study of the directionality with the ZnWO$_4$ detectors is based on the anisotropic properties of these scintillators. Fig. 6 shows the dependence of the $\alpha/\beta$ light ratio (quenching factor) on energy and direction of the $\alpha$ beam relatively to the crystal planes in a ZnWO$_4$ crystal [57].
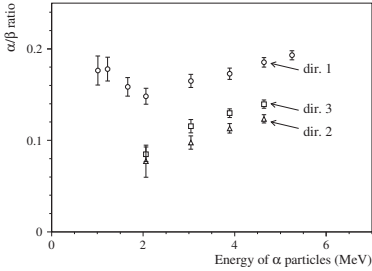


Figure 6: Dependence of the $\alpha/\beta$ ratio on the energy of $\alpha$ particles measured with ZnWO$_4$ scintillator. The crystal was irradiated in the directions perpendicular to (010), (001) and (100) crystal planes (directions 1, 2 and 3, respectively). The anisotropic behaviour of the crystal is evident [57].
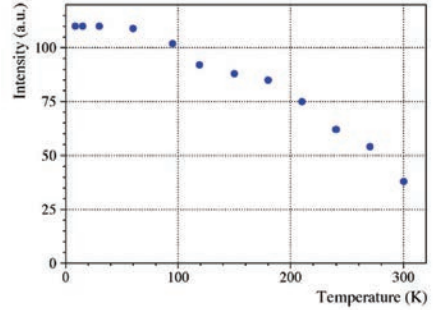


Figure 7: Dependence of the light output of the ZnWO$_4$ as a function of the temperature, for excitation with $^{241}$Am $\alpha$ particles [55].

As shown in Fig. 6, the quenching factor for $\alpha$ particles measured along direction 1 is about 1.5 times larger than that measured along direction 2, and about 1.4 times larger than that measured along direction 3. On the contrary, the anisotropy of the light response of the ZnWO$_4$ scintillator disappears in case of electron excitation. Moreover for ZnWO$_4$, as reported in Ref. [57], also the shape of the scintillation pulse depends on the type of irradiation; this feature allows one to discriminate $\gamma(\beta)$ events from those induced by $\alpha$ particles. This pulse shape discrimination capability can be of interest not only for a DM experiment but also for double beta decay searches. Measurements with a neutron beam to study the anisotropy response of the crystal for recoils at keV energy range will be performed in near future [58].

Another feature of this scintillator, important for a DM experiment, is the relatively high light output which is about 13-20% of the Na(Tl) scintillator. It has been observed that the light output largely increase when the crystal scintillator working temperature is decreased [55] (see Fig. 7).

# 8   Conclusions and Perspectives

The cumulative exposure with ultra low background NaI(Tl) target by the former DAMA/NaI and DAMA/LIBRA–phase1 is 1.33 ton × yr (orders of magnitude larger than those available in the field) giving a model-independent positive evidence at 9.3 $\sigma$ C.L. for the presence of DM candidates in the galactic halo with full sensitivity to many kinds of astrophysical, nuclear and particle physics scenarios. Other rare processes have also been searched for by DAMA/LIBRA-phase1 (see for details Refs. [22, 23, 24]) and by DAMA/NaI [60].

After the phase1, an important upgrade has been performed when all the PMTs have been replaced with new ones having higher Quantum Efficiency (QE). In this new configuration a software energy threshold below 2 keV has been reached [19]. DAMA/LIBRA is thus in its phase2, and after optimization periods it is continuously running with higher sensitivity.

The main goals of DAMA/LIBRA–phase2 are: (1) to increase the experimental sensitivity thanks to the lower software energy threshold of the experiment; (2) to improve the corollary investigation on the nature of the DM particle and related astrophysical, nuclear and particle physics arguments; (3) to investigate other signal features; (4) to investigate rare processes other than DM with high sensitivity.

Future improvements to increase the sensitivity of the set-up can be considered by using high QE and ultra-low background PMTs directly coupled to the NaI(Tl) crystals. In this way a further large improvement in the light collection and a further lowering of the software energy threshold would be obtained. Thus, R&D's towards the phase3 of DAMA/LIBRA are in progress.

Finally, the perspectives of a pioneering experiment with anisotropic ZnWO$_4$ detectors to further explore, with the directionality approach, those DM candidate particles inducing just nuclear recoils have been addressed.

# 9   Acknowledgement

# References

[1] A.K. Drukier, K. Freese, and D.N. Spergel, *Phys. Rev. D* **33**, 3495 (1986); K. Freese, J. A. Frieman and A. Gould, *Phys. Rev. D* **37**, 3388 (1988).

[2] D. Tucker-Smith and N. Weiner, *Phys. Rev. D* **64**, 043502 (2001).

[3] K. Freese et al., *Phys. Rev. D* **71**, 043516 (2005); K. Freese et al., *Phys. Rev. Lett.* **92**, 11301 (2004).

[4] R. Bernabei et al., *Int. J. Mod. Phys. A* **22**, 3155 (2007).

[5] R. Bernabei et al., *Mod. Phys. Lett. A* **23**, 2125 (2008).

[6] R. Bernabei et al., *Phys. Rev. D* **77**, 023506 (2008).

[7] R. Bernabei et al., *Int. J. Mod. Phys. A* **21**, 1445 (2006).

[8] R. Bernabei et al., *Il Nuovo Cim. A* **112**, 545 (1999).

[9] R. Bernabei et al., *Eur. Phys. J. C* **18**, 283 (2000).

[10] R. Bernabei el al., *La Rivista del Nuovo Cimento* **26** n.1, 1-73 (2003).

[11] R. Bernabei et al., *Int. J. Mod. Phys. D* **13**, 2127 (2004).

[12] R. Bernabei et al., *Eur. Phys. J. C* **47**, 263 (2006).

[13] R. Bernabei et al., *Eur. Phys. J. C* **53**, 205 (2008).

[14] R. Bernabei et al., *Nucl. Instr. and Meth. A* **592**, 297 (2008).

[15] R. Bernabei et al., *Eur. Phys. J. C* **56**, 333 (2008).

[16] R. Bernabei et al., *Eur. Phys. J. C* **67**, 39 (2010).

[17] R. Bernabei et al., *Eur. Phys. J. C* **73**, 2648 (2013).

[18] P. Belli et al., *Phys. Rev. D* **84**, 055014 (2011).

[19] R. Bernabei et al., *J. of Instr.* **7**, P03009 (2012).

[20] R. Bernabei et al., *Eur. Phys. J. C* **72**, 2064 (2012).

[21] R. Bernabei et al., *Int. J. of Mod. Phys. A* **28**, 1330022 (2013).

[22] R. Bernabei et al., *Eur. Phys. J. C* **62**, 327 (2009).

[23] R. Bernabei et al., *Eur. Phys. J. C* **72**, 1920 (2012).

[24] R. Bernabei et al., *Eur. Phys. J. A* **49**, 64 (2013).

[25] R. Bernabei et al., *Eur. Phys. J. C* **74**, 2827 (2014).

[26] R. Bernabei et al., *Eur. Phys. J. C* **74**, 3196 (2014).

[27] R. Bernabei et al., *Eur. Phys. J. C* **75**, 239 (2015).

[28] A. Addazi et al, *Eur. Phys. J. C* **75**, 400 (2015).

[29] R. Cerulli et al, *Eur. Phys. J. C* **77**, 83 (2017).

[30] DAMA coll., *Int. J. of Mod. Phys. A* **31**, 1642001–11 (2016).

[31] K. Freese et al., *Phys. Rev. D* **71**, 043516 (2005); *New Astr. Rev.* **49**, 193 (2005); `astro-ph/0310334`; `astro-ph/0309279`.

[32] G. Gelmini, P. Gondolo, *Phys. Rev. D* **64**, 023504 (2001).

[33] F.S. Ling, P. Sikivie and S. Wick, *Phys. Rev. D* **70**, 123503 (2004).

[34] R. Bernabei et al., *AIP Conf. Proceed.* **1223**, 50 (2010) [`arXiv:0912.0660`].

[35] R. Bernabei et al., *J. Phys.: Conf. Series* **203**, 012040 (2010) [`arXiv:0912.4200`]; *http://taup2009.lngs.infn.it/slides/jul3/nozzoli.pdf*, talk given by F. Nozzoli.

[36] R. Bernabei et al., in the volume *Frontier Objects in Astrophysics and Particle Physics*, ed. S.I.F. (Vulcano, 2010), p. 157 [`arXiv:1007.0595`].

[37] R. Bernabei et al., *Can. J. Phys.* **89**, 11 (2011).

[38] R. Bernabei et al., *Physics Procedia* **37**, 1095 (2012).

[39] R. Bernabei et al., `arXiv:1210.6199`.

[40] R. Bernabei et al., `arXiv:1211.6346`.

[41] S. Scopel et al., `arXiv:1512.08577`, to appear in the Proceed. of the 14th Marcel Grossmann Meeting.

[42] R. Bernabei et al., in *Liquid Noble gases for Dark Matter searches: a synoptic survey* (Exorma Ed., Roma, ISBN 978-88-95688-12-1, 2009), pp. 1–53; `arXiv:0806.0011v2`.

[43] R. Bernabei et al., *Int. J. Mod. Phys. A* **30**, 1530053 (2015), 73 pages.

[44] J.I. Collar and D.N. McKinsey, `arXiv:1005.0838`; `arXiv:1005.3723`; J.I. Collar, `arXiv:1006.2031`; `arXiv:1010.5187`; `arXiv:1103.3481`; `arXiv:1106.0653`; `arXiv:1106.3559`.

[45] D.N. Spergel, *Phys. Rev. D* **37**, 1353 (1988).

[46] P. Belli et al., *In Nuovo Cim. C* **15**, 475 (1992).

[47] R. Bernabei et al., *Eur. Phys. J. C* **28**, 203 (2003).

[48] F. Cappella et al., *Eur. Phys. J. C* **73**, 2276 (2013).

[49] P. Belli et al., *Nucl. Instrum. Meth. A* **626-627**, 31 (2011).

[50] P. Belli et al., *J. Phys. G* **38**, 115107 (2011).

[51] E.N. Galashov et al., *Functional Materials* **16**, 63 (2009).

[52] P. Belli et al., *Phys. Lett. B* **658**, 193 (2008).

[53] P. Belli et al., *Nucl. Phys. A* **826**, 256 (2009).

[54] L.L. Nagornaya et al., *IEEE Trans. Nucl. Sci.* **55**, 1469 (2008).

[55] L.L. Nagornaya et al., *IEEE Trans. Nucl. Sci.* **56**, 994 (2009).

[56] A.S. Barabash et al., *Nucl. Instrum. Meth. A* **833**, 77 (2016).

[57] F.A. Danevic et al., *Nucl. Instrum. Meth. A* **544**, 553 (2005).

[58] C. Taruggi, ROM2F/2016/06.

[59] V.I. Tretyak, *Astropart. Phys.* **33**, 40 (2010).

[60] R. Bernabei et al., *Phys. Lett. B* **408**, 439 (1997); P. Belli et al., *Phys. Lett. B* **460**, 236 (1999); R. Bernabei et al., *Phys. Rev. Lett.* **83**, 4918 (1999); P. Belli et al., *Phys. Rev. C* **60**, 065501 (1999); R. Bernabei et al., *Il Nuovo Cimento A* **112**, 1541 (1999); R. Bernabei et al., *Phys. Lett. B* **515**, 6 (2001); F. Cappella et al., *Eur. Phys. J.-direct C* **14**, 1 (2002); R. Bernabei et al., *Eur. Phys. J. A* **23**, 7 (2005); R. Bernabei et al., *Eur. Phys. J. A* **24**, 51 (2005).

# Elementary particles, dark matters, cosmic rays and extended standard model

Jae - Kwang   Hwang

JJJ Physics Laboratory, Brentwood, TN 37027, USA

Three generations of leptons and quarks correspond to the lepton charges (LC) in the present work. Then, the leptons have the electric charges (EC) and lepton charges (LC). The quarks have the EC, LC and color charges (CC). Three heavy leptons and three heavy quarks are introduced to make the missing third flavor of EC. Then the three new particles which have the electric charges (EC) are proposed as the bastons (dark matters) with the rest masses of 26.121 eV/c$^2$, 42.7 GeV/c$^2$ and 1.9 10$^{15}$ eV/c$^2$. These new particles are applied to explain the origins of the astrophysical observations like the ultra-high energy cosmic rays and super-nova 1987A anti neutrino data. The 3.5 keV x ray peak observed from the cosmic x-ray background spectra is originated not from the pair annihilations of the dark matters but from the x-ray emission of the Q1 baryon atoms. The new force carrying bosons for the dark matters, leptons and quarks are introduced for the further researches.

## 1.  Introduction

The new physics search beyond standard model has been done by the extended standard models with the new particles. These new particles include the SUSY particles, techniquarks, leptoquarks, Z-prime boson, W-prime boson and heavy quarks (T, B, X and Y), sterile ν, neutralinos, X- and Y- bosons, WIMPS, axions, preons. But there are no experimental evidences for these new particles. The previously known models including the string theory and the supersymmetry model have been developed on the unquantized space. In the present work, the three-dimensional quantized space model is introduced as the new extended standard model for the new elementary particles in Tables 1 and 2. The three dark matters (B1,B2,B3), three heavy leptons (Le, Lμ, Lτ) and three heavy quarks (Q1, Q2,Q3) are introduced. The rest masses of the quarks, leptons and dark matters are calculated by using the simple equations to show the energy scales. These new particles can be indirectly searched for from the astronomical observations like the cosmic rays and cosmic gamma rays. The unsolved questions of the astronomical observations are explained by using the decays and interactions of these new particles in the present work. For example, the ultra-high energy cosmic rays are proposed to be originated from the decays and annihilations of the hadrons including the new heavy quarks (Q1,Q2,Q3). The super-nova 1987A is discussed in the relation with the B1 dark matter. And the observed 18.7 keV, 3.5 keV and 74.9 keV x-ray peaks are emitted from the Q1 baryon atoms.

## 2.  Three-dimensional quantized space model and dark matters

In Table 1, the leptons and quarks have the same properties of the three generations. Three generations separate the leptons and quarks with the same electric charges (EC). Three generations are called as the lepton charges (LC) or lepton flavors in the present work. The difference between the quarks and leptons is that the quarks have the three color flavors or three color charges (CC) of red (r), green (g) and blue (b) but the leptons do not. The quarks with the same charges of EC and LC are separated with three color charges (CC). Because the lepton charges and color charges have the three flavors, the electric charges are expected to have the three flavors. But the electric charges of the leptons and quarks have two flavors. The particles with the same lepton charges are separated with two electric charges of 0 and -1 for the leptons and 2/3 and -1/3 for the quarks. The electric charges are quantized on the basis of the electron electric charge of -1 in
Table 1. Therefore, the heavy quarks with the electric charge of -4/3 and heavy leptons with the electric charge of -2 for the third missing electric charges are added to complete the three flavors of EC, LC and CC in the quarks and leptons in Table 1. The elementary fermions in Table 1 can be explained only by the three-dimensional quantized spaces [1,2]. Each flavor corresponds to each dimensional axis in Table. 1. This work needs the further researches on the new concepts.

Table 1. Elementary fermions in the three-dimensional quantized space model. The bastons (Dark matters) interact gravitationally but not electro-magnetically with the electrons, protons and quarks because the bastons do not have the lepton and color charges.

| | Bastons (EC) | | | Leptons(EC,LC) | | | | Quarks(EC,LC,CC) | | |
|---|---|---|---|---|---|---|---|---|---|---|
| | EC | | | EC | | | | EC | | |
| X1 | -2/3 | B1 | | 0 | $\nu_e$ | $\nu_\mu$ | $\nu_\tau$ | 2/3 | u | c | t |
| X2 | -5/3 | B2 | | -1 | e | $\mu$ | $\tau$ | -1/3 | d | s | b |
| X3 | -8/3 | B3 | | -2 | Le | L$\mu$ | L$\tau$ | -4/3 | Q1 | Q2 | Q3 |
| Total | -5 | | | -3 | | | | -1 | | | |
| | Dark matters | | | LC | | | | LC | | |
| X4 | | | | -2/3 | $\nu_e$ | e | Le | 0 | u | d | Q1 |
| X5 | Each flavor (charge) | | | -5/3 | $\nu_\mu$ | $\mu$ | L$\mu$ | -1 | c | s | Q2 |
| X6 | corresponds to each | | | -8/3 | $\nu_\tau$ | $\tau$ | L$\tau$ | -2 | t | b | Q3 |
| Total | dimensional axis. | | | -5 | | | | -3 | | | |
| | | | | | | | | CC | | |
| X7 | Baryon: CC = -5 (3 quarks) | | | | | | | -2/3(r) | | |
| X8 | Meson: CC = 0 (quark - anti quark) | | | | | | | -5/3(g) | | |
| X9 | Paryon: LC = -5 (3 leptons) Koron: LC = 0 (lepton - anti lepton) | | | | | | | -8/3(b) | | |
| Total | | | | | | | | -5 | | |

Only the electric charges have been quantized on the basis of the electron electric charge of -1. First, the new heavy leptons and new heavy quarks have the electric charges of -2 and -4/3, respectively in Table 1. Then the sum of three electric charges is -3 for the leptons and -1 for the quarks. The summed electric charge (-3) of the leptons is decreased by -2 when compared with the summed electric charge (-1) of the quarks. In Table 1, systematically three particles called as the bastons are expected. The sum of three electric charges is -5 for these new particles called as bastons. The electric charges for the bastons are -2/3, -5/3 and -8/3 which make the summed electric charge of -5. The three-dimensional quantized spaces with the summed charges of -5, -3 and -1 are colored in blue, red and green, respectively in Table 1. Let's build up the three-dimensional quantized spaces of the leptons and quarks from the three-dimensional quantized space of the bastons. The three-dimensional quantized space of the bastons is in blue in Table 1. The leptons have the three-dimensional quantized spaces in red and in blue in Table 1. The quarks have the three-dimensional quantized spaces in green, in red and in blue in Table 1. Therefore, the leptons are made by adding the three-dimensional quantized space in red to the bastons. The lepton charges of the leptons are the same as the electric charges of the bastons. And the quarks are made by adding the three-dimensional quantized space in green to the leptons. The lepton charges of the quarks are the same as the electric charges of the leptons and the color charges of the quarks are the same as the lepton charges of the leptons and the electric charges of the bastons in Table 1. Therefore, all quantized charges of the elementary fermions can be assigned as shown in Table 1. Then, the lepton charges are 0, -1 and -2 for the quarks and -2/3, -5/3 and -8/3 for the leptons. And the color charges for quarks are -2/3, -5/3 and -8/3. Therefore, the leptons and quarks should be described as (EC,LC) and (EC,LC,CC), respectively as shown in Table 1. Therefore, the bastons are described as (EC). These new particles have the properties the same as the dark matters have. These new particles interact gravitationally but not electromagnetically with the electrons, protons and quarks because the bastons do not have the lepton and color charges. Then, the bastons are the dark matters. Also, the leptons interact gravitationally but not electromagnetically with the quarks because the leptons do not have the color charges. The leptons can interact electromagnetically with the hadrons like protons because the hadrons of the mesons and baryons have the color charges of 0 and -5, respectively [1,2]. It is called as the hadronization.

The leptons have the electric charges of 0 for the neutrinos and -1 for the electron, muon and tau in terms of the standard model. The weak force carrying bosons have the electric charges of 0 for the Z boson and -1 for the W$^-$ boson in terms of the standard model. These Z and W$^-$ bosons do not care about the lepton charges. These Z and W$^-$ bosons are separated as the Z(0,LC) and W(-1,LC) bosons with the three generations (three lepton charges) in the present extended standard model of Table 2. The rest masses of the Z and W$^-$ bosons in the standard model correspond to the rest masses of the Z(0,0) and W(-1,0) bosons in Table 2,

respectively. The quarks have the electric charges of 2/3 for the u, c and t quarks and -1/3 for the d, s and b quarks in terms of the standard model. The strong force carrying bosons have the electric charges of 0 and double color charges for the massless gluon bosons in terms of the standard model. The electric force carrying boson of the photon has the electric charge of 0. But in the present extended standard model, the new heavy leptons have the electric charge of -2 and the new heavy quarks have the electric charge of -4/3. And the force carrying bosons with the electric charges of 0, -1 and -2 are possible as shown in Table 2. Because the lepton charges and color charges are quantized in Table 1, the corresponding force carrying Z, W and Y bosons for the bastons, leptons and quarks are newly proposed to have the EC, LC and CC charges of 0, -1 and -2, respectively, in Table 2.

Table 2. Complete table of the elementary bosons in the three-dimensional quantized space model.

| | Dark matter force | | | Weak force (EC,LC) | | | | Strong force (EC,LC,CC) | | | |
|---|---|---|---|---|---|---|---|---|---|---|---|
| | EC | | | EC | | | | EC | | | |
| X1 | 0 | Z(0) | | 0 | Z(0,0) | Z(0,–1) | Z(0,–2) | 0 | Z(0,0) | Z(0,–1) | Z(0,–2) |
| X2 | -1 | W(-1) | | -1 | W(-1,0) | W(-1,-1) | W(-1,-2) | -1 | W(-1,0) | W(-1,-1) | W(-1,-2) |
| X3 | -2 | Y(-2) | | -2 | Y(-2,0) | Y(-2,-1) | Y(-2,-2) | -2 | Y(-2,0) | Y(-2,-1) | Y(-2,-2) |
| Total | -3 | | | -3 | | | | -3 | | | |
| | | | | LC | | | | LC | | | |
| X4 | | | | 0 | Z(0,0) | W(–1,0) | Y(–2,0) | 0 | Z(0,0) | W(–1,0) | Y(–2,0) |
| X5 | | | | -1 | Z(0,-1) | W(-1,-1) | Y(-1,-1) | -1 | Z(0,-1) | W(-1,-1) | Y(-1,-1) |
| X6 | | | | -2 | Z(0,-2) | W(-1,-2) | Y(-2,-2) | -2 | Z(0,-2) | W(-1,-2) | Y(-2,-2) |
| Total | | | | -3 | | | | -3 | | | |
| | | | | | | | | CC | | | |
| X7 | Z, W-, gluons (SM) → | | | | | | | 0 | | | |
| X8 | Z(0,LC),W(-1,LC), Z(0,0,CC) (ESM) | | | | | | | -1 | | | |
| X9 | Z/W/Y(EC,LC,0) ←→ Z/W/Y(EC,LC) | | | | | | | -2 | | | |
| Total | Z/W/Y(EC,0) ←→ Z/W/Y(EC) | | | | | | | -3 | | | |
| | Z/W/Y(-1,0)CC(-2) = Z/W/Y(-1,0,-2) | | | | | | | | | | |

By using Tables 1 and 2, all interactions between the elementary particles can be successfully described by using these massive Z, W and Y bosons with the short force range in Fig. 1. In Fig. 1, the Z(0,0,CC) bosons with CC values of 0, -1 and -2 can play the same roles as the gluons do. In fact the massless gluons are replaced with the massive Z/W/Y(EC,LC,CC) bosons in Table 2. Then, the strong force carrying bosons are Z/W/Y(EC,LC,CC) bosons for the quarks, and the weak force carrying bosons are Z/W/Y(EC,LC) bosons for the leptons. And the dark matter force carrying bosons are newly proposed by the Z/W/Y(EC) bosons for the bastons in Table 2. In the present extended standard model, the three charge conservations of EC, LC and CC should be considered. The standard model has

the conservation rules of many quantum numbers such as baryon number, lepton number, B-L symmetry, hyper charge, weak charge, electric charge, color charge, quark flavor quantum number, lepton family number and x-charge. However, the present model has only one conservation rule of EC, LC and CC charges.

Because the neutrinos have the nonzero lepton charges in Table 1, the neutrinos are not the Majorana particles. Therefore, the neutrinoless double beta decay is not possible. The dark matters can interact with the leptons as shown in Fig. 2. The B1-e and B1- $\mu$ interactions in Fig. 2 can enhance the numbers of the cosmic $\nu_e$ and $\nu_\mu$ neutrinos when the electrons and muons get through the dense dark matter clouds near the galaxy center. Also, the B1 dark matters can be produced from the LHC accelerator. The observation of the enhanced $\nu_e$ neutrinos will be the indirect evidence of the B1 dark matters produced from the LHC accelerator. The LHC and cosmic neutrino experiments will be interesting.
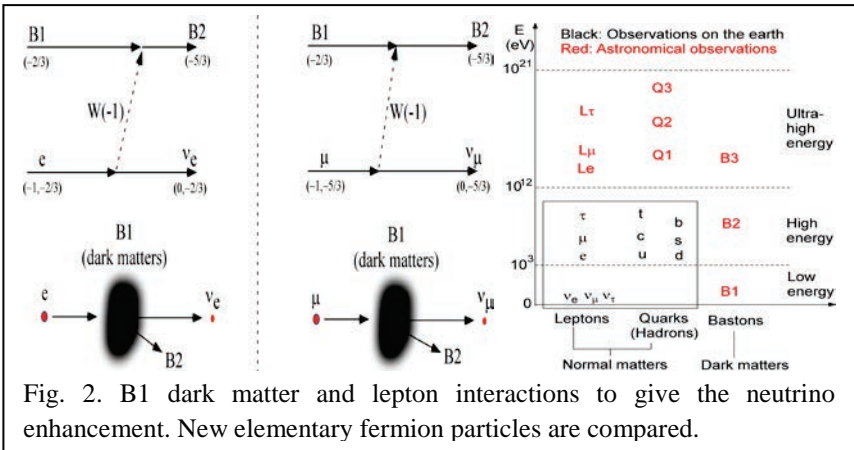


Fig. 2. B1 dark matter and lepton interactions to give the neutrino enhancement. New elementary fermion particles are compared.

## 3. Origins of high and ultra-high energy cosmic rays

And the rest mass energies of the leptons with the charge configuration of (EC,LC) and bastons (dark matters) with the charge configuration of (EC) are calculated by using the simple equations under the assumptions of E(B2) = 42.7 GeV and E($\nu_\tau$) = 0.1 eV.

F(EC,LC) = -23.24488 + 7.26341|EC| - 1.13858EC$^2$ + 0.62683|LC| + 0.22755LC$^2$

E = 8.1365 $10^{38+2F}$ eV for leptons

E = 17.1501 $10^{38+2F}$ eV for bastons (dark matters)

Only the EC and LC charges of the leptons and bastons are used for the calculations of the rest masses. The rest masses of the leptons and bastons (dark matters) are compared with the experimental values in Table 3. The rest mass energies of the leptons and dark matters are calculated in order to show the energy scales of these particles by using the simple equations. The parameter values are assigned by fitting the experimental rest mass energies. Then, the unknown neutrino masses and the masses of the heavy leptons (Le, Lμ, Lτ) can be calculated in Table 3. And the masses of the B1 and B3 dark matters can be calculated, too. Also, it is assumed that the rest mass energies of Q1, Q2 and Q3 quarks correspond to the energies of the first knee, second knee and ankle parts of the ultra-high energy cosmic ray spectra, respectively [1,3]. And the color charge effects on the rest mass energies of the quarks are assumed to be negligibly small. Then $E = 10^F$ eV and $F(EC,LC) = 10.34076 - 16.01455|EC| + 15.02553 EC^2 + 2.14 |LC| + 0.005 LC^2$ for Q1,Q2 and Q3 quarks. The obtained rest mass energies are $E(Q1) = 5 \cdot 10^{15}$ eV, $E(Q2) = 7 \cdot 10^{17}$ eV and $E(Q3) = 10^{20}$ eV.

Table 3. Rest masses of the leptons and bastons(dark matters) are calculated and compared with the experimental values [1]. $E=mc^2$.

| (EC,LC) | $E_{exp}$ (eV) | $E_{calc}$ (eV) | (EC,LC) | $E_{exp}$ (eV) | $E_{calc}$ (eV) |
|---|---|---|---|---|---|
| $\nu_e$(0,-2/3) | ? | $2.876 \cdot 10^{-7}$ | e(-1,-2/3) | $5.11 \cdot 10^5$ | $5.11 \cdot 10^5$ |
| $\nu_\mu$(0,-5/3) | ? | $5.947 \cdot 10^{-5}$ | μ(-1,-5/3) | $1.057 \cdot 10^8$ | $1.057 \cdot 10^8$ |
| $\nu_\tau$(0,-8/3) | ? | $1.000 \cdot 10^{-1}$ | τ(-1,-8/3) | $1.777 \cdot 10^9$ | $1.777 \cdot 10^9$ |
| Le(-2,-2/3) | $10^{12-14}$ | $2.533 \cdot 10^{13}$ | B1(-2/3) | ? | 26.121 |
| Lμ(-2,-5/3) | ? | $5.239 \cdot 10^{15}$ | B2(-5/3) | $4.27 \cdot 10^{10}$ | $4.27 \cdot 10^{10}$ |
| Lτ(-2,-8/3) | ? | $8.811 \cdot 10^{18}$ | B3(-8/3) | ? | $1.948 \cdot 10^{15}$ |

In Fig. 3, the e - e$^+$, and B2- anti B2 plots are shown for the comparison. The 42.7(7) GeV peak was identified in the gamma-ray spectrum from the Fermi Large Area Telescope (LAT) in the directions of 16 massive nearby Galaxy Clusters [4]. The 42.7 GeV peak is proposed as the B2 – anti B2 annihilation peak. Then, the rest mass of the B2 dark matter particle is 42.7(7) GeV/c$^2$. And the enhanced intensity was observed around 42.7 GeV for the gamma ray spectra of supernova remnant (SNR), W44, as measured with the Fermi-LAT. This might be the B2 – anti B2 annihilation peak [5].

The calculated rest mass energy of the B1 dark matter is 26.121 eV. It will be interesting to look for the 26.121 eV peak at the cosmic x-ray. The calculated rest mass energies of three neutrinos are $2.876 \ 10^{-7}$ eV for $\nu_e$, $5.947 \ 10^{-5}$ eV for $\nu_\mu$ and $1.000 \ 10^{-1}$ eV for $\nu_\tau$ in Table 3. It will be interesting to confirm these rest mass energies of three neutrinos in Table 3. The rest masses of the elementary fermions depend on both of EC and LC according to the above mass energy equations. The leptons are separated into three groups. First group is made of the three neutrinos with EC=0 which have the low energy range. Second group is made of the electron, muon and tau lepton with EC=-1 which have the high energy range. The third group is made of the Le, Lμ and Lτ leptons with EC=-2 which have the ultra-high energy range. The B1 dark matter with EC=-2/3 has the rest mass energy between the first group with EC=0 and second group with EC=-1. The B2 dark matter with EC=-5/3 has the rest mass energy between the second group with EC=-1 and third group with EC=-2. The B3 dark matter with EC=-8/3 has the rest mass energy similar to those of the third group with EC=-2.
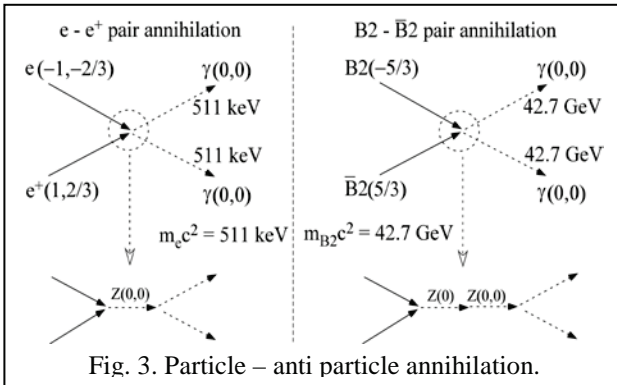


Fig. 3. Particle – anti particle annihilation.

The electron-positron annihilation peaks associated with the outburst of the microquasar V404 Cygni [6] were identified at the energy range of $4 \ 10^5 – 2 \ 10^6$ eV consistent with the rest mass energy ($5.11 \ 10^5$ eV) of the electron. The possible Le – anti Le annihilation peak was identified at the energy range of $10^{12-14}$ eV in the TeV gamma ray spectrum from RXJ1713.7-3946 with HESS and Fermi-Lat data [7]. The calculated rest mass energy ($2.534 \ 10^{13}$ eV) is consistent with the energy of the observed peak in Table 3. The high and ultra-high energy cosmic rays with the energy higher than $10^9$ eV are originated from the decay and annihilations of the hadrons including the Q1, Q2 and Q3 quarks with the possible rest masses of $10^{15-20}$ eV/c$^2$ and the heavy leptons as shown in Figs. 4 and 5 [8,9].

## Several sources of high and ultra high energy cosmic rays
## Decays of baryons and leptons

$p$ (1,0,−5) ⟶ $n$ (0,0,−5) + $e^+$ (1,2/3) + $\nu_e$ (0,−2/3)

$n$ (0,0,−5) ⟶ $p$ (1,0,−5) + $e$ (−1,−2/3) + $\bar\nu_e$ (0,2/3)

I ⟶ $e^+/e$ — Low energy beta decay spectra

---

$Le$ (−2,−2/3) ⟶ $2e$ 2(−1,−,2/3) + $\bar\nu_e$ (0,2/3)

$\overline{Le}$ (2,2/3) ⟶ $2e^+$ 2(1,2/3) + $\nu_e$ (0,−2/3)

I ⟶ $e^+/e$ , $\bar p/p$ neutrinos — High and ultra high energy $e^+/e$, $\bar p/p$ and neutrinos cosmic ray spectra

$L\mu$ (−2,−5/3) ⟶ $Le$ (−2,−2/3) + $e^+$ (1,2/3) + $\mu$ (−1,−5/3) ; $Le$ (−2,−2/3) + $\bar\nu_e$ (0,2/3) + $\nu_\mu$ (0,−5/3)

$L\tau$ (−2,−8/3) ⟶ $L\mu$ (−2,−5/3) + $e^+$ (1,2/3) + $\mu$ (−1,−5/3) ; $L\mu$ (−2,−5/3) + $\bar\nu_e$ (0,2/3) + $\nu_\mu$ (0,−5/3)

---

(Q1,d,d) (−2,0,−5) ⟶ $p$ (1,0,−5) + $3e$ 3(−1,−2/3) + $3\bar\nu_e$ 3(0,2/3)   (Q1,u,u) (0,0,−5) ⟶ $p$ (1,0,−5) + $e$ (−1,−2/3) + $\bar\nu_e$ (0,2/3)

⟶ $n$ (0,0,−5) + $2e$ 2(−1,−2/3) + $2\bar\nu_e$ 2(0,2/3)    ⟶ $n$ (0,0,−5) + $\nu_e$ (0,−2/3) + $\bar\nu_e$ (0,2/3)

(Q2,d,d) (−2,−1,−5) ⟶ (Q1,d,d) (−2,0,−5) + $e^+$ (1,2/3) + $\mu$ (−1,−5/3) ; (Q1,d,d) (−2,0,−5) + $\bar\nu_e$ (0,2/3) + $\nu_\mu$ (0,−5/3)

(Q3,d,d) (−2,−2,−5) ⟶ (Q2,d,d) (−2,−1,−5) + $e^+$ (1,2/3) + $\mu$ (−1,−5/3) ; (Q2,d,d) (−2,−1,−5) + $\bar\nu_e$ (0,2/3) + $\nu_\mu$ (0,−5/3)

$(\overline{Q3,d,d})$ (2,2,5) ⟶ $(\overline{Q2,d,d})$ (2,1,5) + $e$ (−1,−2/3) + $\bar\mu$ (1,5/3) ; $(\overline{Q2,d,d})$ (2,1,5) + $\nu_e$ (0,−2/3) + $\bar\nu_\mu$ (0,5/3)

Fig. 4. Decays of the heavy leptons and heavy hadrons.

For the cosmic gamma ray spectra in Fig. 5, the B2 - anti B2 annihilation peak is at $4.27 \ 10^{10}$ eV and Le – anti Le annihilation peak is at $2.53 \ 10^{13}$ eV. And the smooth background curve of the cosmic gamma rays are caused by the gamma rays emitted from the Le decay. These shapes of the cosmic gamma ray spectra have been observed and reported in several references [7-10]. For the cosmic electrons, positrons and neutrinos, the cosmic ray spectra have the same origins. These cosmic electron, positron and neutrino spectra are mainly originated from the Le decays [1,11-13]. It can be confirmed from the observed cosmic electron and positron spectra at the TeV energy range. And the cosmic electron, positron and neutrino spectra coming from the Q1 hadron decays are added around $5 \ 10^{15}$ eV. The positron anomaly, e and $e^+$ spectra can be explained by the Le and anti Le decays [1,12-14]. The astrophysical neutrino spectra observed at the PeV energy range can be explained by using the Q1 hadron decays [1,11]. It is assumed that the decays of other heavy leptons and heavy hadrons have the relatively small contributions when compared with the Le decays. The ultra-high energy cosmic rays are mostly composed of the protons. The smooth background curve of the

ultra-high energy cosmic ray spectra is caused by the gamma induced protons in Fig. 5 [3]. These protons are accelerated by the inelastic Compton scattering with the gamma rays emitted from the pair annihilations of Q1, Q2 and Q3 hadrons. And the first knee, second knee and ankle parts of the ultra-high energy cosmic ray spectra [1,3] are explained by using the Q1-hadron, Q2-hadron and Q3-hadron decays, respectively. The observed cosmic ray spectra can be found in Ref. [3,15].



Fig. 5. Origins of the high and ultra-high energy cosmic rays and gamma rays.
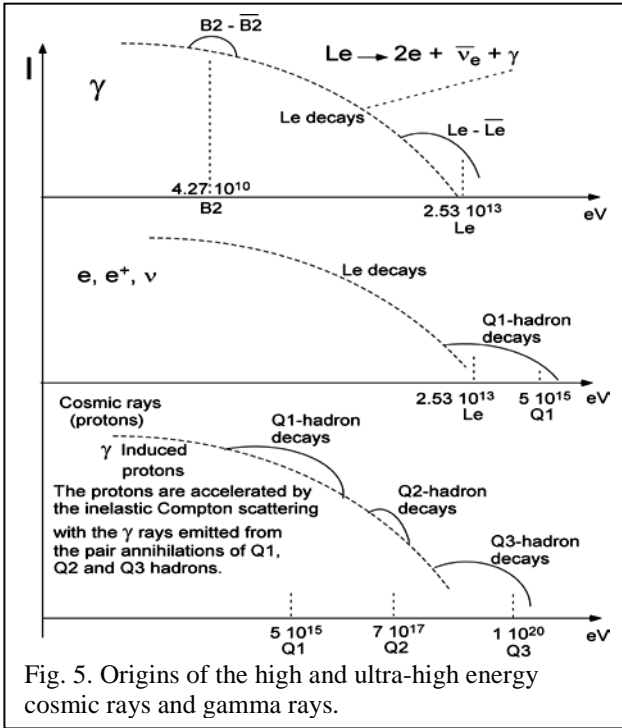
## 4. Possible two Koron discoveries of $ee^+$ and $\mu^-\mu^+$

In Table 1, quarks and leptons have the similar patterns for the EC and LC charges. So, the, so called, Koron made of the lepton and antilepton is suggested like the Meson made of the quark and antiquark. It will be interesting to look for the Korons. The $\pi^0$ meson with u and anti u quarks has the rest mass of 135 MeV/c$^2$. The rest mass of the u quark is about 2.3 MeV/c$^2$. So the Koron of $\pi_l^0$ with e and $e^+$ could have the rest mass of the several MeV/c$^2$ scale. The electron has the rest mass of 0.511 MeV. The X(16.70(35) MeV) peak with the spin of $1^+$ was observed from the invariant $ee^+$ mass distribution from the 18.15 MeV transition in $^8$Be by Krasznahorkay et al. [16]. This unknown neutral X boson with the rest mass of

59

16.7 MeV/c$^2$ is the good candidate of the Koron of $\pi_l^0$ with e and e$^+$. Also, the neutral X boson with the rest mass of 1.6 MeV/c$^2$ – 20 MeV/c$^2$ was introduced by Goudeis et al. [17] in order to explain the cosmological lithium abundance problem at the Big Bang Nucleosysthesis (BBN) [16,17]. This X boson will reduce the abundances of $^7$Be and $^7$Li through the $^7$Be(X,$\alpha$)$^3$He and D(X,p)n [17]. I suggest that this X boson is the same as the X boson observed from the invariant mass distribution from the 18.15 MeV transition in $^8$Be by Krasznahorkay et al. [16]. Then, the Koron of $\pi_l^0$ with e and e$^+$ can explain the cosmological lithium abundance problem at the Big Bang Nucleosysthesis (BBN) [16,17].

Also, a narrow dimuon, M($\mu^-\mu^+$), mass resonance at 30.4 GeV = 3.04 10$^{10}$ eV was obtained from the archived data of the ALEPH experiment at LEP [18,19]. The data, taken in 1992-95, involve 1.9 million hadronic decays of Z-bosons produced at rest in e--e+ annihilation. This dimuon resonance is considered to be a good candidate of the $\mu^-\mu^+$ Koron. The rest mass of the $\mu^-$ lepton is 1.07 10$^8$ eV/c$^2$. The dimuon mass resonance decay scheme including the B1 and B2 dark matters is shown in Fig. 6. A Z(0,0) boson decays to a pair of B2 and anti B2 dark matters.



Fig. 6. Two Koron examples of ee$^+$ and $\mu^-\mu^+$. A neutral Z(0,0) boson decay scheme leads to the dimuon, M($\mu^-\mu^+$), mass resonance.
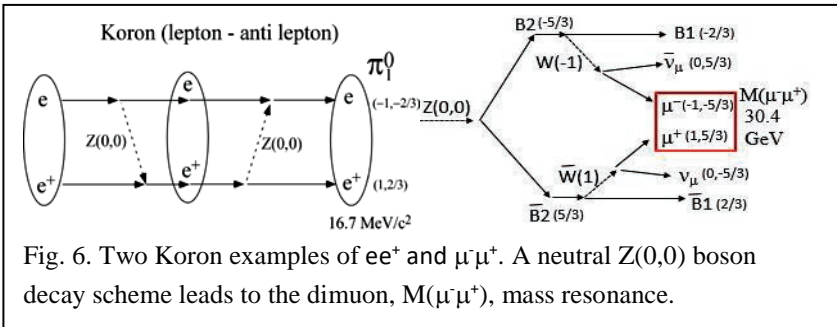
## 5.  Dark matter and super-nova 1987A

The super-nova 1987A has been seen to have the three rings on the Hubble space telescope pictures.  And the evidence of the neutron star is missing in the super-nova 1987A [20-22]. The neutrino masses of 21.4(12) eV/c$^2$ and 4.0(5) eV/c$^2$ are extracted from the antineutrino data from the super-nova 1987A [20]. These neutrino masses are too large. So, I tried to solve these two questions by using the B1 dark matter. Then, the new concept of the dark matter core collapse in addition to the normal matter core collapse is introduced in order to build the super-nova structure. The experimental anti-neutrino data are used to draw the conclusions in the present work.  The more details on the experimental neutrino measurements can be found from the references [20,21,22].

The super-nova 1987A anti-neutrino data can be drawn as shown in Fig. 7. The neutrino energy of $E(v)$ is related to the time of t. The equation of $2E^2t = m^2c^4t_0$ is used [20]. The curve A fits other data well except the 6 data. The curve A uses the proposed dark matter mass of B1. It is proposed that the B1 particles come from the SN 1987A to the earth. The B1 and anti $B1$ dark matters coming from the SN1987A change the directions by the neutral boson (Z(0)) interactions with p and e in the earth atmosphere. The B1 and anti $B1$ dark matters are pair-annihilated within the earth atmosphere and the $v$ and anti $v$ pair is created. These neutrinos are observed by using the detectors under the earth surface. The energies, $E(v)$ of the observed neutrinos are similar to the energies, $E(B1)$ of the B1 dark matters. This supports indirectly that the rest mass energy of the B1 dark matter is 26.12 eV.
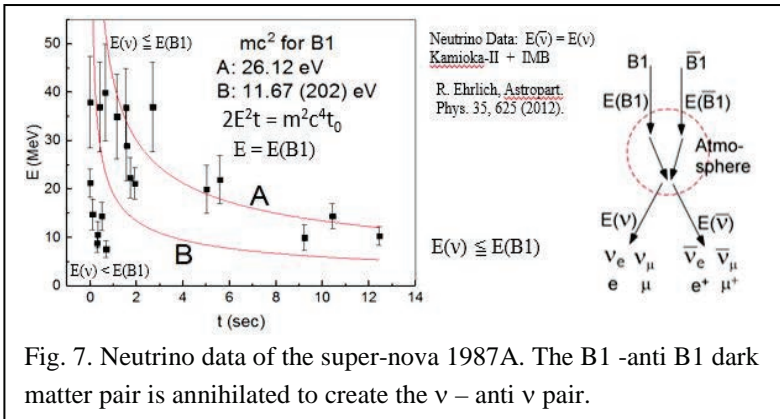


Fig. 7. Neutrino data of the super-nova 1987A. The B1 -anti B1 dark matter pair is annihilated to create the $v$ – anti $v$ pair.

In Fig. 8, two kinds of super-nova explosions including the dark matter core collapse in addition to the normal matter collapse are shown. The upper one is for the super-nova 1987A with three rings and without the neutron star. The Dark matter core burst triggers the normal matter core burst without forming the neutron star. The down one is for the normal super-nova with the neutron star. In this case, both of dark matter core and normal matter core are collapsing. Then outside normal matters blast into the space and the inside dark matter and normal matter cores are collapsing to form the neutron star which consists of the neutrons and B1 dark matters.

The D core burst triggers the N core burst without forming the neutron star. A supernova without the D and N core bursts forms a neutron star of the neutrons and B1 dark matters.

Fig. 8. Two kinds of super-nova explosions including the dark matter core collapse in addition to the normal matter collapse. The upper one is for the super-nova 1987A with three rings and without the neutron star.

## 6. 3.5 keV 18.7 keV and 74.9 keV x-ray peaks and Q1 baryon atoms

The heavy baryons including the Q1 heavy quark (Q1 baryons) can be made in the active galatic nucleus. This Q1 baryon can have the electric charges (EC) of -1 and -2. For example, the Q(Q1,d,d) and R(Q1,d,u) baryons in Fig. 9 have the charge configurations of (EC,LC) = (-2,0) and (EC,LC) = (-1,0), respectively. Then the protons with the charge configurations of (EC,LC) = (1,0) can rotate around these Q and R baryons to form the Q1 baryon atoms. These Q1 baryon atoms are similar to the hydrogen atoms. The proton energy levels in the Q1 baryon atom are easily calculated in the same way as the electron energy levels in the hydrogen atom are calculated.

Fig. 9. Proron energy levels and x-rays in the
Q1 baryon atoms of the R atom and Q atom.

The calculated x-ray energies are 18.7 keV and 3.5 keV from the R atom and 74.9 keV and 13.9 keV from the Q atom in Fig. 9. The possible 18.7 keV and 74.9 keV x-ray peaks are found at the cosmic x-ray background spectra [1,23,24]. And the 74.9 keV x-ray peak is even seen more clearly on the broadband energy spectrum of the X-ray pulsar 4U 0115+63 from IBIS/ISGRI and JEM-X(INTEGRAL) data in its bright state during the out-burst in May-June 2011 [1,25]. So it is thought that these 18.7 keV and 74.9 keV x-ray peaks are originated from the Q1 baryon atoms in Fig. 9. Also, the 3.5 keV x-ray peak is expected from the Q1 baryon atom of the R atom in Fig. 9. And an emission line at 3.5 keV was detected in the spectrum of the Cosmic X-ray Background using a total of 10 Ms Chandra observations towards the COSMOS Legacy and CDFS survey fields [26]. So it is thought that this observed 3.5 keV x-ray peak is originated from the Q1 baryon atom of the R atom but not from the pair annihilation of the dark matters.

## 7. Summary

In summary, the three-dimensional quantized space model is introduced as the new extended standard model. Three generations of the leptons and quarks correspond to the lepton charges. Quarks have three charges of EC, LC and CC, and leptons

have two charges of EC and LC. New particles of bastons with only one charge of EC are the dark matters. The dark matter force is introduced with the new Z/W/Y(EC) bosons. The massless gluons are replaced with the new massive Z/W/Y(EC,LC,CC) bosons. And the rest mass energies of the leptons with the charge configuration of (EC.LC) and bastons (dark matters) with the charge configuration of (EC) are calculated by using the simple equations. The standard model has the conservation rules of many quantum numbers such as baryon number, lepton number, B-L symmetry, hyper charge, weak charge, electric charge, color charge, quark flavor quantum number, lepton family number and x-charge. However, the present model has only one conservation rule of EC, LC and CC charges. Several examples of elementary particle decays are shown in Fig. 10. The calculated rest mass energies of three neutrinos are $2.876 \ 10^{-7}$ eV for $\nu_e$, $5.947 \ 10^{-5}$ eV for $\nu_\mu$ and $1.000 \ 10^{-1}$ eV for $\nu_\tau$ in Table 3. The assigned neutrino masses need to be confirmed experimentally. And the calculated rest mass energy of the B1 dark matter is 26.121 eV. It will be interesting to look for the 26.121 eV peak at the cosmic x-ray and at LHC. The ultra-high energy cosmic rays and gamma rays are originated from the decay and annihilations of the hadrons including the Q1, Q2 and Q3 quarks with the possible rest masses of $10^{15-20}$ eV/$c^2$. The super-nova 1987A structure is explained by using the dark matter core collapse. This supports that the rest mass of the B1 dark matter is 26.121 eV/$c^2$. The structures of the super-nova with the neutron star and the normal super-nova without the neutron star are introduced and compared by using the new concept of the dark matter core collapse. It is thought that the 18.7 keV, 3.5 keV and 74.9 keV x ray peaks observed from the cosmic x-ray background spectra are originated not from the pair annihilations of the dark matters but from the x-ray emission of the Q1 baryon atoms.

The X(16.70(35) MeV) peak with the spin of $1^+$ is proposed as the first Koron of $\pi_l^0$ ($e^+e^-$)(0,0) observed experimentally. The first Koron of $\pi_l^0$ ($e^+e^-$) (0,0) is the good candidate of the neutral boson (X) for the lithium problem. The dimuon resonance is considered to be a good candidate of the $\mu^-\mu^+$ Koron. Dark matters (Bastons) are interacting with the electrons and protons by the gravitational force but not by electromagnetic force. Z and W$^-$ boson in the standard model are Z(0,0) and W(-1,0) in the present work, respectively. Dark matter force, weak force and strong force are explained consistently in Table 2. From the B1–e and B1-$\mu$ reactions, the cosmic e and $\mu$ particles are transferred to the cosmic $\nu_e$ and $\nu_\mu$ neutrinos, respectively. The observation of the enhanced cosmic $\nu_e$ and $\nu_\mu$ neutrinos is the indirect evidence of the B1 dark matters. Also, the B1 dark matters can be produced from the LHC accelerator. The reaction between this B1 dark matter and the electron can enhance the electron neutrinos. It will be interesting to carry out this experiment at LHC.
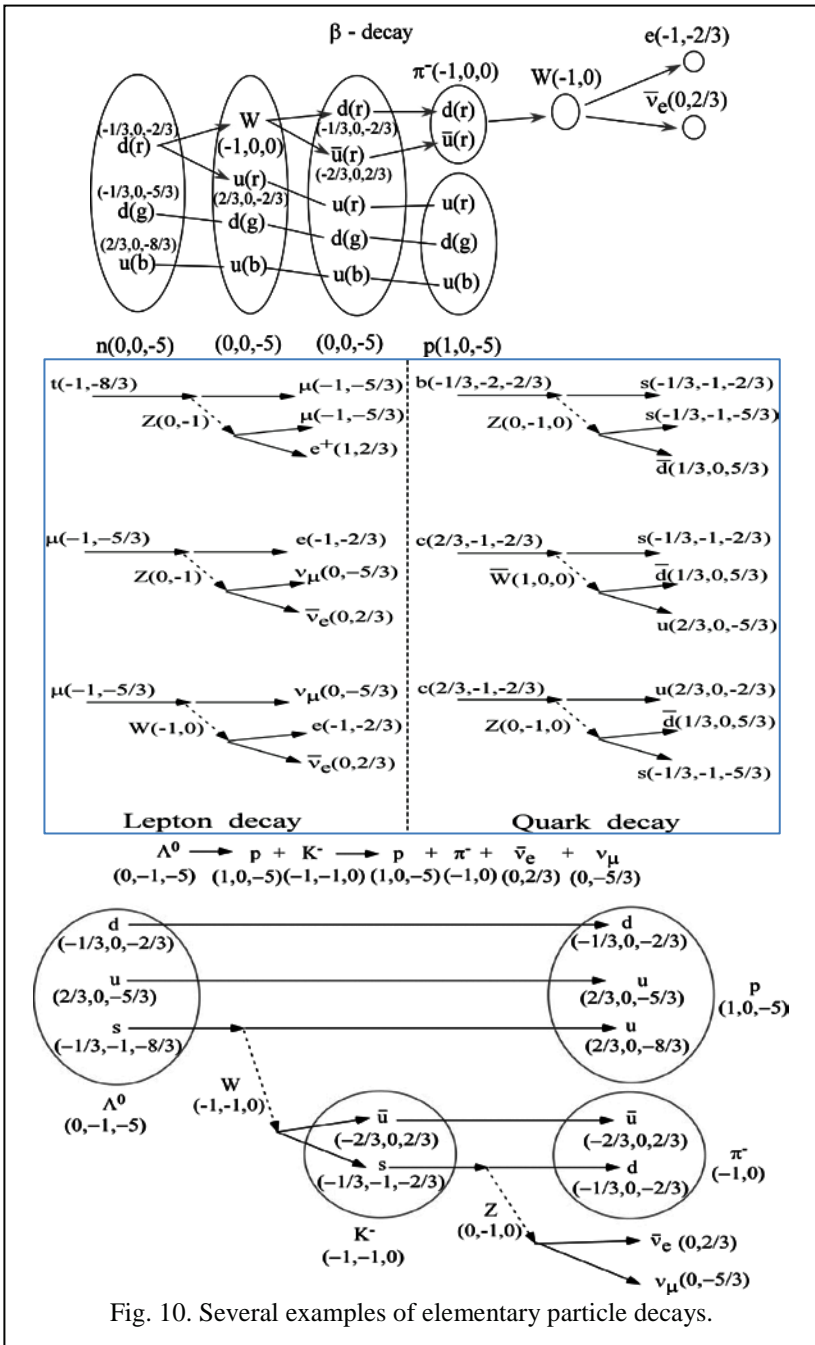
Fig. 10. Several examples of elementary particle decays.

More details can be found in Refs. 1, 2 and 27.

E-mail contact address of Jae-Kwang Hwang is jkhwang.koh@gmail.com

# References

[1] Jae-Kwang Hwang, https://www.researchgate.net/publication/313247136

[2] Jae-Kwang Hwang, https://www.researchgate.net/publication/297270485

[3] S. Hussain, arXiv: 1301.6619v1 (2013).

[4] Y.F. Liang et al., Phys. Rev. D 93, 103525 (2016).

[5] M. Ackermann et al., arXiv: 1302.3307v1 (2013).

[6] T. Siegert et al., arXiv: 1603.01169 (2016).

[7] V. Gammaldi, arXiv: 1412.7639 (2014).

[8] P. Meszaros et al., www2.astro.psu.edu/users/nnp/cr.html.

[9] J.N. Bahcall and E. Waxman, Phys. Lett. B556, 1 (2003).

[10] S. Federicici et al., arXiv: 1502.06355v1 (2015).

[11] M.G. Aartsen et al., arXiv: 1412.5106 (2014).

[12] L. Accardo et al., Phys. Rev. Lett. 113, 121101 (2014).

[13] M. Aguilar et al., Phys. Rev. Lett. 113, 121102 (2014); 110, 141102 (2013).

[14] P. Lipari, arXiv: 1608.02018 (2016) and references there in.

[15] M.T. Dova, arXiv: 160407584v1 (2016).

[16] A.J. Krasznahorkay et al., Phys. Rev. Lett. 116, 042501 (2016).

[17] A. Goudeis et al., Phys. Rev. Lett. 116, 211303 (2016).

[18] K. Lane and L. Pritchett, arXiv: 1701.07376 (2017).

[19] A. Heister, arXiv: 1610.06536 (2016).

[20] R. Ehrlich, Astropart. Phys. 35, 625 (2012).

[21] F. Vissani et al., arXiv: 1008.4726v1 (2010).

[22] G. Schatz, arXiv: 1507.07107v1 (2015).

[23] M. Turler et al., A&A 512, A49 (2010).

[24] Yong Shi et al., The Astrophysical Journal 777, 6 (2013).

[25] P.A. Boldin et al., Astronomy Letters 39, 375 (2013).

[26] N. Cappelluti et al., arXiv: 1701.07932 (2017).

[27] Jaekwang Hwang, Talk at American physical society April meeting 2017, January 28-31, 2017, https://absuploads.aps.org/presentation.cfm?pid=12521

# The Recent Results from Super-Kamiokande

Takatomi Yano for Super-Kamiokande Collaboration

**Abstract:**

The Super-Kamiokande (SK) is the world-largest water Cherenkov detector, running for neutrino observations and proton decay search over 20 years. Because of its high statistics due to the large fiducial volume of 22.5 kt, lower cosmic-ray background environment in a mine at 1000m underground, and well-calibrated detector itself, Super-K has been making the world-leading results in several region of particle physics. Here, recent results from the study of atmospheric and solar neutrino are presented.

## 1. The Super-Kamiokande Detector

Super-Kamiokande (SK) is the world-largest water Cherenkov detector, located at 1,000 m underground (2,700 m water equivalent) in Ikenoyama mountain, Gifu-prefecture, Japan [1]. The cylindrical detector tank with the dimensions of the 39.3 (33.8) m in diameter and 41.4 (36.2) m in height provides 50 (22.5) kton full (fiducial) volume of ultra-pure water. The detector tank is optically and physically separated into inner detector (ID) and outer detector (OD), which have the 11,129 20-inch-diameter photomultipliers (PMTs) and 1,885 8-inch-PMTs for the Cherenkov light detection respectively. The Cherenkov light patterns provide the information about the original charged particles, on thier energies, directions and particle types. SK detector covers the energy range from a few MeV to tens of GeV. The measurement by SK was started at 1996 and has been continued over twenty years. The most recent and fourth experimental period, called SK-IV, is stated at September 2008 with new data acquisition frontends. SK has also cooperated with the accelerator neutrino experiments as the far detector, for K2K [2] and T2K [3] experiments.

## 2. Atmospheric neutrinos

Atmospheric neutrinos originated with the interaction of cosmic rays with nuclei in the air. The interaction provides pions and kaons, and neutrinos as the results of their decay. The atmospheric neutrinos have the wide energy range of 100 MeV to 100 TeV, the wide range of travel length of 10 km to 13,000 km, and the various components of $\nu_e$, $\nu_\mu$ and their anti-particles [4]. Utilizing these properties, various studies on the properties of neutrinos have been conducted. The data from all the phases of SK-I/II/III (0.33 Mt year) and 2520 days live time of SK-IV, until March 2016, are used for following analysis.

The neutrino oscillations of atmospheric neutrinos are led by $\nu_\mu$ to $\nu_\tau$ oscillation, which causes the deficit of $\nu_\mu$ in the upward-going Multi-GeV and partially contained event samples. Though, it is difficult to identify the appearance of $\nu_\tau$.

This is because the production of τ leptons requires high energy neutrinos, where the flux is small, and also τ leptons decay into hadronic particles mainly. It is still important to confirm the appearance of $\nu_\tau$, to check the oscillation framework. The analysis with neural network was applied to search tau-neutrino decay in SK detector. The neural network was trained by non-τ and τ Monte Carlo (MC) events and likelihood ranging from 0 to 1 was provided as the output for each event. Some more details could be found in our previous papers [5,6]. Figure 1 shows the two-dimensional histogram of τ (left) and non-τ MC (center) events. We can see, the τ-like events are concentrated at the upward direction, at around -1 in cosine of the zenith angle, for the τ MC events. These distributions are utilized as the probability density functions for tau-neutrino events and background (BG) events. The analysis was conducted by fitting real data to a linear combination of two-dimensional histograms, which included a systematic error term:

Data = BG PDF + α τ-PDF + $\Sigma\varepsilon_i$ PDF$_i$

α is the parameter to be fitted, and it was expected to be 1 under the assumption of the standard three-flavor oscillation framework and the standard cross-section of neutrinos. PDF$_i$ is the PDF of the i$^{th}$ systematic errors, and $\varepsilon_i$ is the magnitude of a nuisance parameter in the fit. After the unbinned likelihood fit, we got the result of α= 1.47±0.32 under the hypothesis of normal neutrino mass hierarchy (4.6σ from 0, whereas 3.3σ was expected). Figure 1 (right) shows the zenith angle distribution of tau-like events overlaid by the fitted MC distributions; the shaded part shows the contributions of tau-neutrino events. This is the evidence of the tau-neutrino appearance in atmospheric neutrino, and the result is consistent with the standard three-flavor oscillation framework.
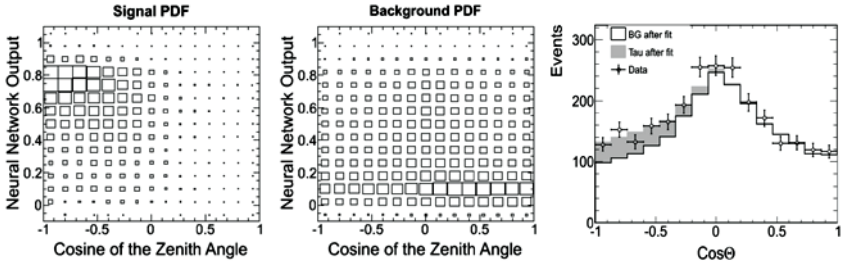


Fig. 1 Probability distribution functions for the τ neutrino (left) and non-τ neutrino events (center). The zenith angle distribution of data and Monte Carlo events (right).

Because of the recent result of large $\theta_{13}$ value in several neutrino experiments, the three-flavor oscillation analysis is required for precise understanding of the neutrino properties with atmospheric neutrinos, such as $\Delta m^2_{32}$, $\theta_{23}$ octant, $\delta_{CP}$ and

mass hierarchy. The atmospheric neutrino samples are subdivided into 19 event categories by their topologies (fully-contained, partially-contained and up-going-muon), energies (sub-GeV and multi-GeV), flavors (electron- or muon-like) and the number of Cherenkov rings. Multi-GeV- multi-ring- electron-like- events are further classified into neutrino and anti-neutrino categories, using a difference of number of associated decay electrons, number of rings, transverse momentum, and the fraction of momentum carried out by most energetic rings. It is motivated by the oscillation scenario, that the oscillation from $\nu_\mu$ to $\nu_e$ is enhanced by the Earth matter effect under normal mass hierarch hypothesis, at around 5-10 GeV. Anti-$\nu_\mu$ to anti-$\nu_e$ oscillation will be enhanced at same energies, in case of inverted mass hierarchy. In following likelihood analysis, $\sin^2\theta_{13}$ is fixed by the reactor neutrino experimental results of $\sin^2\theta_{13} = 0.0219$ (PDG2015 [7]). $\sin^2\theta_{12}$ and $\Delta m^2_{21}$ is constrained by the result of solar neutrino experiments and that of KamLAND.

Figure 2 shows the obtained oscillation analysis results using only SK data. In the figure, $\Delta\chi^2$ is determined as a function of $|\Delta m^2_{32}|$ or $|\Delta m^2_{13}|$, $\sin^2\theta_{23}$ and $\delta_{CP}$. The best fit parameters for normal and inverted hierarchy hypotheses are shown in Table "**". The result of $\Delta\chi^2 = \chi^2_{NH} - \chi^2_{IH} = -4.3$ is achieved and prefers the normal hierarchy hypothesis, where $\Delta\chi^2 = -3.1$ of sensitivity is expected from Asimov data set with normal hierarchy. To check the significance, Monte Carlo samples are generated and analyzed as the real data. In case we adopt the inverted hierarchy for MC samples, the probability to obtain $\Delta\chi^2 = -4.3$ or less is 0.031 ($\sin^2\theta_{23} = 0.6$) and 0.007 ($\sin^2\theta_{23} = 0.4$). In case we adopt normal hierarchy for MC generation, the probability was 0.446 ($\sin^2\theta_{23} = 0.4$).
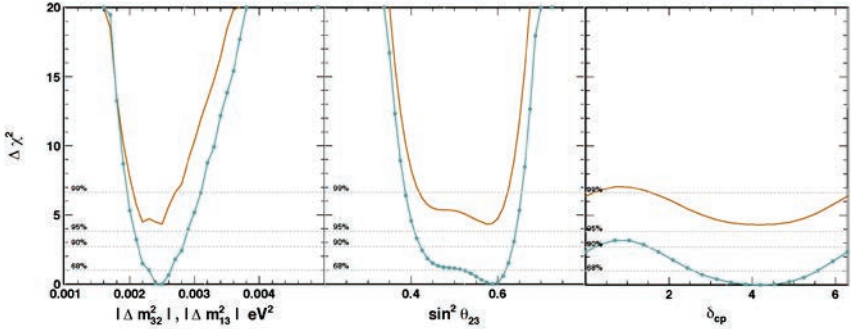


Fig. 2 $\Delta\chi^2$ as a function of $|\Delta m^2_{32}|$ or $|\Delta m^2_{13}|$ (left), $\sin^2\theta_{23}$ (center) and $\delta_{CP}$ (right) with SK data only. The blue and orange lines show $\Delta\chi^2$ for a normal and inverted hierarchy hypothesis, respectively

Tab. 1 Best-fit values for the 3-flavor oscillation analysis with SK only data.

| Fit (517 dot) | $\chi^2$ | $\sin^2\theta_{13}$ | $\delta_{CP}$ | $\sin^2\theta_{23}$ | $\Delta m^2_{23}$ [eV$^2$] |
|---|---|---|---|---|---|
| SK (NH) | 571.74 | 0.0219 (fixed) | 4.189 | 0.587 | $2.5 \cdot 10^{-3}$ |
| SK (IH) | 576.08 | 0.0219 (fixed) | 4.189 | 0.575 | $2.5 \cdot 10^{-3}$ |

Figure 3 shows the preliminary results using SK and public T2K data. Table 2 shows the best-fit values for the likelihood fit. The result is $\Delta\chi^2 = \chi^2_{NH} - \chi^2_{IH} = -5.2$ and also prefers normal hierarchy hypothesis. $\Delta\chi^2 = -3.8$ of sensitivity is expected from Asimov data set assuming normal hierarchy. With a toy Monte Carlo study assuming inverted hierarchy, the probability to have $\Delta\chi^2$ less than -5.2 is 0.024 ($\sin^2\theta_{23} = 0.6$) and 0.001 ($\sin^2\theta_{23} = 0.4$).
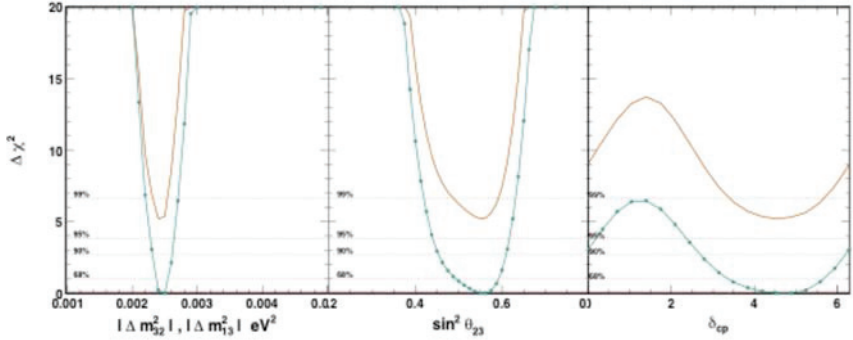


Fig. 3 $\Delta\chi^2$ as a function of $|\Delta m^2_{32}|$ or $|\Delta m^2_{13}|$ (left), $\sin^2\theta_{23}$ (center) and $\delta_{CP}$ (right) with SK + T2K external data. The blue and orange lines show $\Delta\chi^2$ for a normal and inverted hierarchy hypothesis, respectively.

Tab. 2 Best-fit values for the 3-flavor oscillation analysis with SK + T2K external data.

| Fit (585 dot) | $\chi^2$ | $\sin^2\theta_{13}$ | $\delta_{CP}$ | $\sin^2\theta_{23}$ | $\Delta m^2_{23}$ [eV$^2$] |
|---|---|---|---|---|---|
| SK (NH) | 639.61 | 0.0219 (fixed) | 4.887 | 0.55 | $2.4 \cdot 10^{-3}$ |
| SK (IH) | 644.82 | 0.0219 (fixed) | 4.538 | 0.55 | $2.5 \cdot 10^{-3}$ |

## 3. Solar neutrinos

The dominant solar neutrino signals at SK are so called $^8$B neutrinos generated in pp-chain, a series of nuclear fusion reactions in the Sun. The observed event rate at SK is about 20 events/day with the large fiducial volume of 22.5 kton. With the high statistics data, we have performed searches for time variation of the solar neutrino flux, energy spectrum distortion due to the oscillation effect as well as precise measurement of the oscillation parameter $\Delta m^2_{21}$, $\sin^2\theta_{12}$. In following analysis, we use the SK-I, II, III (1496, 791 and 548 days) + 2365 days of SK-IV data, until March 2016. Here, two years equivalent data is newly added, comparing to previous paper with 1664 days data of SK-IV [8]. Because we lowered the trigger threshold at May 2015, some of the new data sets have the analysis threshold of $E_{kin} = 3.5$ MeV at kinetic energy of electrons. It aims at measuring the solar neutrino energy spectrum distortion, and the effort to lower the threshold down to $E_{kin} = 2.5$ MeV is now underway with new data acquisition system.

As the result of SK I-IV combined flux analysis, about 84,000 signals of solar neutrinos is extracted. The flux ratio of the data to the standard solar model (SSM) prediction is Data/SSM = 0.4486±0.0062 (stat. + sys.), where the neutrino oscillation is not taken into account for SSM prediction. In the comparison of each experimental phases of SK, these solar rate measurement results are fully consistent with a constant solar neutrino flux. Figure 4 shows the yearly variation of the solar neutrino flux. The solar activity cycle estimated from the sunspot number is about 11 years. SK has observed the solar neutrinos over these 19 years and above 1.5 cycles has passed. However, no significant correction with the solar activity is seen. For the constant flux hypothesis, $\chi^2 = 15.52/19$ D.O.F, which correspond to 68.9% probability.

Using the most up-to-date SK solar neutrino data and the latest results of other solar neutrino experiments, the allowed regions of the oscillation parameters are obtained. In Fig. 5, we performed the oscillation analysis by constraining $\sin^2\theta_{13}$ as 0.0219±0.0014, referring reactor neutrino experiments. We see 2σ tension between the solar-global and KamLAND reactor data in $\Delta m^2_{21}$. A there-flavor oscillation analysis without the constraint on $\sin^2\theta_{13}$ is also performed. The result is also shown in Fig 5. By combining the SK solar measurement results, the results of other solar experiments and KamLAND, the non-zero $\theta_{13}$ value is obtained by 2σ level ($\sin^2\theta_{13} = 0.029^{+0.014}_{-0.015}$). The result is also consistent with that of reactor experiments.
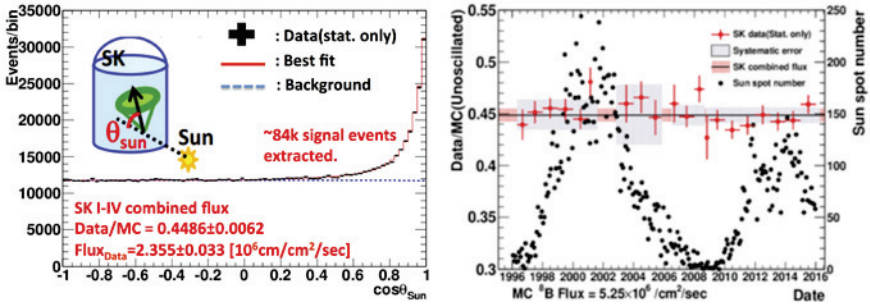
Fig. 4 The distribution of the cosine between the direction of the Sun and the reconstructed direction of electrons (left). The yearly variation of relative ratio between SK data and an un-oscillated MC prediction (right). The black dots show the sunspot numbers for referring solar activity, taken from [9].

## 4. Other recent results

With its indispensable detector characteristics, SK has been making unique searches for new physics. The first of them would be nucleon decay search, strongly motivated by Grand Unification Theories (GUTs). Some GUTs predict the proton lifetimes shorter than $10^{34}$ years and SK could prove it. Since the grand unification occurs at around $10^{16}$ GeV, which cannot be achieved by any accelerator experiments, nucleon decay at SK is a unique way to directly probe them. So far, no evidence of nucleon decay is observed in any decay mode yet. Our past search results for several decay mode, e.g. proton to $e^+\pi^0$ or $\nu K^+$, can be found at [10,11].

The searches for new neutrino sources are also our interest and important for the astroparticle physics. Searches for WIMPs (Weakly Interacting Massive Particles) by neutrinos, which are produced by the annihilation of WIMPs occurring inside Sun, are ongoing in SK. The previous work can be found in [12]. There were no significant signals but stringent limits were set. SK gives limits lower than 200 GeV for the spin-dependent cross section, and lower than 6 GeV for the spin-independent cross section. Searches for neutrino signals from the Earth and the Galaxy are currently ongoing.

On September 2015, LIGO identified the first evident signal of a gravitational wave originated a merger of two black holes [13]. Given the fact, a search for coincident neutrino signals in SK was performed for GW150914 and GW151226. Coincident production of neutrinos are possible to imagine, because of the tremendous energies involved in the mergers and unknown nature of the region of black holes, e.g. formation of relativistic jets. The signal searches were performed for the time window of ±500 seconds around these gravitational wave detection times and for a wide energy range from 3.5 MeV to 100 PeV. Four neutrino

candidates are found for GW150914 and no candidates are found GW151226. These candidates were consistent with the expected background events [14].
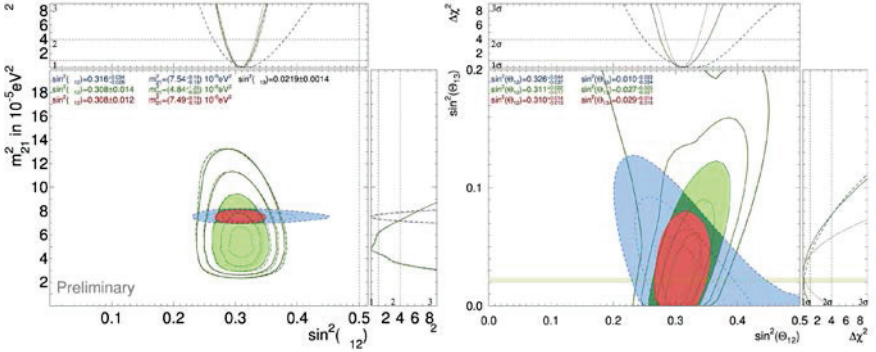


Fig. 5 Allowed regions of oscillation parameters for $\theta_{13}$ constrained analysis (left) and 3-flavor oscillation analysis with solar experiments and KamLAND (right). The green area shows the results of solar global analysis (green), light blue for KamLAND reactor and red for solar + KamLAND. The best-fit parameters and their $1\sigma$ errors are shown in the figure.

## 5. Conclusions

Recent results from the study of atmospheric, solar neutrinos and other topics for nucleon decay and astrophysical neutrino searches are presented.. Using the large data samples of atmospheric neutrinos at SK, three-flavor oscillation analyses are performed. The result of neutrino mass hierarchy test was obtained as $\Delta\chi^2 = \chi^2_{NH} - \chi^2_{IH} = -4.3$ with SK only data, where -3.1 is expected from the same analysis of Asimov data set assuming the best fit parameters. With the SK+T2K data sets, the result was $\Delta\chi^2 = \chi^2_{NH} - \chi^2_{IH} = -5.2$ with SK only data, where -3.8 is expected. These results strongly support the normal hierarchy hypothesis. The analysis of tau neutrino appearance in atmospheric neutrino oscillation is updated and gives a non-zero significance of $4.6\sigma$. The measurement of solar neutrino is also updated. The observed neutrino flux ratio comparing to un-oscillated SSM expectation was Data/MC = $0.4486\pm0.0062$, and measurements in each experimental period of SK is fully consistent with constant solar neutrino flux. No significant correlation with the solar activity is seen. The solar neutrino oscillation analysis is also updated. The global analysis with the results of other solar experiments gives lower $\Delta m^2_{21}$ value than that of KamLAND by more than $2\sigma$. A three-flavor oscillation analysis with solar neutrinos, without constrain of $\sin^2\theta_{13}$ by the reactor experiments, also give the consistent results for the oscillation

parameters and non-zero $\theta_{13}$ value by $2\sigma$ level.

**References**

[1] Super-Kamiokande collaboration (Y. Fukuda et al.), Nucl. Instrum. Meth. A501: 418-462 (2003).

[2] K2K collaboration (S.H. Ahn et al.), Phys. Lett. B 411:178-184 (2001).

[3] T2K collaboration (Y. Itow et al.), arXiv:hep-ex/0106019 (2001).

[4] Super-Kamiokande collaboration (E. Richard et al.), Phys. Rev. D 94   052001 (2016).

[5] Super-Kamiokande collaboration (K. Abe et al.), Phys. Rev. Lett., 97 171801 (2006).

[6] Super-Kamiokande collaboration (K. Abe et al.), Phys. Rev. Lett., 110 181802 (2013).

[7] K A Olive et al. (Particle Data Group), Chin. Phys. C, 38 090001 (2014) and 2015 update.

[8] Super-Kamiokande collaboration (K. Abe et al.), Phys. Rev. D 94 052010 (2016).

[9] http://www.sidc.be/silo/datafile. Source: WDC-SILSO, Royal Observatory of Belgium, Brussels

[10] Super-Kamiokande collaboration (H. Nishino et al.), Phys. Rev. D 85 112001 (2012).

[11] Super-Kamiokande collaboration (K. Abe et al.), Phys. Rev. D 90 072005 (2014).

[12] Super-Kamiokande collaboration (K. Choi et al.), Phys. Rev. Lett., 114 141301 (2015).

[13] LIGO and Virgo collaborations (B. P. Abbott et al.), Phys. Rev. Lett., 116 061102 (2016).

[14] Super-Kamiokande collaboration (K. Abe et al.), Astrophys. J. Lett. Vol. 830 1 (2016).

# Double-Beta Decay with Single-Electron Emission

A. Babič,[1, 2] D. Štefánik,[3] M. I. Krivoruchenko,[2, 4, 5] and F. Šimkovic[1, 2, 3]

[1] *Czech Technical University in Prague, 128 00 Prague, Czech Republic*
[2] *Joint Institute for Nuclear Research, 141980 Dubna, Russia*
[3] *Comenius University in Bratislava, 842 48 Bratislava, Slovakia*
[4] *Institute for Theoretical and Experimental Physics, 117218 Moscow, Russia*
[5] *Moscow Institute of Physics and Technology, 141700 Moscow, Russia*

**Abstract:** We study a new mode of the neutrinoless and two-neutrino double-beta decay in which a single electron is emitted from the atom. The other electron is directly produced in one of the available $s_{1/2}$ or $p_{1/2}$ subshells of the daughter ion. The neutrinoless electron-production mode $0\nu EP\beta^-$, which would manifest through a monoenergetic peak at the endpoint of the single-electron energy spectrum, is shown to be inaccessible to the future experiments. Conversely, its two-neutrino counterpart $2\nu EP\beta^-$ might have already influenced the single-electron spectra measured, e.g., for the isotope $^{100}$Mo in the experiment NEMO 3. We discuss the prospects for detecting these new modes also for $^{82}$Se in its forthcoming successor SuperNEMO.

**Keywords:** double-beta decay, atomic shell, single-electron spectrum

## I. Introduction

The discovery of neutrino oscillations marked the beginning of a new era in neutrino physics, main feature of which is the question of the origin and absolute scale of neutrino masses. Observation of the neutrinoless double-beta decay would imply a Majorana nature of massive neutrinos $\nu_i$ ($i = 1, 2, 3$), a consequence of which would be the identity of the flavor neutrinos $\nu_\alpha$ ($\alpha = e, \mu, \tau$) and their respective antineutrinos $\bar{\nu}_\alpha$ [1]. Moreover, it would bring us compelling evidence that the total lepton number $L$ is not strictly conserved in the nature. The search for this elusive process provides us with means to set upper limits on the absolute scale of neutrino masses, as well as with a unique access to the mechanism of CP violation in the lepton sector which is necessary in order to explain the observed baryon asymmetry of the Universe [2].

The most widespread form of the double-beta decay $2\nu\beta^-\beta^-$ involves a transmutation of an even-even parent nucleus $^A_Z$X into an even-even daughter nucleus $^A_{Z+2}$Y, accompanied by an emission of two electrons $e^-$ and a pair of electron antineutrinos $\bar{\nu}_e$ from the atom, while in its hypothetical neutrinoless version $0\nu\beta^-\beta^-$ the antineutrinos are absent:

$$^A_Z\text{X} \longrightarrow {}^A_{Z+2}\text{Y} + e^- + e^- + (\bar{\nu}_e + \bar{\nu}_e).$$

The neutrinoless mode $0\nu\beta^-\beta^-$ increases $L$ by 2 units and could be discovered in calorimetric measurements of the sum of electron energies by revealing a monoenergetic peak at the two-electron spectrum endpoint corresponding to the total released kinetic energy $Q$. The two-neutrino mode $2\nu\beta^-\beta^-$ has been so far observed for 11 out of 35 even-even isotopes for which the ordinary $\beta^-$ decay into the odd-odd intermediate nucleus is either energetically forbidden or substantially suppressed by spin selection rules [3]. In this work, we focus on the $0^+ \rightarrow 0^+$ ground-state transition of the isotope $^{100}$Mo which had been extensively studied throughout the operation of the tracking-and-calorimetry double-beta-decay experiment NEMO 3 located at the Modane Underground Laboratory (LSM), France [4].

In 1992, Jung *et al.* have observed for a first time the bound-state $\beta^-$ decay in which the electron is directly produced in atomic K or L shell and the monochromatic electron antineutrino carries away essentially the entire energy of the decay [5]. The group has studied bare $^{163}_{66}$Dy$^{66+}$ ions collected in a heavy-ion storage ring at GSI, Darmstadt, and deduced a half-life of 47 d for the otherwise stable isotope. It has been since stressed that such rare form of the $\beta^-$ decay might play a crucial role in stellar plasma where highly-ionized atoms participate in the nucleosynthesis. In this work, we propose to study the bound-state double-beta decay $0\nu$EP$\beta^-$ ($2\nu$EP$\beta^-$):

$$_Z^A\text{X} \longrightarrow {}_{Z+2}^A\text{Y} + e_b^- + e^- + (\bar{\nu}_e + \bar{\nu}_e),$$

where a single free electron $e^-$ is emitted from the nucleus, while the electron production (EP) of a bound electron $e_b^-$ is assumed to fill one of the available $s_{1/2}$ or $p_{1/2}$ orbitals above the valence shell of the daughter ion $_{Z+2}^A\text{Y}^{2+}$. Inclusion of the bound states with higher angular momenta is not necessary since their wave functions experience only a negligible overlap with the nucleus. These new single-electron modes exhibit a distinctive kinematics and could be in principle recognized by their characteristic signal induced in the double-beta-decay detectors. For instance, $0\nu$EP$\beta^-$ (being effectively a two-body decay) should be searched for in the form of a monoenergetic peak at the endpoint of the energy distribution of individual electrons. The single-electron spectra have been measured in the NEMO 3 experiment and will be surveyed with enhanced accuracy in its forthcoming successor SuperNEMO [6].

## II. Calculation of Phase-Space Factors

The double-beta decay can occur in the 2$^{\text{nd}}$ order of the effective $\beta$-decay Hamiltonian [7]:

$$\mathcal{H}_\beta(x) = \frac{G_\beta}{\sqrt{2}} \bar{e}(x)\gamma^\mu(1-\gamma^5)\nu_e(x)j_\mu(x) + \text{H.c.},$$

where $G_\beta = G_F \cos\theta_C$ contains the Fermi constant $G_F$ and Cabibbo angle $\theta_C \cong 13°$ [8], $e(x)$ and $\nu_e(x)$ denote the electron and electron-neutrino fields, respectively, and $j_\mu(x) = \bar{p}(x)\gamma_\mu(g_V - g_A\gamma^5)n(x)$ is the hadronic charged current involving the proton $p(x)$ and neutron $n(x)$ fields with the vector $g_V = 1$ and (unquenched) axial-vector $g_A = 1.269$ weak coupling constants. Due to neutrino mixing, the left-handed components of the flavor-neutrino fields $\nu_\alpha(x)$ are in fact linear combinations of the underlying massive-neutrino fields $\nu_i(x)$ given by the unitary PMNS matrix: $\nu_{\alpha L}(x) = \sum_i U_{\alpha i}\nu_{iL}(x)$.

Assuming the Majorana nature of massive neutrinos and employing the standard approximations, the formula for the inverse $0\nu\beta^-\beta^-$ half-life can be brought into the following form [1]:

$$\left(T_{1/2}^{0\nu\beta\beta}\right)^{-1} = g_A^4 G^{0\nu\beta\beta}(Z,Q)\left|M^{0\nu\beta\beta}\right|^2 \left|\frac{m_{\beta\beta}}{m_e}\right|^2.$$

Here, the phase-space factor $G^{0\nu\beta\beta}(Z,Q)$ depends solely on the kinematics of the involved particles, the nuclear matrix element $M^{0\nu\beta\beta}$ can be in principle determined from the theory of nuclear structure, and the effective Majorana neutrino mass $m_{\beta\beta} = \sum_i U_{ei}^2 m_i$ is a function of (yet unknown) parameters of the neutrino physics; to this day, arguably the most stringent limits have been obtained in the $^{136}$Xe double-beta-decay experiments KamLAND-Zen and EXO-200, with the former providing a constraint as low as [9]: $\left|m_{\beta\beta}\right| < 165$ meV. On the contrary, the formula for the inverse $2\nu\beta^-\beta^-$ half-life can be derived within the Standard Model [10]:

$$\left(T_{1/2}^{2\nu\beta\beta}\right)^{-1} = g_A^4 G^{2\nu\beta\beta}(Z,Q)\left|m_e M^{2\nu\beta\beta}\right|^2.$$

For the single-electron modes $0\nu\text{EP}\beta^-$ and $2\nu\text{EP}\beta^-$, their respective inverse half-lives $\left(T_{1/2}^{0\nu\text{EP}\beta}\right)^{-1}$ and $\left(T_{1/2}^{2\nu\text{EP}\beta}\right)^{-1}$ exhibit a structure fully analogous to the aforementioned, the only distinction being in the corresponding phase-space factors $G^{0\nu\text{EP}\beta}(Z,Q)$ and $G^{2\nu\text{EP}\beta}(Z,Q)$. Since these quantities depend crucially on the atomic structure, we employed a fully relativistic description of the final-state electrons in terms of the solutions to the Dirac equation with centrally-symmetric potential [11]:

$$\psi_{\kappa\mu}(\vec{r}) = \begin{pmatrix} f_\kappa(r)\Omega_{\kappa\mu}(\hat{r}) \\ ig_\kappa(r)\Omega_{-\kappa\mu}(\hat{r}) \end{pmatrix},$$

where the radial wave functions $f_\kappa(r)$ and $g_\kappa(r)$ depend on the energy of the electron, while the angular functions $\Omega_{\kappa\mu}(\hat{r})$, also known as the spinor spherical harmonics, are common for both the discrete and continuous spectrum. The quantum number $\kappa = (l - j)(2j + 1) = \pm 1, \pm 2, ...$ collectively labels all possible couplings of the orbital $l = 0,1, ...$ and spin $s = \pm 1/2$ angular momenta, while $\mu = -j, ..., +j$ denotes the projection of the total angular momentum $j = |l + s|$ onto the $z$-axis.

For the $0\nu\mathrm{EP}\beta^-$ and $2\nu\mathrm{EP}\beta^-$ phase-space factors we have derived the following formulae:

$$G^{0\nu\mathrm{EP}\beta} = \frac{G_\beta^4 m_e^2}{32\pi^4 R^2 \ln 2} \sum_{n=n_{\min}}^{\infty} B_n(Z,A)F(Z + 2, E)Ep,$$

$$G^{2\nu\mathrm{EP}\beta} = \frac{G_\beta^4}{8\pi^6 m_e^2 \ln 2} \sum_{n=n_{\min}}^{\infty} B_n(Z,A) \int_{m_e}^{m_e+Q} \mathrm{d}EF(Z + 2, E)Ep \int_{0}^{m_e+Q-E} \mathrm{d}\omega_1 \omega_1^2 \omega_2^2.$$

In the first equation, the nuclear radius $R$ is by convention included explicitly in order to make the nuclear matrix element $M^{0\nu\beta\beta}$ dimensionless. The factor of $\ln 2$ comes from the relation between the decay rate $\Gamma = \ln 2/T_{1/2}$ and half-life $T_{1/2}$.

The quantity $B_n(Z,A)$ is a bound-state analogue of the Fermi function familiar from the theory of beta decay:

$$B_n(Z,A) = f_{n,-1}^2(R) + g_{n,+1}^2(R),$$

where the two terms originate from the inclusion of $\mathrm{s}_{1/2}$ and $\mathrm{p}_{1/2}$ bound states, respectively. In order to properly account for the relativistic many-electron atomic structure and the shielding effect of nuclear charge, the radial wave functions $f_{n,-1}(R)$ and $g_{n,+1}(R)$ of the bound electron $e_{\mathrm{b}}^-$ at the nuclear radius $R = 1.2$ fm $A^{1/3}$ were evaluated by means of the multiconfiguration Dirac–Hartree–Fock package GRASP2K [12, 13]. The computation was performed assuming the electron configuration of the parent atom $_Z^A\mathrm{X}$, with the daughter isotope $_{Z+2}^A\mathrm{Y}$ being the source of nuclear Coulomb attraction, for all available electron shells above the valence shell ($n_{\min} = 5$ for $_{42}^{100}\mathrm{Mo}$) up to $n = 9$. Since in the absence of atomic shielding the squared electron wave functions near the origin decrease as $n^{-3}$ [14], the rest of electron shells were to a good accuracy approximated by a fit of the calculated values using the power function $cn^{-p}$ and summed analytically via the Riemann zeta function $\zeta(p)$. Since the convergence could not be achieved in case of the $6\mathrm{s}_{1/2}$ orbital, the value of $f_{6,-1}^2(R)$ has been replaced by the one predicted by the fit.

The Fermi function $F(Z,E)$, which involves the continuous-spectrum radial wave functions $f_{-1}(E,R)$ and $g_{+1}(E,R)$ evaluated on the nuclear surface $R$, can be approximated by the expression for the relativistic $\mathrm{s}_{1/2}$ wave [15]:

$$F(Z,E) = f_{-1}^2(E,R) + g_{+1}^2(E,R) \approx 4 \left[ \frac{|\Gamma(\gamma+iy)|}{\Gamma(2\gamma+1)} \right]^2 (2pR)^{2\gamma-2} e^{\pi y},$$

where $\gamma = \sqrt{1-(\alpha Z)^2}$, $y = \alpha Z E/p$, and $p = |\vec{p}|$ is the momentum magnitude of the free electron $e^-$ with energy $E = \sqrt{\vec{p}^2 + m_e^2}$. In the results, the Fermi function $F(Z+2,E)$ assumes the full charge of the daughter nucleus $_{Z+2}^A Y$, since in the continuum the shielding effect has been shown to be rather insignificant [16].

In $G^{0\nu EP\beta}$, the free-electron energy is fixed by the energy conservation: $E = m_e + Q$, where we have neglected the nuclear recoil as well as the binding energy of the bound electron $e_b^-$. In $G^{2\nu EP\beta}$, similar approximations erase the dependence on $n$ from the integral boundaries and, in turn, an infinite sum of integrals simplifies into a product of $\sum_{n=n_{\min}}^{\infty} B_n(Z,A)$ and just one double integral; in the integral over the first-neutrino energy $\omega_1$, the second-neutrino energy is once again constrained by the energy conservation: $\omega_2 = m_e + Q - E - \omega_1$.

## III. Half-Lives and Single-Electron Spectra

In Table I, we present the values of the $0\nu\beta^-\beta^-$ and $0\nu EP\beta^-$ phase-space factors $G^{0\nu\beta\beta}$ and $G^{0\nu EP\beta}$ obtained for the $0^+ \rightarrow 0^+$ ground-state transition of the isotope $^{100}$Mo with total released kinetic energy $Q = 3.034$ MeV [17], assuming the unquenched value of the axial-vector weak coupling constant $g_A = 1.269$. We also evaluate the ratio between the corresponding decay rates: $\Gamma^{0\nu EP\beta}/\Gamma^{0\nu\beta\beta} = G^{0\nu EP\beta}/G^{0\nu\beta\beta}$, which is independent of the nuclear matrix element $M^{0\nu\beta\beta}$ and effective Majorana neutrino mass $m_{\beta\beta}$, and hence free of the peculiarities of the nuclear and neutrino physics. Finally, we estimate the $0\nu\beta^-\beta^-$ and $0\nu EP\beta^-$ half-lives $T_{1/2}^{0\nu\beta\beta}$ and $T_{1/2}^{0\nu EP\beta}$ based on the value of the nuclear matrix element $|M^{0\nu\beta\beta}| = 5.850$ calculated in [18] via the spherical pn-QRPA approach including the realistic CD-Bonn nucleon-nucleon potential with short-range correlations and partial isospin-symmetry restoration, and assuming the value of the effective Majorana neutrino mass $|m_{\beta\beta}| = 50$ meV which is compatible with the inverted hierarchy of neutrino masses. The value obtained for the decay-rate ratio $\Gamma^{0\nu EP\beta}/\Gamma^{0\nu\beta\beta}$ suggests a suppression of the single-electron mode $0\nu EP\beta^-$ by 6 orders of magnitude, which is mainly attributed to the presence of other electrons in the inner atomic shells: the lowest-lying orbitals (which would otherwise provide the largest contributions to the decay rate $\Gamma^{0\nu EP\beta}$) are already occupied, while the shielding effect of nuclear charge substantially reduces the bound-state wave functions on the surface of the nucleus. The estimated half-life $T_{1/2}^{0\nu EP\beta}$ further confirms that the mode $0\nu EP\beta^-$ is very unlikely to be observed in the present and near-future experiments.

Table I. $0\nu\beta^-\beta^-$ and $0\nu\text{EP}\beta^-$ phase-space factors $G^{0\nu\beta\beta}$ and $G^{0\nu\text{EP}\beta}$, decay-rate ratio $\Gamma^{0\nu\text{EP}\beta}/\Gamma^{0\nu\beta\beta} = G^{0\nu\text{EP}\beta}/G^{0\nu\beta\beta}$ and half-lives $T_{1/2}^{0\nu\beta\beta}$ and $T_{1/2}^{0\nu\text{EP}\beta}$ for the isotope $^{100}$Mo, assuming the nuclear matrix element $|M^{0\nu\beta\beta}| = 5.850$ [18] and the effective Majorana neutrino mass $|m_{\beta\beta}| = 50$ meV.

| $G^{0\nu\beta\beta}$ [y$^{-1}$] | $G^{0\nu\text{EP}\beta}$ [y$^{-1}$] | $\Gamma^{0\nu\text{EP}\beta}/\Gamma^{0\nu\beta\beta}$ | $T_{1/2}^{0\nu\beta\beta}$ [y] | $T_{1/2}^{0\nu\text{EP}\beta}$ [y] |
|---|---|---|---|---|
| $1.887 \times 10^{-14}$ | $7.400 \times 10^{-20}$ | $3.92 \times 10^{-6}$ | $6.24 \times 10^{25}$ | $1.59 \times 10^{31}$ |

In Table II, we show analogous results for the $2\nu\beta^-\beta^-$ and $2\nu\text{EP}\beta^-$ phase-space factors $G^{2\nu\beta\beta}$ and $G^{2\nu\text{EP}\beta}$, as well as the decay-rate ratio $\Gamma^{2\nu\text{EP}\beta}/\Gamma^{2\nu\beta\beta} = G^{2\nu\text{EP}\beta}/G^{2\nu\beta\beta}$. The $2\nu\beta^-\beta^-$ half-life $T_{1/2}^{2\nu\beta\beta}$ for the $0^+ \rightarrow 0^+$ ground-state transition of $^{100}$Mo has been measured experimentally [3], from which the value of $g_A^2|M^{2\nu\beta\beta}|$ can be deduced regardless of the details of the nuclear-structure theory, and used to predict the $2\nu\text{EP}\beta^-$ half-life $T_{1/2}^{2\nu\text{EP}\beta}$ without any further assumptions; for the unquenched value $g_A = 1.269$ it follows: $|m_e M^{2\nu\beta\beta}| = 0.1194$. We observe that the decay-rate ratio $\Gamma^{2\nu\text{EP}\beta}/\Gamma^{2\nu\beta\beta}$ indicates a relative suppression of the mode $2\nu\text{EP}\beta^-$ to be 1 order of magnitude lower when compared to the neutrinoless case. Moreover, the absolute half-life $T_{1/2}^{2\nu\text{EP}\beta}$ even turns out to fall within the sensitivity of some of the running experiments, which points to somewhat more optimistic prospects for finding the traces of such rare decay in the available double-beta-decay detectors.

Table II. $2\nu\beta^-\beta^-$ and $2\nu\text{EP}\beta^-$ phase-space factors $G^{2\nu\beta\beta}$ and $G^{2\nu\text{EP}\beta}$, decay-rate ratio $\Gamma^{2\nu\text{EP}\beta}/\Gamma^{2\nu\beta\beta} = G^{2\nu\text{EP}\beta}/G^{2\nu\beta\beta}$ and half-lives $T_{1/2}^{2\nu\beta\beta}$ [3] (which implies the nuclear matrix element: $|m_e M^{2\nu\beta\beta}| = 0.1194$) and $T_{1/2}^{2\nu\text{EP}\beta}$ for the isotope $^{100}$Mo.

| $G^{2\nu\beta\beta}$ [y$^{-1}$] | $G^{2\nu\text{EP}\beta}$ [y$^{-1}$] | $\Gamma^{2\nu\text{EP}\beta}/\Gamma^{2\nu\beta\beta}$ | $T_{1/2}^{2\nu\beta\beta}$ [y] | $T_{1/2}^{2\nu\text{EP}\beta}$ [y] |
|---|---|---|---|---|
| $3.809 \times 10^{-18}$ | $1.367 \times 10^{-22}$ | $3.59 \times 10^{-5}$ | $7.10 \times 10^{18}$ | $1.98 \times 10^{23}$ |

In Fig. 1, we compare the calculated $0\nu\beta^-\beta^-$ and $0\nu\text{EP}\beta^-$ single-electron spectra. These are represented by differential decay rates $1/\Gamma^{0\nu\beta\beta}\,\text{d}\Gamma/\text{d}E$ (with the former normalized to unity) as functions of the electron kinetic energy $E - m_e$. In particular, we consider the $0^+ \rightarrow 0^+$ ground-state transition of the isotope $^{100}$Mo ($Q = 3.034$ MeV), which had been extensively used in the NEMO 3 experiment [4]. From the obtained phase-space factor $G^{0\nu\text{EP}\beta}$ it follows that the single-electron mode $0\nu\text{EP}\beta^-$ constitutes a sharp peak at the endpoint of the $0\nu\beta^-\beta^-$ single-electron spectrum, i.e., the free electron effectively carries away the entire released kinetic energy $Q$. For illustration purposes, we present the $0\nu\text{EP}\beta^-$ peak as a Gaussian with $\sigma = 50$ keV (which coincides with the desired energy resolution of SuperNEMO calorimeters [6]) and exaggerate its height by a factor of $10^4$. From such disproportion it is clear that the $0\nu\text{EP}\beta^-$ peak will hardly be observed in the forthcoming measurements; nevertheless, the future double-

beta-decay experiments with tracking capability (most notably SuperNEMO) should be able to set limits on the single-electron mode $0\nu EP\beta^-$ for other isotopes.
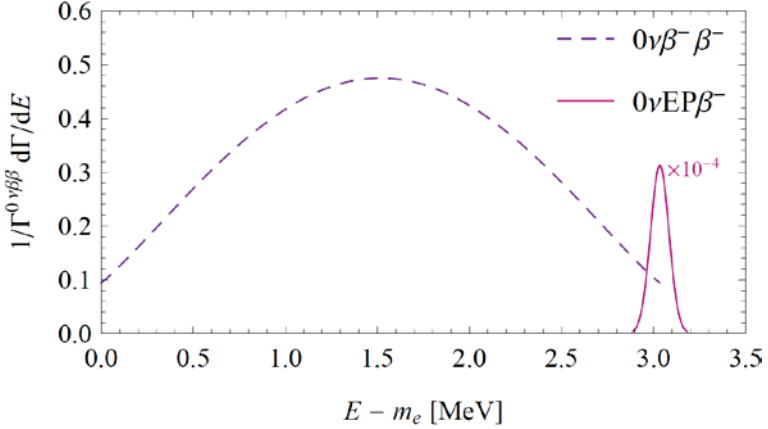


Figure 1. Single-electron $0\nu\beta^-\beta^-$ and $0\nu EP\beta^-$ spectra $1/\Gamma^{0\nu\beta\beta} \, d\Gamma/dE$ (the former normalized to unity) as functions of electron kinetic energy $E - m_e$ for the isotope $^{100}$Mo ($Q = 3.034$ MeV). The $0\nu EP\beta^-$ peak is represented by a Gaussian with $\sigma = 50$ keV and exaggerated by a factor of $10^4$.

In Fig. 2, we show the computed single-electron spectra for the $2\nu\beta^-\beta^-$ and $2\nu EP\beta^-$ modes, defined as the differential decay rates $1/\Gamma \, d\Gamma/dE$ normalized to unity, for the $0^+ \rightarrow 0^+$ ground-state transition of $^{100}$Mo ($Q = 3.034$ MeV). We immediately observe that the single-electron mode $2\nu EP\beta^-$ exhibits a different shape of the spectrum, which should in turn manifest through a slight deformation of the measured $2\nu\beta^-\beta^-$ single-electron spectra. With more than 700,000 positive events coming from approximately 7 kg of enriched $^{100}$Mo during 3.49 y of exposure (the low-radon phase) and very high signal-to-background ratio, we suggest that a thorough reassessment of the NEMO 3 data could provide us with valuable insight into the connection between the atomic physics and mechanisms of the double-beta decay [19].
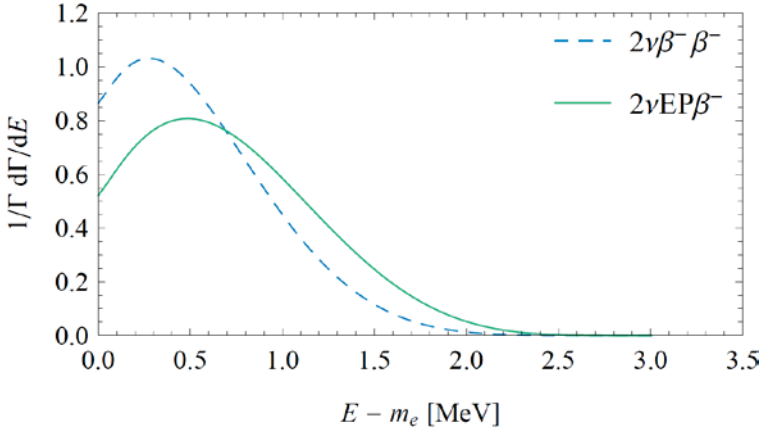
Figure 2. Single-electron $2\nu\beta^-\beta^-$ and $2\nu EP\beta^-$ spectra $1/\Gamma\, d\Gamma/dE$ (normalized to unity) as functions of electron kinetic energy $E - m_e$ for the isotope $^{100}$Mo ($Q = 3.034$ MeV).

## IV. Conclusion

We have examined new modes of $0\nu\beta^-\beta^-$ and $2\nu\beta^-\beta^-$ in which only one electron is emitted from the atom, the second one being directly produced in the atomic shell of the daughter ion. Such processes would constitute the double-beta-decay counterparts of the bound-state beta decay observed some 25 years ago [5]. We have calculated the phase-space factors, estimated the half-lives and derived the single-electron spectra for the $0^+ \rightarrow 0^+$ ground-state transition of the isotope $^{100}$Mo, which was the primary source used in the NEMO 3 experiment [4, 19]. We conclude that while the $0\nu EP\beta^-$ mode is strongly suppressed and unlikely to be observed in the future experiments, the $2\nu EP\beta^-$ mode could readily contribute to a slight deformation of the measured NEMO 3 data. The forthcoming experiment SuperNEMO will possess all means to set more stringent limits on both single-electron modes $0\nu EP\beta^-$ and $2\nu EP\beta^-$ for the isotope $^{82}$Se [6].

## References

[1] J. D. Vergados, H. Ejiri, and F. Šimkovic, Rept. Prog. Phys. **75**, 106301 (2012).

[2] Babič and F. Šimkovic, AIP Conf. Proc. **1572**, 7 (2013).

[3] S. Barabash, Nucl. Phys. A **935**, 52 (2015).

[4] R. Arnold *et al.* (NEMO 3 Collaboration), Phys. Rev. D **92**, 072011 (2015).

[5] M. Jung *et al.*, Phys. Rev. Lett. **69**, 2164 (1992).

[6] R. Arnold *et al.* (SuperNEMO Collaboration), Eur. Phys. J. C **70**, 927 (2010).

[7] S. M. Bilenky and S. T. Petcov, Rev. Mod. Phys. **59**, 671 (1987).

[8] K. A. Olive *et al.* (Particle Data Group), Chin. Phys. C **38**, 090001 (2014).

[9] Gando *et al.* (KamLAND-Zen Collaboration), Phys. Rev. Lett. **117**, 082503 (2016).

[10] J. Kotila and F. Iachello, Phys. Rev. C **85**, 034316 (2012).

[11] M. E. Rose, *Relativistic Electron Theory* (Wiley, 1961).

[12] GRASP2K Relativistic Atomic Structure Package, version 1.1, P. Jönsson, G. Gaigalas, J. Bieroń, C. Froese Fischer, and I. P. Grant, Comput. Phys. Commun. **184**, 2197 (2013).

[13] GRASP2K development version, P. Jönsson *et al.* (The Computational Atomic Structure Group), downloaded from: *http://ddwap.mah.se/tsjoek/compas/* (2015).

[14] V. B. Berestetskii, E. M. Lifshitz, and L. P. Pitaevskii, *Quantum Electrodynamics* (Butterworth–Heinemann, 1982).

[15] M. Doi, T. Kotani, and E. Takasugi, Prog. Theor. Phys. Suppl. **83**, 1 (1985).

[16] D. Štefánik, R. Dvornický, F. Šimkovic, and P. Vogel, Phys. Rev. C **92**, 055502 (2015).

[17] V. I. Tretyak and Y. G. Zdesenko, Atom. Data Nucl. Data Tabl. **80**, 83 (2002).

[18] F. Šimkovic, V. Rodin, A. Faessler, and P. Vogel, Phys. Rev. C **87**, 045501 (2013).

[19] S. Barabash and F. Piquemal, Nucl. Phys. News **23**, 12 (2013).

# HERA Results on Proton Structure and Hard QCD

Nataša Raičević on behalf of the H1 and ZEUS Collaborations

University of Montenegro, Faculty of Science, 81000 Podgorica, Montenegro

**Abstract**. We give a report of the relevant results obtained from HERA experiments H1 and ZEUS in the past two years. A short summary of the recently published HERA results on proton structure is given. New results on combined electroweak and QCD fits of inclusive neutral and charged current data with polarised lepton beams from the H1 and ZEUS experiments are discussed. We also show new preliminary results on (multi)jet production studied in neutral current deep-inelastic scattering with low photon virtuality using data taken by the H1 detector. A measurement of the jet cross sections normalized to the neutral current deep-inelastic scattering inclusive cross sections will be presented and compared to next-to-leading order and novel next-to-next-to-leading order predictions in perturbative QCD. We also show new preliminary results from ZEUS on (multi)jet and on prompt photon production studied in neutral current deep-inelastic scattering with low photon virtuality.

E-mail: natasar@ac.me

## INTRODUCTION

At the HERA collider a center of mass energy of 318 GeV was achieved by colliding electrons or positrons with energy of 27.5 GeV and protons with energy of 920 GeV. Until the year 2000 (HERA-I period) the experiments H1 and ZEUS at HERA collected an integrated luminosity of about 120 pb$^{-1}$ each. Afterwards HERA underwent a major upgrade aiming for higher luminosity and until 2007 (HERA-II period) HERA provided in total about 500 pb$^{-1}$ of e$^{\pm}$p collisions to each of the experiments.

In the last three months of HERA operation, special runs with lower proton beam energies of 460 GeV and 575 GeV were performed, each experiment collecting approximately 13 pb$^{-1}$ and 7 pb$^{-1}$ of data respectively. The main purpose of this data was the measurement of the longitudinal proton structure function which is related to the longitudinally polarised virtual boson exchange process.

# HERA RESULTS ON PROTON STRUCTURE

Deep Inelastic Scattering (DIS) of leptons on protons is considered as the best tool to examine proton structure via the measurement of Parton Density Functions (PDFs) and their dependence on virtuality of exchanged boson, $Q^2$, and Bjorken variable, x, which is fraction of proton momentum carried by the stuck quark. Proton structure described by precise PDFs is necessary for making accurate predictions for any process involving protons. DGLAP QCD evolution provides a $Q^2$ dependence of the PDFs and x PDF dependence must come from data.

To get high precision measurements of PDFs, H1 and ZEUS results are combined into one coherent data set [1]. All together, 41 Neutral Current (NC) and Charged Current (CC) data sets from H1 and ZEUS covering large kinematic plane in $Q^2$ and x, $0.045 \leq Q^2 \leq 50000$ GeV$^2$, $6 \cdot 10^{-7} \leq x \leq 0.65$, are combined. The data sets were collected over 15 years giving a total luminosity of 1 fb$^{-1}$ of e$^{\pm}$p interactions at center of mass energies of: 318, 300, 251 and 225 GeV. Close to 3000 cross sections are combined to about 1300 points with 169 correlated systematic errors and
$\chi^2$/d.o.f. = 1685/1620.

Figure 1 shows individual and combined reduced cross sections for NC e$^+$p DIS scattering as a function of $Q^2$ for selected values of Bjorken variable *x*. The improvement due to combination is clearly visible with significant reduction of statistical and systematic errors. The total uncertainty is less than 1.5 % for $Q^2 \leq 500$ GeV$^2$.
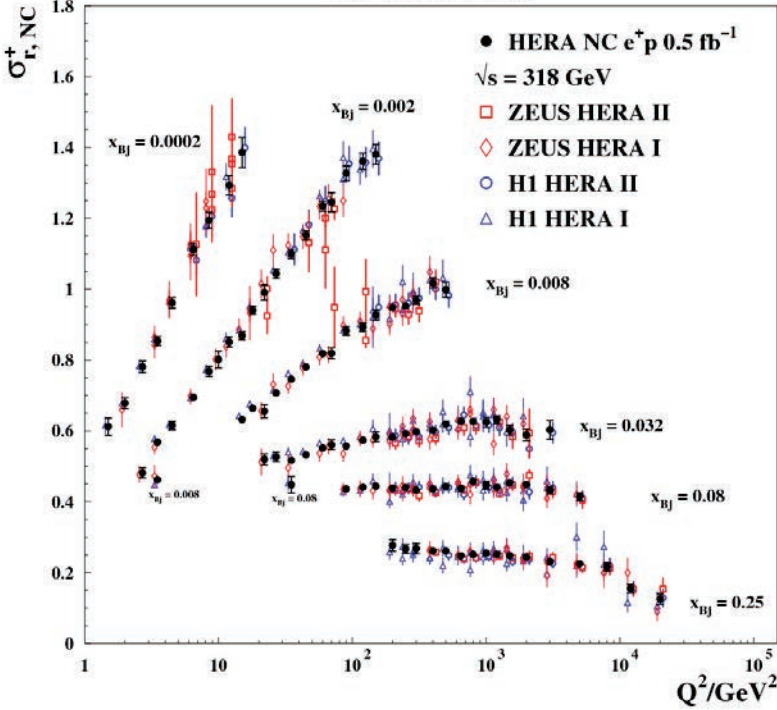
**FIGURE 1**. $Q^2$ dependence of a selection of combined HERA data for the inclusive NC $e^+p$ reduced cross sections for different values of Bjorken x compared to the individual H1 and ZEUS data. The individual measurements are shifted horizontally for better visibility. Error bars represent the total uncertainties.

The NC reduced cross section is related to the proton structure functions $F_2$, $F_L$ and $xF_3$,

$$\sigma_{NC}(e^{\pm}p) = F_2 - \frac{y^2}{1+(1-y)^2} F_L \mp \frac{1-(1-y)^2}{1+(1-y)^2} xF_3,$$

with y being the interaction inelasticity. The structure function $F_2$ measures the contribution from valence and sea quarks, $F_L$ is directly related to gluon in perturbative QCD and $xF_3$ measures contribution from valence quarks at high $Q^2$.

The combined data precisely measure electroweak effects as shown in Figure 2 which displays the cross-sections $d\sigma/dQ^2$ for NC and CC $e^-p$ and $e^+p$ scattering

86

together with predictions from HERAPDF2.0 NLO, the most recent PDF fit from HERA discussed bellow. At low $Q^2$, the CC cross section is about two orders of magnitude smaller than the NC cross section due to the $\gamma$-exchange contribution, while at high $Q^2$ they are about the same demonstrating electroweak unification at $Q^2$ around $M_Z^2$, $M_W^2$. Also, $e^+p$ NC and $e^-p$ NC are the same at low $Q^2$, in the $\gamma$-exchange domain, and differ at high $Q^2$ mainly due to $\gamma Z$ interference. The differences in $e^+p$ and $e^-p$ CC cross sections are related to u, d content of the proton and to the helicity factors $(1-y)^2$,

$$\sigma_{cc}^{e+p} \sim (x\bar{u} + x\bar{c}) + (1-y)^2 (xd + xs)$$
$$\sigma_{cc}^{e-p} \sim (xu + xc) + (1-y)^2 (x\bar{d} + x\bar{s}),$$

where xu, xd, xs and xc are u, d, strange and charm quark distributions. All the data are well described by the Standard Model expectations.
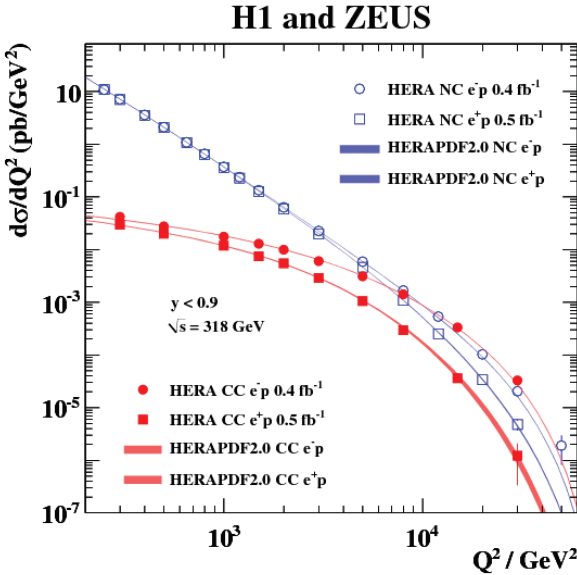


**FIGURE 2.** $Q^2$ dependence of the combined HERA NC and CC $e^-p$ and $e^+p$ cross sections, together with predictions from HERAPDF2.0 NLO. The bands represent the total uncertainty on the predictions.

Figure 3 shows the inclusive NC $e^+p$ and $e^-p$ HERA data together with fixed-target data and the predictions of HERAPDF2.0 NLO. There is $F_2$ scaling at moderate x and precise measurement of scaling violations at low and high $Q^2$. The cross section rises with $Q^2$ at low x but drops at high x - at low x due to gluon splitting and at high x due to gluon emission. Also, the electroweak effects are clearly pronounced at high $Q^2$ due to $xF_3$ contribution.

The shown data are used in a QCD analysis within the DGLAP formalism for extraction of PDFs. The most recent fit from the combined HERA data is termed as HERAPDF2.0 in which the PDFs are parameterized at a starting scale of $Q_0^2 = 1.9$ GeV$^2$ and are based on data with Q$^2$ above $Q_{min}^2 = 3.5$ GeV$^2$.

Figure 4 shows HERAPDF2.0 NLO distributions at Q$^2 = 10$ GeV$^2$ for the valence distributions for up and down quarks as well as the gluon and sea-quark distributions.The gluon and sea quark (xg and xS) are the dominant parton distributions at low x and are determined with high accuracy due to the high precision of the cross section measurements. As can be seen from the figure, the PDF parameterization uncertainty, resulting from the parameterization choice, dominates the high x region and the valence distributions, while the low x region is dominated by the model uncertainties which are obtained by varying: the charm mass, the bottom mass, the strange fraction, the minimum Q$^2$ used in the fit and the starting scale $Q_0^2$. Experimental uncertainties of the fit were determined using the Hessian method with the criterion $\Delta\chi^2 = 1$ (68 % CL).

The resulting parton distribution functions were also obtained at LO and NNLO. Also an extensive investigation included fits with different heavy flavor schemes, different $Q_{min}^2$, with an alternative gluon parameterization and with a scan of $\alpha_s(M_Z)$ in steps of 0.001.
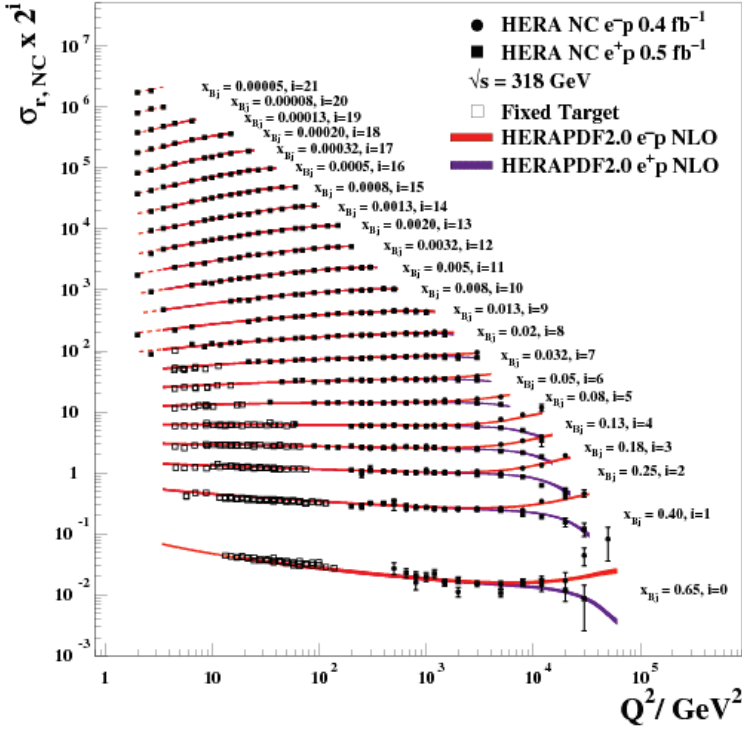
**FIGURE 3**. $Q^2$ dependence of combined HERA data for the inclusive NC $e^{\pm}$preduced cross sections for different values of Bjorken x. Fixed-target data and the predictions of HERAPDF2.0 NLO are also shown.
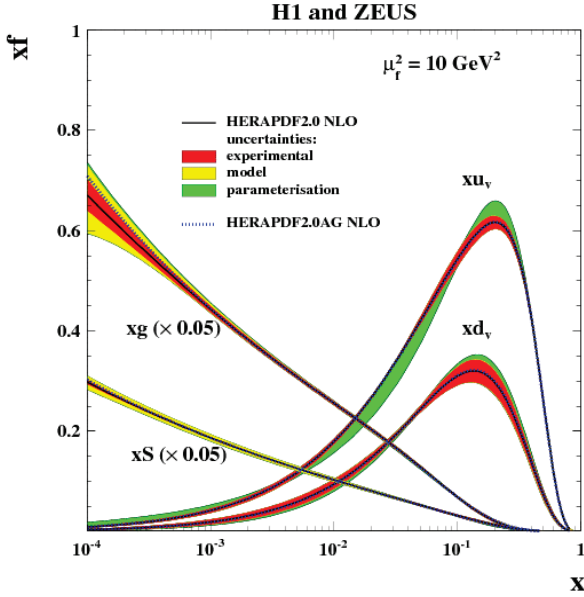
**FIGURE 4**. Parton distributions as determined by the HERAPDF2.0 QCD fit at $Q^2 = 10$ GeV$^2$. The gluon and sea-quark densities are scaled down by a factor 0.05. The inner error bands show the experimental uncertainty, the middle error bands include the theoretical model uncertainties of the fit assumptions, and the outer error bands represent the total uncertainty including the parameterization uncertainty.

## H1 AND ZEUS COMBINED ELECTROWEAK AND QCD FITS

Using the e$^\pm$p NC and CC cross sections, combined electroweak (EW) and QCD analyses were performed by both collaborations to determine the vector and axial-vector couplings $v_q$ and $a_q$ to the light quarks u and d to the $Z^0$ boson, accounting for their correlation with PDFs. For this analysis H1 collaboration have used only H1 data [2] and ZEUS used uncombined H1 and ZEUS data of NC and CC cross sections [3]. Preliminary results from H1 and published results from ZEUS for the couplings $a_u$, $v_u$ and $a_d$, $v_d$ are shown in figure 5. The figure also shows published results from H1 obtained using only HERA I data [4]. Also shown are Standard Model expectations.

Figure 5 shows that the results from H1 and ZEUS are compatible and also consistent with the SM expectation. There is remarkable sensitivity of HERA data

to u-type quark couplings and there is a considerable improvement over published results of H1 from HERA-I data. Significantly improved sensitivity comes from using polarized HERA-II data and polarization in HERA-II is important in particular for vector couplings.
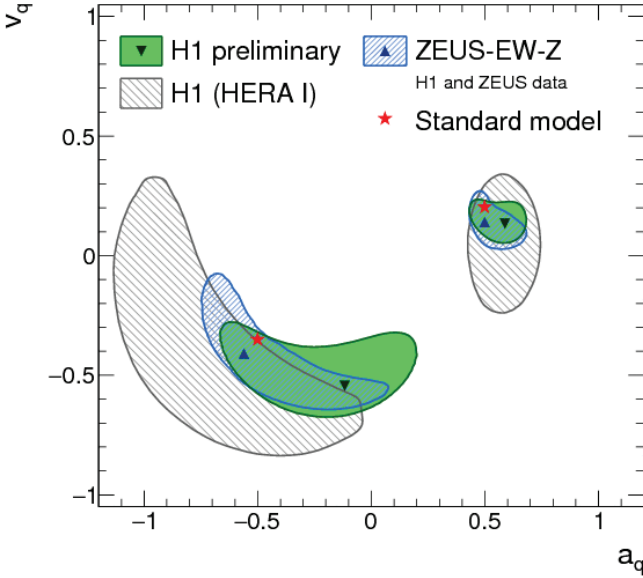


**FIGURE 5**. The 68% C.L. contours for (ad, vd) - left part of the figure and (au, vu) – right part of the figure, obtained from ZEUS and H1 combined EW+QCD fits. Also shown are published results from HERA-I and the SM values.

Figure 6 shows the results from ZEUS compared to other measurements from LEP, TEVATRON and from H1 based on HERA-I data. The PDG14 values are also shown. HERA results are consistent with other experiments and resolving the LEP sign-ambiguity. HERA results on u-type coupling are highly accurate and present the most precise determination of the axial-vector and vector couplings of the Z boson to u-type quarks.

Both collaborations also extracted the values of $M_W$ and of Weinberg angle, $\sin^2\theta_W$ with combined EW+QCD parameter fits. The value extracted by the ZEUS fit for $M_W$ is

$$M_W = 80.68$$
$$\pm\ 0.28\ \text{(experimental/fit)}^{+0.12}_{-0.01}\text{(model)}^{+0.23}_{-0.01}\text{(parameterisation) GeV}\ .$$

The on-shell value of $\sin^2\theta_W$ obtained by ZEUS fit was determined as

$$\sin^2\theta_W = 0.2252 \pm 0.0011$$

(experimental/fit)$^{+0.0003}_{-0.0001}$ (model)$^{+0.0007}_{-0.0001}$ (parameterisation).

The values of $\sin^2\theta_W$ and $M_W$ are in agreement with Standard Model expectations.
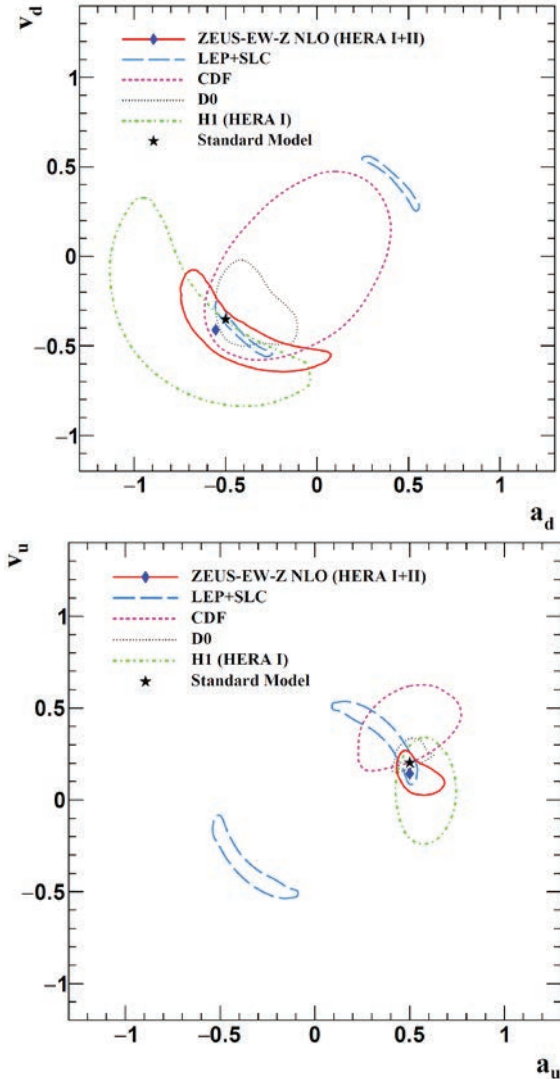
**FIGURE 6**. The 68% C.L. contours for $(a_d, v_d)$ and $(a_u, v_u)$ obtained from ZEUS combined EW+QCD fit compared with published results from LEP, TEVATRON and from H1 based on HERA-I data. The PDG14 values are also shown.

# MULTIJET PRODUCTION IN DIS AT LOW $Q^2$

The H1 collaboration has a new measurement of jet cross sections in neutral current deep inelastic scattering normalized to the neutral current deep-inelastic scattering inclusive cross sections [5, 6]. The normalized jet cross sections are defined as the ratio of the double differential absolute jet cross sections to the inclusive NC DIS cross section in the respective $Q^2$ bin. Such normalization provides full cancellation of normalization uncertainties and partial cancellation of other experimental uncertainties. Inclusive jet, dijet and trijet cross sections, absolute and normalized to NC are measured in bins of $Q^2$ and jet transverse momentum in the Breit frame, $P_T^{jet}$, with $5.5 < Q^2 < 80$ GeV$^2$ and $P_T^{jet} > 4.5$ GeV (for inclusive jets).

Figure 7 shows double-differential cross sections for normalized inclusive jet production in neutral current DIS as function of $Q^2$ and $P_T^{jet}$. For the NC DIS cross sections in the denominator of the normalized jet cross sections the program QCDNUM in NLO [7] is used. The figure also shows, new cross sections for $5 < P_T^{jet} < 7$ GeV in the range $150 < Q^2 < 15\,000$ GeV$^2$ and previously published results in the high $Q^2$ domain [8]. The data are compared to NLO and NNLO predictions. This is first ever comparison with brand new NNLO QCD calculations, approximate NNLO prediction [9] obtained from the program JetVip [10] and full NNLO prediction [11] obtained from the NNLOJET [11,12].

Figure 8 shows the ratio of normalized inclusive jet cross sections, NNLO and aNNLO predictions to the NLO predictions. The inclusive jet data are reasonably well described by NLO (obtained from the program NLOJET++[13]), but NLO scale uncertainty is rather large. There is an improved description of data (particularly in shape) by NNLO with significantly reduced scale uncertainty for higher values of jet $p_T$. There is also an improvement of the inclusive jet data description with a NNLO on absolute level at higher values of transverse momentum of the jets.
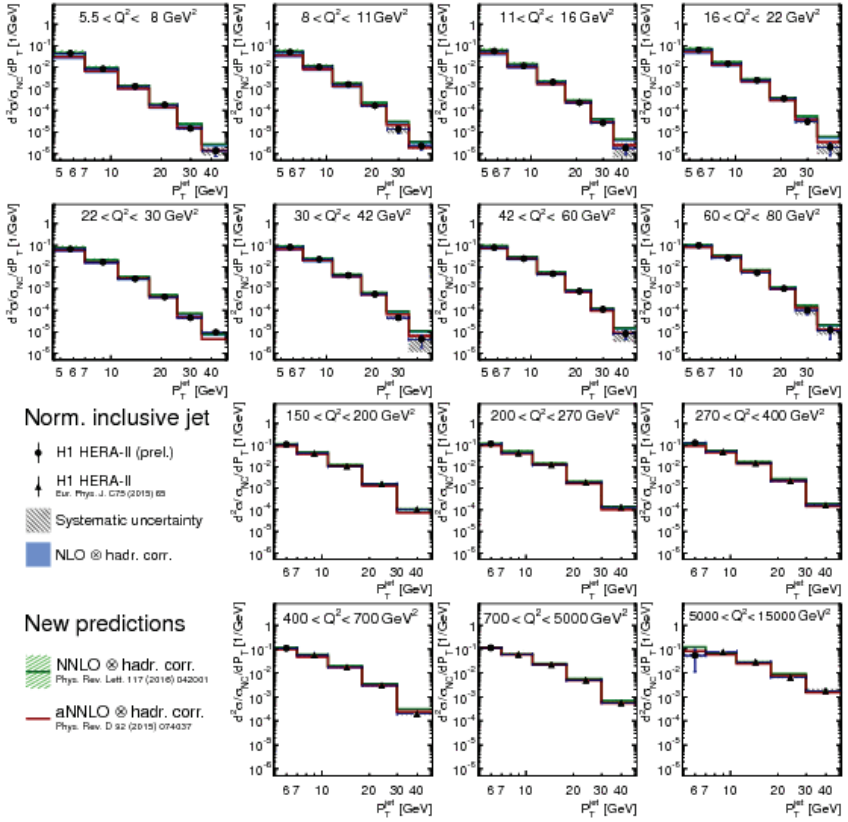
**FIGURE 7**. Double-differential cross sections for normalized inclusive jet production in neutralcurrent DIS as function of $Q^2$ and $P_T^{jet}$. The vertical error bars indicate the statistical uncertainties.The shaded areas around the data points show the systematic uncertainties. The data are compared to NLO predictions, approximate NNLO and full NNLO predictions.

Normalized dijet and trijet cross sections, where events with at least two or three jets are counted, are obtained as a function of $Q^2$ and the average transverse momentum of the two or three leading jets, $\langle P_T \rangle_2$ and $\langle P_T \rangle_3$, respectively, in the ranges $5 < \langle P_T \rangle_2 < 50$ GeV and $5.5 < \langle P_T \rangle_3 < 40$ GeV.

Ratio of normalized dijet cross sections and NNLO predictions to NLO predictions shows similar trend as can be seen in figure 9. NNLO predictions for trijets are not available yet.
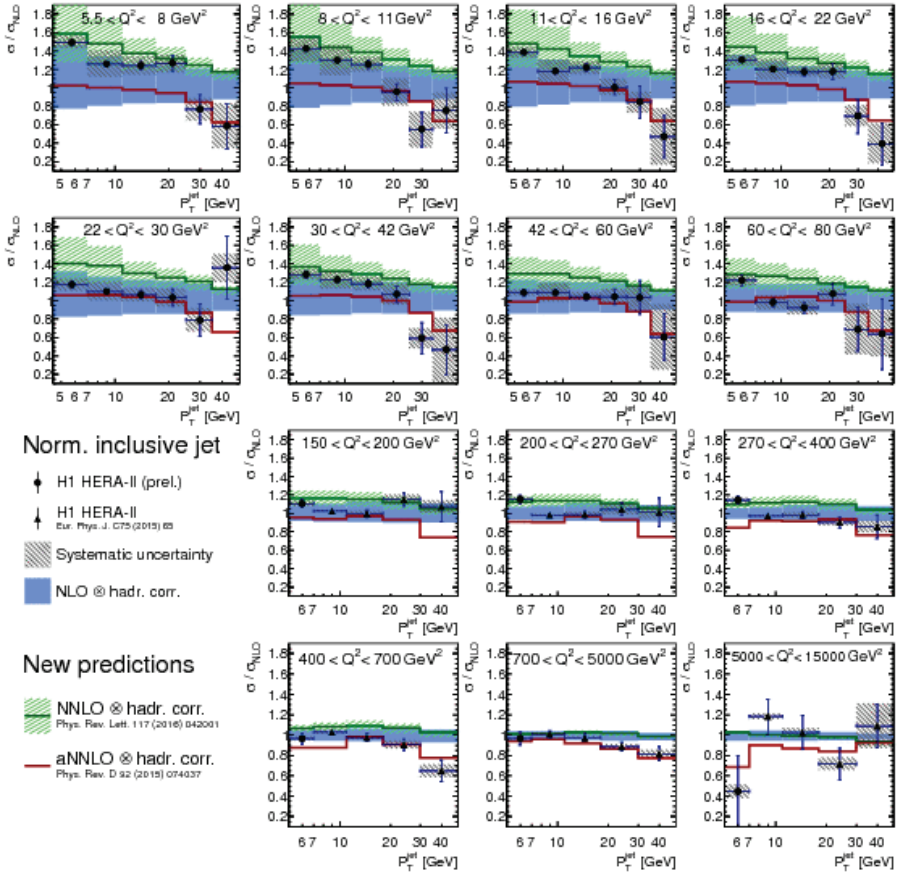
**FIGURE 8**. Ratio of normalized inclusive jet cross sections, NNLO and aNNLO predictions to the NLO predictions as function of $Q^2$ and $P_T^{jet}$. Other details as in figure 7.

The new normalized multijet data are used for extraction of the strong coupling constant at the Z-boson mass, $\alpha_s(M_Z)$, and also are sensitive to the running of $\alpha_s(\mu_r)$. The behavior of the strong coupling constant is studied in a fit of NLO predictions to data and shown in figure 10. The data for normalized inclusive jet, dijet and trijet production are separated into six groups with similar values of $\mu_r$ and the value of $\alpha_s(M_Z)$ is obtained from minimizing $\chi^2$.

The value of $\alpha_s(\mu_r)$ is calculated from $\alpha_s(M_Z)$ by applying the solution for the evolution equation of $\alpha_s(\mu_r)$. The scale uncertainty is obtained by repeating the fits with the different choices for scale factors. The running of the strong coupling

constant is probed by the new data in the range of approximately $5 < \mu_r < 35$ GeV. The uncertainties on the NLO predictions dominate significantly over the experimental uncertainties. Also, data points from the high-$Q^2$ domain may be considered in the fit. A fit to all the data yields an experimental precision on $\alpha_s(M_Z)$ of about 4 permille. Relevant theoretical uncertainties are much higher than the experimental uncertainties mainly due to the scale uncertainties.
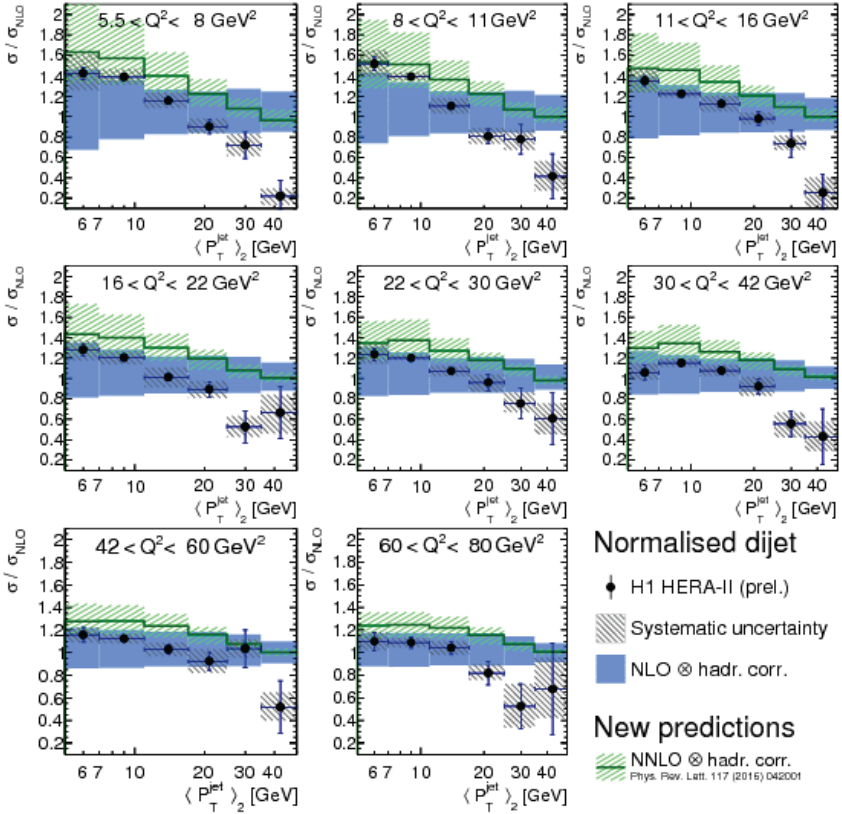


**FIGURE 9**. Ratio of normalized dijet cross sections and NNLO predictions to NLO predictions as a function of $Q^2$ and the average transverse momentum of the two leading jets. Other details as in figure 7.
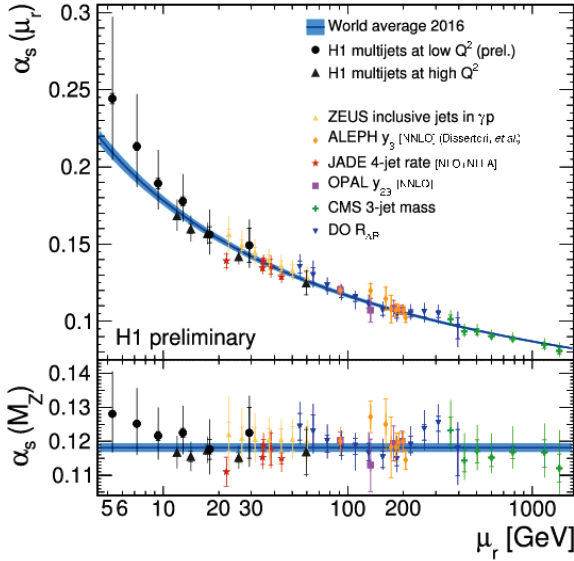
**FIGURE 10**. The values of the strong coupling $\alpha_s(\mu_r)$ (upper panel) and of the equivalent values of $\alpha_s(M_Z)$ for all measurements (lower panel) obtained from the normalized inclusive jet, dijet and trijet cross sections using NLO predictions and compared to values extracted from other jet data. The solid line shows the world average value of $\alpha_s(M_Z)$ and its value evolved to $\mu_r$ using the solution of the QCD renormalization group equation.

## ISOLATED PHOTON ACCOMPAINED BY JET IN DIS

Isolated high-energy photons emitted in high-energy collisions can provide information on the proton structure and give a probe of underlying partonic process since they are detected unaffected by parton hadronisation. High energy photons can be produced in DIS either by the incoming or outgoing quark ("QQ" photons ) or by the incoming or outgoing lepton ("LL" leptons). QQ photons are classified as "prompt" and LL photons are treated as background to the QCD process. ZEUS obtained new results [14] from analysis of DIS events with the production of an isolated photon and at least one additional jet, $ep \rightarrow e`\gamma + jet$.

Differential cross sections are obtained as functions of the fraction of the incoming photon energy that is given to the photon and the jet, $x_\gamma$, fraction of proton energy taken by the parton that interacts with the photon $x_p$, azimuthal angle between the prompt photon and the jet $\Delta\Phi$, pseudorapidity difference between the prompt photon and the jet $\Delta\eta$, azimuthal angle between the prompt photon and the

98

scattered electron $\Delta\Phi_{e,\gamma}$ and pseudorapidity difference between the prompt photon and the scattered electron $\Delta\eta_{e,\gamma}$.
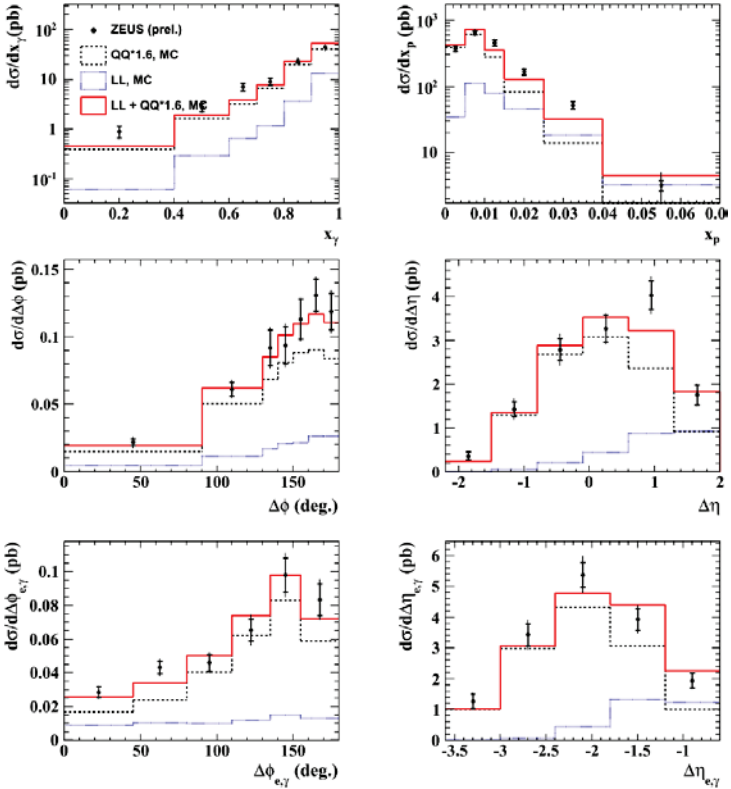


**FIGURE 11**. Differential cross sections in (a) $x_\gamma$, (b) $x_p$, (c) $\Delta\Phi$, (d) $\Delta\eta$, (e) $\Delta\Phi_{e,\gamma}$, and (f) $\Delta\eta_{e,\gamma}$ compared to the reweighted Monte Carlo predictions from the sum of QQ photons from Pythia normalized by a factor 1.6 plus Djangoh LL photons. The dashed (dotted) lines show the QQ (LL) contributions.
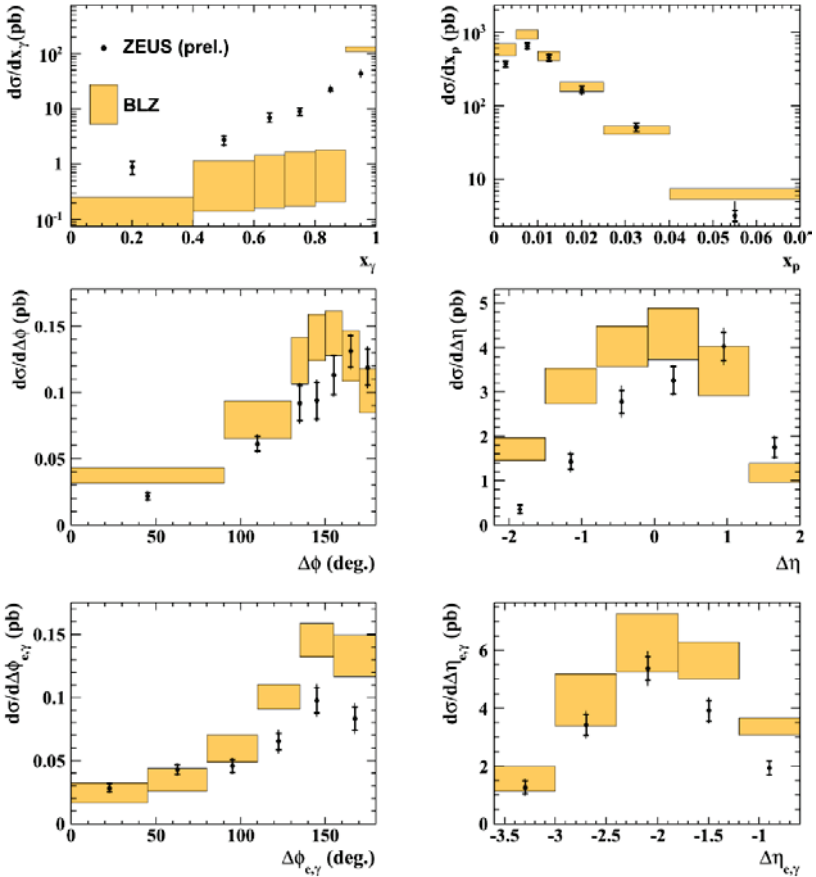
**FIGURE 12**. Differential cross sections in (a) $x_\gamma$, (b) $x_p$, (c) $\Delta\Phi$, (d) $\Delta\eta$, (e) $\Delta\Phi_{e,\gamma}$, and (f) $\Delta\eta_{e,\gamma}$ compared to the BLZ model based on the $k_T$ factorization.

Figure 11 shows that the resulting cross sections agree well with the theory calculations based on the predictions for the sum of the expected LL contribution from Djangoh [15] and a factor of 1.6 times the expected QQ contribution from Pythia [16] without further weighting.

Figure 12 shows the resulting cross sections compared to the theory calculations based on the $k_T$ factorisation method used by BLZ (Baranov, Lipatov, Zotov) model [17]. This approach takes into account both QQ and LL photons, neglecting the small interference contribution (LQ). In the $k_T$ factorisation theory some part of final state jets can originate not only from hard subprocess, but also from the

parton evolution cascade in initial state. As can be seen, $x_\gamma$ and $\Delta\eta$ distributions are not described by $k_T$-factorization.


## SUMMARY

HERA experiments, H1 and ZEUS, have finalized measurements of inclusive NC and CC DIS cross sections and QCD fits. H1 and ZEUS have combined all inclusive measurements into one coherent data set for $e^+p$ and $e^-p$ collisions at $\sqrt{s}$ = 318, 300, 251 and 225 GeV. The combined inclusive HERA data are used as a sole input to the QCD analysis resulting in the set of parton distribution functions HERAPDF2.0.

Both collaborations have performed new combined EW and QCD fits providing high precision measurements of electroweak parameters. The data show high sensitivity to light quark couplings and the SM parameters. The fits provide important complementary tests of the SM.

Concerning the hard QCD domain, inclusive jets, dijets, trijets cross sections as well as those normalized to inclusive NC cross section are now available for the whole $Q^2$ range, based on H1 data. The data provide first ever comparisons with brand new NNLO QCD calculations presented for some of these normalized jet cross sections; the scale uncertainty is visibly reduced and the shape is better described compared to NLO. The experimental precision of $\alpha_s$ determination based on these data is now ~0.4% and is significantly better than theory uncertainty.

The production of isolated photons accompanied by jets has been measured in deep inelastic scattering with the ZEUS detector. The results are in agreement with Pythia after a rescaling has been applied and can be used to make further improvements in the QCD calculations.

## REFERENCES

1. H1 and ZEUS Collaborations, Eur. Phys. J. C75, 580 (2015).
2. H1 Collaboration, H1prelim-16-041, (2016).
3. ZEUS Collaboration, Phys.Rev. D 93, 092002(2016).
4. H1 Collaboration, Phys.Lett.B 632, 35 (2006).
5. H1 Collaboration, H1prelim-16-061, (2016).
6. H1 Collaboration, H1prelim-16-062, (2016).
7. M. Botje, Comput. Phys. Commun. 182, 490 (2011).
8. H1 Collaboration, Eur. Phys. J. C75, 65 (2015).
9. T. Biekötter, M. Klasen and G. Kramer, Phys. Rev. D92 7, 074037 (2015).

10. B. Pötter, Comput. Phys. Commun. 133, 105 (2000).
11. J. Currie, T. Gehrmann and J. Niehues, Phys. Rev. Lett. 117, 042001 (2016).
12. A. Gehrmann-De Ridder, T. Gehrmann, E.W.N. Glover, A. Huss and T.A. Morgan, JHEP 1607, 133 (2016).
13. Z. Nagy and Z. Trocsanyi, Phys. Rev. Lett. 87, 082001 (2001).
14. ZEUS Collaboration, ZEUS-prel-16-001, (2016).
15. K. Charchula, G. A. Schuler, and H. Spiesberger, Comput. Phys. Commun. **81,** 381 (1994).
16. T. Sjöstrand et al., JHEP 0605, 26 (2006).
17. S. Baranov, A. Lipatov and N. Zotov, Phys. Rev. D 81, 094034 (2010).

# Searches for lepton number violation and resonances in the K± → πμμ decays at the NA48/2 experiment

**D. Madigozhin** [1]

*Joint Institute for Nuclear Research, Dubna, Russia,*

*e-mail: madigo@mail.cern.ch*

---

[1]      for the NA48/2 Collaboration: G. Anzivino, R. Arcidiacono, W. Baldini, S. Balev, J.R. Batley, M. Behler, S. Bifani, C. Biino, A. Bizzeti, B. Bloch-Devaux, G. Bocquet, N. Cabibbo, M. Calvetti, N. Cartiglia, A. Ceccucci, P. Cenci, C. Cerri, C. Cheshkov, J.B. Chèze, M. Clemencic, G. Collazuol, F. Costantini, A. Cotta Ramusino, D. Coward, D. Cundy, A. Dabrowski, P. Dalpiaz, C. Damiani, M. De Beer, J. Derré, H. Dibon, L. DiLella, N. Doble, K. Eppard, V. Falaleev, R. Fantechi, M. Fidecaro, L. Fiorini, M. Fiorini, T. Fonseca Martin, P.L. Frabetti, L. Gatignon, E. Gersabeck, A. Gianoli, S. Giudici, A. Gonidec, E. Goudzovski, S. Goy Lopez, M. Holder, P. Hristov, E. Iacopini, E. Imbergamo, M. Jeitler, G. Kalmus, V. Kekelidze, K. Kleinknecht, V. Kozhuharov, W. Kubischta, G. Lamanna, C. Lazzeroni, M. Lenti, L. Litov, D. Madigozhin, A. Maier, I. Mannelli, F. Marchetto, G. Marel, M. Markytan, P. Marouelli, M. Martini, L. Masetti, K. Massri, E. Mazzucato, A. Michetti, I. Mikulec, N. Molokanova, E. Monnier, U. Moosbrugger, C. Morales Morales, D.J. Munday, A. Nappi, G. Neuhofer, A. Norton, M. Patel, M. Pepe, A. Peters, F. Petrucci, M.C. Petrucci, B. Peyaud, M. Piccini, G. Pierazzini, I. Polenkevich, Yu. Potrebenikov, M. Raggi, B. Renk, P. Rubin, G. Ruggiero, M. Savrié, M. Scarpa, M. Shieh, M.W. Slater, M. Sozzi, S. Stoynev, E. Swallow, M. Szleper, M. Valdata-Nappi, B. Vallage, M. Velasco, M. Veltri, S. Venditti, M. Wache, H. Wahl, A. Walker, R. Wanke, L. Widhalm, A. Winhart, R. Winston, M.D. Wood, S.A. Wotton, A. Zinchenko, M. Ziolkowski.

**Abstract**

The NA48/2 experiment at CERN collected a large sample of charged kaon decays into final states with multiple charged particles in 2003-2004. A new upper limit on the rate of the lepton number violating decay $K^{\pm} \to p^+ m^{\mp} m^{\pm}$ obtained from this sample is set: $8.6 \times 10^{-11}$ at 90% CL, which improves by more than an order of magnitude upon the previous measurements. Results of the search for two-body resonances like heavy neutral leptons and inflatons in $K^{\pm} \to pmm$ decays are also presented.

## 1 Introduction

The important consequence of the neutrino oscillations discovery is the existence of neutrino masses and right-handed neutrino states [1]. In the Neutrino Minimal Standard Model (nMSM) [2] three right-handed sterile neutrinos are proposed in order to explain simultaneously neutrino oscillations and the baryon asymmetry of the observed Universe. The first of these right-handed neutrinos has a mass of O(1 KeV) and is a dark matter candidate. The other two neutrinos have masses in the range of (0.1-10) GeV/c$^2$ and may induce the barion asymmetry by means of additional CP violating phases.

The (nMSM) model can be extended by adding of the scalar field called inflaton which helps to explain the inflation and provides a common source of the electroweak symmetry breaking and the right-handed neutrino masses [3].

These models predict new particles – heavy Majorana neutrinos and inflatons, that can be detected in $K^{\pm} \to pmm$ decays. In particular the decay mode $K^{\pm} \to p^+ m^{\mp} m^{\pm}$ is a Lepton Number Violating (LNV) one. It is forbidden in SM, but it can proceed via the on-shell Majorana neutrino. Inflatons c can be produced in the $K^{\pm} \to p^{\pm} c$ decay, and then they may be detected via $c \to m^+ m^-$ process as a peak in the mm invariant mass spectrum.

The main goal of NA48/2 experiment was the search for CP-violating asymmetry in $K^{\pm} \to 3p$ decays [4]. Additionally, it has provided in 2003-2004 a large data sample for charged kaon rare decay studies, including the search for LNV kaon decays and a possible two-body sharp resonanses in the mass spectra of mm and pm final states. Results of this search are briefly reported in the present work and are published in details in [5].

## 2 The NA48/2 beam and detector

The NA48/2 detector and beam at CERN SPS are described in details in [4, 6]. Two simultaneous and collinear K$^+$ and K$^-$ beams were produced by 400 GeV/c protons on a beryllium target. Particles of opposite charge with a central momentum of 60 GeV/c and a momentum band of ±3.8%(RMS) were selected by the system of magnets and collimators. Both beams of about 1 cm width were

following almost the same path in the decay volume contained in a 114 m long vacuum tank. The downstream end of the tank was sealed by a convex Kevlar window separating vacuum from helium at atmospheric pressure. The beams were dominated by $p^{\pm}$, the kaon component was about 6%.

Charged products of $K^{\pm}$ decays were measured by the magnetic spectrometer installed in helium. It was consisting of four drift chambers (DCH1–DCH4) and a dipole magnet providing a horisontal momentum kick of about 120 MeV/c, that was located between DCH2 and DCH3. The spatial resolution of each chamber was nearly 90 mm and the spectrometer momentum resolution was $s_p/p = (1.02 \oplus 0.044\ p)\%$ (p in Gev/c).

The spectrometer was followed by a scintillator hodoscope HOD with a time resolution of ~150 ps, whose fast signals were used to trigger the readout of events with a charged track. It consisted of a horizontal and a vertical planes of strip-shaped counters.

A Liquid Krypton calorimeter (LKr), located behind the hodoscope, was used to measure the energy of electrons and photons. It is an almost homogeneous ionization chamber with an active volume of 7 $m^3$ of liquid krypton $27X_0$ deep, segmented transversally into projective cells, 2x2 $cm^2$ each. Transverse position of isolated shower was measured with a spatial resolution $s_X=s_Y=(0.42/\sqrt{E} \oplus 0.06)$ cm. Energy resolution for photons and electrons was $s_E/E = (3.2/\sqrt{E} \oplus 9.0/E \oplus 0.42)\%$ (E in GeV), and a single shower time resolution was $s_t = (2.5/\sqrt{E})$ ns.

The muon system MUV, consisted of three scintillator planes (MUV1,MUV2,MUV3) and 80 cm thick iron walls, was used for the muons identification. An aluminium beam pipe of 16 cm outer diameter and 1.1 mm thickness was traversing the centres of all the detector elements, providing the path in vacuum for undecayed beam particles and for muons from beam $p^{\pm}$ decays.

## 3 Events selection

Event selection is based on the three-track vertex reconstruction, as for the experimental longitudinal position resolution of about 50 cm, both $K^{\pm} \rightarrow p^{\mp}m^{\pm}m^{\pm}$ (LNV) and $K^{\pm} \rightarrow p^{\pm}m^{+}m^{-}$ (LNC) decays mediated by a short-lived resonant particle are indistinguishable from a three-track decay. $K^{\pm} \rightarrow p^{\pm}p^{+}p^{-}$ ($K_{3p}$) decays were used as a normalization channel. The corresponding samples were collected concurrently using the same trigger logic.

In order to select $K_{pmm}$ or $K_{3p}$ candidate, a vertex satisfying the following common criteria was required: the total charge of the three tracks is ±1; the vertex longitudinal position is within the 98 m long fiducial decay volume; the vertex tracks momentum is between 5 GeV/c and 55 GeV/c; the total momentum of three tracks is consistent with the beam nominal range (55-65) GeV/c; and the total
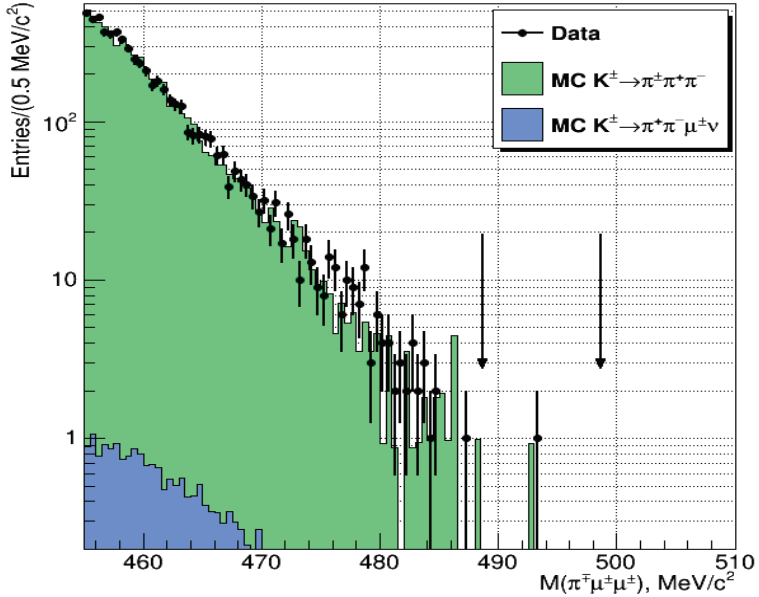
transverse momentum of three tracks with respect to the beam axis is below 0.01 GeV/c.

Figure 1: Lepton number violating $K^{\pm} \to p^{\mp} m^{\pm} m^{\pm}$ decay invariant mass spectrum for data and MC. The signal region is indicated with vertical arrows.

The vertex with a lowest fit $c^2$ is considered in the case of a few selected combinations. The vertex tracks are required to be consistent in time and to be in DCH, HOD, LKr and MUV geometric acceptances. Track separations are required to exceed 2 cm in the DCH1 plane to suppress photon conversions, and 20 cm in the LKr, MUV1 and MUV2 front planes to minimize particle misidentification due to shower overlaps and Coulomb scattering.

The $K^{\pm} \to pmm$ candidate vertex must be composed of one pion candidate (with the ratio of energy E in the LKr calorimeter to momentum p measured in the spectrometer E/p < 0.95, and without in-time associated hits in the MUV), and a pair of identically or oppositely charged muon candidates (with E/p < 0.2 and with the associated hits in MUV).

106
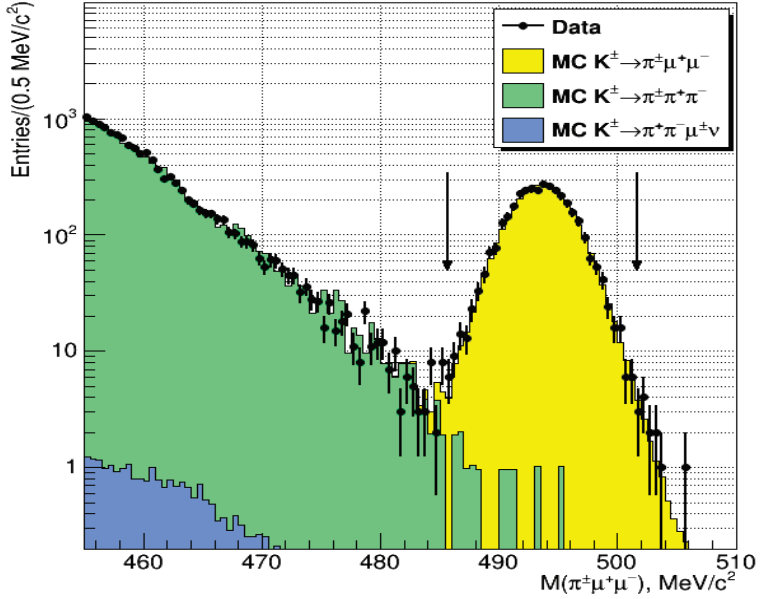
Figure 2: Lepton number conserving $K^{\pm} \to p^{\pm}m^{+}m^{-}$ decay invariant mass spectrum for data and MC. The signal region is indicated with vertical arrows.

The pion candidate is required to have momentum above 15 GeV/c for high muon rejection efficiency. The invariant mass of three tracks in the $K^{\pm} \to pmm$ hypothesis must satisfy the requirement of $|M(p^{+}m^{\pm}m^{\pm})-M_K| < 5$ MeV/c$^2$ ($|M(p^{\pm}m^{+}m^{-})-M_K| < 8$ MeV/c$^2$ ), where $M_K$ is the PDG kaon mass [1]. The invariant mass distributions for LNV and LNC decay modes are shown in Fig. 1 and Fig. 2.

An additional requirement is applied to the $K^{\pm} \to pmm$ samples, when searching for resonances: $|M_{ij} - M_X| < 2s(M_{ij})$, where $M_{ij}$ is the invariant mass of the pair (ij = $p^{\pm}m^{\mp}$ or $m^{+}m^{-}$), $M_X$ is the assumed resonance mass, and $s(M_{ij})$ is the resolution on the invariant masses.

Independently, the following criteria are applied to select the $K_{3p}$ sample: the pion identification criterion is applied to the odd-sign pion only in order to symmetrize the selection of the signal and normalisation modes, and the invariant mass of three tracks in the $3p^{\pm}$ hypothesis is in the range $|M_{3p} - M_K| < 5$ MeV/c$^2$.

## 4 Resonance searches

A search for peaks was performed over the distributions of the invariant masses of $p^{\pm}m^{\mp}$ and $m^{+}m^{-}$ pairs. The precise evaluation of acceptance for $K^{\pm} \to m^{\pm}X$ and

$K^{\pm}\to p^{\pm}X$ decays with a subsequent $X\to p^{\pm}m^{\mp}$ or $X\to m^{+}m^{-}$ decay as a function of resonance mass and lifetime has been performed with a dedicated MC simulations.

The mass steps for the resonance searches and the width of the signal windows are determined by the resolutions on the invariant masses. The mass step is set to be equal to $s(M_{ij})/2$, while the half-width of the signal mass window is $2s(M_{ij})$. Therefore, the results obtained in the neighbouring mass hypotheses are highly correlated, as the windows are overlapped. In total, 284, 267 and 280 mass hypotheses were tested respectively for the search of resonances in M(pm) distribution of LNV, LNC candidates and in the M(mm) distribution of LNC candidates, covering the full kinematic ranges.

The statistical analysis of the obtained results in each mass window is done by means of the quasi-Newton minimisation algorithm to find numerically the 90% confidence intervals for the case of a Poisson process in presence of unknown backgrounds, by applying an extension of the Rolke-Lopez method [7]. The number of considered background sources for LNV mode was 4 ( $3p^{\pm}$, $p^{+}p^{-}m^{\pm}n$, $p^{\pm}m^{+}m^{-}$, $m^{+}m^{-}m^{\pm}n$), and for LNC it was only $K^{\pm}\to 3p^{\pm}$.

## 5 Results

Only one LNV event is observed, while the estimated background expectation was $1.163\pm0.867_{stat}\pm0.021_{ext}\pm0.116_{syst}$ . So no signal evidence is observed, and a 90% upper limit on the branching ratio $B(K^{\pm}\to p^{\mp}m^{\pm}m^{\pm})$ is set applying the statistical analysis. Using the values of the signal acceptance estimated with MC simulations and the $N_{LNV}$ number of kaon decays in the fiducial volume, the upper limit on the number of signal events leads to a constraint on the signal branching ratio:

$$B(K^{\pm}\to p^{\mp}m^{\pm}m^{\pm}) = B(K_{3p}) N_{LNV} A(K_{3p}) / [N_{3p} A(LNV)] < 8.6 \times 10^{-11} \text{ at 90\% CL.}$$

The total systematic uncertainty on the quoted upper limit is 1.5%. he largest source is the limited accuracy of the MC simulations (1.0%), followed by the external errors from PDG values of $B(K^{\pm}\to p^{\pm}m^{+}m^{-})$ (0.8%), $B(K_{3p})$(0.73%) and $B(K^{\pm}\to p^{+}p^{-}m^{\pm}n)$ (0.05%).

For each of the three resonance searches a local significance z of the signal has been evaluated for each mass hypothesis: $z=(N_{obs} - N_{exp})/\sqrt{(dN^{2}_{obs}+dN^{2}_{exp})}$, where $N_{obs}$ is the number of observed events, $N_{exp}$ is the number of expected background events, and $dN_{obs}$ ($dN_{exp}$) is the statistical uncertainty for $N_{obs}$ ($N_{exp}$). The local significance never exceed 3 standard deviations, therefore no signal is observed.
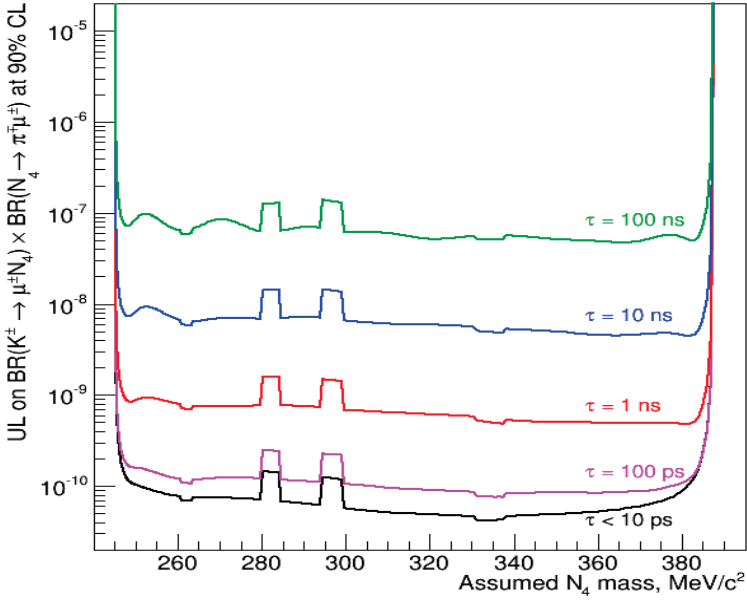
Figure 3: Obtained upper limits at 90% CL on $B(K^\pm \to m^\pm N_4)B(N_4 \to p^\mp m^\pm)$
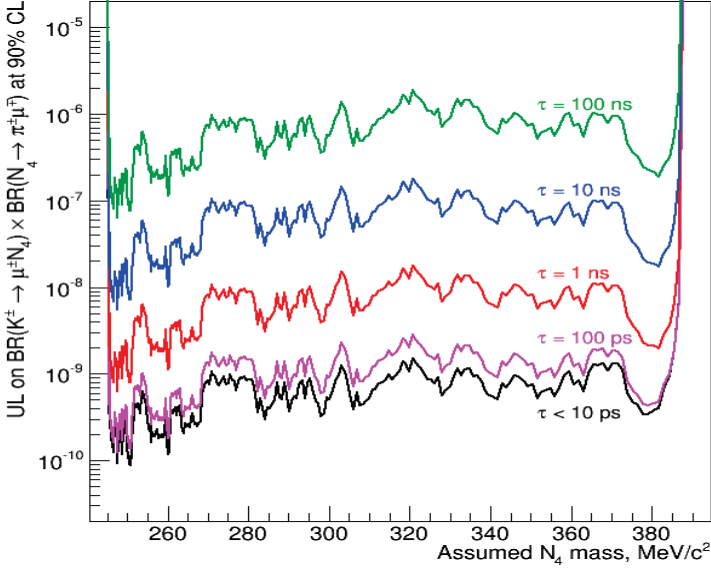


Figure 4: Obtained upper limits at 90% CL on $B(K^\pm \to m^\pm N_4)B(N_4 \to p^\pm m^\mp)$
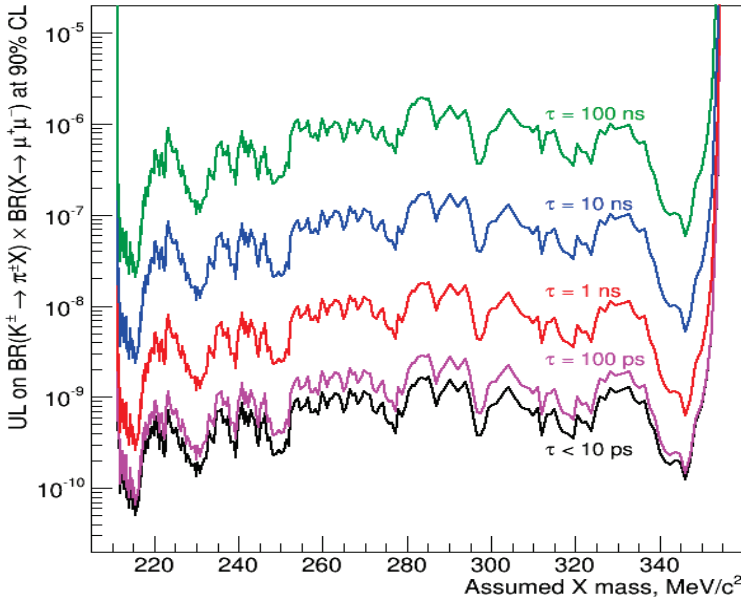
Figure 5: Obtained upper limits at 90% CL on $B(K^{\pm} \to p^{\pm}c)B(c \to m^{+}m^{-})$

    In the absence of a signal, upper limits has been set on the products of branching fractions. The upper limits corresponding to the observed signal events for the three resonance searches for several lifetimes are presented on Figures 3, 4, 5.

**Conclusion**

The searches for LNV $K^{\pm} \to p^{\mp}m^{\pm}m^{\pm}$ decay and resonances in $K^{\pm} \to pmm$ decays have been performed by NA48/2 experiment on the basis of 2003-2004 data. No signals are observed. An obtained upper limit of $8.6 \times 10^{-11}$ for the LNV decay branching ratio improves the best earlier limit [8] by the order of magnitude.

    Apart from that, an upper limits are set on the products of branching ratios $B(K^{\pm} \to m^{\pm}N_4)B(N_4 \to p^{\mp}m^{\pm})$ and $B(K^{\pm} \to p^{\pm}X)B(X \to m^{+}m^{-})$ for the various masses and lifetimes of the possible resonances.

**References**

[1]      Particle Data Group, K. Olive *et al.*, Chin. Phys. C **38** (2014) 090001.
[2]      T. Asaka and M. Shaposhnikov. Phys. Lett. B **620** (2005) 17.

[3]     M. Shaposhnikov and I. Tkachev. Phys. Lett. B **639** (2006) 414 .

[4]     J.R.Batley, *et al.*, Eur. Phys. J. C **52** (2007) 875.

[5]     J.R.Batley, *et al.*,  Phys. Lett. B **769** (2017) 67.

[6]     V. Fanti, *et al.*, Nucl.Instrum.Meth. A **574** (2007) 433.

[7]     W.A. Rolke and A. M. Lopez, Nucl. Instrum. Meth. A **458** (2001) 745.

[8]     J.R. Batley *et al.*, Phys. Lett. B **697** (2011) 107.

# Neutral pion form factor by the NA62 experiment

Marco Mirra[*]

Università degli studi di Napoli "Federico II" e Sezione INFN di Napoli, Italy
marco.mirra@na.infn.it

## Abstract

The NA62 experiment collected a large sample of charged kaon decays in 2007 with a highly efficient trigger for decays into electrons. A measurement of the $\pi^0$ electromagnetic transition form factor slope parameter from $1.11 \times 10^6$ fully reconstructed $K^\pm \to \pi^\pm \pi_D^0$, $\pi_D \to e^+ e^- \gamma$ events is reported. The measured value $a = (3.70 \pm 0.53_{stat} \pm 0.36_{syst}) \times 10^{-2}$ is in good agreement with theoretical expectations and previous measurements, and represents the most precise experimental determination of the slope in the time-like momentum transfer region. The limits on dark photon production in $\pi^0$ decays from the earlier kaon experiment NA48/2 at CERN are also reported.

---

[*]for the NA62 collaboration: F. Ambrosino, A. Antonelli, G. Anzivino, R. Arcidiacono, W. Baldini, S. Balev, J. R. Batley, M. Behler, S. Bifani, C. Biino, A. Bizzeti, T. Blazek, B. Bloch-Devaux, G. Bocquet, V. Bolotov, F. Bucci, N. Cabibbo, M. Calvetti, N. Cartiglia, A. Ceccucci, P. Cenci, C. Cerri, C. Cheshkov, J. B. Chze, M. Clemencic, G. Collazuol, F. Costantini, A. Cotta Ramusino, D. Coward, D. Cundy, A. Dabrowski, G. DAgostini, P. Dalpiaz, C. Damiani, H. Danielsson, M. De Beer, G. Dellacasa, J. Derr, H. Dibon, D. Di Filippo, L. DiLella, N. Doble, V. Duk, J. Engelfried, K. Eppard, V. Falaleev, R. Fantechi, M. Fidecaro, L. Fiorini, M. Fiorini, T. Fonseca Martin, P. L. Frabetti, A. Fucci, S. Gallorini, L. Gatignon, E. Gersabeck, A. Gianoli, S. Giudici, A. Gonidec, E. Goudzovski, S. Goy Lopez, E. Gushchin, B. Hallgren, M. Hita-Hochgesand, M. Holder, P. Hristov, E. Iacopini, E. Imbergamo, M. Jeitler, G. Kalmus, V. Kekelidze, K. Kleinknecht, M. Koval, V. Kozhuharov, W. Kubischta, V. Kurshetsov, G. Lamanna, C. Lazzeroni, M. Lenti, E. Leonardi, L. Litov, D. Madigozhin, A. Maier, I. Mannelli, F. Marchetto, G. Marel, M. Markytan, P. Marouelli, M. Martini, L. Masetti, P. Massarotti, E. Mazzucato, A. Michetti, I. Mikulec, M. Misheva, N. Molokanova, E. Monnier, U. Moosbrugger, C. Morales Morales, M. Moulson, S. Movchan, D.J. Munday, M. Napolitano, A. Nappi, G. Neuhofer, A. Norton, T. Numao, V. Obraztsov, V. Palladino, M. Patel, M. Pepe, A. Peters, F. Petrucci, M. C. Petrucci, B. Peyaud, R. Piandani, M. Piccini, G. Pierazzini, I. Polenkevich, I. Popov, Y. Potrebenikov, M. Raggi, B. Renk, F. Retire, P. Riedler, A. Romano, P. Rubin, G. Ruggiero, A. Salamon, G. Saracino, M. Savri, M. Scarpa, V. Semenov, A. Sergi, M. Serra, M. Shieh, S. Shkarovskiy, M. W. Slater, M. Sozzi, T. Spadaro, S. Stoynev, E. Swallow, M. Szleper, M. Valdata-Nappi, P. Valente, B. Vallage, M. Velasco, M. Veltri, S. Venditti, M. Wache, H. Wahl, A. Walker, R. Wanke, L. Widhalm, A. Winhart, R. Winston, M. D. Wood, S. A. Wotton, O. Yushchenko, A. Zinchenko and M. Ziolkowski

# I. THE $\pi^0$ ELECTROMAGNETIC TRANSITION FORM FACTOR SLOPE PARAMETER

The $\pi^0$ decays almost instantaneously via the electromagnetic interaction with two photons. The second most important decay channel, the so-called Dalitz decay $(\pi_D^0)$, is $\pi_D^0 \to e^+e^-\gamma$ and proceeds via the same $\pi^0$ vertex with probability $(1.174 \pm 0.035)\%$ [1]. In the $\pi_D^0$ process one of the two photons from the $\pi^0$ vertex becomes off-shell and decays to an $e^+e^-$ pair. Independent kinematic variables $x$ and $y$ can be defined in terms of particle four-momenta $p_{e^\pm}$ and $p_{\pi^0}$ :

$$x = \left(\frac{M_{ee}}{m_{\pi^0}}\right)^2 = \frac{(p_{e^+} + p_{e^-})^2}{m_{\pi^0}^2} \qquad y = \frac{2p_{\pi^0}(p_{e^+} + p_{e^-})}{m_{\pi^0}(1-x)} \tag{1}$$

where $M_{ee}$ is the invariant mass of the $e^+e^-$ pair. The $x$ variable is the normalised square of the electron-positron pair invariant mass, while $y$ is related to the angles between the final state particle momenta. The limits on the variables are given by

$$r^2 \leq x \leq 1 \quad -\beta \leq y \leq \beta \quad \text{where} \quad r = \frac{2m_e}{m_{\pi^0}} \quad \text{and} \quad \beta = \sqrt{1 - \frac{r^2}{x}} \tag{2}$$

where $m_e$ and $m_{\pi^0}$ are the the corresponding PDG [1] masses of $e^\pm$ and $\pi^0$. The differential decay width is [2]

$$\frac{d^2\Gamma(\pi_D^0)}{dxdy} = \frac{\alpha}{4\pi}\Gamma(\pi_{2\gamma}^0)\frac{(1-x)^3}{x}\left(1+y^2+\frac{r^2}{x}\right)(1+\delta(x,y))|F(x)|^2 \tag{3}$$

where $\Gamma(\pi_{2\gamma}^0)$ is the $\pi^0 \to \gamma\gamma$ decay width, the function $\delta(x,y)$ describes the radiative corrections and $F(x)$ is the electromagnetic transition form factor (TFF) of the $\pi^0$ to a real and virtual photon. The TFF describes the deviation of this transition from a point-like interaction. It is also an input to the computation of the $\pi^0 \to e^+e^-$ decay rate [3], as well as the hadronic light-by-light scattering contribution to the muon anomalous magnetic moment $(g-2)$ which at present contributes the second largest uncertainty on its Standard Model value [4].

The function $F(x)$ is expected to vary slowly in the kinematic region of the $\pi_D^0$ decay and it is usually approximated by a linear expansion $F(x) = 1 + ax$ , where $a$ is the slope parameter. The TFF slope has been determined in the time-like momentum transfer region by measuring the $\pi_D^0$ decay rate [5] [6] [7] [8] [9], all including radiative corrections. The TFF has been also measured in the space-like momentum transfer region in the reaction $e^+e^- \to e^+e^-\pi^0$ , where the $\pi^0$ is produced by the fusion of two photons radiated by the incoming beams and decays to two detected photons [10]. The current world average $a = 0.032 \pm 0.004$ [1] is obtained from time-like measurements and the extrapolation of space-like data using a vector meson dominance (VMD) model. So a comparison of TFF slope prediction with model independent measurement represents a remarkable test of the theory models.

## i.  The $\pi^0$ TFF slope in NA62

The NA62 experiment at the CERN SPS collected in 2007 a large sample of charged kaons decaying in flight in vacuum with a minimum-bias trigger configuration [17]. The $K^\pm$ decays represent a source of tagged neutral pions by means of the $K^\pm \to \pi^+\pi^0$ $(K_{2\pi})$ decay channel. The mean free path of the neutral pion in the NA62 experimental conditions is negligible (few $\mu$m). An analysis of $1.11 \times 10^6 K_{2\pi}$ decays followed by the prompt $\pi_D^0$ decay (denoted $K_{2\pi D}$) using the full NA62 2007 data set has been performed: a model-independent measurement of the $\pi^0$ TFF slope parameter is reported in this work.

## II.  NA62 EXPERIMENTAL APPARATUS

The NA62 experimental setup used in 2007 was composed of the NA48 detector [11] and a modified beam line [12] of the earlier NA48/2 experiment. The beam line was designed to provide simultaneously $K^+$ and $K^-$ beams. The primary 400 GeV/c proton beam delivered by the SPS impinged on a beryllium target of 40 cm length and 0.2 cm diameter. The secondary beam momenta were selected by magnets in a four dipole achromat and a momentum-defining slit incorporated into a beam dump. This 3.2m thick copper/iron block provided the possibility to block either of the $K^+$ or $K^-$ beams. The selected particles had a central momentum of 74 GeV/c with a spread of $\pm 1.4$ GeV/c (rms). The beams were focused and collimated before entering a 114m long cylindrical vacuum tank containing the fiducial decay volume. The beams were mostly composed of $\pi^\pm$, with a $\sim 6\%$ $K^\pm$ fraction. Since the muon halo sweeping system was optimised for the positive beam in 2007, most of the data were recorded with the single $K^+$ beam to reduce the halo background. In figure 1 a schematic of the setup is shown. The momenta of charged
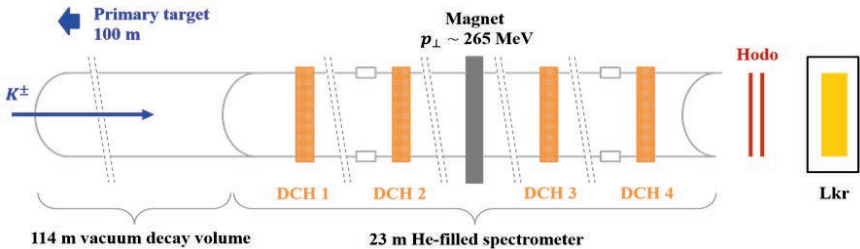


**Figure 1:** *Layout of the NA62 experimental setup.*

particles were measured by a spectrometer composed of four drift chambers (DCH) and a dipole magnet placed between the second and third chamber providing a transverse momentum kick of 265MeV/c. The measured momentum resolution was $\sigma_p/p = 0.48\% \oplus 0.009\%\dot{p}$, where the momentum $p$ is expressed in GeV/c. The spectrometer was housed in a tank filled with helium at nearly atmospheric pressure.

The photons were detected and measured by a liquid krypton (LKr) electromagnetic calorimeter, which is a quasi-homogeneous ionisation chamber with a thickness of 127 cm, corresponding to $27X_0$. The LKr volume is divided into 13248 cells of about $2 \times 2$ cm$^2$ cross section without longitudinal segmentation. The measured energy resolution was $\sigma_E/E = 3.2\%/\sqrt{(E)} \oplus 9\%/E \oplus 0.42\%$, and the spatial resolution for the transverse coordinates x and y was 0.42 cm/$\sqrt{E} \oplus 0.06$ cm, where the energy is given in GeV in both cases. A scintillator hodoscope (Hodo) was located between the spectrometer and the LKr calorimeter. It consists of a set of scintillators arranged into a plane of 64 vertical counters followed by a plane of 64 horizontal counters. Each plane was divided into four quadrants of 16 counters providing a fast trigger signal for charged particles. The time resolution of the Hodo was $\sim 150$ ps.

The analysis is based on the full data set collected during 4 months in 2007, corresponding to about $2 \times 10^{10}$ $K^{\pm}$ decays in the vacuum tank. A total of 65% (8%) of the $K^+$ ($K^-$) flux was collected in single-beam mode while the remaining 27% were collected with simultaneous $K^{\pm}$ beams with a $K^+/K^-$ flux ratio of 2.0. The 100 kHz kaon decay rate in the vacuum volume during the spill enabled the use of a minimum-bias trigger configuration with a highly efficient trigger chain optimised to select events with at least one electron track. The low level hardware trigger required a coincidence of hits in at least one hodoscope quadrant in both planes, upper and lower cuts on the hit multiplicity in the drift chambers, and a minimum total energy deposit of 10 GeV in the LKr calorimeter. The high level software trigger (HLT) condition required at least one track with 5 GeV/c < $p$ < 90 GeV/c and $E/p$ > 0.6, where $E$ is the energy reconstructed in the calorimeter and $p$ is the momentum reconstructed in the spectrometer. Downscaled minimum bias trigger streams were collected to evaluate the trigger efficiencies.

## III. MONTECARLO SIMULATION

Monte Carlo (MC) simulations of the $K_{2\pi D}$ decay chain and two other $K^{\pm}$ decay chains producing $\pi^0$ Dalitz decays, $K^{\pm} \to \pi^0_D e^{\pm}\nu$ and $K^{\pm} \to \pi^0_D \mu^{\pm}\nu$ (denoted $K_{e3D}$ and $K_{\mu3D}$, respectively), were performed with a $\pi^0$ TFF slope $a_{MC} = 3.2 \times 10^2$. Separate simulated samples, proportionally to the number of kaon decays recorded, were produced for each data taking condition. The total simulated sample amounts to 386 M $K_{2\pi D}$, 105 M $K_{\mu3D}$ and 103 M $K_{e3D}$ events within the fiducial decay region. All these modes contribute to the $\pi^0_D$ sample, although the selection is optimized for $K_{2\pi D}$. The radiative corrections to the total and differential $\pi^0_D$ decay widths have been studied extensively since their effect is comparable to the effect of the TFF. The first study of radiative corrections was done in [13] and extended in [14], where diagrams in figures 2 and 3 were considered. Recent improvements in [15] include additional one-loop one-photon irreducible contributions (see figure 4) and they have been applied in this simulation. Higher order correction terms not included in the simulation contribute to the slope by
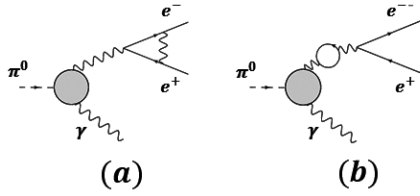
**Figure 2:** *Virtual radiative corrections to $\pi_D^0$: (a) correction to the QED vertex and (b) vacuum polarization insertion*
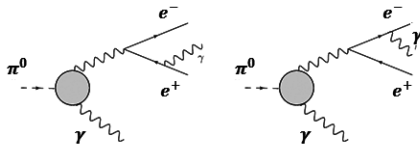


**Figure 3:** *Bremsstrahlung corrections to $\pi_D^0$*
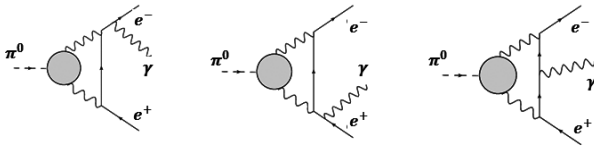


**Figure 4:** *One-loop one-photon irreducible contribution to $\pi_D^0$*

$|a| < 0.01 \times 10^2$, which is considered as a systematic uncertainty.

## IV. TFF MEASUREMENT

### i. Event selection

The main $K_{2\pi D}$ selection criteria are the following.

- The event should contain exactly one reconstructed 3-track vertex, which should be located within the fiducial decay region and be geometrically compatible with a beam kaon decay. The vertex charge qvtx, defined as the sum of the track charges, should match the beam charge in the single-beam mode. The track with the charge opposite to qvtx is necessarily an $e^\pm$ candidate, while the same-sign tracks can be either $\pi^\pm$ or $e^\pm$ candidates. The tracks are required to be in time and within the geometrical acceptance of the drift chambers. Events with a photon converting into an $e^+e^-$ pair in the material before DCH1 are suppressed by requiring a minimum distance of 2 cm between the impact points of every track pair in the first drift chamber, as verified by simulation.

- Reconstructed clusters of energy deposition in the LKr calorimeter are used to identify photon candidates. A photon candidate cluster should be geometrically isolated from the track impact points in the LKr calorimeter (distance larger than 20 cm from the same-sign tracks and larger than 10 cm from the remaining track), within 10 ns of each track and with more than 2 GeV of energy. The photon 4-momentum is reconstructed assuming that the photon originates from the same vertex as the tracks. If more than one photon candidate is found, the event is rejected.

- The total reconstructed momentum should be compatible with the beam momentum and there should be no missing transverse momentum with respect to the beam axis within the resolution: $p_t^2 < 10^5 (\text{GeV/c})^2$. The $\pi/e$ ambiguity for the two same-sign tracks is resolved by testing the two possible mass assignments. For each hypothesis, the reconstructed kinematic variables should be $|x|, |y| < 1$, and the reconstructed $e^+e^-\gamma$ and $\pi^\pm\pi^0$ masses should be close to the nominal ones: $M_{ee\gamma}$ in the range $(115 - 145)\text{MeV/c}^2$ and $M_{\pi^\pm\pi^0}$ in the range $(460 - 520)\text{MeV/c}^2$. Both invariant mass spectra are shown in figure 5; Only events with a single valid hypothesis are selected. The probability of correct (incorrect) mass assignment evaluated with the $K_{2\pi D}$ MC sample is 99.62% (0.02%); the remaining 0.36% of events have either zero or two valid hypotheses are rejected.

The selection was restricted to area with Dalitz variable $x > 0.01$ because a 1% deficit in the data/MC ratio was observed for events with $x < 0.01$ due to the steeply falling acceptance.
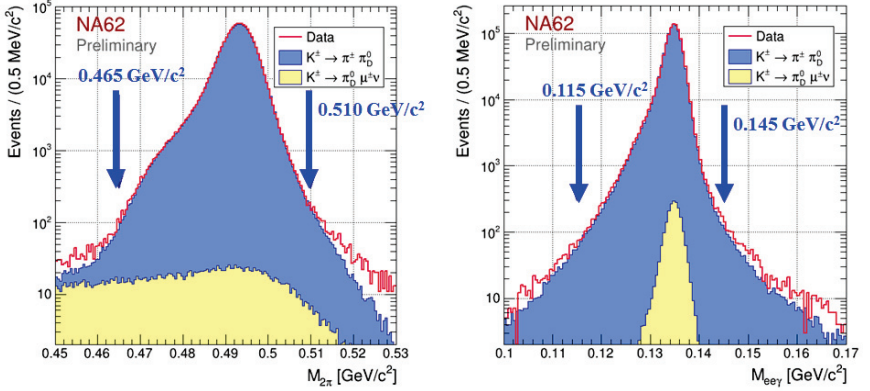
**Figure 5:** *Reconstructed $\pi^{\pm}\pi^0$ (left) and $e^+e^-\gamma$ (right) mass distributions for data and simulated components. The radiative shoulders in the reconstructed masses are well reproduced in the MC thanks to the simulation of the radiative photon.*

## ii. Fit procedure and result

The reconstructed spectrum of the $x$ variable is shown in figure 6 (left). The TFF was obtained by adjusting the simulation to the data $x$ spectrum. In particular a $\chi^2$ fit with free MC normalisation in equally populated bins comparing the data and MC reconstructed $x$ distributions is performed to extract the TFF slope. The fit result is illustrated in figure 6 (right) where the effect of a positive TFF slope is clearly seen from the ratio of the data and MC distribution with $a = 0$. The horizontal positions of black markers correspond to the barycenters of the data divided into 20 equipopulous bins. MC events are re-weighted to obtain the distribution corresponding to the flat form factor (zero TFF slope value). Red solid line represents the TFF function with the slope value equal to the fit central value. Red dashed lines correspond to the $1\,\sigma$ band.

The NA62 preliminary result on $\pi^0$ TFF slope parameter is:

$$a = (3.70 \pm 0.53_{stat} \pm 0.36_{syst}) \times 10^{-2} \tag{4}$$

A comparison with previous $\pi^0$ TFF measurements is shown in figure 7 . The measurement performed by NA62 is in good agreement with theoretical expectations and previous measurements, and represents the most precise experimental determination of the slope in the time-like momentum transfer region.

## V. A RELATED RESEARCH: DARK PHOTON

In a rather general set of hidden sector models with an extra U(1) gauge symmetry [16], the interaction of the dark photon (DP, denoted A') with the visible sector proceeds through kinetic mixing with the Standard Model (SM) hypercharge. Such
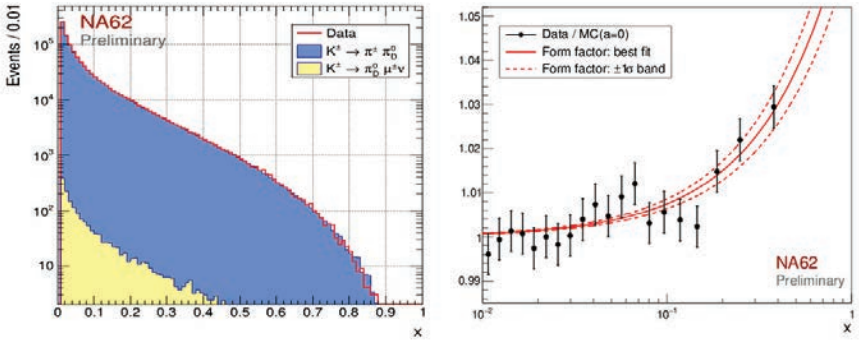
**Figure 6:** *Left: Spectra of the reconstructed $x$ variable for data and MC components. Right: Ratio of the reconstructed $x$ distributions for data and MC, where the MC sample corresponds to $a = 0$. The effect of a positive TFF slope ($a > 0$) is clearly seen in this illustration. Data and MC events are distributed into 20 equally populated bins; the horizontal positions of the markers correspond to the bin barycentres. The solid line represents $|F(x)|^2$ with the measured central slope value: $a = 3.70 \times 10^2$. The dashed lines indicate the $\pm 1\sigma$ band. Only the statistical uncertainties are shown.*
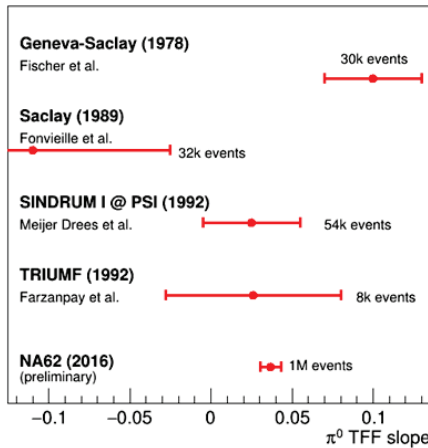


**Figure 7:** *Results on the TFF slope from $\pi_D^0$ measurements.*

119

scenarios with GeV-scale dark matter provide possible explanations to the observed rise in the cosmic-ray positron fraction with energy and the muon gyromagnetic ratio $(g-2)$ measurement [17]. The DP is characterized by two a priori unknown parameters, the mass $m_{A'}$ and the mixing parameter $\epsilon^2$. Its possible production in the $\pi^0$ decay and its subsequent decay proceed via the chain $\pi^0 \to \gamma A'$, $A' \to e^+ e^-$. The expected branching fraction of the above $\pi^0$ decay [18]:

$$BR(\pi^0 \to \gamma A') = 2\epsilon^2 \left(1 - \frac{m_{A'}^2}{m_{\pi^0}^2}\right)^3 BR\left(\pi^0 \to \gamma\gamma\right) \qquad (5)$$

In the DP mass range $2m_e < m_{A'} < m_\pi^0$ accessible in pion decays, the only allowed tree-level decay into SM fermions is $A' \to e^+ e^-$. Therefore, for a DP decaying only into SM particles, $BR(A' \to e^+ e) \approx 1$, and the expected total decay width is [18]:

$$\Gamma_{A'} \approx \Gamma\left(A' \to e^+ e\right) = \frac{1}{3}\alpha\epsilon^2 m_{A'} \overline{\sqrt{1 - \frac{4m_e^2}{m_{A'}^2}}} \left(1 + \frac{2m_e^2}{m_{A'}^2}\right) \qquad (6)$$

It follows that, for $2m_e << m_{A'} < m_\pi^0$, the DP mean proper lifetime $\tau_A'$ satisfies the relation

$$c\tau_{A'} = \hbar c/\Gamma_{A'} \approx 0.8\mu m \left(\frac{10^{-6}}{\epsilon^2}\right) \times \left(\frac{100\text{MeV}/\text{c}^2}{m_{A'}}\right) \qquad (7)$$

The DP is assumed to decay at the production point, which is valid for sufficiently large values of $m_{A'}$ and $\epsilon^2$. In this case, the DP production and the signal decay chain has the same particles in the final state as the $\pi_D^0$ decay, which therefore represents an irreducible but well controlled background and determines the sensitivity. The result of the analysis of the full data set of NA48/2 counting in total $1.69 \times 10^7 \pi_D^0$ reconstructed events is reported. The $\pi_D^0$ events are selected from kaon decays $K_{2\pi D}$ and $K_{\mu 3D}$. The two event selections are identical up to the momentum, invariant mass and particle identification c onditions. A scan for a DP signal in the mass range $9\text{MeV}/\text{c}^2 \le m_{A'} \le 120\text{MeV}/\text{c}^2$ is performed. The lower boundary of the mass range is determined by the limited accuracy of the $\pi_D^0$ background simulation at low $e^+ e^-$ mass. At high DP mass approaching the upper limit of the mass range, the sensitivity to the mixing parameter $\epsilon^2$ is not competitive with the existing limits due to the kinematic suppression of the $\pi^0 \to \gamma A'$ decay. The obtained upper limits on the numbers of DP candidates in each mass hypothesis considered are presented in figure 8 ( left). The obtained upper limits at 90% CL on the mixing parameter $\epsilon^2$ for each DP mass value are shown in figure 8 (right), together with the constraints from other experiments.

The obtained limits are more stringent than the previous ones in the mass range 9-70 MeV/c$^2$. In combination with other experimental searches, this result rules out the DP as an explanation for the muon $(g-2)$ measurement under the assumption that the DP couples to quarks and decays predominantly to SM fermions.
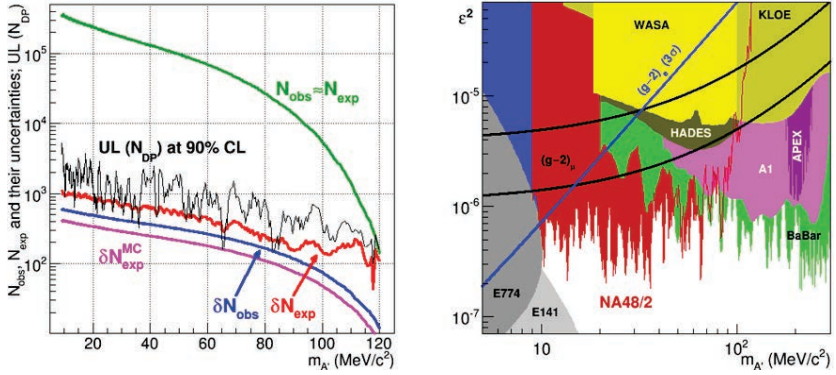
**Figure 8:** *Left: Numbers of observed data events and expected $\pi_D^0$ background events passing the selection, estimated uncertainties and obtained upper limits at 90% CL on the numbers of DP candidates for each mass value $m_{A'}$. Right: The NA48/2 preliminary upper limits at 90% CL on the mixing parameter $\epsilon^2$ versus the $A'$ mass, compared to the other published exclusion limits. Also shown are the band for the muon $(g-2)$ and the region excluded by the electron $(g-2)$ measurement.*

## VI.   CONCLUSION

Kaon decay in flight experiments are also exposed to large numbers of tagged neutral pion decays. The most precise measurement of the $\pi^0$ transition form factor slope has been performed by analyzing the NA62 data set. The final result including slightly smaller uncertainties has been published recently [19].

Improved limits in the 9-70 $\mathrm{MeV}/c^2$ mass range of the dark photon search in $\pi^0$ decays has been achieved by exploring NA48/2 data. The whole region favored by $(g-2)$ is excluded now, assuming that DP decays into SM fermions only.

## REFERENCES

[1]  C. Patrignani et al., Chin. Phys. C 40, 100001 (2016).

[2]  D. W. Joseph, Il Nuovo Cimento 16, 997 (1960).

[3]  T. Husek, K. Kampf, and J. Novotny, Eur. Phys. J. C 74, 3010 (2014).

[4]  A. Nyffeler, Phys. Rev. D 94, 053006 (2016).

[5]  J. Fischer et al., Phys. Lett. B 73, 359 (1978).

[6]  H. Fonvieille et al., Phys. Lett. B 233, 65 (1989).

[7]  F. Farzanpay et al., Phys. Lett. B 278, 413 (1992).

[8]  R. Meijer Drees et al., Phys. Rev. D 45, 1439 (1992).

[9]  P. Adlarson et al., arXiv:1611.04739 [hep-ex] (2016).

[10]  H. J. Behrend et al., Z. Phys. C 49, 401 (1991).

[11]  V. Fanti et al., Nucl. Instrum. Meth. A 574, 433 (2007).

[12]  J. R. Batley et al., Eur. Phys. J. C 52, 875 (2007).

[13]  B E Lautrup and J Smith, Phys. Rev. D 3, 1122 (1971).

[14]  Mikaelian and Smith, Phys. Rev. D 5, (1972) 1763.

[15]  T Husek et al, Phys. Rev. D 92, 054027 (2015).

[16]  B. Holdom, Phys. Lett. B166 (1986) 196.

[17]  M. Pospelov, Phys. Rev. D80 (2009) 095002.

[18]  B. Batell, M. Pospelov and A. Ritz, Phys. Rev. D80 (2009) 095024.

[19]  CERN-EP-2016-323 and arXiv:1612.08162, accepted for publication by Phys. Lett. B.

# Search for $K^+ \to \pi^+ \nu\overline{\nu}$ at NA62

Jacopo Pinzino[*]

INFN Sezione di Pisa, Italy

E-mail: jacopo.pinzino@cern.ch

March 14, 2017

## Abstract

$K^+ \to \pi^+ \nu\overline{\nu}$ is one of the theoretically cleanest meson decay where to look for indirect effects of new physics complementary to LHC searches.

[*]for the NA62 Collaboration: G. Aglieri Rinella, R. Aliberti, F. Ambrosino, R. Ammendola, B. Angelucci, A. Antonelli, G. Anzivino, R. Arcidiacono, I. Azhinenko, S. Balev, M. Barbanera, J. Bendotti, A. Biagioni, L. Bician, C. Biino, A. Bizzeti, T. Blazek, A. Blik, B. Bloch-Devaux, V. Bolotov, V. Bonaiuto, M. Boretto, M. Bragadireanu, D. Britton, G. Britvich, M.B. Brunetti, D. Bryman, F. Bucci, F. Butin, J. Calvo, E. Capitolo, C. Capoccia, T. Capussela, A. Cassese, A. Catinaccio, A. Cecchetti, A. Ceccucci, P. Cenci, V. Cerny, C. Cerri, B. Checcucci, O. Chikilev, S. Chiozzi, R. Ciaranfi, G. Collazuol, A. Conovaloff, P. Cooke, P. Cooper, G. Corradi, E. Cortina Gil, F. Costantini, F. Cotorobai, A. Cotta Ramusino, D. Coward, G. D'Agostini, J. Dainton, P. Dalpiaz, H. Danielsson, J. Degrange, N. De Simone, D. Di Filippo, L. Di Lella, S. Di Lorenzo, N. Dixon, N. Doble, B. Dobrich, V. Duk, V. Elsha, J. Engelfried, T. Enik, N. Estrada, V. Falaleev, R. Fantechi, V. Fascianelli, L. Federici, S. Fedotov, A. Filippi, M. Fiorini, J. Fry, J. Fu, A. Fucci, L. Fulton, S. Gallorini, S. Galeotti, E. Gamberini, L. Gatignon, G. Georgiev, S. Ghinescu, A. Gianoli, M. Giorgi, S. Giudici, L. Glonti, A. Goncalves Martins, F. Gonnella, E. Goudzovski, R. Guida, E. Gushchin, F. Hahn, B. Hallgren, H. Heath, F. Herman, T. Husek, O. Hutanu, D. Hutchcroft, L. Iacobuzio, E. Iacopini, E. Imbergamo, O. Jamet, P. Jarron, E. Jones, T. Jones K. Kampf, J. Kaplon, V. Kekelidze, S. Kholodenko, G. Khoriauli, A. Khotyantsev, A. Khudyakov, Yu. Kiryushin, A. Kleimenova, K. Kleinknecht, A. Kluge, M. Koval, V. Kozhuharov, M. Krivda, Z. Kucerova, Yu. Kudenko, J. Kunze, G. Lamanna, G. Latino, C. Lazzeroni, G. Lehmann-Miotto, R. Lenci, M. Lenti, E. Leonardi, P. Lichard, R. Lietava, V. Likhacheva, L. Litov, R. Lollini, D. Lomidze, A. Lonardo, M. Lupi, N. Lurkin, K. McCormick, D. Madigozhin, G. Maire, C. Mandeiro, I. Mannelli, G. Mannocchi, A. Mapelli, F. Marchetto, R. Marchevski, S. Martellotti, P. Massarotti, K. Massri, P. Matak, E. Maurice, M. Medvedeva, A. Mefodev, E. Menichetti, E. Migliore, E. Minucci, M. Mirra, M. Misheva, N. Molokanova, J. Morant, M. Morel, M. Moulson, S. Movchan, D. Munday, M. Napolitano, I. Neri, F. Newson, J. Noël, A. Norton, M. Noy, G. Nuessle, T. Numao, V. Obraztsov, A. Ostankov, S. Padolski, R. Page, V. Palladino, G. Paoluzzi, C. Parkinson, E. Pedreschi, M. Pepe, F. Perez Gomez, M. Perrin-Terrin, L. Peruzzo, P. Petrov, F. Petrucci, R. Piandani, M. Piccini, D. Pietreanu, J. Pinzino, I. Polenkevich, L. Pontisso, Yu. Potrebenikov, D. Protopopescu, F. Raffaelli, M. Raggi, P. Riedler, A. Romano, P. Rubin, G. Ruggiero, V. Russo, V. Ryjov, A. Salamon, G. Salina, V. Samsonov, C. Santoni, G. Saracino, F. Sargeni, V. Semenov, A. Sergi, M. Serra, A. Shaikhiev, S. Shkarovskiy, I. Skillicorn, D. Soldi, A. Sotnikov, V. Sugonyaev, M. Sozzi, T. Spadaro, F. Spinella, R. Staley, A. Sturgess, P. Sutcliffe, N. Szilasi, D. Tagnani, S. Trilov, M. Valdata-Nappi, P. Valente, M. Vasile, T. Vassilieva, B. Velghe, M. Veltri, S. Venditti, P. Vicini, R. Volpe, M. Vormstein, H. Wahl, R. Wanke, P. Wertelaers, A. Winhart, R. Winston, B. Wrona, O. Yushchenko, M. Zamkovsky, A. Zinchenko.

The NA62 experiment at CERN SPS is designed to measure the branching ratio of this decay with 10% precision. NA62 took data in pilot runs in 2014 and 2015 reaching the final designed beam intensity. The quality of 2015 data acquired, in view of the final measurement, will be presented.

# 1 The NA62 experiment

## 1.1 Introduction

The NA62 experiment is located in the CERN North Area SPS extraction site and it aims at measuring the Branching Ratio of the ultra-rare FCNC kaon decay $K^+ \to \pi^+ \nu \overline{\nu}$ collecting about 100 events in two years of data taking [2]. This decay, with its neutral partner $K_L \to \pi^0 \nu \overline{\nu}$, is a very useful process to study flavour physics and to obtain a stringent test of the Standard Model; the Branching Ratio of these decays can be computed with high precision [4], $BR(K^+ \to \pi^+ \nu \overline{\nu})(SM) = 8.4 \pm 1.0 \times 10^{-11}$ where the uncertainty is dominated by the current precision of the CKM mixing matrix input parameters.

The strong suppression of the SM contributions and the remarkable theoretical precision of the SM rate make this decay a powerful probe for possible new physics, complementary to direct searches at the LHC and potentially sensitive to much higher energy scales. The combination of the Branching Ratio of these two decays ($K^+ \to \pi^+ \nu \overline{\nu}$ and $K^0 \to \pi^0 \nu \overline{\nu}$) allows to determine the $\beta$ angle of the Unitarity Triangle from K decays only and, in this way, to have a powerful test on Standard Model.

The most accurate measurement of this decay, $BR(K^+ \to \pi^+ \nu \overline{\nu}) = 17.3^{+11.5}_{-10.5} \times 10^{-11}$, was obtained by the E787 experiment and its upgrade E949 at BNL (from 1995 to 2002) which collected seven events [3]. NA62 aims to improving the measurement of this Branching Ratio reaching a precision of at least 10%: the experiment is currently in data taking and the performances achieved in 2015 will be discussed.

## 1.2 NA62 Experimental Setup

NA62 uses the SPS 400 GeV/$c$ proton beam from the SPS in order to produce $K^+$ decaying in-flight.

The total beam rate at the end of the beam line is of the order of 750 MHz but kaons are about 6% of the flux. Downstream detectors aren't affected by this large flux because the undecayed particles remain inside the beam pipe; the integrated rate over these detectors is of the order of 10 MHz.

The downstream detectors start about 100 m after the beryllium target and are distributed along 170 m longitudinally; the fiducial region for decays extends from 100 m to 165 m after the target. Detectors have an approximate azimuthal symmetry around the beam axis, with an inner hole to let the high

flux of undecayed particles pass through without hitting the downstream detectors.

The NA62 experimental setup [1], shown in figure 1, consists of these detectors:

- The *Cerenkov differential counter* (KTAG) is used to identify $K^+$ in the beam. It has a time resolution of about 100 ps to tag the kaon time.

- The Gigatracker (GTK) is composed by three silicon pixel stations placed in vacuum, with transverse dimensions which cover the beam area, and is used to measure particles direction and momentum before they enter the decay region. The GTK has to cope with the full beam intensity of about 750 MHz and provides a time resolution of the order 200 ps to avoid a wrong matching of a beam particle to the reconstructed decay downstream, and a resulting error in the calculation of the missing mass. Between the stations, 4 magnetic dipoles make an achromatic spectrometer for any momentum: the momentum resolution is 0.2%, and the angular resolution for the particle direction is about 15 $\mu$rad.

- The CHarged ANTIcounter (CHANTI) is a set of scintillator rings that follow the last GTK station used as a veto for charged particles before they enter the decay region.

- A system of photon veto detectors covering a polar angle from 0 to about 50 mrad polar angle with respect to the beam direction using 12 large annular vetos (LAV) made of lead glass crystals with attached photomultipliers (PMT) and covering an angle from 8.5 to 50 mrad, a liquid krypton electromagnetic calorimeter (LKr) for angles between 1 and 8.5 mrad, an intermediate calorimeter (IRC), made of alternating layers of lead and scintillators (shashlik), to cover the ring around the beam and a small angle calorimeter (SAC) placed at the end of the beam line after a sweeping magnet and using the same shashlik technology.

- A magnetic spectrometer (STRAW) made of four straw tube chambers inside the vacuum tank is used to measure the position of the decay vertex, the direction and momentum of the charged secondary particle. The reason to operate in vacuum is to minimize the multiple scattering. The dipole magnet from the earlier NA48 experiment is located after the second chamber and provides a 270 MeV/*c* kick in the horizontal plane, for track momentum determination. In the center of each chamber a region without straw let the beam particles pass undisturbed.

- The Ring Imaging Cerenkov (RICH) is designed to distinguish $\pi$ and $\mu$ in the momentum range between 15 and 35 GeV/*c* and to measure direction and velocity of such particles. This detector is 17 m long, filled with Neon at atmospheric pressure and equipped with 2000 photomultipliers
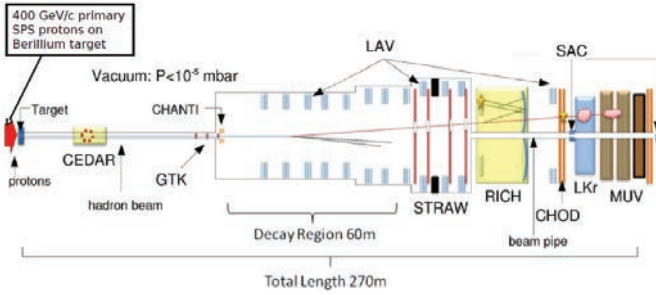
Figure 1: Longitudinal view of the NA62 experimental setup.

and has an inner beam pipe to avoid beam interactions with the gas. The timing resolution is of the order of 100 ps.

- The Charged Hodoscope (CHOD) is placed after the RICH to reduce the inefficiency in photon detection due to conversion or photo-nuclear interactions inside the material of the RICH; moreover it is used for trigger purposes.

- A system of muon vetoes composed of two iron-scintillator hadronic calorimeters (MUV1 and MUV2), and a plane of fast scintillators (MUV3) placed after an iron wall, gives additional power in muon vetoing and a fast trigger information.

## 2 Experimental strategy

The $K^+ \to \pi^+ \nu \bar{\nu}$ signature is one track in the final state matched in time with one $K^+$ track upstream the decay region and nothing else, because the two neutrinos are undetectable. Backgrounds can originate from all the kaon decays that result in a single detected charged track with no other particles, or from beam related activity. Kinematic reconstruction is a useful rejection technique: the squared missing mass distribution of the signal, $m_{miss}^2 \stackrel{def}{=} (P_K - P_{\pi^+})^2$ (where $P_K$ and $P_{\pi^+}$ are, respectively, the 4-momenta of the kaon and the charged particles produced from kaon decay under the $\pi^+$ mass hypothesis), has a three body decay shape, while more than 90% of the charged kaon decays are mostly peaking, as shown in figure 2.

The distribution of the $m_{miss}^2$ for the signal and the main decay modes led to define two signal regions, where the main backgrounds should be limited by the kinematic constrains, around the $K^+ \to \pi^+ \pi^0$ peak. Semileptonc decays, radiative processes, main kaon decay modes via reconstruction tails and beam induced tracks span across these regions. Therefore kinematic reconstruction,
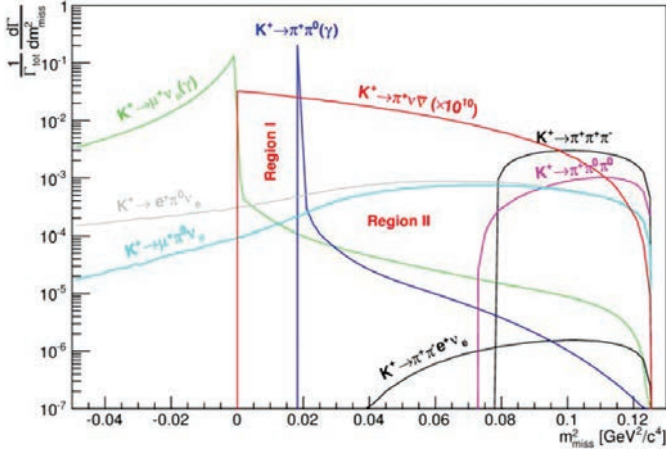
Figure 2: $m_{miss}^2$ distributions for signal and backgrounds from the main $K^+$ decay modes. The backgrounds are normalized according to their branching fraction; the espected signal is shown multiplied by a factor $10^{10}$.

photon rejection, particle identification and sub-nanoseconds timing coincidences between subdetectors must be employed to obtain the final background rejection. A tight requirement on $P_{\pi^+}$ between 15 and 35 GeV/c boosts the background suppression further, as will be shown in the next section. Monte Carlo studies performed in past years [5] have shown that NA62 can reach the goal, exploiting multiple and almost uncorrelated techniques to suppress the main background sources.

# 3 Preliminary result of the 2015 run and prospect for the $K^+ \rightarrow \pi^+ \nu \overline{\nu}$ measurement

The main goal of the 2015 run was to verify on data the expected detector performances, the timing,, the particle identification a nd t he k inematic and photon rejection. A single track selection was chosen as a preliminary step towards the $K^+ \rightarrow \pi^+ \nu \overline{\nu}$ measurement. We selected tracks reconstructed in the STRAW spectrometer matching with CHOD signals and with energy depositions in calorimeters. The CHOD signals define the track time with 200 ps resolution. A single track event is defined by a track not forming a common vertex with any other in-time track within the decay region. The position of the vertex is defined using using a Closest Distance of Approach (CDA) less than 1.5 cm between two tracks. The downstream track has to match a Gigatracker track in time and space, forming a vertex in the decay region with it, in order
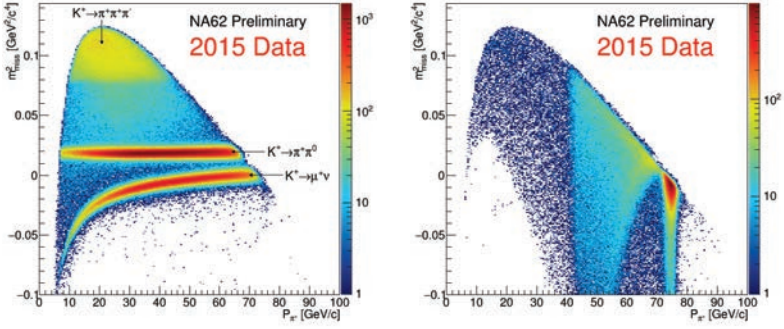
Figure 3: $m_{miss}^2$ distribution under $\pi^+$ mass hypothesis as a function of the momentum of the track measured in the straw spectrometer after selection for single track from kaon decays (left). Same distribution as left-side picture, but asking for single track without a positive kaon tag in time in KTAG (right).

to select events originating from kaon decays. The Gigatracker track has to be in-time with a kaon-like signal in KTAG. On the right, the KTAG is used to select events related to kaons. Time resolutions of the KTAG and GTK are found to match the design values (100 and 200 ps respectively). The $m_{miss}^2$ distributions for the 2015 data, recorded at low intensity, are shown in figure 3: the figure on the left is done with a kaon-like signal in the KTAG, while, in the second, the KTAG is used in anti-coincidence with a Gigatracker track to select single track events not related to kaons and shows that decay from beam $\pi^+$, elastic scattering of beam particles in the material along the beam line (KTAG and Gigatracker stations) and inelastic scattering in the last Gigatracker station are the main sources of tracks downstream originating from beam related activity.

The resolution of the $m_{miss}^2$ is measured using the width of the $K^+ \rightarrow \pi^+\pi^0$ peak and it is found to be $1.2 \times 10^{-3} GeV^2/c^4$ close to design value. The resolution as a function of momentum is shown in figure 4. The resolution is a factor 3 larger if the nominal kaon momentum is taken, instead of the event by event Gigatracker measured value.

The tracking system of NA62 is also designed to provide a rejection factor in the range of $10^4 \div 10^5$ for $K^+ \rightarrow \pi^+\pi^0$ and $K^+ \rightarrow \mu^+\nu$ using $m_{miss}^2$ to separate signal from backgrounds, respectively. The $K^+ \rightarrow \pi^+\pi^0$ kinematic suppression is measured using a sub-sample of single track events from kaon decays selected by requiring the additional presence of two $\gamma$s' compatible with a $\pi^0$ in the LKr calorimeter. This constraint defines a sample of $K^+ \rightarrow \pi^+\pi^0$ with negligible background even in the signal $m_{miss}^2$ regions, allowing the study of the far tails of the $m_{miss}^2$. The measured $K^+ \rightarrow \pi^+\pi^0$ kinematic suppression factor is of the order of $10^3$. The partial hardware Gigatracker
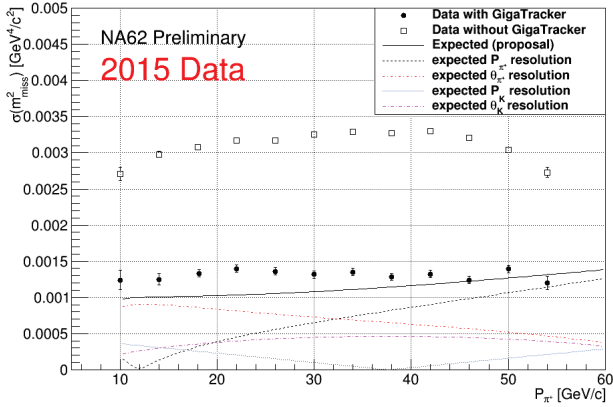
Figure 4: Resolution of the $m^2_{miss}$ miss vs momentum. Empty squares correspond to the values obtained with the nominal kaon momentum, black points - with the kaon momentum measured by GTK.

arrangement used in 2015 mainly limits the suppression because of $m^2_{miss}$ tails due to beam track mis-reconstruction.

The particle identification of NA62 is designed to separate $\pi^+$ from $\mu^+$ and $e^+$ in order to guarantee at least 7 order of magnitude suppression of $K^+ \to \mu^+\nu$ in addition to the kinematic rejection. The identification of secondary charged particles is done employing together RICH and calorimeters. The $K^+ \to \pi^+\pi^0$ sample used for kinematic studies and a pure muon sample of $K^+ \to \mu^+\nu$ were used to study the $\pi^+ - \mu^+$ separation in the RICH. The required muon contamination of 1% was achieved with a $\pi^+$ ID efficiency of 80% measured in a momentum region between 15 and 35 GeV/c. The RICH provides also an even better separation between $\pi^+$ and $e^+$. The same $\pi^+$ and $\mu^+$ samples allow the calorimetric muon-pion separation to be investigated. Simple cut and count analysis provide a muon suppression factor within $10^4 \div 10^6$ for a $\pi^+$ efficiency in a 90% ÷ 50% range. Several analysis techniques are under study to get the optimal separation.

The photon veto system is designed to suppress decays with photons in the final state. For photons from $\pi^0$ decays the rejection power provided by LAV, LKr, IRC and SAC detectors should be at least 8 orders of magnitude. The measured $\pi^0$ veto inefficiency on the 2015 data is statistically limited at $10^6$ (90% CL) as an upper limit. The corresponding signal efficiency is above 90%, being the losses mainly due to $\pi^+$ interactions in the RICH material producing extra clusters in LKr. To conclude, the preliminary analysis of the low intensity 2015 data shows that NA62 is approaching the design sensitivity for measuring $K^+ \to \pi^+\nu\bar{\nu}$.

# 4 NA62 physics besides $K^+ \to \pi^+ \nu \bar{\nu}$

The performances of the apparatus allow physics opportunities beyond the $K^+ \to \pi^+ \nu \bar{\nu}$ to be addressed. NA62 can significantly improve the existing limits on lepton flavour and number violating decays like $K^+ \to \pi^+ \mu^{\pm} e^{\mp}$ or $K^+ \to \pi^- l^+ l^+$. Experimentally $\pi^0$ physics can take advantage of the performances of the electromagnetic calorimeters and processes like $\pi^0 \to invisible$ or dark photon production can be investigated. Thanks to the quality of the kinematic reconstruction, searches for heavy neutrino produced in $K^+ \to l^+ \nu$ decays can improve the present sensitivity. The longitudinal scale of the apparatus open the possibility to search for long living particles through their decays, like dark photon, heavy neutral leptons or axion-like particles produced at the target or in beam dump configurations. NA62 is already addressing part of the above physics program simultaneously with the $K^+ \to \pi^+ \nu \bar{\nu}$ program. The full exploitation of this physics will constitute the core of the NA62 program beyond 2018.

# References

[1] A. Ambrosino et al. "NA62 Technical Design Document". In: (2010). URL: https://na62.web.cern.ch/NA62/Documents/TD_Full_doc_v10.pdf.

[2] G. Anelli et al. "Proposal to measure the rare decay K+ —> pi+ nu anti-nu at the CERN SPS". In: (2005).

[3] A. V. Artamonov et al. "New measurement of the $K^+ \to \pi^+ \nu \bar{\nu}$ branching ratio". In: *Phys. Rev. Lett.* 101 (2008), p. 191802. DOI: 10.1103/PhysRevLett.101.191802. arXiv: 0808.2459 [hep-ex].

[4] Andrzej J. Buras et al. "$K^+ \to \pi^+ \nu \bar{\nu}$ and $K_L \to \pi^0 \nu \bar{\nu}$ in the Standard Model: status and perspectives". In: *JHEP* 11 (2015), p. 033. DOI: 10.1007/JHEP11(2015)033. arXiv: 1503.02693 [hep-ph].

[5] Ferdinand Hahn. "Status and Prospects for $K^+ \to \pi^+ \nu \bar{\nu}$ Observation at CERN". In: *PoS* KAON13 (2013), p. 032.

# Review of Higgs Results from the ATLAS Experiment at the LHC

I.I. Tsukerman for the ATLAS Collaboration,
National Research Center "Kurchatov Institute", Institute of Theoretical and
Experimental Physics (ITEP), Moscow, 117218, Russia
e-mail: Ilya.Tsukerman@cern.ch

**Abstract.** The LHC has now delivered a large amount of data at 13 TeV center of mass energy. The experimental sensitivity is equivalent to that of Run-1 for the Higgs boson (125 GeV), and surpasses it for searches of higher masses Higgs-like particles. This paper will review recent ATLAS results on both of these topics.

## Introduction

A new boson with a mass of 125 GeV was discovered by the ATLAS [1] and CMS [2] Collaborations at the Large Hadron Collider [3] (LHC) more than four years ago. Studies of the Higgs boson properties were based on full dataset accumulated at proton-proton (*pp*) collision at 7 TeV center of mass energy ($\approx$5 fb$^{-1}$) and on partial of 8 TeV data ($\approx$5 fb$^{-1}$). Since that time both experiments recorded another 20 fb$^{-1}$ of 8 TeV data in 2012 and about 40 fb$^{-1}$ taken at 13 TeV *pp*-collision energy in 2015–2016. The ATLAS experiment [4] has analyzed the full statistics at 7 and 8 TeV as well as about 40% of the 13 TeV statistics. All measured properties of the new boson are found to be compatible with the Standard Model (SM) predictions for the Higgs boson (*H*). It was a great success of the SM. However, the SM does not explain particle mass hierarchy, dark matter, dark energy, baryon asymmetry of the Universe and has problems with the unification of fundamental interactions [5]. Different extensions of the SM were proposed by theorists to solve these problems. These extensions contain different amount of extra Higgs bosons. The ATLAS Collaboration performed neutral and charged Higgs boson searches in different decay modes. This report contains a short summary of these searches and is organized as follows. Section 1 briefly describes SM Higgs boson decay modes. In Section 2, results on some bosonic and fermionic decay modes obtained at 13 TeV are given. Beyond-the-Standard-Model (BSM) Higgs boson searches are reviewed in Section 3 together with a pair production of Higgs bosons. Section 4 contains summary of results for the SM *H* obtained at 7–8 TeV *pp*-collision energy; the conclusion is drawn in Section 5.

## 1 SM Higgs boson decay channels

The main production mechanisms of the SM Higgs boson at hadron colliders at LHC energies are gluon fusion (ggF), vector boson fusion (VBF), associated production with a *W*- or a *Z*-boson (*VH*) or with a pair of top quarks (*ttH*); expected cross sections $\sigma_H$ at the mass 125 GeV [6] are shown in Fig. 1(a) in the *pp* energy

range 6–15 TeV. The total $\sigma_H$ is O(10 pb). The ggF mechanism provides main, about 90%, contribution to the $H$ production cross section. In ≈5% cases, the Higgs boson is produced through the vector boson fusion; the signature of such process is a presence of two hadron jets with high transverse momenta going mostly at small polar angles. The $WH$, $ZH$ and $ttH$ processes have even smaller cross sections; another production mechanisms like $bbH$ and $tH$ are not considered here.

Calculated branching ratios (BR) of the main Higgs boson decay channels at a mass 125 GeV [7] are shown in Table 1. Despite of 58% probability, the $H \rightarrow bb$ channel is very difficult experimentally due to a huge background and it is not possible to see it via the ggF mechanism. However, one can try to extract the signal in the associated production of the $H$ with a vector boson or a pair of top quarks. The $H \rightarrow WW^\star \rightarrow \ell\nu\ell\nu$ channel (here and further $\ell$ stands for an electron/positron or a muon) is better for searches, despite having branching ratio of only ≈1%. However, it does not allow to reconstruct a Higgs boson mass. The cleanest decay channels where this is possible are the $H \rightarrow ZZ^\star \rightarrow 4\ell$ (BR≈1.3×10$^{-4}$) and the $H \rightarrow \gamma\gamma$ (BR≈2.3×10$^{-3}$). In the last case a signal is searched above strongly overwhelming background. Expected signal event rates normalized to 15 fb$^{-1}$ data sample collected at 13 TeV are also shown in Table 1. Here 100% detection efficiency is assumed.

Table 1. Information about predicted branching ratios (BR, column 2), observability in the experiment (column 3) and event rates normalized to 15 fb$^{-1}$ LHC data samples taken at 13 TeV (column 4) for the most important SM Higgs boson decays. 100% detection efficiency is assumed

| Decay mode | BR, % | Observability | Event rates |
|---|---|---|---|
| $H \rightarrow bb$ | 57.5 ± 1.9 | Mainly in $VH$ and $ttH$ production | ≥10000 |
| $H \rightarrow WW$ | 21.6 ± 0.9 | Leptonic decays of both $W$' | ≈ 7000 |
| $H \rightarrow gg$ | 8.56 ± 0.86 | No good experimental signature | |
| $H \rightarrow \tau\tau$ | 6.30 ± 0.36 | Mainly in VBF production | ≈ 4000 |
| $H \rightarrow cc$ | 2.90 ± 0.35 | No good experimental signature | |
| $H \rightarrow ZZ$ | 2.67 ± 0.11 | Leptonic decays of both $Z$' | ≈ 100 |
| $H \rightarrow \gamma\gamma$ | .228 ± .011 | Big continuum background | ≈ 2000 |
| $H \rightarrow Z\gamma$ | .155 ± .014 | Leptonic decays of $Z$ | ≈ 100 |
| $H \rightarrow \mu\mu$ | .022 ± .001 | Big continuum background | ≈ 200 |

## 2 The SM Higgs boson searches at 13 TeV

The $H \rightarrow ZZ^\star \rightarrow 4\ell$ signature is two pairs of isolated, opposite-sign leptons. The invariant-mass distribution, $m_{4\ell}$, measured by the ATLAS experiment after the combination of all lepton cases [8] is shown in Fig. 1(b). Clear peak above a background is seen in the region around 125 GeV. The ATLAS experiment

observes 44 events in the mass window 118–129 GeV with an estimated background $9.7 \pm 0.8$ events and an expected signal 22.3 events. Based on these numbers, the fiducial cross section measurement is performed and the extracted total cross section is found to be $\sigma_{\text{meas}}^{H}=81^{+18}_{-16}$ pb. It agrees with the SM within $1.6\sigma$ ($\sigma_{\text{SM}}^{H}=55.5^{+3.8}_{-4.4}$) pb. So the 13 TeV result is compatible with the previous one obtained at 8 TeV.
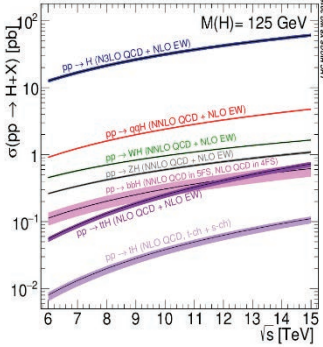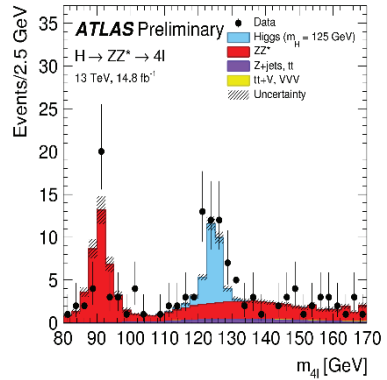


(a)          (b)

Figure 1. (a) Predicted total $\sigma_H$ in $pp$-collisions at different $\sqrt{s}$ together with separate contributions from different production mechanisms [6]. (b) The measured four-lepton invariant-mass distribution in the $H \rightarrow ZZ^\star \rightarrow 4\ell$ decay mode in the ATLAS experiment [8].

The $H \rightarrow \gamma\gamma$ signature is two isolated photons with invariant mass equal to $m_H$. To increase the discovery potential, the ATLAS experiment subdivided events into independent categories having different expected $m_{\gamma\gamma}$ resolution and signal-to-background ratio and optimized for the best separation of the Higgs boson production processes. The $m_{\gamma\gamma}$-distribution after the corresponding re-weighting is given in Fig. 2 together with the spectra after a background subtraction [9]. The excess of events with $4.7\sigma$ significance is seen around 125 GeV. The value of the signal strength in the SM units is measured to be $\mu = \sigma_{\text{meas}}/\sigma_{\text{SM}} = 0.85 \pm 0.21$.

The results obtained for the individual channels $H \rightarrow ZZ^\star \rightarrow 4\ell$ [8] and $H \rightarrow \gamma\gamma$ [9] are combined to extract a Higgs boson signal strength in different production mechanisms (Fig. 3(a)) and its production cross section at 13 TeV $pp$ energy (Fig. 3(b)) [10]. The average signal strength is measured to be $\mu = 1.13 \pm 0.18$, in good agreement with the SM prediction. The measured cross section is also compatible with the SM expectations.

The $VH \rightarrow bb + X$ signature includes two jets originating from $b$-quarks with an invariant mass close to $m_H$. In addition, only events with tight lepton(s) and/or high missing transverse energy $E_T^{\text{miss}}$ depending on
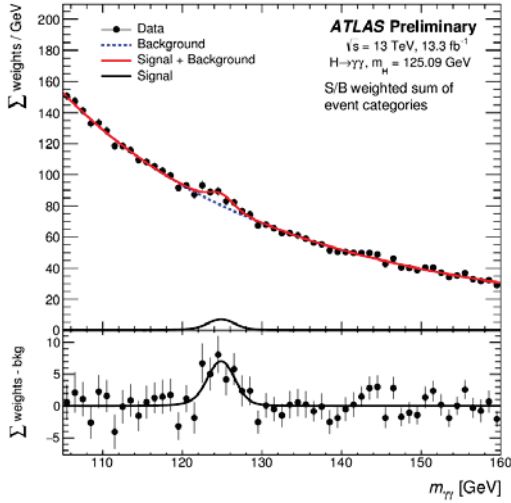
Figure 2. The measured two-photon invariant-mass distribution in the $H \rightarrow \gamma\gamma$ decay mode in the ATLAS experiment [9].



(a)            (b)
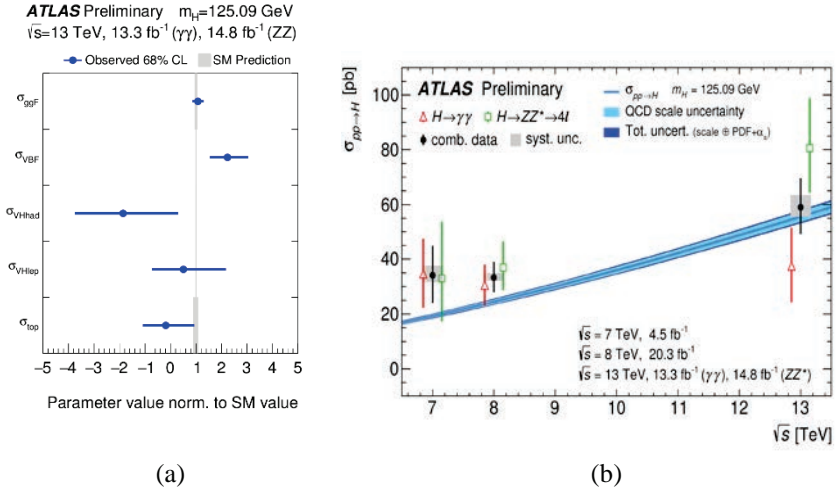
Figure 3. (a) Cross sections for the ggF, VBF, *VH* and top production mechanisms measured as a result of the combination of the $H \rightarrow ZZ^{\star} \rightarrow 4\ell$ and $H \rightarrow \gamma\gamma$ decay modes [10], (b) total $pp \rightarrow H + X$ cross sections measured at

different center of mass energies compared to the Standard Model predictions, in the ATLAS experiment [10].

$Z/W$ final state: $Z \rightarrow \nu\nu$ (0 leptons), $W \rightarrow \ell\nu$ (one lepton) and $Z \rightarrow \ell\ell$ (two leptons) are considered. A multivariate analysis is performed to discriminate the signal from a background. The procedure is successfully tested on the *(W/Z)Z* process with subsequent $Z \rightarrow bb$ decay. The measured $\mu$ is $0.2 \pm 0.5$ [11], compatible both with the background-only and the SM hypotheses.

The *ttH*-production mechanism is studied using three signatures. With the first signature, where events with at least one top decaying leptonically are selected, one can search for the $H \rightarrow bb$ decay mode. The event categorization is performed according to the jet multiplicity and a number of *b*-jets. A multivariate technique to discriminate the signal from the dominant $tt$ + jets background is used. The measured $\mu$ is $2.1 \pm 1.0$ [12] which is compatible with the SM *ttH* hypothesis. The second signature contains multiple leptons mostly from the $H \rightarrow WW^\star$ and $H \rightarrow \tau\tau$ decays. Here the measured $\mu$ is found to be $2.5 \pm 1.2$ [13]. In the third signature the decay $H \rightarrow \gamma\gamma$ is studied. The corresponding value of the signal strength is measured to be $-0.3 \pm 1.1$ [9], compatible both with the SM and the background-only hypotheses. The combined result is $\sigma_{meas}/\sigma_{SM} = 1.8 \pm 0.7$ [14], so the *ttH*-production is established at the $2.8\sigma$ level in the ATLAS experiment.

The $H \rightarrow \mu\mu$ signature is a small peak at the value of $m_H$ in the invariant-mass distribution of isolated, opposite-sign muons above strongly overwhelming Drell-Yan background. To increase the signal sensitivity events are categorized. The ATLAS experiment is able to exclude $\sigma_{meas}/\sigma_{SM} \leq 4.4$ at 95% CL [15]; in the combination with the related Run-1 results this number is reduced down to 3.5.

## 3 Search for the Higgs boson beyond the SM at 13 TeV

The simplest extension of the SM is the so-called Narrow Width Approximation (NWA) where additional high-mass Higgs boson (*H*) behaves as the SM Higgs boson *h*, except the width is fixed to be equal to 4 MeV, which is the expected width of the SM Higgs boson at $m_h = 125$ GeV. This simplified model allows to produce MC samples easily. In addition, the interference of the signal with background processes can be neglected simplifying the analysis. The predictions for the Higgs boson production cross section at 13 TeV in different mechanisms are shown in Fig.4 as a function of $m_H$. It is interesting to note that above 1.5 TeV mass the VBF mechanism starts to dominate. Another extensions of the SM contain five Higgs bosons (neutral light and neutral heavy CP-even states, *h* and *H*, one CP-odd neutral state *A* and two charged states, $H^+$ and $H^-$). Four masses $m_h,\ m_H,\ m_A,\ m_{H^+}$ , mixing angle $\alpha$ between the light and the heavy neutral Higgs boson, and the ratio *tan β* of two vacuum expectation values are usual free parameters.

### 3.1 High mass Higgs boson searches in the bosonic decay modes

The searches for a high mass Higgs boson in the bosonic decay modes are performed in the following channels: $H \rightarrow \gamma\gamma$ [16], $H \rightarrow WW \rightarrow \ell\nu\ell\nu$ [17], $H \rightarrow WW \rightarrow \ell\nu qq$ [18], $H \rightarrow ZZ \rightarrow 4\ell$ [8], $H \rightarrow ZZ \rightarrow \ell\ell\nu\nu$ [19], $H \rightarrow ZZ \rightarrow \ell\ell qq$ [20], $H \rightarrow ZZ \rightarrow \nu\nu qq$ [20], and $H \rightarrow Z\gamma$ [21].
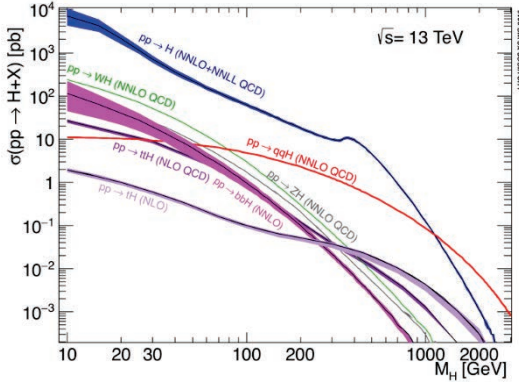


Figure 4. Expected Higgs boson production cross section at 13 TeV *pp*-collisions in different mechanisms as a function of $m_H$ in the NWA model [6].

The $H \rightarrow \gamma\gamma$ decay mode has a special interest because of the observation of an excess at around 750 GeV in the di-photon invariant-mass distribution both by the ATLAS and CMS collaborations in the 2015 data sample [22]–[23]. In the ATLAS case, the deviation from the SM was at $3.4\sigma$ level (local significance). The ATLAS Collaboration performed a new analysis based on five times larger dataset mostly obtained in 2016. The search mass range is 200–2500 GeV. Some 35891 events with hard photons were selected and the resulting $m_{\gamma\gamma}$-distribution is shown in Fig. 5. No significant excess is observed. The resulting 95% CL upper limit on the fiducial cross section multiplied by the BR($H \rightarrow \gamma\gamma$) lies between 0.2 fb and 13 fb depending on the value of $m_{\gamma\gamma}$.

The mass range between 300–3000 GeV is covered by the $H \rightarrow WW \rightarrow e\nu\mu\nu$ decay channel. Selection criteria are specially optimized for the high-mass case and a multivariate analysis is performed. Events are subdivided into ggF- and two VBF-enriched categories. No significant excess above a background is found in the search mass range (Fig. 6). 95% CL upper limits on $\sigma_H \times$ BR($H \rightarrow WW$) are established separately in the ggF and VBF production mechanisms in the framework of the NWA model [17]. They are 4.3 pb (51 fb) at $m_H$ =300 GeV ($m_H$ =3000 GeV) in the ggF case and 1.1 pb (30 fb) at $m_H$ =300 GeV ($m_H$ =3000 GeV) in the VBF case.
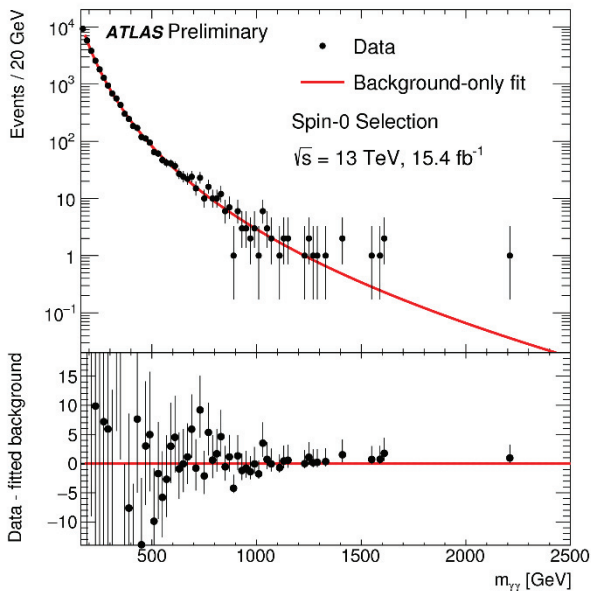
Figure 5. The measured two-photon invariant-mass distribution in the $H \rightarrow \gamma\gamma$ decay mode in the ATLAS experiment [22].



(a)　　　　　　　　　　　　　　(b)
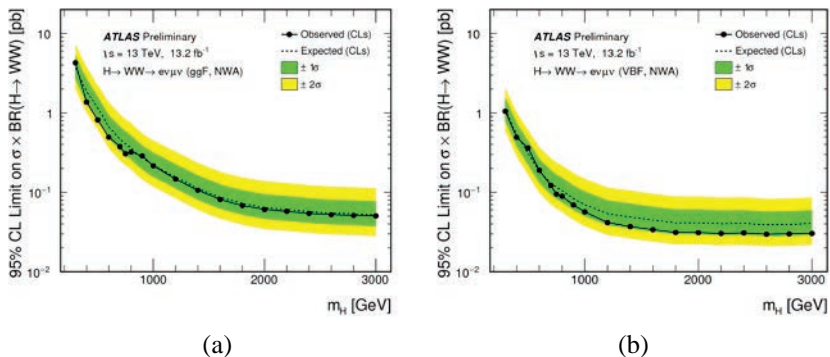
Figure 6. The measured 95% CL upper limits as a function of $m_H$ on $\sigma_H \times \mathrm{BR}(H \rightarrow WW)$ for the ggF (a) and VBF (b) production mechanisms in the framework of the NWA model in the ATLAS experiment [17].

A similar study is performed for the $H \rightarrow ZZ \rightarrow 4\ell$ channel. No significant excess is observed in the search mass range 200–1000 GeV (Fig. 7). The resulting upper limits on $\sigma_H \times \mathrm{BR}(H \rightarrow 4\ell)$ in the NWA model lie between 4.6 fb ($m_H =$ 244

GeV) and 0.22 fb ($m_H$ =1000 GeV) for the ggF production mechanism. They are as large as 1.9 fb (0.2 fb) for the VBF case.



(a)                                    (b)
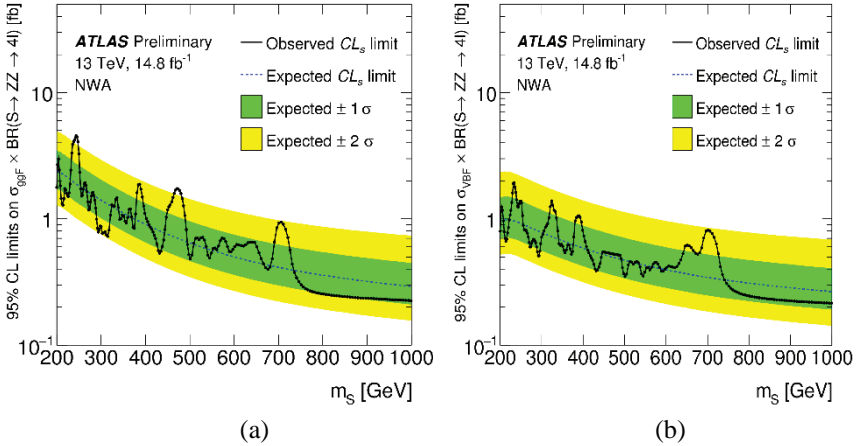
Figure 7. The measured 95% CL upper limits as a function of $m_S$ on $\sigma_S \times$ BR($S \rightarrow ZZ \rightarrow 4\ell$) for the ggF (left) and VBF (right) production mechanisms in the framework of the NWA model in the ATLAS experiment [17].

Upper limits on the $\sigma_H \times$ BR($H \rightarrow ZZ$) are also put using the $H \rightarrow ZZ \rightarrow \ell\ell\nu\nu$ [19], $H \rightarrow ZZ \rightarrow \ell\ell qq$ [20] and $H \rightarrow ZZ \rightarrow \nu\nu qq$ [20] decay modes. In the second case both the ggF and VBF cases are considered while in the first and in the third ones only the ggF mechanism is tried. Again, no significant deviation from the SM is observed (Fig. 8). Analyzing the $X \rightarrow Z\gamma$ decay channel, where $X$ is hypothetic scalar state, it is concluded that the 95% CL upper limit on the $\sigma_X \times$ BR($X \rightarrow Z\gamma$) is as large as 215 fb (5 fb) at $m_H$ =270 (2400) GeV, respectively in the NWA approach [18] (Fig. 9(a)). Similar limits are obtained for the $\sigma_X \times$ BR($X \rightarrow WW$) (Fig. 9(b)). They are 1 pb (2.5 fb) at $m_H$ =500 (3000) GeV [21].

### 3.2 MSSM Higgs boson searches at 13 TeV

In the Minimal Super Symmetric Model (MSSM), the main $A/H$ production mechanisms are the gluon fusion or the associated production with one or two $b$-quarks. The mass range between 200–1200 GeV is covered by the $A/H \rightarrow \tau\tau$ decay channel. Among possible final states with two $\tau$-leptons only those with hadrons ($hh$) and with a lepton and hadrons ($\ell h$) are considered. Results are interpreted in the MSSM benchmark scenarios. The 95% CL upper limits on $\sigma_{A/H} \times$ BR($A/H \rightarrow \tau\tau$) lie between 25 fb and 1.3 pb in the case of the ggF [24]. They are changed to 30 fb and 1.5 pb for the associated production.
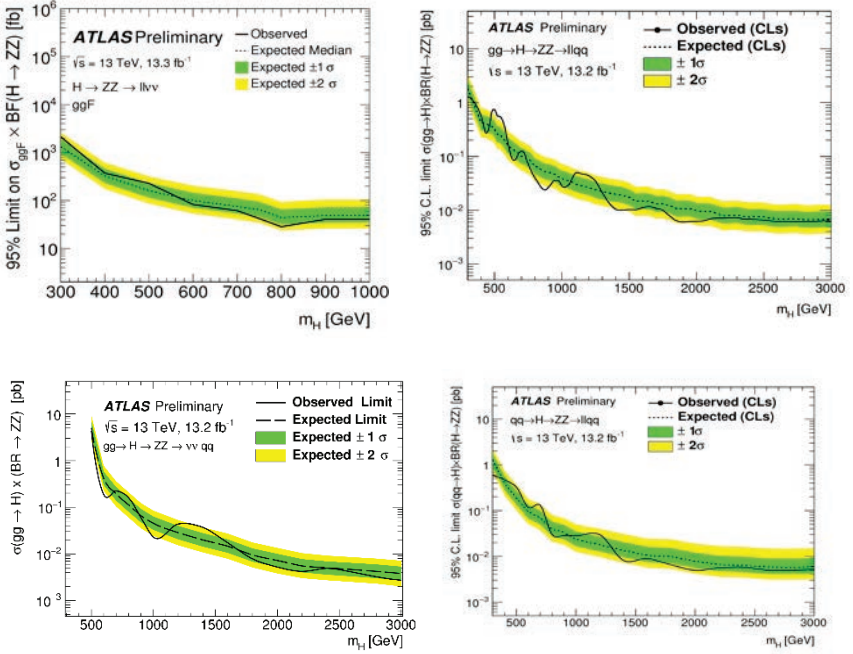
Figure 8. The measured 95% CL upper limits as a function of $m_H$ on $\sigma_H \times$ BR($H \to ZZ$) for the ggF production in the $\ell\ell\nu\nu$ channel (top left), ggF production in the $\ell\ell qq$ channel (top right), ggF production in the $\nu\nu qq$ channel (bottom left) and VBF production in the $\ell\ell qq$ channel (bottom right), in the framework of the NWA model in the ATLAS experiment [19, 20].



(a)                                              (b)
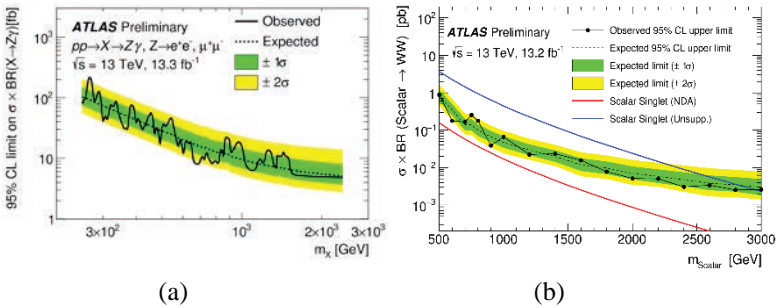
Figure 9. The measured 95% CL upper limits as a function of $m_X$ on $\sigma_X \times$ BR($X \to Z\gamma$) (a) and on $\sigma_X \times$ BR($X \to WW$) (b) in the framework of the NWA model in the ATLAS experiment [18, 21].

In the MSSM a relation between top quark mass $m_{\text{top}}$ and $m_{H^+}$ dictates both the production mode and decay channels of $H^+$. If $m_{H^+} \geq m_{\text{top}}$, the $H^+$ is produced together with $t$- and $b$-quarks. The charged Higgs boson can decay into a $tb$ or into a $\tau\nu$ final state.

The mass range for the $H \to tb$ searches is between 300–1000 GeV [25]. Multi-jet final states with one lepton from top decay are studied. A multivariate analysis is performed; its result is interpreted within benchmark scenarios of the MSSM models. 95% CL upper limits on the $\sigma_H \times \text{BR}(H \to tb)$ are established (Fig. 11(a)). They are as large as 1.09 pb (0.18 pb) at $m_H = 300$ (1000) GeV, respectively. This results to exclusion of very small and very large values of $\tan\beta$ mostly for low $m_H$ if interpreted in the MSSM $m^{\text{mod-}}_h$ scenario (Fig. 11 (b)).



(a)                                                    (b)
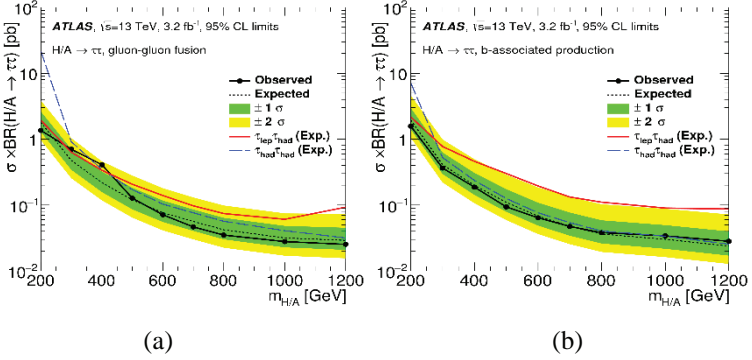
Figure 10. 95% CL upper limits as a function of $m_{H/A}$ on the $\sigma_H \times \text{BR}(H/A \to \tau\tau)$ in the ggF (a) and in the associated production (b) in the ATLAS experiment [24].



(a)                                                    (b)
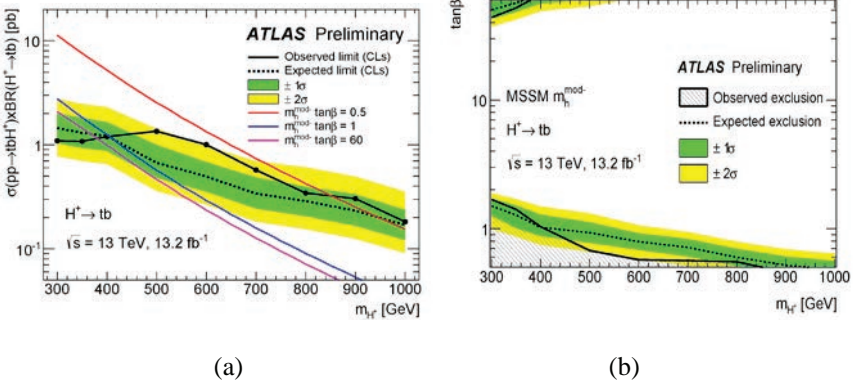
Figure 11. 95% CL upper limits as a function of $m_{H^+}$ on the $\sigma_H \times \text{BR}(H^+ \to tb)$ (a) and on $\tan\beta$ in the MSSM $m^{\text{mod-}}_h$ scenario (b) in the ATLAS experiment [25].

The mass range for the $\tau\nu$ decay searches is between 300–2000 GeV [26]. Final states with one $\tau$-lepton and one $W$ decaying hadronically are considered. The hMSSM model is used to interpret the results. The obtained 95% CL upper limits on the $\sigma_H \times BR(H \to \tau\nu)$ vary from 2 pb at $m_H =200$ GeV to 8 fb at $m_H =2000$ GeV. Very large values of $tan\,\beta$ are excluded in the hMSSM scenario in the mass range between 300 and 600 GeV.



<div align="center">(a)       (b)</div>
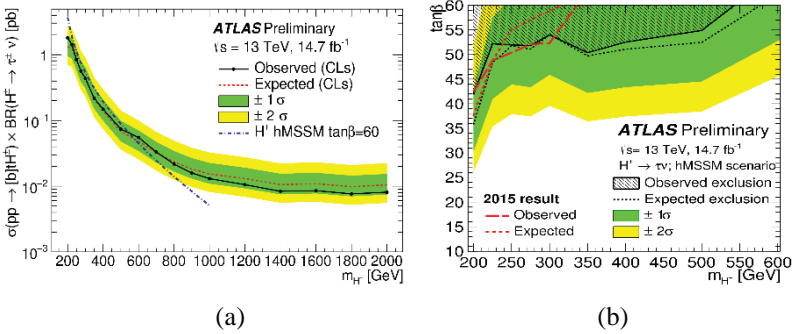
Figure 12. 95% CL upper limits as a function of $m_{H+}$ on the $\sigma_H \times BR(H^+ \to \tau\nu)$ (a) and on $tan\,\beta$ in the hMSSM scenario (b) in the ATLAS experiment [26].

In the SM, the cross section of Higgs bosons pair production ($hh$) is too small to be observed at the LHC with the current dataset. However, in some BSM models, the $hh$-rates could be much higher. The ATLAS experiment searches for non-resonant and resonant $hh$-production in the $hh \to WW\gamma\gamma$ [27] and $hh \to bbbb$ [28] decay channels; in the first case $\ell\nu\ell\nu$ and $\ell\nu qq$ final states of two $W$'s are considered. No significant excess above a background is found in the search range 250–500 GeV in the first case and in the 300-3000 GeV range in the second one. The observed 95% CL exclusion limit for the $\sigma_{gg} \to X \times BR(H \to hh)$ is 25 pb in the non-resonant case [27]. This number is changed to 47.7 pb (24.7 pb) in the resonant case for $m_X =260$ GeV (500 GeV), respectively. For the $\sigma_{gg \to H} \times BR(H \to hh \to bbbb)$ the 95% CL exclusion limit is 330 fb while the SM prediction is $11.3 \pm 1.0$ fb [28].

## 4 Brief summary of the SM $H$ measurements at 7–8 TeV $pp$-collision energy

Using the 7 TeV and 8 TeV collision data produced at the LHC, the ATLAS experiment measured properties of the Higgs boson such as its couplings, mass, spin and parity. The results of these measurements are summarized in Table 2. The Higgs boson mass is found to be $125.36 \pm 0.41$ GeV [29], based on the studies of the $H \to ZZ \to 4\ell$ and $H \to \gamma\gamma$ channels. This number becomes $125.09 \pm 0.24$ GeV when combined with the CMS measurements [30]. The signal strength $\mu$ in the

SM is measured to be $1.18 \pm 0.15$ [31]. This result is obtained from the analysis of the $H \to ZZ^\star \to 4\ell$, $H \to \gamma\gamma$, $H \to WW^\star \to \ell\nu\ell\nu$, $H \to \tau\tau$ and $H \to bb$ decay channels. Note that the first three channels are seen in the ATLAS experiment.

Table 2. Brief summary of the results related to the SM Higgs boson obtained at 7 and 8 TeV collision energy in the ATLAS experiment.

| Parameter | Value | Ref. | Comment |
|-----------|-------|------|---------|
| Mass, GeV | $125.36 \pm 0.41$ | [29] | $125.09 \pm 0.24$ with the CMS |
| Average $\mu$ | $1.18 \pm 0.15$ | [31] | $1.09 \pm 0.10$ with the CMS |
| $\mu$ for $H \to \gamma\gamma$ | $1.17^{+0.28}_{-0.26}$ | [31] | $5.2\sigma$ (discovery) |
| $\mu$ for $H \to 4\ell$ | $1.46^{+0.40}_{-0.34}$ | [31] | $8.1\sigma$ (discovery) |
| $\mu$ for $H \to \ell\nu\ell\nu$ | $1.18^{+0.24}_{-0.21}$ | [31] | $6.5\sigma$ (discovery) |
| $\mu$ for $H \to \tau\tau$ | $1.44^{+0.42}_{-0.37}$ | [31] | $4.5\sigma$ (evidence) |
| $\mu$ for $H \to bb$ | $0.63^{+0.39}_{-0.37}$ | [31] | $1.4\sigma$ (no evidence) |
| $\mu$ for ggF | $1.23^{+0.23}_{-0.20}$ | [31] | $1.03^{+0.17}_{-0.15}$ with the CMS |
| $\mu$ for VBF | $1.23^{+0.32}_{-0.32}$ | [31] | $1.18^{+0.25}_{-0.23}$ with the CMS |
| $\mu$ for $VH$ | $0.80 \pm 0.36$ | [31] | $0.84^{+0.40}_{-0.38}$ with the CMS |
| $\mu$ for $ttH$ | $1.81 \pm 0.80$ | [31] | $2.3^{+0.7}_{-0.6}$ with the CMS |
| Spin/parity | $0^+$ | [32] | $4\ell$, $\ell\nu\ell\nu$ and $\gamma\gamma$ modes |
| Width, MeV | $\leq 22.7$ (95% CL) | [33] | Off-shell $H \to ZZ/WW$ |
| BR($H \to inv.$) | $\leq 0.28$ (95% CL) | [34] | Important for WIMP searches |

with $\geq 5\sigma$ significance. The resulting signal strength from two LHC experiments is found to be $1.09 \pm 0.10$ [7]. Analyzing the $H \to ZZ^\star \to 4\ell$, $H \to WW^\star \to e\nu\mu\nu$ and $H \to \gamma\gamma$ decay modes, we conclude with very high confidence level that a spin-parity of the Higgs boson is $0^+$, as predicted by the SM [32]. From the off-shell measurements of the $H \to ZZ^\star \to 4\ell$ and $H \to WW^\star \to \ell\nu\ell\nu$ channels the upper limit is put to the $H$ width as 22.7 MeV at 95% CL [33]. The ATLAS experiment also looks for invisible decay of the Higgs boson, $H \to inv.$, which is interesting for WIMP searches. The upper limit on BR($H \to inv.$) $\leq 0.28$ is established at 95% CL [34].

In summary, no significant deviation from the SM is observed in the ATLAS studies of the Higgs boson at 7–8 TeV.

## 5 Conclusion

With the 7 and 8 TeV LHC data the ATLAS experiment measured properties of the Higgs boson such as its couplings, mass, spin and parity. No significant deviation from the SM is found. Using 13-15 fb$^{-1}$ of the 13 TeV LHC data, the ATLAS obtained preliminary results reconfirming the Higgs boson discovery in the $4\ell$ and $\gamma\gamma$ modes. With the same dataset, the ATLAS performed searches for neutral and charge Higgs bosons predicted by some extensions of the SM. No

evidence for new physics was found yet. Limits on the *H* boson production cross sections in different models were put. The ATLAS Collaboration continues to study properties of the SM-like *H* boson improving precision of their measurements and to search for exotic Higgs bosons with new 13 TeV data.

**References**

[1] ATLAS Collaboration, Phys. Lett. B716, 1 (2012)
[2] CMS Collaboration, Phys. Lett. B716, 30 (2012)
[3] L. Evans and P. Bryant (editors), Journal of Instrumentation 3, S08001 (2008)
[4] ATLAS Collaboration, Journal of Instrumentation, 3, S08003 (2008)
[5] C. Patrignani *et al.* (Particle Data Group), Chin. Phys. C, **40**, 100001 (2016)
[6] LHC Higgs boson cross section working group,
https://twiki.cern.ch/twiki/bin/view/LHCPhysics/LHCHXSWG
[7] ATLAS and CMS Collaborations, JHEP 08 (2016) 045
[8] ATLAS Collaboration, ATLAS-CONF-2016-079,
http://cds.cern.ch/record/2206253/files/ATLAS-CONF-2016-079.pdf
[9] ATLAS Collaboration, ATLAS-CONF-2016-067,
http://cds.cern.ch/record/2206210/files/ATLAS-CONF-2016-067.pdf
[10] ATLAS Collaboration, ATLAS-CONF-2016-081,
http://cds.cern.ch/record/2206272/files/ATLAS-CONF-2016-081.pdf
[11] ATLAS Collaboration, ATLAS-CONF-2016-091,
http://cds.cern.ch/record/2206813/files/ATLAS-CONF-2016-091.pdf
[12] ATLAS Collaboration, ATLAS-CONF-2016-080,
http://cds.cern.ch/record/2206255/files/ATLAS-CONF-2016-080.pdf
[13] ATLAS Collaboration, ATLAS-CONF-2016-058,
http://cds.cern.ch/record/2206153/files/ATLAS-CONF-2016-058.pdf
[14] ATLAS Collaboration, ATLAS-CONF-2016-068,
http://cds.cern.ch/record/2206211/files/ATLAS-CONF-2016-068.pdf
[15] ATLAS Collaboration, ATLAS-CONF-2016-041,
http://cds.cern.ch/record/2206079/files/ATLAS-CONF-2016-041.pdf
[16] ATLAS Collaboration, ATLAS-CONF-2016-059,
http://cds.cern.ch/record/2206154/files/ATLAS-CONF-2016-059.pdf
[17] ATLAS Collaboration, ATLAS-CONF-2016-074,
http://cds.cern.ch/record/2206243/files/ATLAS-CONF-2016-074.pdf
[18] ATLAS Collaboration, ATLAS-CONF-2016-062,
http://cds.cern.ch/record/2206199/files/ATLAS-CONF-2016-062.pdf
[19] ATLAS Collaboration, ATLAS-CONF-2016-056,
http://cds.cern.ch/record/2206138/files/ATLAS-CONF-2016-056.pdf
[20] ATLAS Collaboration, ATLAS-CONF-2016-082,
http://cds.cern.ch/record/2206275/files/ATLAS-CONF-2016-082.pdf
[21] ATLAS Collaboration, ATLAS-CONF-2016-044,

http://cds.cern.ch/record/2206125/files/ATLAS-CONF-2016-044.pdf
[22] ATLAS Collaboration, JHEP 09 (2016) 1
[23] CMS Collaboration, arXiv:1609.02507, submitted to Phys. Lett. B.
[24] ATLAS Collaboration, ATLAS-CONF-2016-085,
http://cds.cern.ch/record/2206278/files/ATLAS-CONF-2016-085.pdf
[25] ATLAS Collaboration, ATLAS-CONF-2016-089,
http://cds.cern.ch/record/2206809/files/ATLAS-CONF-2016-089.pdf
[26] ATLAS Collaboration, ATLAS-CONF-2016-088
http://cds.cern.ch/record/2206282/files/ATLAS-CONF-2016-088.pdf
[27] ATLAS Collaboration, ATLAS-CONF-2016-071,
http://cds.cern.ch/record/2206222/files/ATLAS-CONF-2016-071.pdf
[28] ATLAS Collaboration, ATLAS-CONF-2016-049,
http://cds.cern.ch/record/2206131/files/ATLAS-CONF-2016-049.pdf

[29] ATLAS Collaboration, Phys. Rev. D90 (2014) 052004
[30] ATLAS and CMS Collaborations, Phys. Rev. Lett. 114 (2015) 191803
[31] ATLAS Collaboration, Europ. Phys. J. C76 (2016) 6
[32] ATLAS Collaboration, Europ. Phys. J. C75 (2015) 476
[33] ATLAS Collaboration, Europ. Phys. J. C75 (2015) 335
[34] ATLAS Collaboration, JHEP 01 (2016) 172

# Two-particle Bose–Einstein correlations in $pp$ collisions at $\sqrt{s}$ = 0.9 and 7 TeV measured with the ATLAS detector

## Y.A. Kulchitsky [1), 2)]

On behalf of the ATLAS Collaboration

[1)]   *Joint Institute for Nuclear Research, Dubna, Russia*
[2)]   *Institute of Physics, National Academy of Sciences, Minsk, Belarus*

## Abstract

The paper presents studies of Bose–Einstein Correlations for pairs of like-sign charged particles measured in the kinematic range $p_{\mathrm{T}} > 100$ MeV and $|\eta| < 2.5$ in proton–proton collisions at centre-of-mass energies of 0.9 and 7 TeV with the ATLAS detector at the CERN Large Hadron Collider. The multiplicity dependence of the Bose–Einstein Correlations parameters characterizing the correlation strength and the correlation source size are investigated for charged-particle multiplicities of up to 240. A saturation effect in the multiplicity dependence of the correlation source size parameter is observed using the high-multiplicity 7 TeV data sample. The dependence of the Bose–Einstein Correlations parameters on the average transverse momentum of the particle pair is also investigated.

## 1   Introduction

Correlations between identical bosons, called Bose-Einstein correlations (BEC), are a well-known phenomenon in high-energy and nuclear physics. The BEC are often considered to be the analogue of the Hanbury-Brown and Twiss effect [1] in astronomy, describing the interference of incoherently emitted identical bosons [2–4]. They represent a sensitive probe of the space-time geometry of the hadronization region and allow the determination of the size and the shape of the source from which particles are emitted.

The production of identical bosons that are close together in phase space is enhanced by the presence of BEC. The first observation of BEC effects in identically charged pions produced in $p\bar{p}$ collisions was reported in Ref. [5]. Since then, BEC have been studied for systems of two or more identical bosons produced in various types of collisions, from leptonic to hadronic and nuclear collisions.

Studies of the dependence of BEC on particle multiplicity and transverse momentum help to understand the multiparticle production mechanism. The size of the source emitting the correlated particles has been observed to increase with particle multiplicity. This can be understood as arising from the increase in the initial geometrical region of overlap of the colliding objects [6]: a large overlap implies a large multiplicity. While this dependence is natural in nucleus–nucleus collisions, the increase of size with multiplicity has also been observed in hadronic and leptonic interactions. In the latter, it is understood as a result of superposition of many sources [7–9] or related to the number of jets [10, 11]. High-multiplicity data in proton-proton interactions can serve as a reference for studies of nucleus–nucleus collisions. The effect is reproduced in both the hydrodynamical/hydrokinetic [12–14] and Pomeron-based [15,16] approaches for hadronic interactions where high multiplicities play a crucial role. The dependence on the transverse momentum of the emitter particle pair is another important feature of the BEC effect [17].

In this studies of one-dimensional Bose–Einstein Correlations effects in *pp* collisions at centre-of-mass energies of 0.9 and 7 TeV, using the ATLAS detector [18] at the Large Hadron Collider (LHC) [19], are presented in the Ref. [20]. At the LHC, BEC have been studied by the CMS [21, 23] and ALICE [24, 25] experiments. In the analysis reported here, the studies are extended to the region of high-multiplicities available thanks to the high multiplicity track trigger.

# 2 Analysis

## 2.1 Two-particle correlation function

Bose–Einstein correlations are measured in terms of a two-particle correlation function,

$$C_2(p_1, p_2) = \frac{\rho(p_1, p_2)}{\rho_0(p_1, p_2)}, \tag{1}$$

where $p_1$ and $p_2$ are the four-momenta of two identical bosons in the event, $\rho$ is the two-particle density function, and $\rho_0$ is a two-particle density function (known as the reference function) specially constructed to exclude BEC effects. The densities $\rho$ and $\rho_0$ are normalized to unity, i.e. they are the probability density functions.

In order to compare with data over the widest possible range of centre-of-mass energies and system sizes, the density function is parameterized in terms of the Lorentz-invariant four-momentum difference squared, $Q^2$, of the two particles,

$$Q^2 = -(p_1 - p_2)^2. \tag{2}$$

The BEC effect is usually described by a function with two parameters: the effective radius parameter $R$ and the strength parameter $\lambda$ [26], where the latter is also called the incoherence or chaoticity parameter. A typical functional form is

$$C_2(Q) = \frac{\rho(Q)}{\rho_0(Q)} = C_0[1 + \Omega(\lambda, QR)](1 + \varepsilon Q).$$ 
(3)

In a simplified scheme for fully coherent emission of identical bosons, $\lambda = 0$, while for incoherent (chaotic) emission, $\lambda = 1$. The $QR$ dependence comes from the Fourier transform of the distribution of the space-time points of boson emission. Several different functional forms have been proposed for $\Omega(\lambda, QR)$. Those used in this paper are described in Sect. 2.4. The fitted parameter $\varepsilon$ takes into account long-distance correlations not fully removed from $\rho_0$. Finally, $C_0$ is a normalization constant, typically chosen such that $C_2(Q)$ is unity for large $Q$. In this paper, the density function $\rho$ is calculated for like-sign charged-particle pairs, with both the $++$ and $--$ combinations included, $\rho(Q) \equiv \rho(++,--)$. All particles are treated as charged pions and no particle identification is attempted. The purity of the analysis sample in terms of identical boson pairs is estimated from MC to be about 70% (where about 69% are $\pi^\pm \pi^\pm$ and about 1% are $K^\pm K^\pm$). The effect of the purity is absorbed in the strength parameter $\lambda$, while the results of the analysis on the effective radius parameter $R$ were found to be not affected.

## 2.2 Coulomb correction

The long-range Coulomb force causes a momentum shift between the like-sign and unlike-sign pairs of particles. The density distributions are corrected for this effect by applying the Gamow penetration factor per track pair with a weight $1/G(Q)$ [27–29],

$$\rho_{\mathrm{corr}}(Q) = \frac{\rho(Q)}{G(Q)},$$
(4)

where the Gamow factor $G(Q)$ is given by

$$G(Q) = \frac{2\pi\zeta}{\mathrm{e}^{2\pi\zeta} - 1}$$
(5)

with the dimensionless parameter $\zeta$ defined as

$$\zeta = \pm\frac{\alpha m}{Q}.$$
(6)

Here $\alpha$ is the electromagnetic fine-structure c onstant a nd $m$ i s t he pion mass. The sign of $\zeta$ is positive for like-sign pairs and negative for unlike-sign pairs. The resulting correction on $\rho(Q)$ decreases with increasing $Q$

and at $Q = 0.03$ GeV it is about 20%. A systematic uncertainty on $G(Q)$ is considered to cover effects like the extended size of the emission source and other effects, see discussion in Ref. [30]. Neither the Coulomb interaction nor the BEC effect are present in the generation of MC event samples which are used in the analysis. The Coulomb correction is thus not applied to MC events.

## 2.3 Reference sample

A good choice of the reference sample is important to allow the experimental detection of the BEC signal. Ideally, $\rho_0(Q)$ should include all momentum correlations except those arising from BEC. Thus, several different choices have been studied to construct an appropriate reference sample.

Most of the proposed approaches use random pairing of particles, such as mixing particles from different events (the "mixed event" technique [31]), or choosing them from the same event but from opposite hemispheres or by rotating the transverse momentum vector of one of the particles of the like-sign pair [32]. Although these mixing techniques reproduce the topology and some properties of the event under consideration and destroy BEC, they violate energy-momentum conservation. Moreover, there are many possible ways to construct the pairs, such as mixing the particles randomly, or keeping some topological constraints such as the event multiplicity, the invariant mass of the pair or the rapidity of the pair. All of these introduce additional biases in the BEC observables. For example, it was observed in dedicated MC studies that the single-ratio correlation functions $C_2$ using reference samples constructed with the event mixing or opposite hemispheres techniques exhibit an increase in the low-$Q$ BEC sensitive region. This effect is found to be more pronounced with increase of the multiplicity or average particle-pair transverse momentum and indicates that these reference samples are not suitable.

A natural choice is to use the unlike-sign particle pairs from the same events that are used to form pairs of like-sign particles, i.e., $\rho_0(Q) \equiv \rho(+-)$, called in the following the unlike-charge reference sample. This sample has the same topology and global properties as the like sign sample $\rho(++, --)$, but is naturally free of any BEC effect. Studying the $C_2$ correlation functions on MC, none of the deficits of the event mixing and opposite hemispheres techniques described above were observed. However, this sample contains hadron pairs from the decay of resonances such as $\rho$, $\eta, \eta'$, $\omega$, $\phi$, $K^*$, which are not present in the like-sign combinations. These contribute to the low-$Q$ region and can give a spurious BEC signature with a large effective radius of the source [33–39].

In this paper, the unlike-charge reference sample is used. To account for the effects of resonances, the two-particle correlation function $C_2(Q)$ is corrected using Monte Carlo simulation without BEC effects via a double-

ratio $R_2(Q)$ defined as

$$R_2(Q) = \frac{C_2(Q)}{C_2^{MC}(Q)} = \frac{\rho(++,--)}{\rho(+-)} \quad \frac{\rho^{MC}(++,--)}{\rho^{MC}(+-)} . \qquad (7)$$

## 2.4 The parameterizations of BEC

Various parameterizations of the $\Omega(\lambda, QR)$ function can be found in the literature, each assuming a different shape for the particle-emitting source. In the studies presented here, the data are analysed using the following parameterizations:

- the Goldhaber parameterization [5] of a static Gaussian source in the plane-wave approach,

$$\Omega = \lambda \cdot \exp\left(-R^2 Q^2\right), \qquad (8)$$

which assumes a spherical shape with a radial Gaussian distribution of the emitter;

- the exponential parameterization of a static source

$$\Omega = \lambda \cdot \exp\left(-RQ\right), \qquad (9)$$

which assumes a radial Lorentzian distribution of the source. This parameterization provides a better description of the data at small $Q$ values, as discussed in [32].

The first moment of the $\Omega(QR)$ distribution corresponds to $1/R$ for the exponential form and to $1/(R\sqrt{\pi})$ for the Gaussian form. To compare the values of the radius parameters obtained from the two functions, the $R$ value of the Gaussian should be compared to $R/\sqrt{\pi}$ of the exponential form.

# 3 Experimental details

## 3.1 The ATLAS detector

The ATLAS detector [18] is a multi-purpose particle physics experiment operating at one of the beam interaction points of the LHC. The detector covers almost the whole solid angle around the collision point with layers of tracking detectors, calorimeters and muon chambers. It is designed to study a wide range of physics topics at LHC energies. For the measurements presented in this paper, the tracking devices and the trigger system are of particular importance.

The innermost part of the ATLAS detector is the inner detector (ID), which has full coverage in $\phi$ and covers the pseudorapidity range $|\eta| < 2.5$.

It consists of a silicon pixel detector (Pixel), a silicon microstrip detector (SCT) and a transition radiation tracker (TRT). These detectors are immersed in a 2 T solenoidal magnetic field. The Pixel, SCT, and TRT detectors have typical position resolutions of 10, 17 and 130 $\mu$m for the $r$-$\phi$ coordinate, respectively. In the case of the Pixel and SCT, the resolutions are 115 and 580 $\mu$m, respectively, for the second measured coordinate. A track from a charged particle traversing the full radial extent of the ID would typically have three Pixel hits, eight or more SCT hits and more than 30 TRT hits.

High-multiplicity track (HM) events were collected at 7 TeV using a dedicated high-multiplicity track trigger. At level trigger L1, the collisions were triggered using the summed transverse energy ($\Sigma E_{\mathrm{T}}$) in all calorimeters, calibrated at the electromagnetic energy scale [40]. The high-multiplicity minimum-bias (MB) events were required to have $\Sigma E_{\mathrm{T}} > 20$ GeV. A high number of hits in the SCT was required at level trigger L2, while at the Event Filter EF level at least 124 tracks with $p_{\mathrm{T}} > 400$ MeV were required to originate from a single vertex.

## 3.2 Data and Monte Carlo samples

The study is carried out using the $pp$-collision datasets at the centre-of-mass energies $\sqrt{s} = 0.9$ and 7 TeV that were used in previously published ATLAS studies of minimum-bias interactions [41, 42].

The event and track selection criteria are the same as the ones used for the ATLAS minimum-bias multiplicity analysis [41] with the same minimum-bias trigger and quality criteria for the track reconstruction. All events in these datasets are required to have at least one vertex [43], formed from a minimum of two tracks with $p_{\mathrm{T}} > 100$ MeV and consistent with the average beam spot position within the ATLAS detector (primary vertex) [44]. The tracks satisfying the above-mentioned selection criteria are used as the input to determine the corrected distributions, as described in Sect. 3.3. The multiplicity of selected tracks with $p_{\mathrm{T}} > 100$ MeV and $|\eta| < 2.5$ within an event is denoted by $n_{\mathrm{sel}}$.

The same event selection criteria are applied to high-multiplicity events, which are defined to be those with at least 120 selected tracks. To estimate the possible influence of multiple $pp$ interactions in the 7 TeV high-multiplicity track trigger data, the distribution of the distances $\Delta z$ between the $z$ coordinates of primary and pile-up vertices are studied. The study shows that on average there is less than one pile-up track selected in the HM sample, which has a negligible influence on the BEC studies.

Large Monte Carlo samples of minimum-bias and high-multiplicity events were generated using the PYTHIA 6.421 Monte Carlo event generator [45] with the ATLAS MC09 set of optimised parameters (tune) [46] ($1.1 \times 10^{7}$ for $\sqrt{s} = 900$ GeV, $2.7 \times 10^{7}$ for $\sqrt{s} = 7$ TeV and $1.8 \times 10^{6}$ for $\sqrt{s} = 7$ TeV

high-multiplicity data) with non-diffractive, single-diffractive and double-diffractive processes included in proportion to the cross sections predicted by the model. As discussed in Sec. 2.2, no simulation of the BEC effect is implemented in the generator. This is the baseline Monte Carlo generator which reproduces single-particle spectra [42]. The generated events were passed through the ATLAS simulation and reconstruction chain; the detector simulation program [47] is based on GEANT4 [48]. Dedicated sets of high-multiplicity events were also generated.

## 3.3   Data correction procedure

Following the procedure applied in the previous ATLAS minimum-bias measurements [41,42], each track is assigned a weight which corrects for the track reconstruction efficiency, for the fraction of secondary particles, for the fraction of the primary particles outside the kinematic range and for the fraction of fake tracks. In addition, the effect of events lost due to trigger and vertex reconstruction inefficiencies is corrected for using an event-by-event weight applied to pairs of particles in the $Q$ distribution.

The multiplicity distributions are corrected to the particle level using an iterative method that follows the Bayesian approach [49] as it is described in Refs. [41, 42].

# 4   Systematic uncertainties

The following contributions to the systematic uncertainties on the fitted parameters, $R$ and $\lambda$, are considered. The systematic uncertainties resulting from the track reconstruction efficiency, which are parameterized in bins of $p_T$ and $\eta$, were determined in earlier analyses [41, 42]. These cause uncertainties in the track weights of particle pairs in the $Q$ distributions entering the correlation functions.

The effects of the track splitting and merging are sizeable only for very low $Q$ values (smaller than 5 MeV), and are found to be negligible for the measurements with $Q \geq 20$ MeV. The leading source of systematic uncertainty is due to differences in the Monte Carlo generators used to calculate the $R_2$ correlation function from the $C_2$ correlation function. The corresponding contribution to the systematic uncertainty is estimated as the root-mean-squared (RMS) spread of the results obtained for the different Monte Carlo datasets. The statistical uncertainties arising from the Monte Carlo datasets are negligibly small. The systematic uncertainty due to Coulomb corrections is estimated by varying the corrections by ±20%. The influence of the fit range is estimated by changing the upper bound of the $Q$ range from the nominal 2 GeV: decreasing it to 1.5 GeV and increasing it up to 2.5 GeV. The latter better estimates the uncertainty due the long-

range correlations. This contribution is taken into account by the value of $\varepsilon$, the parameter in the linear term of Eq. (3) describing the long-range correlations. Other effects contributing to the systematic uncertainties are the lowest value of $Q$ for the fit, the bin size and exclusion of the interval $0.5 \leq Q \leq 0.9$ GeV due to the overestimate of the $\rho$ meson contribution in the Monte Carlo simulations, as discussed in the following Sec. 5.1. These uncertainties are estimated by varying the lowest $Q$ value in the fit by $\pm 10$ MeV, by changing the bin size by $\pm 10$ MeV, and by broadening the excluded interval by 100 MeV on both sides, respectively. The background of photon conversions into $e^+e^-$ pairs was studied and found to be negligible. To test the effect of treating all charged particles as pions, the double-ratio correlation functions $R_2$ are also obtained using only identical particles in the Monte Carlo sample to compute the correction. The resulting BEC parameters fitted to the $R_2$ functions defined this way show negligible differences to the nominal result and no further systematic uncertainties are assigned. The same sources of uncertainty are considered for the differential measurements in $n_{\text{ch}}$ and the average transverse momentum $k_{\text{T}}$ of a pair, and their impact on the fit parameters is found to be similar in size.

# 5   Results

## 5.1   Two-particle correlations

In Fig. 1 the double-ratio $R_2(Q)$ distributions, measured for 0.9 and 7 TeV, are compared with Gaussian and exponential fitting functions, Eqs. (8) and (9). The fits are performed in the $Q$ range 0.02 GeV to 2 GeV and with a bin width of 0.02 GeV. The upper $Q$ limit is chosen to be far away from the low-$Q$ region, which is sensitive to BEC effects and resonances. Around $Q \sim 0.7$ GeV there is a visible bump which is due to an overestimate of $\rho \to \pi^+\pi^-$ decays in the Monte Carlo simulation. Therefore the region $0.5 \leq Q \leq 0.9$ GeV is excluded from the fits. As seen in Fig. 1, the Gaussian function does not describe the low-$Q$ region while the exponential function provides a good description of the data.

The resolution of the $Q$ variable is better than 10 MeV for the region most sensitive to BEC effect, $Q < 0.4$ GeV. The $Q$ resolution is included in the fit of $R_2$ by convolving the fitting function with a Gaussian detector resolution function. The change in the fit results from those with no convolution applied is found to be negligible.

In the process of fitting $R_2(Q)$ with the exponential function, large $\chi^2$ values are observed, in particular for the 7 TeV sample where statistical uncertainties on the fitted data points are below $2-4\%$. These large $\chi^2$ values can be traced back to a small number of individual points or small cluster of points. The removal of these points does not change the results of the fit

152
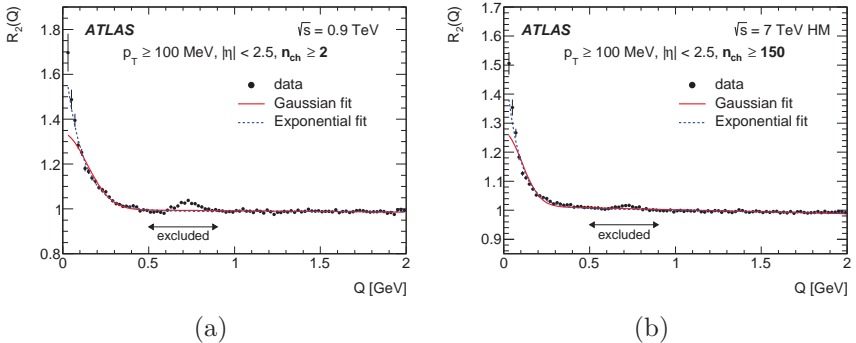
Figure 1: The two-particle double-ratio correlation function $R_2(Q)$ for charged particles in *pp* collisions at (a) $\sqrt{s} =$0.9 TeVand (b) 7 TeV high-multiplicity events. The lines show the Gaussian and exponential fits as described in the legend. The region excluded from the fits is indicated. The error bars represent the statistical uncertainties.

while the $\chi^2$ substantially improves. In the analysis of the 7 TeV data, for most of the considered cases, the expected statistical uncertainties are small compared to the systematic ones, therefore only total uncertainties on the fitted parameters are given. The latter include the statistical uncertainties rescaled by $\sqrt{\chi^2/\mathrm{ndf}}$ [22]. For consistency, the same treatment is applied to the 0.9 TeV analysis where the statistical uncertainties are of the same order of magnitude as the systematic ones.

The results of BEC parameters for exponential fits of the two-particle double-ratio correlation function $R_2(Q)$ for events with the unlike-charge reference sample are

$$\lambda = 0.74 \pm 0.11, \ R = (1.83 \pm 0.25) \text{ fm at } \sqrt{s} = 0.9 \text{ TeV for } n_{\mathrm{ch}} \geq 2,$$
$$\lambda = 0.71 \pm 0.07, \ R = (2.06 \pm 0.22) \text{ fm at } \sqrt{s} = 7 \text{ TeV for } n_{\mathrm{ch}} \geq 2,$$
$$\lambda = 0.52 \pm 0.06, \ R = (2.36 \pm 0.30) \text{ fm at } \sqrt{s} = 7 \text{ TeV for } n_{\mathrm{ch}} \geq 150.$$

The values of the fitted parameters are close to the values obtained by the CMS [23] and ALICE [24] experiments.

## 5.2   Multiplicity dependence

The multiplicity intervals are chosen so as to be similarly populated and comparable to those used by other LHC experiments [21, 23–25]. Only the exponential fit is shown. As in the fit procedure for the inclusive case, the detector $Q$ resolution is included in the fits.

Within the multiplicity studies, the BEC parameters are also measured by excluding the low-multiplicity events, $n_{\mathrm{ch}} < 8$, expected to be contaminated by diffractive physics [42]. No noticeable changes in the strength and
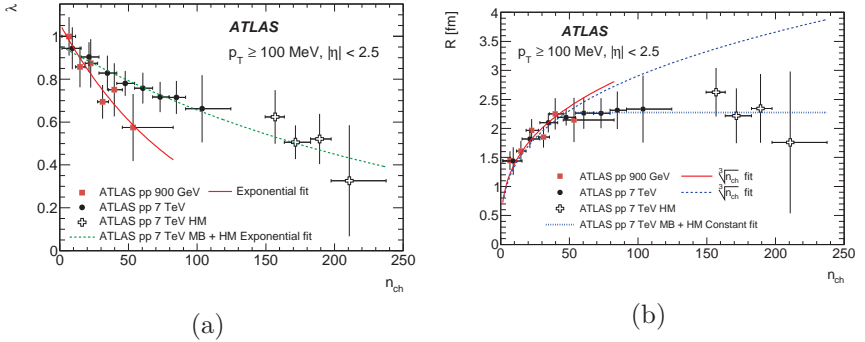
Figure 2: Multiplicity, $n_{ch}$, dependence of the parameters (a) $\lambda$ and (b) $R$ obtained from the exponential fit to the two-particle double-ratio correlation functions $R_2(Q)$ at $\sqrt{s} = 0.9$ and 7 TeV. The solid and dashed curves are the results of (a) the exponential and (b) $\sqrt[3]{n_{ch}}$ for $n_{ch} < 55$ fits. The dotted line in (b) is a result of a constant fit to minimum-bias and high-multiplicity events data at 7 TeVfor $n_{ch} \geq 55$. The error bars represent the quadratic sum of the statistical and systematic uncertainties.

radius parameters for $n_{ch} \geq 8$ are observed compared to the full multiplicity range for $n_{ch} \geq 2$.

The multiplicity dependence of the $\lambda$ and $R$ parameters is shown in Fig. 2. The $\lambda$ parameter decreases with multiplicity, faster for 0.9 TeV than for 7 TeV interactions. The decrease of the $\lambda$ parameter with $n_{ch}$ is found to be well fitted with the exponential function $\lambda(n_{ch}) = \gamma\,e^{-\delta n_{ch}}$.

The $R$ parameter increases with multiplicity up to about $n_{ch} \simeq 50$ independently of the center of mass energy. For higher multiplicities, the measured $R$ parameter is observed to be independent of multiplicity. For $n_{ch} \leq 82$ at 0.9 TeV and $n_{ch} < 55$ at 7 TeV the $n_{ch}$ dependence of $R$ is fitted with the function $R(n_{ch}) = \alpha\,\sqrt[3]{n_{ch}}$, similar to that used in heavy-ion studies [25]. The results of the fit are close to the CMS results [23]. The fit parameters do not change significantly within uncertainties if data points with $n_{ch} > 55$ are included in the fit, while the quality of the fit significantly degrades. Therefore the fit is limited to the data points with $n_{ch} \leq 55$. The $n_{ch}$ dependence of $R$ at 7 TeV is fitted with a constant $R(n_{ch}) = \beta$ for $n_{ch} > 55$. Qualitatively CMS [23] and UA1 [50] results for radius parameter follow the same trend as a function of $n_{ch}$ as ATLAS data points up to $n_{ch} \leq 55$. The ATLAS and ALICE [24, 25] results on the multiplicity dependence of the radius parameter cannot be directly compared due to much narrower $\eta$ region used by ALICE.

The observed change of the fitted parameters with multiplicity has been predicted in Refs. [7–9, 32], and is similar to the one also observed in $e^+e^-$

interactions [10], however the saturation of $R$ for very high multiplicity is observed for the first time.

The saturation of $R$ at high multiplicities is expected in a Pomeron-based model [15,16] as the consequence of the overlap of colliding protons, with the value of the radius parameter at $n_{ch} \approx 70$ close to the one obtained in the present studies. However, the same model predicts that above $n_{ch} \approx 70$, $R$ will decrease with multiplicity, returning to its low-multiplicity value which is not supported by the data.

## 5.3    Dependence on the transverse momentum

The average transverse momentum $k_T$ of a particle pair is defined as half of the magnitude of the vector sum of the two transverse momenta, $k_T = |\mathbf{p}_{T,1} + \mathbf{p}_{T,2}|/2$. The study is performed in the $k_T$ intervals which are chosen in a way to be similarly populated and, as for the multiplicity bins, to be similar to the intervals used by other LHC experiments [21, 23–25].

For the $R_2(Q)$ correlation function measured at 7 TeV, there is an indication that the Monte Carlo simulation overestimates the production and decay of the $\omega$-meson in the $Q$ region of 0.3–0.44 GeV. This region is thus excluded from the fit range for $k_T > 500$ MeV bin results.

In the region most important for the BEC parameters, the quality of the exponential fit is found to deteriorate as $k_T$ increases. This is due to the fact that at large $k_T$ values, the characteristic BEC peak becomes steeper than the exponential function can accommodate. Despite the deteriorating fit quality, the behaviour of the fitted parameters is presented for comparison with previous experiments.

The fit values of the $\lambda$ and $R$ parameters are shown in Fig. 3 as a function of $k_T$. The values of both $\lambda$ and $R$ decrease with increasing $k_T$.

The decrease of $\lambda$ with $k_T$ is well described by an exponential function, $\lambda(k_T) = \mu\, e^{-\nu k_T}$. The $k_T$ dependence of the $R$ parameter is also found to follow an exponential decrease, $R(k_T) = \xi\, e^{-\kappa k_T}$. The shapes of the $k_T$ dependence are similar for the 7 TeV and the 7 TeV high-multiplicity data.

In Fig. 3(b), the $k_T$ dependence of the $R$ parameter is compared to the measurements performed by the E735 [51] and the STAR [52] experiments with mixed-event reference samples. These earlier results were obtained from Gaussian fits to the single-ratio correlation functions and therefore the values of the measured radius parameters are multiplied by $\sqrt{\pi}$ as discussed in Sect. 2.4. The values of the parameters are observed to be energy-independent within the uncertainties.

In Fig. 4, the $k_T$ dependence of $\lambda$ and $R$, obtained for the 7 TeV data, is also studied in various multiplicity regions: $2 \leq n_{ch} \leq 9$; $10 \leq n_{ch} \leq 24$; $25 \leq n_{ch} \leq 80$; and $81 \leq n_{ch} \leq 125$. The decrease of $\lambda$ with $k_T$ is nearly independent of multiplicity for $n_{ch} > 9$ and the same as for the inclusive case. For $n_{ch} \leq 9$ no conclusions can be drawn due to the large uncertainties.

(a)  (b)
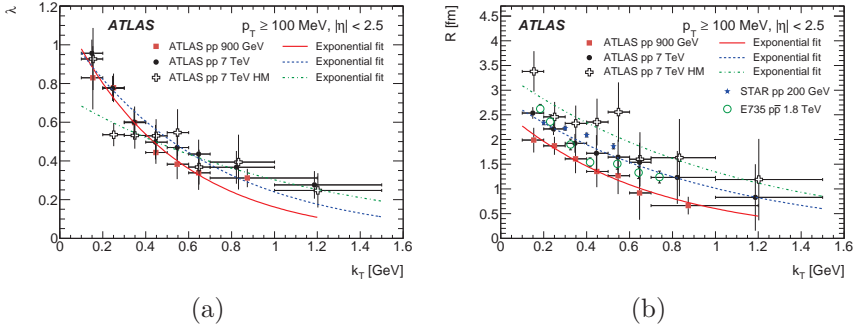
Figure 3: The $k_T$ dependence of the fitted parameters (a) $\lambda$ and (b) $R$ obtained from the exponential fit to two-particle double-ratio at $\sqrt{s}$ =0.9 TeV, 7 TeV and 7 TeV high-multiplicity events. The average transverse momentum $k_T$ of the particle pairs is defined as $k_T = |\mathbf{p}_{T,1} + \mathbf{p}_{T,2}|/2$. The solid, dashed and dash-dotted curves are results of the exponential fits for 0.9 TeV, 7 TeV and 7 TeV high-multiplicity data, respectively. The results are compared to the corresponding measurements by the E735 experiment at the Tevatron [51], and by the STAR experiment at RHIC [52]. The error bars represent the quadratic sum of the statistical and systematic uncertainties.



(a)  (b)
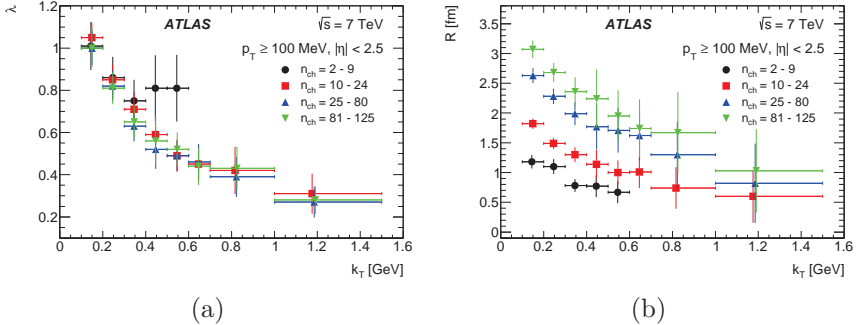
Figure 4: The $k_T$ dependence of the fitted parameters (a) $\lambda$ and (b) $R$ obtained from the exponential fit to the two-particle double-ratio correlation function $R_2(Q)$ at $\sqrt{s} = 7$ TeV for the different multiplicity regions: $2 \leq n_{ch} \leq 9$ (circles), $10 \leq n_{ch} \leq 24$ (squares), $25 \leq n_{ch} \leq 80$ (triangles) and $81 \leq n_{ch} \leq 125$ (inverted triangles). The average transverse momentum $k_T$ of the particle pairs is defined as $k_T = |\mathbf{p}_{T,1} + \mathbf{p}_{T,2}|/2$. The error bars represent the quadratic sum of the statistical and systematic uncertainties.

The $R$-parameter decreases with $k_T$ and exhibits an increase with increasing multiplicity as was observed for the fully inclusive case.

# 6    Conclusions

The two-particle Bose–Einstein correlations of like-sign hadrons with $p_T >$ 100 MeV and $|\eta| < 2.5$ produced in $pp$ collisions recorded by the ATLAS detector at 0.9 and 7 TeV at the CERN Large Hadron Collider are studied. In addition to minimum-bias data, high-multiplicity data recorded at 7 TeV using a dedicated trigger are investigated. The integrated luminosities are about 7 $\mu b^{-1}$, 190 $\mu b^{-1}$ and 12.4 nb$^{-1}$ for 0.9 TeV, 7 TeV minimum-bias and 7 TeV high-multiplicity data samples, respectively. The studies were performed using the double-ratio correlation function. In the double-ratio method, the single-ratio correlation function obtained from the data is divided by a similar single-ratio calculated using Monte Carlo events, which do not have BEC effects. The reference sample for each of the two single-ratios is constructed from unlike-sign charged-particle pairs. The BEC parameters are studied as a function of the charged-particle multiplicity and the transverse momentum of the particle pair. A decrease of the correlation strength $\lambda$ along with an increase of the correlation source size parameter $R$ are found with increasing charged-particle multiplicity. On the other hand no dependence of $R$ on the centre-of-mass energy of $pp$ collisions is observed. For the first time a saturation of the source size parameter is observed for multiplicity $n_{\mathrm{ch}} \geq 55$. The correlation strength $\lambda$ and the source size parameter $R$ are found to decrease with increasing average transverse momentum of a pair. The study of BEC in $(n_{\mathrm{ch}}, k_T)$ bins at 7 TeV shows a decrease of the $R$ parameter with $k_T$ for different multiplicity ranges, while the $R$ values increase with multiplicity. The $\lambda$ parameter is found to decrease with $k_T$ independently of the multiplicity range. These resemble the dependences for the inclusive case at 7 TeV for minimum-bias and high-multiplicity data.

# References

[1] R. Hanbury Brown and R.Q. Twiss, Phil. Mag. **45**, 663 (1954)

[2] G.I. Kopylov and M.I. Podgoretskiǐ, Sov. J. Nucl Phys. **18**, 336 (1974)

[3] E.V. Shuryak, Phys. Lett. B **44**, 387 (1973)

[4] G. Cocconi, Phys. Lett. B **49**, 459 (1974)

[5] G. Goldhaber *et al.,* Phys. Rev. **120**, 300 (1960)

[6] S. Barshay, Phys. Lett. B **130**, 220 (1983)

[7] N. Suzuki, M. Biyajima, Phys. Rev. C **60**, 034903 (1999)

[8] B. Buschbeck, H.C. Eggers, P. Lipa, Phys. Lett. B **481**, 187 (2000)

[9] G. Alexander, E.K.G. Sarkisyan, Phys. Lett. B **487**, 215 (2000)

[10] OPAL Collaboration, Z. Phys. C **72**, 389 (1996)

[11] G. Alexander, J. Phys. G **39**, 085007 (2012)

[12] Yu.M. Sinyukov, V.M. Shapoval, Phys. Rev. D **87**, 094024 (2013) [13]

V.M. Shapoval, *et al.*, Phys. Lett. B **725**, 139 (2013)

[14] Yu.M. Sinyukov, *et al.*, Adv. High Energy Phys. **2013**, 198928 (2013)

[15] V. A. Schegelsky, *et al.*, Phys. Lett. B **703**, 288 (2011)

[16] M.Ryskin, V.Schegelsky, Nucl.Phys.Proc.Suppl. **219-220**, 10 (2011) [17]

For review see: E. Shuryak, arXiv:1412.8393.

[18] ATLAS Collaboration, JINST **3**, S08003 (2008)

[19] L. Evans and P. Bryant (editors) 2008 JINST 3 S08001

[20] ATLAS Collaboration, Eur. Phys. J. C **75**, no. 10, 466 (2015)

[21] CMS Collaboration, Phys. Rev. Lett. **105**, 032001 (2010)

[22] Particle Data Group Chin. Phys. C **38**, 090001 (2014)

[23] CMS Collaboration, J. High Energy Phys. **05**, 029 (2011)

[24] ALICE Collaboration, Phys. Rev. D **82**, 052001 (2010)

[25] ALICE Collaboration, Phys. Rev. D **84**, 112004 (2011)

[26] M. Deutschmann *et al.*, Nucl. Phys. B **204**, 333 (1982)

[27] M. Gyulassy, *et al.*, Phys. Rev. C **20**, 2267 (1979)

[28] S. Pratt, Phys. Rev. D **33**, 72 (1986)

[29] I. Juricic, *et al.*, Phys. Rev. D **39**, 1 (1989)

[30] R.M. Weiner, Phys. Rep. **327**, 249 (2000)

[31] G.I. Kopylov, Phys. Lett. B **50**, 472 (1974)

[32] W. Kittel and E.A. De Wolf, *Soft Multihadron Dynamics* (World Scientific, Singapore, 2005)

[33] P. Grassberger, Nucl. Phys. B **120**, 231 (1977)

[34] M. Gyulassy and S. S. Padula, Phys. Lett. B **217**, 181 (1989)

[35] S. S. Padula and M. Gyulassy, Nucl. Phys. A **498**, 555C (1989)

[36] K. Kulka and B. Lörstad, Z. Phys. C **45**, 581 (1990)

[37] M.G Bowler, Z. Phys. C **46**, 305 (1990)

[38] R. Lednický and T.B. Progulova, Z. Phys. C **55**, 295 (1992)

[39] S.S. Padula and M. Gyulassy, Nucl. Phys. A **544**, 537c (1992)

[40] ATLAS Collaboration, ATLAS-LARG-PUB-2008-002 (2008).

[41] ATLAS Collaboration, Phys. Lett. B **688**, 21 (2010)

[42] ATLAS Collaboration, New J. Phys. **13**, 053033 (2011)

[43] G. Piacquadio, *et al.*, J. Phys. Conf. Ser. **119**, 032033 (2008)

[44] ATLAS Collaboration, ATLAS-CONF-2010-027 (2010)

[45] T. Sjöstrand, *et al.*, J. High Energy Phys. **05**, 026 (2006)

[46] ATLAS Collaboration, ATL-PHYS-PUB-2010-002 (2010).

[47] ATLAS Collaboration, Eur. Phys. J. C **70**, 823 (2010)

[48] GEANT4 Collaboration, Nucl. Instrum. Methods A **506**, 250 (2002)

[49] G. D' Agostini, Nucl. Instr. Meth. A **362**, 487 (1995)

[50] UA1 Collaboration, Phys. Lett. B **226**, 410 (1989)

[51] T. Alexopoulos *et al.*, Phys. Rev. D **48**, 1931 (1993)

[52] STAR Collaboration, Phys. Rev. C **83**, 064905 (2011)

# SECTION "ADVANCES IN THEORETICAL PHYSICS"

# Near-mass-shell form factor $f_-$ of the pion $\beta$-decay

M. I. Krivoruchenko[a,b,c]

[a]Institute for Theoretical and Experimental Physics
B. Cheremushkinskaya 25, 117218 Moscow, Russia
[b]Moscow Institute of Physics and Technology
141700 Dolgoprudny, Russia
[c]Bogoliubov Laboratory of Theoretical Physics, JINR
141980 Dubna, Russia

## Abstract

The generalized Ward-Takahashi identity (gWTI) in the pion sector for broken isotopic symmetry is derived and used for the model-independent estimate of the longitudinal form factor $f_-$ of the $\pi_{e3}$ weak vector vertex. The on-shell $f_-$ is found to be proportional to the mass difference of the pions and the difference between the vector isospin $T = 1$ and scalar isospin $T = 2$ pion radii. Off-shell form factors are in general ambiguous because of the gauge dependence and the freedom in the parameterization of the fields. The near-mass-shell $f_-$ appears to be an exception, allowing for experimental verification of the consequences of the gWTI. We calculate the near-mass-shell $f_-$ using the gWTI and dispersion techniques. The results are discussed in the context of the conservation of vector current (CVC) hypothesis.

## 1. Introduction

The pion $\beta$-decay decay ($\pi_{e3}$) is one of the main semileptonic electroweak processes. The vector nature of the transition, its simple kinematics, and the precise measurement of the partial width make this decay particularly attractive for testing the Standard Model.

Radiative corrections and pion structure effects in the $\pi_{e3}$ decay have been calculated with high accuracy [1-4], sufficient for verification of the unitarity of the CKM matrix. The experimental data, however, are not yet sufficiently precise for this purpose. Measurements of the $\pi_{e3}$ decay are also motivated by the possibility of testing the conservation of vector current (CVC) in the meson sector.

The CVC hypothesis [5-7] suggests that the isovector component of the electromagnetic current and the charged components of the weak vector current belong to the same isospin triplet. In the limit of exact isotopic symmetry, conservation of the electromagnetic current implies conservation of the weak vector current.

Off the mass shell, the CVC is equivalent to the Ward-Takahashi identity (WTI) for the isospin $SU(2)$ group. The WTI, however, is of greater generality and leads to useful relationships between off-shell form factors, including those that vanish when some of the external legs are on shell. The violation of isotopic

symmetry, associated with the small mass difference between the up and down quarks and the electromagnetic and weak interactions, results in the non-conservation of the charge-changing components of the weak vector current. For the broken symmetry, the CVC condition and the WTI are replaced by partial CVC and the generalized WTI (gWTI), which are especially sensitive to the pattern of isotopic symmetry breaking.

The parameterization of the degrees of freedom associated with the pion field can be performed in various ways, which produces off-shell ambiguity in the amplitudes. The on-shell form factors are related to the asymptotic states and are uniquely defined. This statement is known as the equivalence theorem (ET) [8-10]. The off-shell form factors depend on this parameterization and cannot be measured experimentally [11-12].

A notable exception to this rule is established in Ref. [13]. The longitudinal part of the $\pi_{e3}$ vertex appears to be uniquely defined near the mass shell and accessible to measurements. As an application of the gWTI, we derive a model-independent expression for the longitudinal form factor $f_-$ and provide its numerical estimate.

## 2. $U(1)$ vector vertex

The on-shell conserved vector current of a charged scalar particle ($\pi^+$) is determined by one form factor. Off the mass shell, there are two form factors. In the most general case, the current can be written as follows

$$\Gamma_\mu(p^{'}, p) = (p^{'} + p)_\mu \mathcal{F}_1 + q_\mu (p^{'2} - p^2)\mathcal{F}_2, \tag{1}$$

where $q = p^{'} - p$ is the momentum transfer. The form factors $\mathcal{F}_i$ are symmetric functions of $p^{'2}$ and $p^2$ and arbitrary functions of $q^2$ and the physical mass $m$ of the charged pion. The factor $p^{'2} - p^2$ in the second term is added to ensure the negative $C$ parity of the vertex. The decomposition (1) arises e.g., in the scalar quantum electrodynamics. The WTI of the $U(1)$ symmetry group establishes a relationship between $\mathcal{F}_1$ and $\mathcal{F}_2$:

$$q^2 \mathcal{F}_2(p^{'2}, p^2, q^2) = \frac{\Delta^{-1}(p^{'}) - \Delta^{-1}(p)}{p^{'2} - p^2} - \mathcal{F}_1(p^{'2}, p^2, q^2), \tag{2}$$

where $\Delta(p) = p^2 - m^2 - \Sigma(p^2, m)$ is the renormalized pion propagator, $\Sigma(p^2, m)$ is the self-energy operator. In the limit $p^{'2} = p^2 = m^2$, we obtain

$$\mathcal{F}_2(m^2, m^2, q^2) = \frac{1 - \mathcal{F}_1(m^2, m^2, q^2)}{q^2}.$$

In the vicinity of $q^2 = 0$, the form factor $\mathcal{F}_1$ can be expanded to give

164

$$\mathcal{F}_2(m^2, m^2, 0) = -\frac{1}{6}\left\langle r^2 \right\rangle_v,$$

where $\left\langle r^2 \right\rangle_v$ is the vector charge radius of $\pi^+$.

The equivalence of the Coulomb and Lorentz gauges in QED was rigorously proved by Bialynicki-Birula [14]. On shell, the amplitudes are gauge-invariant, whereas the off-shell dependence on the gauge persists. $\mathcal{F}_1$ and $\mathcal{F}_2$ are thus uniquely defined, when both legs of the charged pion are on the mass shell. To first order in the displacement from the mass shell, the longitudinal component of the vertex is also gauge invariant, as is evident from Eq. (1).

$\mathcal{F}_2$ with two on-shell legs $p'^2 = p^2 = m^2$ does not contribute to the current. Off the mass shell, however, $\mathcal{F}_2$ does contribute, and its contribution is uniquely determined by the WTI. Isotopic rotation of $\mathcal{F}_2$ is not sufficient to obtain a full weak-interaction vertex. We show that the violation of isotopic symmetry generates an isospin $T = 2$ contribution that is unrelated to isotopic rotation.

### 3. *SU*(2) vector vertex

The *SU*(2) vector vertex expansion in scalar functions $\mathcal{F}_{i\pm}^a(p'^2, p^2, q^2)$ that are symmetric in $p'^2$ and $p^2$ takes the form

$$\Gamma_\mu^a(p', p) = (p' + p)_\mu \left( \mathcal{F}_{1-}^a + (p'^2 - p^2)\mathcal{F}_{1+}^a \right) \\ + q_\mu \left( (p'^2 - p^2)\mathcal{F}_{2-}^a + \mathcal{F}_{2+}^a \right), \tag{3}$$

The lower index $\pm$ indicates the symmetry with respect to permutation of the isospin indices: $\tilde{\mathcal{F}}_{i\pm}^a = \pm \mathcal{F}_{i\pm}^a$.

If there were no isospin symmetry breaking, we could have $\mathcal{F}_{i-}^a = T^a \mathcal{F}_{i-}$, as there are no other $SU(2)$ generators, and $\mathcal{F}_{i+}^a = 0$, implying that $\Gamma_\mu^a(m^2, m^2, q^2) \propto T^a$.

In order to find relationships for $\mathcal{F}_{i\pm}^a(p'^2, p^2, q^2)$, we derive a generalization of the WTI associated with the replacement of the exact $U(1)$ symmetry by the broken $SU(2)$ symmetry. Using the gWTI gives

$$\mathcal{F}_{2+}^a(m^2, m^2, q^2) = [m^2 + \Sigma(m^2), T^a]\frac{1/D_J^{T=2}(q^2) - 1}{q^2}, \tag{4}$$

$$\mathcal{F}_{2-}^a(m^2, m^2, q^2) = T^a \frac{1 - \mathcal{F}_{1-}(m^2, m^2, q^2)}{q^2}. \tag{5}$$

As a consequence of elastic unitarity and analyticity, the $q^2$ dependence of the on-mass-shell form factor $\mathcal{F}_{2+}^a$ is determined by the Jost function

$$D_J^T(s) = \exp(-\frac{s}{\pi} \int_{4m^2}^{+\infty} \frac{\delta^T(s')ds'}{s'(s'-s)}),$$ (6)

that can be constructed in terms of the phase shift in the corresponding channel; here, the $S$-wave $T = 2$ channel of the pion-pion scattering is relevant.

The on-shell weak vector current is usually parameterized in the form

$$\langle \pi^0(p') | \bar{d}\gamma_\mu(1-\gamma_5)u | \pi^+(p) \rangle = \sqrt{2}((p'+p)_\mu f_+ + q_\mu f_-),$$ (7)

where $q_\mu = (p'-p)_\mu$.

The exact CVC condition implies

$$f_- = 0.$$ (8)

Partial CVC yields

$$f_- = \frac{m_{\pi^+}^2 - m_{\pi^0}^2}{6} \left( \langle r^2 \rangle_v^{T=1} - \langle r^2 \rangle_s^{T=2} \right).$$ (9)

The isovector radius squared is determined by the electromagnetic form factor of the charged pion, whereas the isotensor one can be found from the low-$q^2$ expansion of the Lorentz scalar $\pi^+\pi^0$ transition form factor. Remarkably, for a dressed vertex, the $W^\pm$ boson, being a member of the weak isospin triplet, is coupled to both the strong isospin triplet and the strong isospin quintet.

The WTI of exact symmetry implies, to first order in the displacement $p'^2 - p^2$ and for low momentum transfers,

$$f_- = -\frac{p'^2 - p^2}{6} \langle r^2 \rangle_v^{T=1}.$$ (10)

The WTI of broken symmetry implies, to first order in $\Delta m_\pi^2 = m_{\pi^0}^2 - m_{\pi^+}^2$ and the displacement $p'^2 - p^2$ and for low momentum transfers,

$$f_- = -\frac{p'^2 - p^2}{6} \langle r^2 \rangle_v^{T=1} + \frac{m_{\pi^0}^2 - m_{\pi^+}^2}{6} \langle r^2 \rangle_s^{T=2}.$$ (11)

The on-shell form factor $\mathcal{F}_{1-}^a$ is independent of both the gauge and the parameterization. By virtue of Eqs. (4) and (5), the on-shell form factors $\mathcal{F}_{2\pm}^a$ are also uniquely defined. The longitudinal component of the vertex ((3)) contains the factor $p'^2 - p^2$ in $\mathcal{F}_{2-}^a$, whereas $\mathcal{F}_{2+}^a$ has smallness of $O(\Delta m_\pi^2)$. We thus conclude that the longitudinal component of $\Gamma_\mu^a(p', p)$ is uniquely defined in

the neighborhood of the mass shell to first order in the pion mass splitting and the displacement $p'^2 - p^2$. In the neighborhood of the mass shell, the longitudinal form factor $f_-$ escapes the general rule [8-13] that states that off-shell amplitudes are ambiguous.

The results obtained for the near-mass-shell representation of $f_-$ in terms of the physical masses and radii of the pions exhibit explicit independence on the gauge and the parameterization of the pion field.

The generality of the relationships (9) and (11) is influenced by only the CVC condition at a bare interaction vertex. This condition is satisfied in the Standard Model, so any violation of these relationships can be interpreted as an indication for new physics at or above the electroweak scale.

## 4. Numerical estimates

Experimental value of the $\pi^+$ charge radius equals [15]

$$\langle r^2 \rangle_v^{T=1} = (0.672 \pm 0.008\,\text{fm})^2 .$$

We employ the dispersion techniques for numerical estimation of the pion radius $\langle r^2 \rangle_s^{T=2}$, entering the equations (9) and (11). Expanding the Jost function in the vicinity of $s = 0$, we obtain

$$\langle r^2 \rangle_s^T = \frac{6}{\pi} \int_{4m^2}^{+\infty} \frac{\delta^T(s')}{s'^2}\, ds' . \tag{12}$$

The phase shifts between the experimental points of Refs. [15-17] are interpolated linearly. We obtain the value

$$\langle r^2 \rangle_s^{T=2} = -0.10 \pm 0.05\,\text{fm}^2$$

and, with the help of Eq. (9),

$$f_- = (2.97 \pm 0.25) \times 10^{-3}. \tag{13}$$

This result is a factor of two greater than the light-front quark model prediction [3].

Contribution of the longitudinal form factor to the pion $\beta$-decay rate can be estimated to give $\Delta B / B = -0.94 \times 10^{-3} f_-$; the additional small factor in $f_-$ arises for kinematic reasons. The experimental error in $B$ is 0.6% [15]. We thus reaffirm earlier conclusions that $f_-$ is currently beyond the capabilities of the experimental study. The possibility of measuring the longitudinal weak vector current in the neutron $\beta$-decay [19], muon capture [20] and in the $\tau^- \to \pi^- \pi^0 \nu_\tau$ and $\tau^- \to K^- K^0 \nu_\tau$ decays could be more promising.

## 5. Conclusion

A generalization of the WTI was derived in the pion sector to account for the isotopic symmetry breaking. It was shown that the isovector $T = 1$ part of the

current can be reconstructed through isotopic rotation of the off-shell pion electromagnetic form factors, whereas the isotensor $T = 2$ part has no analogs but rather is uniquely determined by the gWTI combined with the elastic unitarity, analyticity, and the pion-pion scattering data.

The various versions of the CVC condition are distinguished depending on whether the isotopic symmetry is exact or broken and whether the outer legs in the vertex are on or off shell. The corresponding predictions for the longitudinal form factor $f_-$ are given in Eqs. (8), (9), (10), and (11). In the case of the exact isotopic symmetry, the bare and dressed weak vertices are pure isospin triplets; the CVC and the WTI hold on and off shell, respectively. In the case of the broken isotopic symmetry, the dressed weak vertex is no longer a pure isospin triplet; partial CVC and the gWTI hold on and off shell.

To first order in the pion mass splitting and the displacement from the mass shell, the longitudinal component is independent of both the gauge and the parameterization, and therefore, the near-mass-shell form factor $f_-$ appears to be a unique object whose properties are unambiguously determined by the partial CVC condition (the gWTI).

### References

[1] A. Sirlin, Rev. Mod. Phys. **50** (1978) 573 [Erratum ibid. **50** (1978) 905].
[2] V. Cirigliano, M. Knecht, H. Neufeld, H. Pichl, Eur. Phys. J. C **27** (2003) 255.
[3] W. Jaus, Phys. Rev. D **60** (1999) 054026.
[4] W. Jaus, Phys. Rev. D **63** (2001) 053009.
[5] S. S. Gerstein and Ya. B. Zeldovich, ZhETF **29** (1955) 698 [in Russian].
[6] S. S. Gerstein and Ya. B. Zeldovich, Sov. JETP **2** (1956) 576.
[7] R. P. Feynman, M. Gell-Mann, Phys. Rev. **109**, 193 (1958).
[8] R. Haag, Phys. Rev. **112** (1958) 669.
[9] J. S. R. Chisholm, Nucl. Phys. **26** (1961) 469.
[10] S. Kamefuchi, L. O'Raifeartaigh, and A. Salam, Nucl. Phys. **28** (1961) 529.
[11] H. W. Fearing, Few-Body Syst. Suppl. **12** (2000) 263.
[12] H. W. Fearing, S. Scherer, Phys. Rev. C **62** (2000) 034003.
[13] M. I. Krivoruchenko, Adv. High Energy Phys. **2015** (2015) 656239.
[14] I. Bialynicki-Birula, Phys. Rev. D **12** (1970) 2877.
[15] K. A. Olive et al. (Particle Data Group), Chin. Phys. C **38** (2014) 090001.
[16] D. Cohen, T. Ferbel, P. Slattery, and B. Werner, Phys. Rev. D **7** (1973) 661.
[17] N. B. Durusoy et al., Phys. Lett. B **45** (1973) 517.
[18] W. Hoogland et al., Nucl. Phys. B **126** (1977) 109.
[19] H. Abele, Prog. Part. Nucl. Phys. **60** (2008) 1.
[20] D. Gazit, Phys. Lett. B **666** (2008) 472.

# Left-left squark mixing in the $K^+ \to \pi^+ \nu\bar{\nu}$ decay

Tomáš Blažek[*] and Peter Maták[†]

*Comenius University in Bratislava, Slovak Republic*

### Abstract

We study the effects of supersymmetry with non-minimal flavor violation in the rare kaon decay, $K^+ \to \pi^+ \nu\bar{\nu}$. Focusing on the role of the left-left mass matrix elements of the up type squarks we perform the numerical scan through the MSSM parameter space. We demonstrate that in case of the large stop trilinear couplings the observable deviations from the standard model branching ratio are still possible. This study extends our earlier analyses and provides new updated results.

## 1   Introduction

In the standard model effective theory, there is only one dimension-six effective operator,

$$\mathscr{O}_L = (\bar{s}\gamma^\mu P_L d)(\bar{\nu}_l \gamma_\mu P_L \nu_l), \tag{1}$$

contributing to the amplitude of $K^+ \to \pi^+ \nu\bar{\nu}$. New physics in general introduces $\mathscr{O}_R$ with the right-handed quarks in the first bilinear. Then, the short-distance effects are represented by the effective Lagrangian [1–3]

$$\mathscr{L}_{\text{s.d.}} = \frac{4G_F}{\sqrt{2}} \frac{\alpha}{2\pi \sin^2 \theta_W} \sum_{l=e,\mu,\tau} (X_L \mathscr{O}_L + X_R \mathscr{O}_R). \tag{2}$$

With the approximate isospin symmetry, the non-perturbative matrix elements of this operator can be extracted from the tree-level $K^+ \to \pi^0 e^+ \nu_e$ decay [4]. The precise way in which the Wilson coefficients $X_{L,R}$ enter the branching ratio is straightforward and can be found in Ref. 5, where further references are given. In the following we are only interested in a way in which new physics, supersymmetry in particular, modifies the value of $X = X_L + X_R$.

---

[*]blazek@fmph.uniba.sk

[†]peter.matak@fmph.uniba.sk

For the standard model case, this quantity has been calculated, including NLO QCD [6] and two-loop electroweak [7] corrections, leading to $X_{SM} = 1.481 \pm 0.005_{\text{th.}} \pm 0.008_{\text{exp.}}$ [5] and the branching ratio [5]

$$\mathscr{B}(K^+ \rightarrow \pi^+ \nu \bar{\nu})_{\text{SM}} = (7.62^{+0.69}_{-0.70}) \times 10^{-11}. \tag{3}$$

On the experimental side, the value measured by E-787, E-949 at Brookhaven equals [8, 9]

$$\mathscr{B}(K^+ \rightarrow \pi^+ \nu \bar{\nu})_{\text{exp.}} = (1.73^{+1.15}_{-1.05}) \times 10^{-10}. \tag{4}$$

The NA62 experiment at CERN started taking data recently and is expected to improve the measured branching fraction aiming at a 10% uncertainty of the standard model value. Almost any new physics containing flavored degrees of freedom, if discovered at the LHC, will be effectively constrained by Flavor Changing Neutral Currents (FCNC), among which the $K^+ \rightarrow \pi^+ \nu \bar{\nu}$ decay plays a very important role.

## 2 Supersymmetry in charged kaon decay

Supersymmetry affects the FCNC amplitudes in two different ways. First, even in the minimal model, it increases the number of flavor changing loops containing contributions of the scalar partners and additional Higgs bosons. After the quark fields are rotated to their mass eigenstates, the CKM factors appear in the vertices of new particles, contributing to the flavor changing amplitudes in a similar way, as it is in the standard model.

However, quark and squark mass matrices are not necessarily flavor-diagonal in the same basis. By rotating scalars in the same way as their standard model counterparts we obtain the so-called super-CKM basis. The complete squark mass matrices have the general form

$$\mathscr{M}_{\tilde{q}}^2 = \begin{pmatrix} \mathscr{M}_{\tilde{q},LL}^2 & \mathscr{M}_{\tilde{q},LR}^2 \\ \mathscr{M}_{\tilde{q},RL}^2 & \mathscr{M}_{\tilde{q},RR}^2 \end{pmatrix}, \tag{5}$$

where each block represents $3 \times 3$ matrix in the family space. We keep in mind that left-handed up- and down-type squarks come from the same isospin doublet and therefore, their left-left blocks cannot be independent. Instead, they are subject to following constraints

$$\mathscr{M}_{\tilde{u},LL}^2 = V_{CKM} \mathscr{M}_{\tilde{d},LL}^2 V_{CKM}^{\dagger}. \tag{6}$$

According to the standard notation, we introduce dimensionless parameters originating in general flavor structure of the soft supersymmetry breaking terms,

$$\delta_{\tilde{q}XY}^{ij} = \frac{(\mathscr{M}_{\tilde{q},XY}^2)^{ij}}{\sqrt{(\mathscr{M}_{\tilde{q},XX}^2)^{ii}(\mathscr{M}_{\tilde{q},YY}^2)^{jj}}}, \tag{7}$$
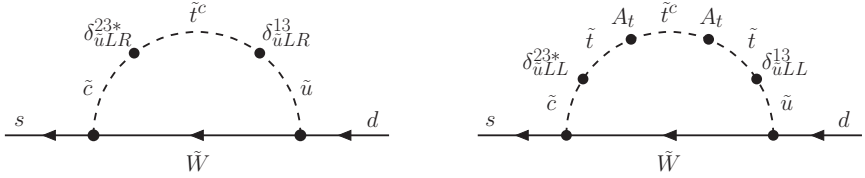
Figure 1: Chargino and stop contribution to the kaon decay amplitude in the mass insertion approximation [1, 16]. The loops represent the entire group of diagrams, in which $Z^0$ propagator connects to any of the stop, chargino, or quark line.

| | |
|---|---|
| $\|V_{us}\| = 0.2253 \pm 0.0008$ [17] | $\|V_{ub}\| = (3.28 \pm 0.29) \times 10^{-3}$ [18] |
| $\|V_{cb}\| = (38.94 \pm 0.76) \times 10^{-3}$ [18] | $\gamma = (73.2^{+6.3}_{-7.0})^\circ$, [19] |
| $\mathscr{B}(B \to X_s\gamma) = (3.12 \pm 0.23) \times 10^{-4}$ [20] | $\varepsilon_K = (2.23 \pm 0.25) \times 10^{-3}$ [5, 17] |
| $\mathscr{B}(B^0 \to \mu\mu) = (3.9 \pm 1.6) \times 10^{-10}$ [18] | $\Delta M_d = 0.506 \pm 0.090$ ps$^{-1}$ [18] |
| $\mathscr{B}(B^0_s \to \mu\mu) = (3.1 \pm 0.5) \times 10^{-9}$ [18] | $\Delta M_s = 17.757 \pm 2.37$ ps$^{-1}$ [18] |

Table 1: The flavor changing constraints used in the numerical analysis. The values of the $|V_{ub}|$ and $|V_{cb}|$ CKM elements come from the exclusive measurement of $\bar{B} \to \pi l^- \bar{\nu}$ and $\bar{B} \to D^* l^- \bar{\nu}$ decays, respectively [18].

with $i \neq j$ being flavor indices, while $X$, $Y$ equals $L$ or $R$ denoting scalar partners of quarks with different chiralities. Hermiticity of 5 requires $\delta_{\tilde{q},RL} = \delta_{\tilde{q},LR}^\dagger$.

In the literature the dependence of the kaon decay amplitude on the $\delta_{\tilde{u},RL}$ has been investigated in a detail [1, 10–13]. However, this mass insertions are constrained by the vacuum stability bounds [14, 15] and for the current limits on the stop and chargino masses their effects are rather limited. Instead, as we suggested in our previous analysis [16], for the large values of the soft supersymmetry breaking stop trilinear coupling $A_t$, motivated by the observed value of the Higgs mass, the non-negligible effect may come from the left-left block of the squark mass matrix 5. In the mass insertion approximation, this contribution can be represented by the second loop diagram in Figure 1.

For our numerical analysis publicly available program SUSY_FLAVOR 2.54 [21–23] has been used. The CKM parameters as well as the experimental constraints that we have taken into account are listed in table 1. Regarding the supersymmetric parameters, we used the unification condition for gaugino masses, $M_2 = 700$ GeV and $M_3 = 3000$ GeV. Such a heavy gluinos make the gluino loops almost irrelevant for the kaon decay itself. On the other hand, the constraints coming from meson mixing processes are partialy reduced. Higgsino mass has been fixed at $\mu = 700$ GeV, while the diagonal squark soft masses were $m_{\tilde{Q}} = m_{\tilde{q}} = 1.3$ TeV. We have performed numerical scan through the values $\tan\beta \in \langle 3,7 \rangle$ and $|A_t| \in \langle 2.5, 3.5 \rangle$ TeV. Finally, the left-left mass squark insertions

171
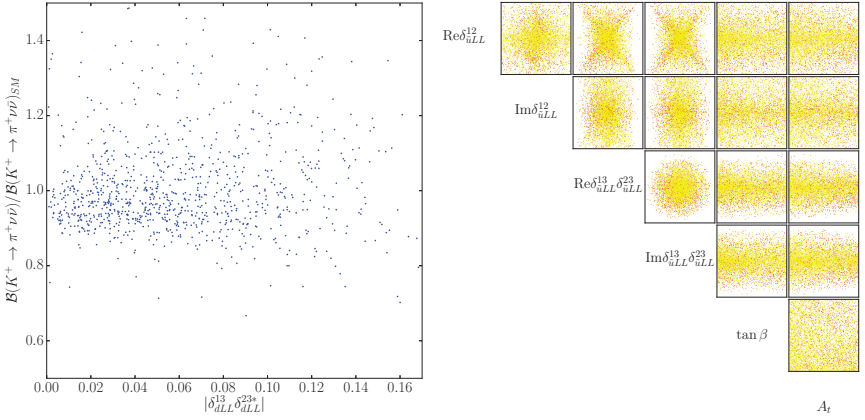
Figure 2: Left: the ratio of the calculated decay rate over the standard model prediction for the $K^+ \to \pi^+ \nu \bar{\nu}$ decay and its dependence on the $\delta_{\tilde{u}LL}^{13} \delta_{\tilde{u}LL}^{23*}$. Right: deviations of the kaon decay branching ratio from the standard model prediction. Light-yellow points correspond to difference smaller than 10%, orange points within $10\% - 20\%$ and red points to more than 20%.

were varied within $\delta_{\tilde{u}LL}^{ij} \in \langle -0.4, 0.4 \rangle$. The results of this analysis are depicted in Figure 2. It is clearly visible in the right plot that the decay branching ratio is particularly sensitive to the combination $\delta_{\tilde{u}LL}^{13} \delta_{\tilde{u}LL}^{23*}$. This dependence is shown in the left plot were one can note that few points exceed the deviations of 30% from the standard model expectation. Although such an effect could be observed at the ongoing NA62 experiment, we note that for these points significant amount of tuning is required to overcome the experimental constraints from the other processes listed in Table 1.

# 3    Conclusions

We conclude that for the rare kaon decay, $K^+ \to \pi^+ \nu \bar{\nu}$, measurable effects can be induced by non-zero values of the left-left squark mass insertions. We emphasize the sensitivity of the branching ratio to the combination $\delta_{\tilde{u}LL}^{13} \delta_{\tilde{u}LL}^{23*}$, that can be more significant than the left-right insertions. The latter were found important in earlier studies. Even though larger effects require fine tuning to overcome the other flavor changing constraints, understanding the sensitivity of the decay remains important. This is especially true in the case of direct discovery of squarks at the LHC. In that case, processes constraining their mass matrices will be important and rare kaon decays may turn out to be very useful.

# References

[1] G. Colangelo and G. Isidori. Supersymmetric contributions to rare kaon decays: Beyond the single mass insertion approximation. *JHEP*, 9809:009, 1998.

[2] Gino Isidori and Paride Paradisi. Higgs-mediated $K^+ \to \pi^+ \nu \bar{\nu}$ in the MSSM at large tan(beta). *Phys.Rev.*, D73:055017, 2006.

[3] Andrzej J. Buras. Weak Hamiltonian, CP violation and rare decays. pages 281–539, 1998.

[4] M.K. Gaillard and Benjamin W. Lee. Rare Decay Modes of the K-Mesons in Gauge Theories. *Phys.Rev.*, D10:897, 1974.

[5] Andrzej J. Buras, Dario Buttazzo, Jennifer Girrbach-Noe, and Robert Knegjens. $K^+ \to \pi^+ \nu \bar{\nu}$ and $K_L \to \pi^0 \nu \bar{\nu}$ in the Standard Model: status and perspectives. *JHEP*, 11:033, 2015.

[6] Andrzet J. Buras, Felix Schwab, and Selma Uhlig. Waiting for precise measurements of $K^+ \to \pi^+ \nu \bar{\nu}$ and $K_L \to \pi^0 \nu \bar{\nu}$. *Rev.Mod.Phys.*, 80:965–1007, 2008.

[7] Joachim Brod, Martin Gorbahn, and Emmanuel Stamou. Two-Loop Electroweak Corrections for the $K \to \pi \nu \bar{\nu}$ Decays. *Phys. Rev.*, D83:034030, 2011.

[8] S. Adler et al. Further search for the decay $K^+ \to \pi^+ \nu \bar{\nu}$. *Phys.Rev.Lett.*, 84:3768–3770, 2000.

[9] V.V. Anisimovsky et al. Improved measurement of the $K^+ \to \pi^+ \nu \bar{\nu}$ branching ratio. *Phys.Rev.Lett.*, 93:031801, 2004.

[10] Andrzej J. Buras, Andrea Romanino, and Luca Silvestrini. $K \to \pi \nu \bar{\nu}$: A Model independent analysis and supersymmetry. *Nucl.Phys.*, B520:3–30, 1998.

[11] Andrzej J. Buras, Thorsten Ewerth, Sebastian Jager, and Janusz Rosiek. $K^+ \to \pi^+ \nu \bar{\nu}$ and $K_L \to \pi^0 \nu \bar{\nu}$ decays in the general MSSM. *Nucl.Phys.*, B714:103–136, 2005.

[12] Yosef Nir and Mihir P. Worah. Probing the flavor and CP structure of supersymmetric models with $K \to \pi \nu \bar{\nu}$ decays. *Phys.Lett.*, B423:319–326, 1998.

[13] Gino Isidori, Federico Mescia, Paride Paradisi, Christopher Smith, and Stephanie Trine. Exploring the flavour structure of the MSSM with rare K decays. *JHEP*, 0608:064, 2006.

[14] Sebastian Jager. Supersymmetry beyond minimal flavour violation. *Eur.Phys.J.*, C59:497–520, 2009.

[15] J.A. Casas and S. Dimopoulos. Stability bounds on flavor violating trilinear soft terms in the MSSM. *Phys.Lett.*, B387:107–112, 1996.

[16] Tomáš Blažek and Peter Maták. Left-left squark mixing, $K^+ \rightarrow \pi^+ \nu \bar{\nu}$ and minimal supersymmetry with large $\tan\beta$. *Int. J. Mod. Phys.*, A29(27):1450162, 2014.

[17] K. A. Olive et al. *Chin. Phys.*, C38:090001, 2014.

[18] Y. Amhis et al. 2014.

[19] J. Charles et al. *Phys. Rev.*, D91(7):073007, 2015.

[20] A. Abdesselam et al. In *38th International Conference on High Energy Physics (ICHEP 2016) Chicago, IL, USA, August 03-10, 2016*, 2016.

[21] Janusz Rosiek. SUSY FLAVOR v2.5: a computational tool for FCNC and CP-violating processes in the MSSM. *Comput. Phys. Commun.*, 188:208–210, 2014.

[22] A. Crivellin, J. Rosiek, P. H. Chankowski, A. Dedes, S. Jaeger, and P. Tanedo. SUSY_FLAVOR v2: A Computational tool for FCNC and CP-violating processes in the MSSM. *Comput. Phys. Commun.*, 184:1004–1032, 2013.

[23] Janusz Rosiek, Piotr Chankowski, Athanasios Dedes, Sebastian Jager, and Philip Tanedo. SUSY_FLAVOR: A Computational Tool for FCNC and CP-violating Processes in the MSSM. *Comput. Phys. Commun.*, 181:2180–2205, 2010.

# Rare decays of heavy mesons in covariant confined quark model

S. Dubnička[1], A. Z. Dubničková[2], M. A. Ivanov[3], A. Liptaj[1]

[1]Institute of Physics, Slovak Academy of Sciences, Dúbravská cesta 9, 84511 Bratislava 45, Slovak Republic

[2]Department of Theoretical Physics, Faculty of Mathematics, Physics and Informatics, Comenius University, Mlynská dolina, 84248 Bratislava, Slovak Republic

[3]Bogoliubov Laboratory of Theoretical Physics, Joint Institute for Nuclear Research, 141980 Dubna, Russia

## Abstract

In this text we present the covariant confined quark model together with its basic features: the so-called compositeness condition and the infrared cutoff generating the quark confinement. The model is applied to two chosen rare heavy meson decays $B \to K^* \mu \mu$ and $B_s \to \Phi \mu \mu$: we compute several observables and present the results in form of graphs and tables.

## 1 Introduction

Rare heavy meson decays are suitable test field for possible manifestations of new physics: hypothetical new particles could contribute into loops of the corresponding Feynman diagrams and modify accordingly the whole decay process. Nowadays these reactions attract a lot of attention because they become accessible experimentally and several types of these decays were measured, some even with the angular information.

From the theory point of view, one usually focuses on the weak decay process which can be computed within the Standard Model and compares the calculations with the observations. However, the theoretical prediction is influenced by the way the hadronic contributions are treated and, for the moment, we do not know how to compute them from first principles. A model-dependent approach is therefore usually adopted and the results may by affected followingly. To suppress the model influence one often looks for observables with low form factor dependence and good sensitivity to weak physics (Wilson coefficients). But even in that case, the hadronic effects cannot by completely neglected.

Up to now, the theoretical evaluations did not confirm a presence of new physics phenomena, but for some observables and phase space regions the tensions between the theory and the experiment reach up to $3\sigma$. It is therefore suitable to cross-check existing theoretical predictions with an independent model of hadronic corrections.

The covariant confined quark model treats the hadronic effects by introducing a quark-hadron vertex via an appropriate interaction Lagrangian. The latter provides the model with full Lorentz invariance and also allows for standard computational techniques known from the quantum field theory. The role of quarks and hadrons is defined by the so-called compositeness condition, which reflects the fact, that, in nature, hadrons are made of quarks. To prevent decays of very heavy hadrons into their constituent quarks a universal infrared cutoff is introduced. The model is non-local and based only on quarks: it is assumed the effect of gluons is properly absorbed into the structure of the model itself (its vertex function, free parameters). The number of free parameters remains limited: the total of five "global" model parameters (4 constituent quark masses and one infrared cutoff) should be augmented by one free parameter for each hadron appearing in the reaction.

We apply the model preferably to heavy hadrons, since for light hadrons concurrency approaches will smaller model dependence are available (ChPT).

# 2 Model

## 2.1 Lagrangian for mesons

In the interaction Lagrangian a meson field is multiplied by a quark current

$$\mathscr{L}_{\text{int}} = g_M \cdot M(x) \cdot J_M(x),$$

where the coupling $g_M$ characterizes the interaction strength. The current is build such as to be Lorentz invariant and quark positions are weighted in the way to match the center of mass of the quark system to the hadron position

$$J_M(x) = \quad dx_1 \quad dx_2 \, F_M(x, x_1, x_2) \cdot \bar{q}_{f_1}^a(x_1) \, \Gamma_M \, q_{f_2}^a(x_2),$$

$$F_M(x, x_1, x_2) = \delta\left(x - \omega_1 x_1 - \omega_2 x_2\right) \Phi_M\left[(x_1 - x_2)^2\right], \; \omega_i = \frac{m_i}{m_1 + m_2}.$$

The vertex function $\Phi$ is chosen to have, in the momentum space, an exponential form

$$\widetilde{\Phi}_M\left(-k^2\right) = \exp\left(\frac{k^2}{\Lambda_M^2}\right),$$

a deliberate choice to facilitate computations. Here $\Lambda_M$ represents a free parameter which can be related to the meson size. The free parameters enclose:

- four constituent quark masses $m_u = m_d = m_q = 0.235$ GeV, $m_s = 0.424$ GeV, $m_c = 2.16$ GeV and $m_b = 5.09$ GeV.

- one universal infrared cutoff parameter $\lambda_{cutoff} = 0.181$ GeV.

- one size parameter for each hadron, for this text the relevant parameters are $\Lambda_{B_S} = 2.05$ GeV, $\Lambda_B = 1.96$ GeV, $\Lambda_{K^*} = 0.75$ GeV and $\Lambda_\Phi = 0.88$ GeV.

The numerical value were extracted from global fits to experimental data.

## 2.2 Compositeness condition

Presence of quark fields and hadron fields in the Lagrangian naturally rises questions: How the model reflects the fact of hadrons being built from quarks? Can hadronic fields enter the internal structure of Feynman diagrams and how the double counting is avoided?

The question of describing composite particles in this situation has already been addressed decades ago [1, 2] and can be formulated in the form of so-called "compositeness condition". Its interpretation relates the "bare" and "dressed" hadronic states and can be stated as follows: a state can be considered to be properly described as bound if it does not contain the "bare" state, i. e. its overlap with it is zero. This can be seen as a requirement on the renormalization constant

$$Z_M^{\frac{1}{2}} = 0.$$

Implementation of this condition into our model (for details see [3, 4]) leads to

$$1 - \frac{3g_M^2}{4\pi^2}\Pi_M'\left(m_M^2\right) = 0,$$

where $\Pi_M'$ denotes the derivative of the meson mass operator.

## 2.3 Computation methods

A general Feynman diagram is written as

$$\Pi(p_1,...,p_j) = [d^4k]^\ell \prod_{i_1=1}^{m} \Phi_{i_1+n}\left(-K_{i_1+n}^2\right) \prod_{i_3=1}^{n} S_{i_3}(\tilde{k}_{i_3} + \tilde{p}_{i_3})$$

where

$$K_{i_1+n}^2 = \sum_{i_2}(\tilde{k}_{i_1+n}^{(i_2)} + \tilde{p}_{i_1+n}^{(i_2)})^2.$$

It contains

- $j$ external momenta

- $n$ quark propagators

- $l$ loop integrations

- $m$ vertices

and $\tilde{k}_i$ and $\tilde{p}_{i_1+n}$ stand for linear combination of loop and external momenta, respectively. We work with the Schwinger representation of the quark propagator

$$\widetilde{S}_q(k) = (m + \hat{k}) \int_0^\infty d\alpha e^{[-\alpha(m^2 - k^2)]}$$

and we achieve the integration over loop momenta using the operator identity

$$\int d^4 k P(k) e^{2kr} = \int d^4 k P\left(\frac{1}{2}\frac{\partial}{\partial r}\right) e^{2kr} = P\left(\frac{1}{2}\frac{\partial}{\partial r}\right) \int d^4 k e^{2kr},$$

where $P$ represents a polynomial. In following steps one can transform the operator polynomial

$$\int_0^\infty d^n\alpha\, P\left(\frac{1}{2}\frac{\partial}{\partial r}\right) e^{-\frac{r^2}{a}} = \int_0^\infty d^n\alpha\, e^{-\frac{r^2}{a}} P\left(\frac{1}{2}\frac{\partial}{\partial r} - \frac{r}{a}\right), \ r = r(\alpha_i), \ a = a(\Lambda_H, \alpha_i)$$

so as to act on identity instead on a more complicated exponential function.

Once the infrared cutoff is applied, the computation is completed by performing a numerical integration over Schwinger parameters on a computer.

## 2.4 Infrared confinement

The stability of mesons is naturally guaranteed for not very heavy hadrons where the sum of masses of constituent quarks exceeds the one of the hadron. In the opposite case (hadrons heavy enough) one needs to implement a specific treatment in order to prevent hadrons from decaying. In out model an infrared cutoff is applied in the space of Schwinger parameters. The integral

$$\Pi = \int_0^\infty d^n\alpha\, F(\alpha_1, \cdots, \alpha_n),$$

where $F$ stands for the whole structure of the corresponding Feynman diagram, can be transformed, by insertion of a unity in form of the delta function

$$1 = \int_0^\infty dt\, \delta(t - \sum_{i=1}^n \alpha_i),$$

to an integral over a simplex convoluted with only one-dimensional improper integral

$$\Pi = \int_0^{\infty \to 1/\lambda^2} dt\, t^{n-1} \int_0^1 d^n\alpha\, \delta\left(1 - \sum_{i=1}^n \alpha_i\right) F(t\alpha_1, \ldots, t\alpha_n).$$

A cutoff is then applied to this integral (as depicted on the formula above) making $\Pi$ a smooth function where thresholds in the quark loop diagrams and corresponding branch points are removed.

178
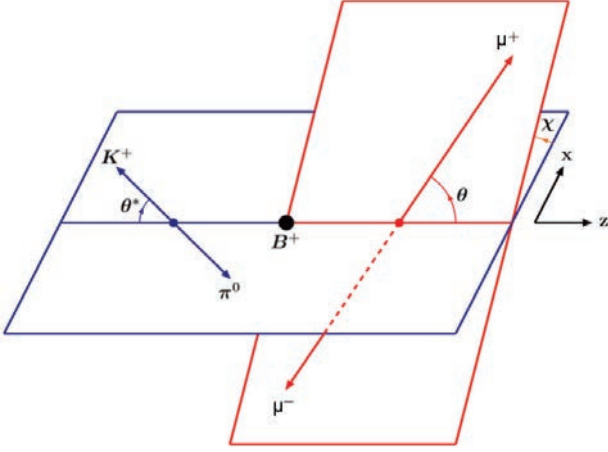
Figure 1: Kinematic quantities.

# 3 Decays $B \to K^* (\to K\pi) + 2\mu$ and $B_S \to \varphi (\to KK) + 2\mu$

## 3.1 Kinematics and form factors

The two processes, $B \to K^* + 2\mu$ and $B_S \to \varphi + 2\mu$, are very similar with identical quantum numbers and they differ only in the flavor of the spectator quark. In both cases we consider a cascade decay of the final hadron in the narrow-width approximation. This introduces additional angular structure which can be compared to the experiment. The kinematics with notations of angles and axes is shown on Fig. 1. The decay can be fully described by 7 form factors

$$\left\langle V_{[\bar{q}_3,q_2]}(p_2,\varepsilon_2) |\bar{q}_2 O^\mu q_1| P_{[\bar{q}_3,q_1]}(p_1)\right\rangle = \frac{\varepsilon_v^\dagger}{m_1+m_2}\Big[ -g^{\mu\nu} P\cdot q A_0(q^2) + P^\mu P^\nu A_+(q^2)$$
$$+ q^\mu P^\nu A_-(q^2) + i\varepsilon^{\mu\nu\alpha\beta} P_\alpha q_\beta V(q^2) \Big],$$

$$\left\langle V_{[\bar{q}_3,q_2]}(p_2,\varepsilon_2) |\bar{q}_2 \Big[\sigma^{\mu\nu} q_\nu \left(1+\gamma^5\right)\Big] q_1| P_{[\bar{q}_3,q_1]}(p_1)\right\rangle =$$
$$\varepsilon_v^\dagger\Big[ -\left(g^{\mu\nu} - \frac{q_\mu q_\nu}{q^2}\right) P\cdot q\, a_0(q^2)$$
$$+ \left(P^\mu P^\nu - q^\mu P^\nu \frac{p\cdot q}{q^2}\right) a_+(q^2) + i\varepsilon^{\mu\nu\alpha\beta} P_\alpha q_\beta\, g(q^2) \Big],$$

the corresponding Feynman diagram is depicted in Fig. 2.

The $b \to s$ flavor transition is described using an effective interaction

$$\mathscr{H}_{eff} = -\frac{4G_F}{\sqrt{2}} \lambda_t \sum_{i=1}^{10} C_i(\mu) O_i(\mu),$$

179
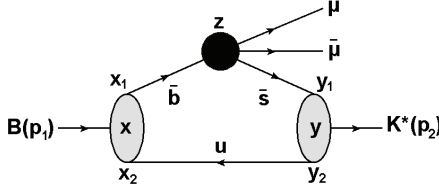
Figure 2: Diagrammatic representation.

where $O_i$ are four-fermion operators, $\lambda_t$ is CKM matrix element squared, $G_F$ is Fermi constant and the value of Wilson coefficients, $C_i(\mu)$, is taken from the literature.

## 3.2 Differential decay distribution

A so-called helicity formalism is used to derive the decay distribution formula. It facilitates the computations by allowing to evaluate the hadronic and leptonic tensors in different frames. First, new set of form factors $A_0$, $A_+$, $A_-$, $V$, $a_0$, $a_+$, $g$ is defined as linear combinations of those introduced in the previous section. Then another redefinition is made

$$V^{(1)} = C_9^{eff} V + C_7^{eff} g \frac{2\overline{m}_b (m_1 + m_2)}{q^2},$$

$$A_0^{(1)} = C_9^{eff} A_0 + C_7^{eff} a_0 \frac{2\overline{m}_b (m_1 + m_2)}{q^2},$$

$$A_+^{(1)} = C_9^{eff} A_+ + C_7^{eff} a_+ \frac{2\overline{m}_b (m_1 + m_2)}{q^2},$$

$$A_-^{(1)} = C_9^{eff} A_- + C_7^{eff} (a_0 - a_+) \frac{2\overline{m}_b (m_1 + m_2)}{q^2} \frac{Pq}{q^2},$$

$$V^{(2)} = C_{10} V, \quad A_0^{(2)} = C_{10} A_0, \quad A_\pm^{(2)} = C_{10} A_\pm,$$

where, this time, also the flavor-changing information enters. Next helicity amplitudes can be defined

$$H^i(t) = \frac{1}{m_1 + m_2} \frac{m_1}{m_2} \frac{|\mathbf{p_2}|}{\sqrt{q^2}} \left[ Pq(-A_0^i + A_+^i) + q^2 A_-^i \right],$$

$$H^i(\pm) = \frac{1}{m_1 + m_2} \left( -PqA_0^i \pm 2m_1 |\mathbf{p_2}| V^i \right),$$

$$H^i(0) = \frac{1}{m_1 + m_2} \frac{1}{2m_2 \sqrt{q^2}} \left[ -Pq \left( m_1^2 - m_2^2 - q^2 \right) A_0^i + 4m_1^2 |\mathbf{p_2}|^2 A_+^i \right],$$

in terms of which the hadronic tensor in the helicity basis can be written

$$H^{ij}(m,n) = H^i(m) H^{\dagger j}(n),$$

$$H^{ij}(m,n) = \varepsilon^{\dagger\mu}(m) \varepsilon^\nu$$

$$(n) H^{ij}_{\mu\nu}.$$

The leptonic tensor is in the helicity basis written as

$$L^{(k)}(m,n) = \varepsilon^{\mu}(m)\varepsilon^{\dagger\nu}(n)L^{(k)}_{\mu\nu}.$$

The full four-differential decay width then is

$$\frac{d\Gamma(B \to K^*(\to K\pi)\bar{\mu}\mu)}{dq^2\, d(\cos\theta)\, (d\chi/2\pi)\, d(\cos\theta^*)} =$$

$$\mathrm{Br}(K^* \to K\pi) \times \left\{ \frac{3}{8}(1+\cos^2\theta) \cdot \frac{3}{4}\sin^2\theta^* \cdot \frac{1}{2}\left(\frac{d\Gamma_{U_{11}}}{dq^2} + \frac{d\Gamma_{U_{22}}}{dq^2}\right) \right.$$

$$+\frac{3}{4}\sin^2\theta \cdot \frac{3}{2}\cos^2\theta^* \cdot \frac{1}{2}\left(\frac{d\Gamma_{L_{11}}}{dq^2} + \frac{d\Gamma_{L_{22}}}{dq^2}\right)$$

$$-\frac{3}{4}\sin^2\theta \cdot \cos 2\chi \cdot \frac{3}{4}\sin^2\theta^* \cdot \frac{1}{2}\left(\frac{d\Gamma_{T_{11}}}{dq^2} + \frac{d\Gamma_{T_{22}}}{dq^2}\right)$$

$$-\frac{9}{16}\sin 2\theta \cdot \cos\chi \cdot \sin 2\theta^* \cdot \frac{1}{2}\left(\frac{d\Gamma_{I_{11}}}{dq^2} + \frac{d\Gamma_{I_{22}}}{dq^2}\right)$$

$$+v\cdot\left[-\frac{3}{4}\cos\theta \cdot \frac{3}{4}\sin^2\theta^* \cdot \frac{d\Gamma_{P_{12}}}{dq^2}\right.$$

$$+\frac{9}{8}\sin\theta \cdot \cos\chi \cdot \sin 2\theta^* \cdot \frac{1}{2}\left(\frac{d\Gamma_{A_{12}}}{dq^2} + \frac{d\Gamma_{A_{21}}}{dq^2}\right)$$

$$\left.-\frac{9}{16}\sin\theta \cdot \sin\chi \cdot \sin 2\theta^* \cdot \left(\frac{d\Gamma_{II_{12}}}{dq^2} + \frac{d\Gamma_{II_{21}}}{dq^2}\right)\right]$$

$$+\frac{9}{32}\sin 2\theta \cdot \sin\chi \cdot \sin 2\theta^* \cdot \left(\frac{d\Gamma_{IA_{11}}}{dq^2} + \frac{d\Gamma_{IA_{22}}}{dq^2}\right)$$

$$+\frac{9}{32}\sin^2\theta \cdot \sin 2\chi \cdot \sin^2\theta^* \cdot \left(\frac{d\Gamma_{IT_{11}}}{dq^2} + \frac{d\Gamma_{IT_{22}}}{dq^2}\right)$$

$$+\frac{3}{4}\sin^2\theta \cdot \frac{3}{4}\sin^2\theta^* \cdot \frac{1}{2}\cdot\frac{d\tilde{\Gamma}_{U_{11}}}{dq^2} - \frac{3}{8}(1+\cos^2\theta) \cdot \frac{3}{4}\sin^2\theta^* \cdot \frac{d\tilde{\Gamma}_{U_{22}}}{dq^2}$$

$$+\frac{3}{2}\cos^2\theta \cdot \frac{3}{2}\cos^2\theta^* \cdot \frac{1}{2}\cdot\frac{d\tilde{\Gamma}_{L_{11}}}{dq^2} - \frac{3}{4}\sin^2\theta \cdot \frac{3}{2}\cos^2\theta^* \cdot \frac{d\tilde{\Gamma}_{L_{22}}}{dq^2}$$

$$+\frac{3}{4}\sin^2\theta \cdot \cos 2\chi \cdot \frac{3}{4}\sin^2\theta^* \cdot \left(\frac{d\tilde{\Gamma}_{T_{11}}}{dq^2} + \frac{d\tilde{\Gamma}_{T_{22}}}{dq^2}\right)$$

$$+\frac{9}{8}\sin 2\theta \cdot \cos\chi \cdot \sin 2\theta^* \cdot \frac{1}{2}\left(\frac{d\tilde{\Gamma}_{I_{11}}}{dq^2} + \frac{d\tilde{\Gamma}_{I_{22}}}{dq^2}\right)$$

$$+\frac{3}{2}\cos^2\theta^* \cdot \frac{1}{4}\frac{d\tilde{\Gamma}_{S_{22}}}{dq^2} - \frac{9}{16}\sin 2\theta \cdot \sin\chi \cdot \sin 2\theta^* \cdot \left(\frac{d\Gamma_{IA_{11}}}{dq^2} + \frac{d\Gamma_{IA_{22}}}{dq^2}\right)$$

$$\left.-\frac{9}{16}\sin^2\theta \cdot \sin 2\chi \cdot \sin^2\theta^* \cdot \left(\frac{d\Gamma_{IT_{11}}}{dq^2} + \frac{d\Gamma_{IT_{22}}}{dq^2}\right)\right\},$$

with

$$\frac{d\Gamma_X}{dq^2} = \frac{G_F^2}{(2\pi)^3}\left(\frac{\alpha|\lambda_t|}{2\pi}\right)^2 \frac{|\mathbf{p_2}|q^2 v}{12 m_1^2}H_X^{ij}, \qquad \frac{d\tilde{\Gamma}_X}{dq^2} = \frac{2m_l^2}{q^2}\frac{d\Gamma_X}{dq^2},$$

181

where $H_X^{ij}$ is a bilinear combination of $H^i$. Often, an alternative expression is used

$$
\frac{1}{d\Gamma/dq^2} \frac{d^3\Gamma}{d\cos\theta_l \, d\cos\theta_k \, d\Phi} = \frac{9}{32\pi}
$$
$$
\times \left[ \tfrac{3}{4}(1-F_L)\sin^2\theta_k + F_L\cos^2\theta_k + \tfrac{1}{4}(1-F_L)\sin^2\theta_k\cos 2\theta_l \right.
$$
$$
- F_L\cos^2\theta_k\cos 2\theta_l + S_3\sin^2\theta_k\sin^2\theta_l\cos 2\Phi
$$
$$
+ S_4\sin 2\theta_k\sin 2\theta_l\cos\Phi + S_5\sin 2\theta_k\sin\theta_l\cos\Phi
$$
$$
+ S_6\sin^2\theta_k\cos\theta_l + S_7\sin 2\theta_k\sin\theta_l\sin\Phi
$$
$$
\left. + S_8\sin 2\theta_k\sin 2\theta_l\sin\Phi + S_9\sin^2\theta_k\sin^2\theta_l\sin 2\Phi \right],
$$

the compatibility of both was checked.

# 4 Observables

When defining observables, one searches for:

- Small model dependence on hadronic corrections (form factors)

- Sensitivity to new physics

- Experimental accessibility (clear signature, high cross-section, small backgrounds)

With this requirements one often arrives to observables defined as asymmetries or asymmetry ratios. It can be argued that in our case suitable observables are

$$
F_T = 1 - F_L, \quad A_{FB} = -\frac{3}{4}S_6, \quad P_{1,2,3} = c_{1,2,3}\frac{S_{3,6,9}}{F_T}, \quad P'_{4,5,6} = c_{4,5,6}\frac{S_{4,5,7}}{\sqrt{F_T F_L}}
$$

together with the differential decay width $d\Gamma/dq^2$. Taking into account the finite $q^2$ bin size in the experimental measurement (from which follows a separate integration of the numerator and denominator) and using the following notation

$$
dX^{ij} = \frac{d\Gamma_X^{ij}}{dq^2}, \quad \beta_l = \sqrt{1 - \frac{4m_\mu^2}{q^2}}
$$

one can rewrite the observables in the helicity language

$$
\frac{d\Gamma}{dq^2} = \frac{1}{2}\left( \frac{d\Gamma_U^{11}}{dq^2} + \frac{d\Gamma_U^{22}}{dq^2} + \frac{d\Gamma_L^{11}}{dq^2} + \frac{d\Gamma_L^{22}}{dq^2} \right) + \frac{1}{2}\frac{d\tilde\Gamma_U^{11}}{dq^2} - \frac{d\tilde\Gamma_U^{22}}{dq^2} + \frac{1}{2}\frac{d\tilde\Gamma_L^{11}}{dq^2} - \frac{d\tilde\Gamma_L^{22}}{dq^2} + \frac{3}{2}\frac{d\tilde\Gamma_S^{22}}{dq^2},
$$

$$
F_L = \frac{\int dq^2 \; H_L^{11} + H_L^{22}}{\int dq^2 \; H_L^{11} + H_L^{22} + H_U^{11} + H_U^{22}}, \quad A_{FB} = -\frac{3}{2}\frac{\int dq^2 \; H_P^{12}}{\int dq^2 \; H_L^{11} + H_L^{22} + H_U^{11} + H_U^{22}},
$$

$$
P_1 = -2\frac{\int dq^2 \; \beta_l^2[dT^{11} + dT^{22}]}{\int dq^2 \; \beta_l^2[dU^{11} + dU^{22}]}, \quad P_2 = -\frac{\int dq^2 \; \beta_l dP^{12}}{\int dq^2 \; \beta_l^2[dU^{11} + dU^{22}]},
$$

$$
P_3 = -\frac{\int dq^2 \; \beta_l^2[dIT^{11} + dIT^{22}]}{\int dq^2 \; \beta_l^2[dU^{11} + dU^{22}]}, \quad P'_4 = 2\frac{\int dq^2 \; \beta_l^2[dI^{11} + dI^{22}]}{N},
$$

$$
P'_5 = -2\frac{\int dq^2 \; \beta_l[dA^{12} + dA^{21}]}{N}, \quad P_8 = 2\frac{\int dq^2 \; \beta_l^2[dIA^{11} + dIA^{22}]}{N},
$$
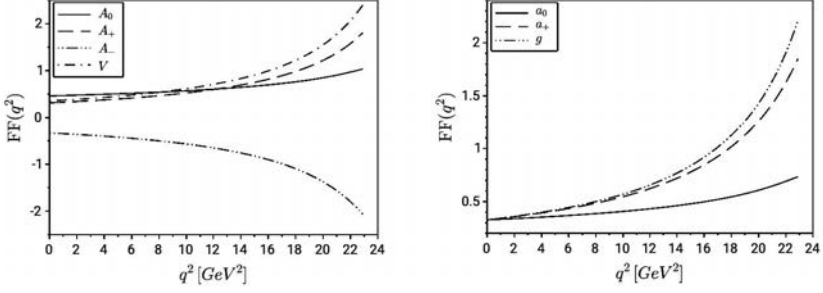
Figure 3: $B \to K^*$ form factors as predicted by the covariant quark model.

| | Belle [6] | LHCb [7] | CDF [8] | CQM |
|---|---|---|---|---|
| $\mathscr{B} \times 10^7$ | $1.49^{+0.45}_{-0.40} \pm 0.12$ | $0.42 \pm 0.06 \pm 0.03$ | - | 2.58 |
| $A_{FB}$ | $0.26^{+0.27}_{-0.30} \pm 0.07$ | $-0.06^{+0.13}_{-0.14} \pm 0.04$ | $0.29^{+0.20}_{-0.23} \pm 0.07$ | $-0.02$ |
| $F_L$ | $0.67^{+0.23}_{-0.23} \pm 0.05$ | $0.55 \pm 0.10 \pm 0.03$ | $0.69^{+0.19}_{-0.21} \pm 0.08$ | 0.75 |

Table 1: Three observables for $B \to K^*(\to K\pi) + 2\mu$: comparison with experiment ($1\text{GeV}^2 < q^2 < 6\text{GeV}^2$).

with

$$N = \sqrt{\int dq^2 \beta_l^2 [dU^{11} + dU^{22}] \cdot \quad dq^2 \beta_l^2 [dL^{11} + dL^{22}]}.$$

# 5 Results

## 5.1 Decay $B \to K^*(\to K\pi) + 2\mu$

The model predicted form factors are plotted in Fig 3. Further results are shown, both, for the muon and the tau lepton in the final state, in Fig. 4 and Tabs. 1 and 2. In the first table we compare, in the $1\text{GeV}^2 < q^2 < 6\text{GeV}^2$ region, our results for branching fraction, $A_{FB}$ and $F_L$ with the experimental numbers. The second table shows values of several observables averaged over the whole kinematic region. More $q^2$-differential information can be found in [5].

| | $<A_{FB}>$ | $<F_L>$ | $<P_1>$ | $<P_2>$ | $<P_3>$ | $<P_4'>$ | $<P_5'>$ |
|---|---|---|---|---|---|---|---|
| $\mu$ | $-0.23$ | 0.47 | $-0.48$ | $-0.31$ | 0.0015 | 1.01 | $-0.49$ |
| $\tau$ | $-0.18$ | 0.092 | $-0.74$ | $-0.68$ | 0.00076 | 1.32 | $-1.07$ |

Table 2: $B \to K^*(\to K\pi) + 2l$ : observables averaged over all kinematic region.
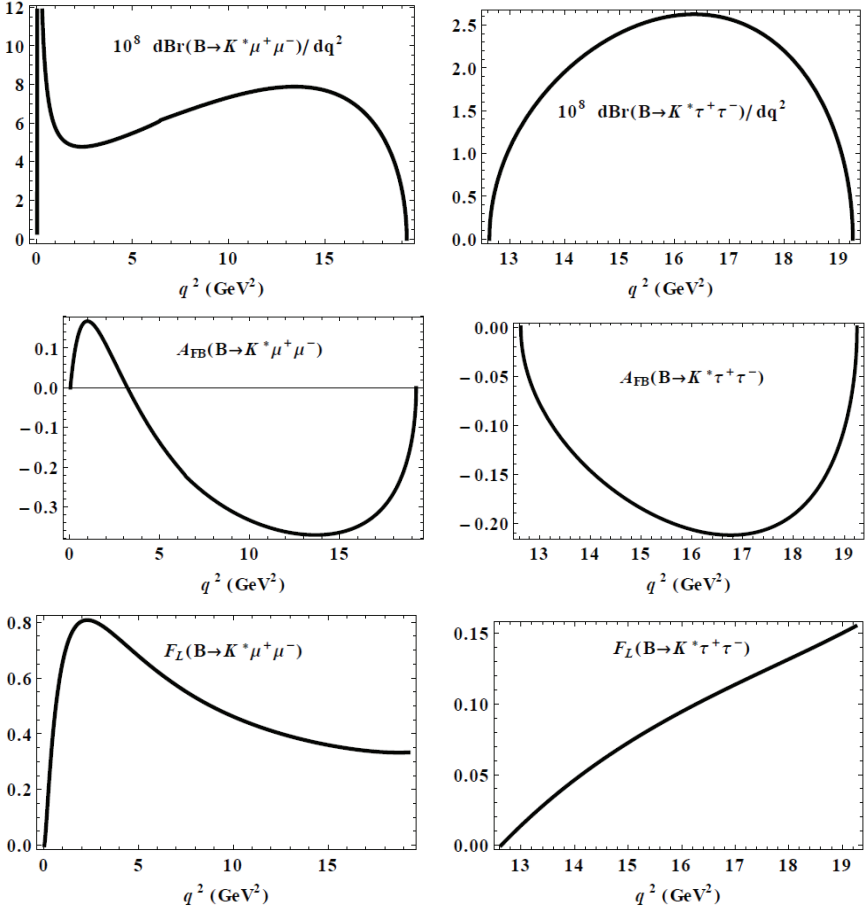
Figure 4: Branching fraction and $A_{FB}$ and $F_L$ observables for muon and tau lepton in the final state of the $B \rightarrow K^*(\rightarrow K\pi) + 2l$ decay.
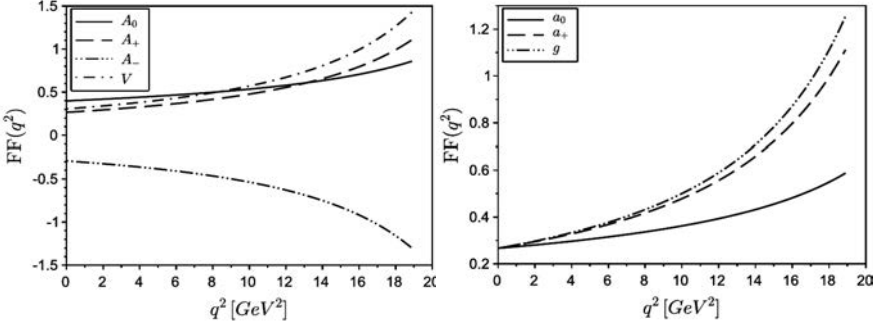
Figure 5: $B_S \to \varphi$ form factors as predicted by the covariant quark model.

| | $<A_{FB}>$ | $<F_L>$ | $<P_1>$ | $<P_4'>$ | $<S_3>$ |
|---|---|---|---|---|---|
| $\mu$ | $-0.24 \pm 0.05$ | $0.45 \pm 0.09$ | $-0.52 \pm 0.1$ | $1.05 \pm 0.21$ | $-0.14 \pm 0.03$ |
| $\tau$ | $-0.18 \pm 0.04$ | $0.090 \pm 0.02$ | $-0.76 \pm 0.15$ | $1.33 \pm 0.27$ | $-0.067 \pm 0.013$ |

Table 3: $B_S \to \varphi (\to KK) + 2l$ : observables averaged over all kinematic region.

## 5.2 Decay $B_S \to \varphi (\to KK) + 2\mu$

The $B_S \to \varphi$ form factors predicted by the covariant quark model are shown in Fig. 5 The branching fraction, $A_{FB}$ and $F_L$ in the whole kinematic region are plotted in Fig. 6. Tab. 3 shows, for studied observables, the averages over all kinematic range. In Tab. 4, our numbers for the total branching fraction are compared with the experiment and with numbers of other authors.

## 5.3 Other results: $B_S \to J/\Psi + \eta$, $B_S \to J/\Psi + \eta'$

Further processes involving mesons were analyzed in the framework of the covariant quark model. As an example one may choose the $B_S \to J/\Psi + \eta^{(')}$ decay. This process was measured at Belle [15] and LHCb [16], its diagram is shown in Fig. 7. Model parameters were, for this case, overconstained by previously existing data fits, therefore giving the results the status of predictions. With methods presented in this text the branching fractions and their rations were computed and an agreement with

| | This work | [9] | [10] | [11] | [12] | [13, 14] |
|---|---|---|---|---|---|---|
| $\mu$ | $9.11 \pm 1.82$ | $11.1 \pm 1.1$ | $19.2$ | $11.8 \pm 1.1$ | $16.4$ | $7.97 \pm 0.77$ |
| $\tau$ | $1.03 \pm 0.20$ | $1.5 \pm 0.2$ | $2.34$ | $1.23 \pm 0.11$ | $1.51$ | |

Table 4: Total branching fractions $\times 10^7$.
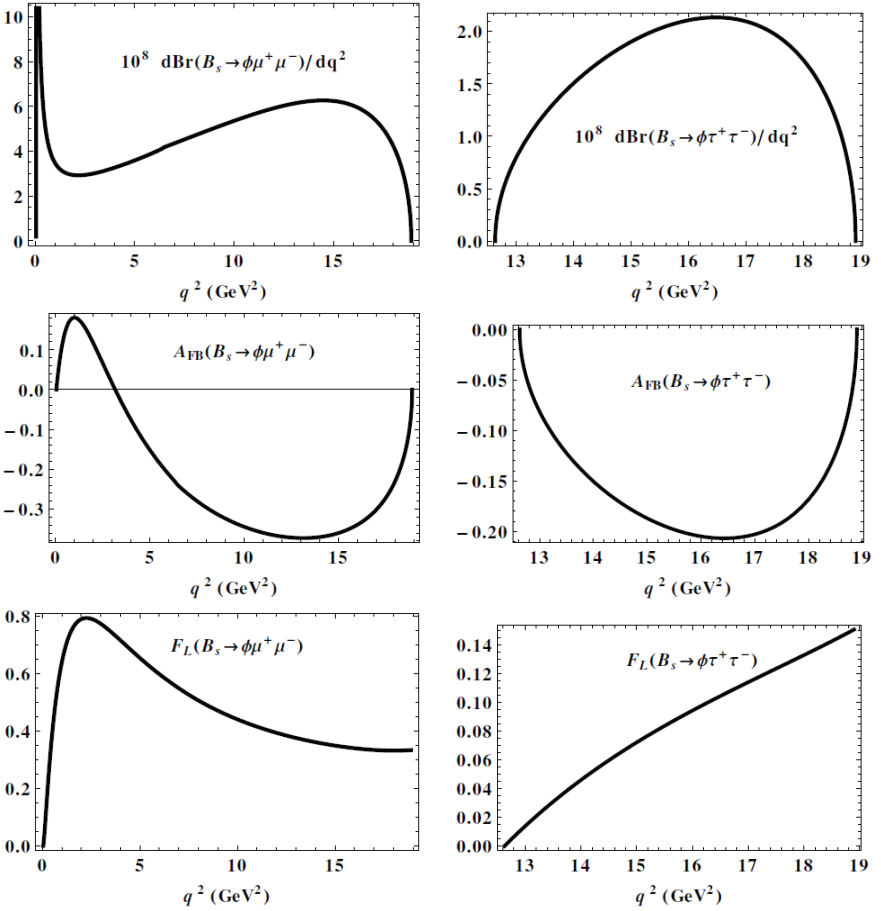
Figure 6: Branching fraction and $A_{FB}$ and $F_L$ observables for muon and tau lepton in the final state of the $B_S \to \varphi\,(\to KK) + 2l$ decay.
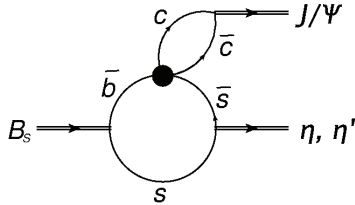


Figure 7: Decay $B_S \to J/\Psi + \eta^{(')}$.

experimental values was observed

$$\mathscr{B}_{CQM}(J/\psi\,\eta) = 4.67 \times 10^{-4}, \quad \mathscr{B}_{Belle}(J/\psi\,\eta) = (5.10 \pm 1.12) \times 10^{-4},$$

$$\mathscr{B}_{CQM}(J/\psi\,\eta') = 4.04 \times 10^{-4}, \quad \mathscr{B}_{Belle}(J/\psi\,\eta') = (3.71 \pm 0.95) \times 10^{-4}.$$

In the ratio

$$R = \frac{\Gamma(J/\psi + \eta')}{\Gamma(J/\psi + \eta)} = \begin{cases} 0.73 \pm 0.14 \pm 0.02 & \text{Belle} \\ 0.90 \pm 0.09^{+0.06}_{-0.02} & \text{LHCb} \end{cases}$$

a model dependent part (form factor ratio) can be factorized

$$R^{CQM} = \underbrace{\frac{|\mathbf{q}_{\eta'}|^3}{|\mathbf{q}_{\eta}|^3} \tan^2 \delta}_{\approx 1.04} \times \underbrace{\left(\frac{F_+^{B_s\eta'}}{F_+^{B_s\eta}}\right)^2}_{\approx 0.83} \approx 0.86,$$

showing the importance of our model: the model-independent value of 1.04 is significantly modified by model prediction 0.83 so that the result becomes compatible with experiment.

# 6 Summary, conclusion

Covariant quark model is relativistic, Lagrangian-based model with limited number of free parameters, well suited for description of heavy hadron decays. In studied decay processes it provided an additional cross-check of the theory-data consistency by describing the hadronic effects, no significant deviation from the SM was observed. In the same way further processes can be evaluated and agreement with the SM checked (e.g. recently measured $B_S^0 \to \mu^+\mu^-$ and $B_s^0 \to K_S^0 K^*(892)^0$ at LHCb and CMS respectively).

# References

[1] Abdus Salam. Lagrangian theory of composite particles. *Nuovo Cim.*, 25:224–227, 1962.

[2] Steven Weinberg. Elementary particle theory of composite particles. *Phys.Rev.*, 130:776–783, 1963.

[3] G. V. Efimov and Mikhail A. Ivanov. Confinement and Quark Structure of Light Hadrons. *Int. J. Mod. Phys.*, A4:2031, 1989.

[4] Gurjav Ganbold, Thomas Gutsche, Mikhail A. Ivanov, and Valery E. Lyubovitskij. On the meson mass spectrum in the covariant confined quark model. *J. Phys.*, G42(7):075002, 2015.

[5] Stanislav Dubnička, Anna Z. Dubničková, Nurgul Habyl, Mikhail A. Ivanov, Andrej Liptaj, and Guliya S. Nurbakova. Decay $B \to K^*(\to K\pi)\ell^+\ell^-$ in covariant quark model. *Few Body Syst.*, 57(2):121–143, 2016.

[6] J. T. Wei et al. Measurement of the Differential Branching Fraction and Forward-Backword Asymmetry for $B \to K^{(*)}\ell^{+}\ell^{-}$. *Phys. Rev. Lett.*, 103:171801, 2009.

[7] R Aaij et al. Differential branching fraction and angular analysis of the decay $B^{0} \to K^{*0}\mu^{+}\mu^{-}$. *Phys. Rev. Lett.*, 108:181806, 2012.

[8] T. Aaltonen et al. Measurements of the Angular Distributions in the Decays $B \to K^{(*)}\mu^{+}\mu^{-}$ at CDF. *Phys. Rev. Lett.*, 108:081807, 2012.

[9] R. N. Faustov and V. O. Galkin. Rare $B_{s}$ decays in the relativistic quark model. *Eur. Phys. J.*, C73(10):2593, 2013.

[10] U. O. Yilmaz. Analysis of $B_{s} \to \phi\ell^{+}\ell^{-}$ decay with new physics effects. *Eur. Phys. J.*, C58:555–568, 2008.

[11] Yue-Liang Wu, Ming Zhong, and Ya-Bing Zuo. B(s), D(s) —> pi, K, eta, rho, K*, omega, phi Transition Form Factors and Decay Rates with Extraction of the CKM parameters |V(ub)|, |V(cs)|, |V(cd)|. *Int. J. Mod. Phys.*, A21:6125–6172, 2006.

[12] C. Q. Geng and C. C. Liu. Study of $B_{s} \to (\eta, \eta', \phi)\ell\bar{\ell}$ decays. *J. Phys.*, G29:1103–1118, 2003.

[13] K. A. Olive et al. Review of Particle Physics. *Chin. Phys.*, C38:090001, 2014.

[14] Roel Aaij et al. Angular analysis and differential branching fraction of the decay $B_{s}^{0} \to \phi\mu^{+}\mu^{-}$. *JHEP*, 09:179, 2015.

[15] J. Li et al. First observation of $B_{s}^{0} \to J/\psi\eta$ and $B_{s}^{0} \to J/\psi\eta'$. *Phys. Rev. Lett.*, 108:181808, 2012.

[16] R Aaij et al. Evidence for the decay $B^{0} \to J/\psi\omega$ and measurement of the relative branching fractions of $B_{s}^{0}$ meson decays to $J/\psi\eta$ and $J/\psi\eta'$. *Nucl. Phys.*, B867:547–566, 2013.

# Why diffractive factorization is broken

B. Z. Kopeliovich[1], Roman Pasechnik[2] and I. K. Potashnikova[1]

[1] *Departamento de Física, Universidad Técnica Federico Santa María*
*Casilla 110-V, Valparaíso, Chile*
[2] *Department of Astronomy and Theoretical Physics*
*Lund University, SE-223 62 Lund, Sweden*

## 1 QCD factorization in diffraction

QCD factorization in inclusive processes is nowadays one of the most power-ful and frequently used theoretical tools [1]. In spite of lack of understanding of the soft interaction dynamics, the contributions of the soft long-distance and hard short-distance interactions factorise. Making a plausible (though not proven) assumption about universality of the former, one can measure it with electro-weak hard probes (DIS, Drell-Yan process) and apply to hard hadronic processes. Although it is tempting to extend this factoriza-tion scheme to diffractive, large rapidity gap processes, it turns out to be heavily broken [2, 3], as is demonstrated below.

*Ingelman-Schlein picture of diffraction* [4].

It looks natural that on analogy of DIS on a hadronic target, DIS on the Pomeron probes its PDF (parton distribution function), like is illustrated in Fig. 1 . Once the parton densities in the Pomeron were known, one could
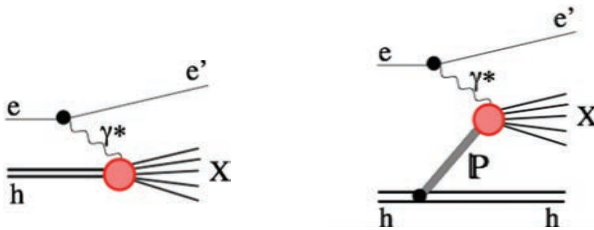


Figure 1: DIS on a hadron taget (left) and on the Pomeron, treated as a target (right).

predict any hard diffractive hadronic reaction.

*The Good-Walker mechanism of diffraction* [6, 7, 8].

According to this quantum mechanical treatment of diffraction, the diffractive amplitude is given by the difference between the elastic amplitudes of different Fock components in the projectile particle. In the dipole representation hard diffraction of a hadron comes from the difference between elastic amplitudes of hadronic states with and without a hard fluctuation,

$$A_{diff}^h \propto \sigma_{\bar{q}q}(R+r) - \sigma_{\bar{q}q}(R) \propto rR \sim 1/Q, \qquad (1)$$

where $\sigma_{\bar{q}q}(R)$ is the total dipole-nucleon cross section [9]; $R$ characterises the hadronic size, while small $r \sim 1/Q \ll R$ is related to the hard process [14, 15]. Apparently such a mild $Q$-dependence contradicts factorization prediction, based on the DIS relation,

$$A_{diff} \propto \sigma_{\bar{q}q}(r) \propto r^2 \sim 1/Q^2, \qquad (2)$$

which is a higher twist effect.

While the phenomenological dipole cross section (or partial dipole amplitude) is a universal ingredient naturally accumulating the soft interactions and fitted to the available precision data, the diffractive amplitudes are represented in terms of a linear superposition of elastic dipole scatterings at different transverse separations which is process-dependent and accumulates all the relevant absorptive corrections fully dynamically. Naturally, the gap survival amplitude gets singled out from such a superposition as a common factor dependent on soft parameters of the dipole model and on the diffractive process concerned.

In the forward scattering limit and in the absence of spectator co-movers a single quark cannot radiate an Abelian particle ($\gamma$, $Z$, $W^\pm$, $H$) in a diffractive quark-hadron scattering (with zero net momentum transfer), in variance to diffractive factorisation [10]. Only a dipole can diffractively radiate due to a small fluctuation in its size induced by the hard scattering (c.f. Eq. (1)) so diffraction becomes possible although is strongly suppressed. Such a mechanism opens up new possibilities for universal description of diffractive reactions specific to the dipole approach beyond QCD factorisation [9]. The diffractive factorisation breaking in non-Abelian radiation is also important although the diffractive gluon radiation off a quark does not vanish in the forward kinematics due to an extra glue-glue interaction. The universal dipole mechanism of diffraction has been employed in a number of diffractive processes so far, and this review aims at a short comprehensive overview of major implications of the diffractive factorisation breakdown in both Abelian and non-Abelian diffractive radiation.

# 2 Drell-Yan process: annihilation or bremsstrahlung?

Parton model is not Lorentz invariant, interpretation of hard reactions varies with reference frame. E.g. DIS is treated as a probe for the proton structure in the Bjorken frame, but looks differently in the target rest frame, as interaction of hadronic components of the photon. Only observables are Lorentz invariant.

The Drell-Yan reaction in the target rest frame looks like radiation of a heavy photon (or Z, W), rather than q-qbar annihilation [11, 12], as is illustrated in Fig. 2
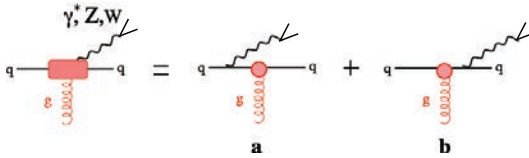


Figure 2: Radiation of a heavy photon, or gauge bosons in the target rest frame, corresponds to $\bar{q}q$ annihilation in the boson rest frame.

The cross section, expressed via the dipoles [11, 12], looks similar to DIS,

$$\frac{d\sigma_{inc}^{DY}(qp \to \gamma^* X)}{d\alpha \, dM^2} = d^2r \, |\Psi_{q\gamma^*}(\vec{r}, \alpha)|^2 \, \sigma(\alpha r, x_2), \qquad (3)$$

where $\Psi_{q\gamma^*}(\vec{r}, \alpha)$ is the distribution function for the $|\gamma^* q\rangle$ Fock component of the quark; $\alpha = p_{\gamma^*}^+/p_q^+$ is the fractional ligh-cone momentum of the heavy photon.

In DY diffraction the Ingelman-Schlein factorization is broken. Indeed, diffractive radiation of an abelian particle vanishes in the forward direction [12], due to cancellation of the graphs a, b and c depicted in Fig. 3,

$$\frac{d\sigma_{inc}^{DY}(qp \to \gamma^* qp)}{d\alpha \, dM^2 \, d^2p_T}\bigg|_{p_T=0} = 0. \qquad (4)$$

In both Fock components of the quark, $|q\rangle$ and $|q\gamma^*\rangle$ only quark interacts, so they interact equally, and according to the Good-Walker picture cancel in the forward diffractive amplitude. This conclusion holds for any abelian diffractive radiation of $\gamma^*$, $W$, $Z$ bosons, Higgs.

Diffractive DIS is dominated by soft interactions [13, 2]. On the contrary, diffractive Drell-Yan gets the main contribution from the interplay of soft and hard scales [14, 15].
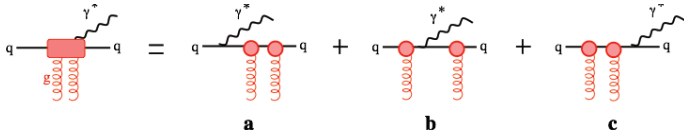
Figure 3: Feynman graphs for diffractive radiation of a heavy photon by a quark.

The saturated shape of the dipole cross section, $\sigma(R) \propto 1 - \exp(-R^2/R_0^2)$, leads to the unusual features of diffractive Drell-Yan cross section (compare with (2)),

$$\frac{\sigma_{sd}^{DY}}{\sigma_{incl}^{DY}} \propto [\sigma(R + r) - \sigma(R)]^2 \propto \frac{\exp(-2R^2/R_0^2)}{R_0^2} \qquad (5)$$

As a result, the fractional diffractive Drell-Yan cross section is steeply falling with energy, but rises with the scale, because of saturation, as is shown in Fig. 4.
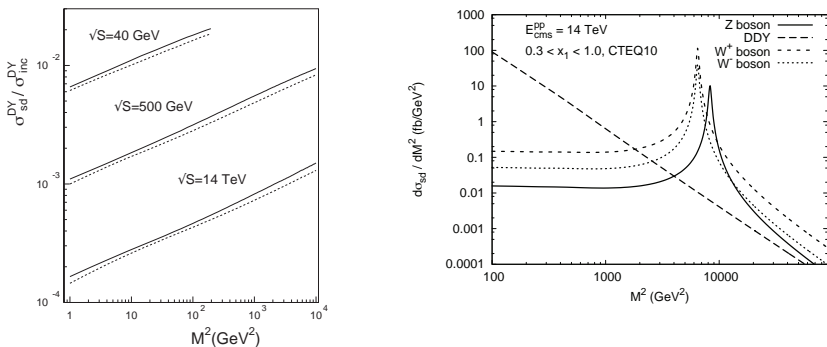


Figure 4: *Left:* Fractional DY cross section vs the dilepton mass squared and at different c.m. energies. *Right:* Diffractive gauge boson and Drell-Yan pair production cross sections as function of di-lepton invariant mass squared.

# 3    Diffractive gauge boson production

Abelian diffractive radiation of any particle is described by the same Feynman graphs, only couplings and spin structure are different [16]. In Fig. 4 (right panel) we present the results for the single diffractive cross sections for $Z^0$, $\gamma^*$ (diffractive DY) and $W^\pm$ bosons production, differential in the di-lepton mass squared, $d\sigma_{sd}/dM^2$.

192

The single diffractive process $pp \to Xp$ at large Feynman $x_F \to 1$ of the recoil proton is described by the triple Regge graphs, as is illustrated in Fig. 5. The results for the fractional diffractive cross sections of $Z$ and
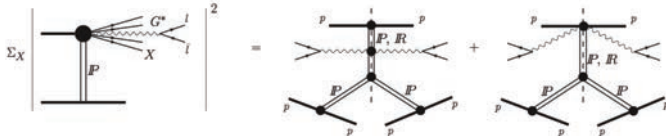


Figure 5: Triple-Regge description of the process $pp \to Xp$, where the diffractively produced state $X$ contains a gauge boson decaying to a lepton pair.

$W$ production are in good agreement with the CDF measurements in Fig. 6 (left panel).
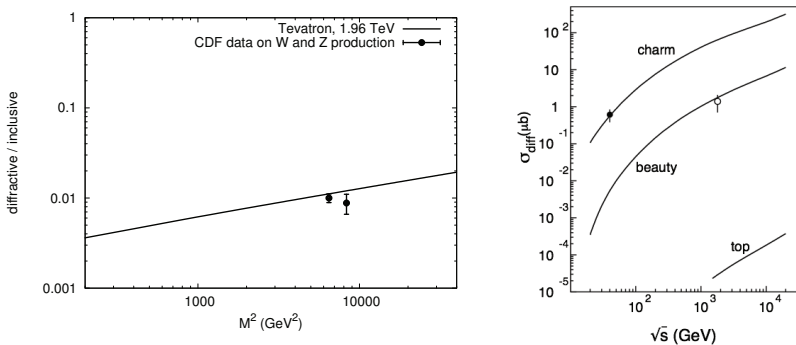


Figure 6: *Left:* The diffractive-to-inclusive ratio vs dilepton invariant mass squared in comparison with the CDF measurements. *Right:* Cross section of diffractive production of heavy flavors in comparison with the CDF data for charm and beauty (see details in [17]).

# 4  Diffractive heavy flavor production

QCD factorisation predicts vanishing $Q\bar{Q}$ production cross sections at large $x_F$ due to a steeply decreasing gluon density in the forward kinematics which contradicts to the end-point behavior predicted by the Regge asymptotics (see e.g. Ref. [3] and references therein). A similar contradiction arises for the DY reaction at large $x_F$, which has been seen in data [18]. Both examples apparently indicate that the conventional QCD factorisation does not hold, at least, at large Feynman $x_F$ [19].
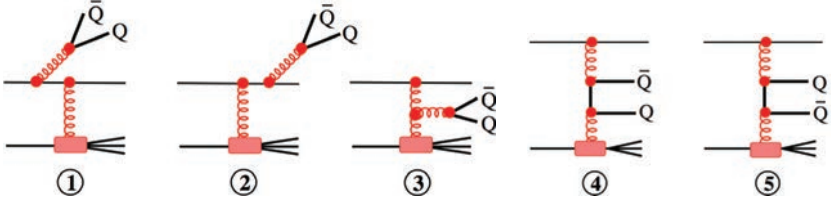
Figure 7: Typical contributions to inclusive production of a heavy quark pair in a quark-proton collision.

A detailed analysis of various contributions into the diffractive $Q\bar{Q}$ production from both diffractive gluon and quark excitations has been performed in Ref. [17]. For example, in the case of diffractive quark excitation $q + g \rightarrow (Q\bar{Q}) + q$ the dynamics of inclusive heavy flavor production is characretized by five distinct topologies which can be classified as: (i) bremsstrahlung (like in DY), and (ii) production mechanisms as illustrated by the Feynman graphs in Fig. 7, such that the total amplitude

$$A_{Q\bar{Q}}^{\mathrm{diff}} = A_{\mathrm{BR}} + A_{\mathrm{PR}} \,. \tag{6}$$

Each of these two contributions is gauge invariant and can be described in terms of three-body dipole cross sections, $\sigma_{g\bar{q}q}$ and $\sigma_{g\bar{Q}Q}$, respectively, which strongly motivates such a separation. Similar graphs and classification hold for the diffractive gluon excitation $g + g \rightarrow (Q\bar{Q}) + g$ as well. The amplitudes for each of the two mechanisms are expressed via the amplitudes $A_i$ corresponding to the graph numbering in Fig. 7. As was elaborated in Ref. [17] such a grouping can be performed for both transversely and longitudinally polarised indermediate gluons. The bremsstrahlung and production components have the following form,

$$A_{\mathrm{BR}} = A_1 + A_2 + \frac{Q^2}{M^2 + Q^2} \, A_3 \,; \tag{7}$$

$$A_{\mathrm{PR}} = \frac{M^2}{M^2 + Q^2} \, A_3 + A_4 + A_5 \,, \tag{8}$$

where $Q^2 = (p_i - p_j)^2$ in terms of the initial $p_i$ and final $p_j$ projectile quark momenta, and $M$ is the invariant mass of the $Q\bar{Q}$ pair.

For diffractive production one has to provide a colorless two-gluon exchange. In analogy to the leading-twist DIS diffraction at large photon virtualities $\gamma^* \rightarrow Q\bar{Q}g$, the BR and PR contributions are dependent on two characteristic length scales: the small separation between the $\bar{Q}$ and $Q$, $s \sim 1/m_Q$, and a typically large separation between $q$ and $Q\bar{Q}$, $\rho \sim 1/m_q$. In analogy to diffractive DY, the diffractive excitation of a quark thus turns out to be a higher twist effect as is depicted in Fig. 8 (left). The leading
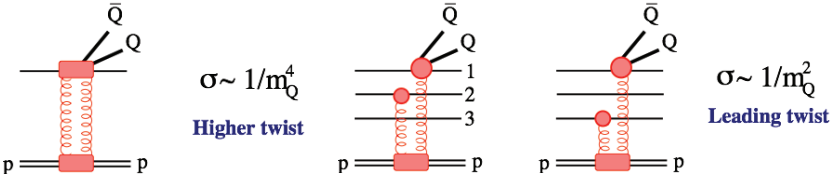
Figure 8: Diffractive production of a heavy quark pair in a quark-proton collision (left panel) and in a proton-proton collision (right panel).
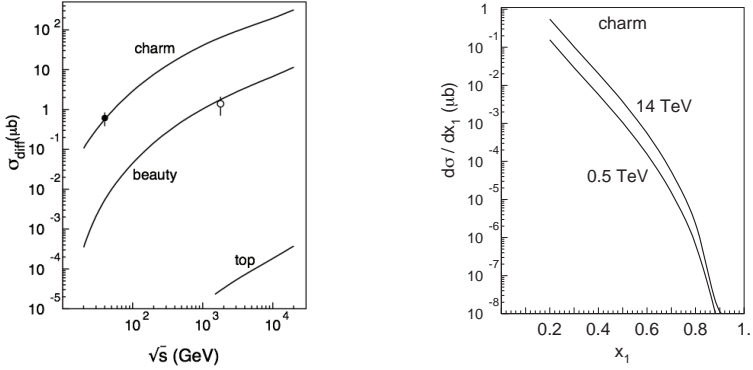


Figure 9: The total cross sections for diffractive heavy flavor production w.r.t. the experimental data from E690 [20] and CDF [21] experiments for charm and beauty as functions of energy and differential cross section $d\sigma/dx_1$ for diffractive charm quark production at $\sqrt{s} = 0.5$ and 14 TeV (more details are in Ref. [17]).

twist contributions to diffractive $Q\bar{Q}$ production come from both sources: when both exchanged gluons couple to the valence quark which gives rise to the $Q\bar{Q}$ pair, and when one of the gluons is coupled to another spectator quark not participating in the hard scattering as is shown in Fig. 8, right [17] (for more details, see Ref. [3]). So the interaction with spectators again plays an important role as one of the source for the diffractive factorisation breaking.

The $Q\bar{Q}$ production amplitudes in diffractive quark scattering off a proton target are related to the effective dipole cross sections $\Sigma_{1,2}$ for colorless $g\bar{q}q$ and $g\bar{Q}Q$ systems as

$$A_{\mathrm{BR}} \quad \propto \quad \Phi_{\mathrm{BR}}(\vec{\rho}, \vec{s})\Sigma_1(\vec{\rho}, \vec{s}) \sim \langle s^2 \rangle \sim \frac{1}{m_Q^2} \,, \tag{9}$$

$$A_{\mathrm{PR}} \quad \propto \quad \Phi_{\mathrm{PR}}(\vec{\rho}, \vec{s})\Sigma_2(\vec{\rho}, \vec{s}) \sim \vec{s} \cdot \vec{\rho} \sim \frac{1}{m_q m_Q} \,, \tag{10}$$

where $\Phi_{\mathrm{BR/PR}}$ are complicated distribution amplitudes for the $q + g \rightarrow (Q\bar{Q}) + q$ subprocess. The bremsstrahlung contribution is of a higher twist

195

effect and is therefore suppressed while for diffractive Abelian radiation it is equal to zero. In opposite, the production contribution is of the leading twist and is thus much larger than the bremsstrahlung term in analogy to the diffractive DY reaction. This is again due to the presence of spectators at large distances from the $Q\bar{Q}$ pair despite of non-Abelian nature of the process which is a rather non-trivial fact. The non-Abelian interactions, however, introduce extra important leading-twist terms into the "production" mechanism, which are independent of the structure of the hadronic wave function, in addition to those from the spectators' interactions.

The leading-twist behavior $1/m_Q^2$ of the diffractive cross section is confirmed by E690 [20] and CDF [21] data as demonstrated in Fig. 9 (left panel), where the corresponding cross sections for charm, beauty and top quarks, $p + p \rightarrow Q\bar{Q}X + p$, are shown as functions of c.m.s. $pp$ energy. Besides, on the right panel we show differential cross section in $x_1$-variable, $d\sigma/dx_1$, for diffractive charm quark production at two different energies $\sqrt{s} = 0.5$ and 14 TeV.

# 5   Diffractive Higgs production

## 5.1   Higgsstrahlung

Consider single diffractive Higgs boson production in hadron-hadron collisions. The Higgs boson decouples from light quarks, in particular, due to a smallness of the corresponding Yukawa coupling so the Higgsstrahlung by light hadrons is vanishingly small. Although a light projectile quark does not radiate the Higgs boson directly, it can do it via production of heavy flavors. Similarly to the diffractive $Q\bar{Q}$ production considered above, the diffractive Higgsstrahlung process off a heavy quark is dominated by the diagrams involving interactions of spectators at large transverse separations as illustrated in Fig. 10.
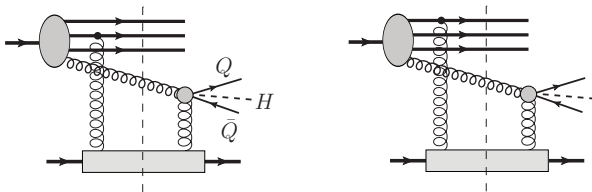


Figure 10: Typical Feynman graphs for the diffractive Higgsstrahlung process off a heavy quark which involve interations of spectator partons.

Therefore, the Higgsstrahlung mechanism is closely related to the non-Abelian mechanism for diffractive heavy quark production discussed in the

previous section. In a sense, it is also similar to diffractive DY, $Z^0$ and $W^\pm$ production since in all these cases the radiated particle does not participate in the interaction with the target although $gg \rightarrow Q\bar{Q} + H$ subprocess is rather involved and more complicated Fock states containing heavy flavors need to be resolved by the exchanged gluons.
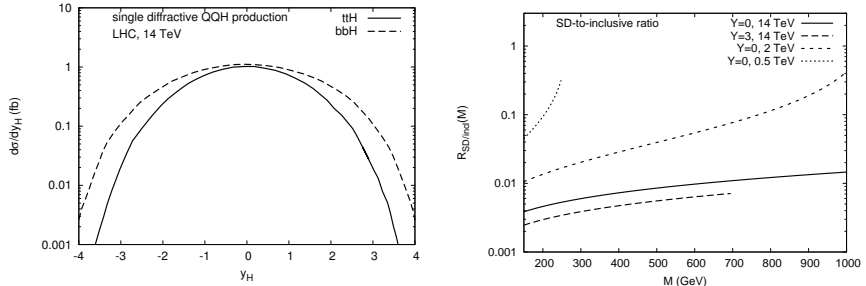


Figure 11: The differential cross section of single diffractive Higgs boson production in association with a heavy quark ($b\bar{b}$ and $t\bar{t}$) pair vs Higgs boson rapidity (left panel) and the SD-to-inclusive ratio for the Higgsstrahlung process as a function of the $Q\bar{Q}H$ invariant mass (right panel) (see more details in Ref. [22]).

The rapidity-dependent cross section of diffractive Higgs boson production off $t\bar{t}$ and $b\bar{b}$ at the LHC energy $\sqrt{s} = 14$ TeV is plotted in Fig. 11 (left panel). At Higgs mid-rapidities, the top and bottom contributions are comparable to each other, whereas top quark provides a wider rapidity distribution and dominates at large Higgs boson transverse momentum [22]. The total cross section is rather small and below 1 fb. In Fig. 11 (right panel) we present the SD-to-inclusive ratio of the corresponding Higgsstrahlung cross sections for different c.m. energies $\sqrt{s} = 0.5, 7, 14$ TeV and for two values of the Higgs boson rapidities $Y = 0$ and 3 as functions of $\bar{Q}QH$ invariant mass. This ratio is in overall agreement with the corresponding data for diffractive beauty production [21].

As expected from above discussion, the diffractive factorisation in diffractive Higgsstrahlung is broken by transverse motion of spectator valence quarks in the projectile hadron leading to a growth of the SD-to-inclusive ratio with the hard scale, $M$, and its descrease with $\sqrt{s}$. Such a behavior is opposite to the one predicted by diffractive factorisation and is in full analogy with the diffractive Abelian radiation.

## 5.2  Diffractive Higgs from intrinsic heavy flavours

The Higgs boson can also be diffractively produced due to fusion of the intrinsic heavy flavours (IQ) in light hadrons, $\bar{Q}Q \rightarrow H$, as is depicted in Fig. 12, left.
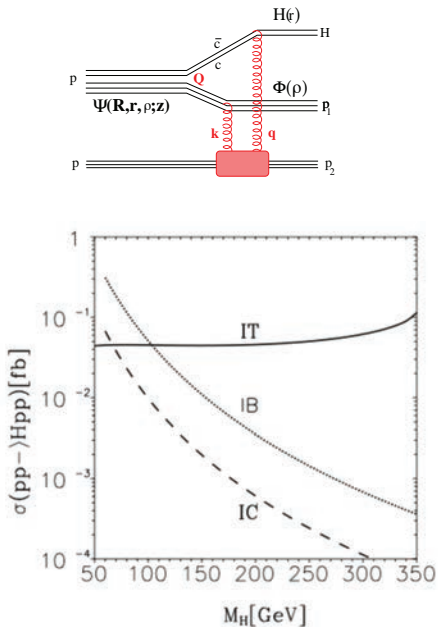
Figure 12: *Upper panel:* The two-gluon exchange diagram for the Higgs exclusive production via coallicense of intrinsic heavy quarks, $\bar{Q}Q \to H$. *Bottom panel:* The cross section of diffractive exclusive Higgs production off different intrinsic flavors as a function of the Higgs boson mass [23].

Such exclusive Higgs production process, $pp \to Hpp$ was analysed in Refs. [23, 24].

The diffractive cross section has the form,

$$\frac{d\sigma(pp \to ppH)}{dx_2 \, d^2p_1 \, d^2p_2} = \frac{1}{(1-x_2)16\pi^2} \left| A(x_2, \vec{p}_1, \vec{p}_2) \right|^2 \; , \quad (11)$$

where the diffractive amplitude in Born approximation reads,

$$
\begin{aligned}
A(x_2, \vec{p}_1, \vec{p}_2) &= \frac{8}{3\sqrt{2}} \quad d^2Q \, \frac{d^2q}{q^2} \frac{d^2k}{k^2} \, \alpha_s(q^2)\alpha_s(k^2) \\
&\times \quad \delta(\vec{q} + \vec{p}_2 + \vec{k}) \, \delta(\vec{k} - \vec{p}_1 - \vec{Q}) \\
&\times \quad d^2\tau \, |\Phi_p(\tau)|^2 \left[ e^{i(\vec{k}+\vec{q})\cdot\vec{\tau}/2} - e^{i(\vec{q}-\vec{k})\cdot\vec{\tau}/2} \right] \\
&\times \quad d^2R \, d^2r \, d^2\rho \, H^\dagger(\vec{r}) \, e^{i\vec{q}\cdot\vec{r}/2} \left( 1 - e^{-i\vec{q}\cdot\vec{r}} \right) \\
&\times \quad \Phi_p^\dagger(\vec{\rho}) e^{i\vec{k}\cdot\vec{\rho}/2} \left( 1 - e^{-i\vec{k}\cdot\vec{\rho}} \right) \Psi_p(\vec{R}, \vec{r}, \vec{\rho}, z) \, e^{i\vec{Q}\cdot\vec{R}}. \quad (12)
\end{aligned}
$$

198

Here $(1-x_1)(1-x_2) = M_H^2/s$. $\Psi_p(\vec{R}, \vec{r}, \vec{\rho}, z)$ is the light-cone wave function of the IQ component of the projectile proton with transverse separations $\vec{R}$ between the $\bar{c}c$ and $3q$ clusters, $\vec{r}$ between the $c$ and $\bar{c}$, $\vec{Q}$ is the relative transverse momentum of the $3q$ and $\bar{c}c$ clusters in the projectile and $\vec{\rho}$ is the transverse separation of the quark and diquark which couple to the final-state proton $p_2$. The density $|\Phi_p(\tau)|^2$ is the wave function of the target proton which we also treat as a color dipole quark-diquark with transverse separation $\tau$. (The extension to three quarks is straightforward [9]). The fraction of the projectile proton light-cone momentum carried by the $\bar{c}c$, $z \approx 1 - x_1$. This wave function is normalized as,

$$\int_0^1 dz \quad d^2R\, d^2r\, d^2\rho \left| \Psi_p(\vec{R}, \vec{r}, \vec{\rho}, z) \right|^2 = P_{IQ} \ , \tag{13}$$

where $P_{IQ}$ is the weight of the IC component of the proton, which is suppressed as $1/m_Q^2$ [25], and is assumed to be $P_{IC} \sim 1\%$. The amplitudes $H(\vec{r})$ and $\Phi_p(\vec{\rho})$ denote the wave functions of the produced Higgs and the outgoing proton, respectively, in accordance with Fig. 12, left.

At the measured Higgs mass value 125 GeV the intrinsic bottom and top provide comparable contributions as can be seen in Fig. 12, right. Comparing the Higgsstrahlung cross section off the produced heavy quarks, i.e. $gg \to Q\bar{Q}H$, and that off the intrinsic component one concludes that the intrinsic contribution to the diffractive Higgs boson production can be relevant at forward Higgs boson rapidities $y_H > 3.5$ [22].

# 6   Summary

Factorization of short and long-distance interactions is heavily broken in hard diffractive hadronic collisions. In particular, forward diffractive radiation of direct photons, Drell-Yan dileptons, and gauge bosons Z, W, by a parton is forbidden. Nevertheless, a hadron can diffractively radiate in the forward direction due to a possibility of soft interaction with the spectators. This property of abelian radiation breaks down diffractive factorization resulting in a leading twist dependence on the boson mass, $1/M^2$.

Non-abelian forward diffractive radiation of heavy flavors is permitted even for an isolated parton. However, interaction with spectators provides the dominant contribution to the cross section. It comes from the interplay between large and small distances. Data well confirm the leading twist behavior.

Diffractive higgsstrahlung is possible due to a double-step process, via heavy quark production. Therefore, the main contribution comes for Higgs production in association with a heavy quark pair. Another important contribution to diffractive Higgs production comes from coalescence of intrinsic

heavy quarks in the proton. For $M_H = 125\,\mathrm{GeV}$ dominance of intrinsic bottom and top is expected.

# References

[1] J. C. Collins, D. E. Soper and G. F. Sterman, Adv. Ser. Direct. High Energy Phys. **5**, 1 (1989).

[2] B. Z. Kopeliovich, I. K. Potashnikova, I. Schmidt, Braz. J. Phys. **37**, 473 (2007).

[3] R. Pasechnik, B. Kopeliovich and I. Potashnikova, Adv. High Energy Phys. **2015**, 701467 (2015).

[4] G. Ingelman, P. E. Schlein, Phys. Lett. **B152** 256 (1985).

[5] UA8 Collaboration, A. Brandt et al., Phys. Lett. **B297**, 417 (1992); **B421**, 395 (1998).

[6] R. J. Glauber, Phys. Rev. 100, 242 (1955).

[7] E. Feinberg and I. Ya. Pomeranchuk, Nuovo. Cimento. Suppl. 3 (1956) 652.

[8] M. L. Good and W. D. Walker, Phys. Rev. 120 (1960) 1857.

[9] B. Z. Kopeliovich, L. I. Lapidus and A. B. Zamolodchikov, JETP Lett. **33**, 595-597 (1981) [Pisma Zh. Eksp. Teor. Fiz. **33**, 612 (1981)].

[10] B. Z. Kopeliovich, A. Schäfer and A. V. Tarasov, Phys. Rev. **D62**, 054022 (2000).

[11] B. Z. Kopeliovich, proc. of the workshop Hirschegg 95: Dynamical Properties of Hadrons in Nuclear Matter, Hirschegg January 16-21, 1995, ed. by H. Feldmeyer and W. Nörenberg, Darmstadt, 1995, p. 102 [hep-ph/9609385].

[12] B. Z. Kopeliovich, A. V. Tarasov and A. Schäfer, Phys. Rev. C **59**, 1609 (1999).

[13] B. Z. Kopeliovich and B. Povh, Z. Phys. A **356**, 467 (1997).

[14] B. Z. Kopeliovich, I. K. Potashnikova, I. Schmidt, A. V. Tarasov, Phys. Rev. **D74**, 114024 (2006).

[15] R. S. Pasechnik and B. Z. Kopeliovich, Eur. Phys. J. C **71**, 1827 (2011).

[16] R. Pasechnik, B. Kopeliovich and I. Potashnikova, Phys. Rev. D **86**, 114039 (2012).

[17] B. Z. Kopeliovich, I. K. Potashnikova, I. Schmidt and A. V. Tarasov, Phys. Rev. D **76**, 034019 (2007).

[18] K. Wijesooriya, P. E. Reimer and R. J. Holt, Phys. Rev. C **72**, 065203 (2005) [nucl-ex/0509012].

[19] B. Z. Kopeliovich, J. Nemchik, I. K. Potashnikova, M. B. Johnson and I. Schmidt, Phys. Rev. C **72**, 054606 (2005) [hep-ph/0501260].

[20] M. H. L. S. Wang, M. C. Berisso, D. C. Christian, J. Felix, A. Gara, E. Gottschalk, G. Gutierrez and E. P. Hartouni *et al.*, Phys. Rev. Lett. **87**, 082002 (2001).

[21] T. Affolder *et al.* [CDF Collaboration], Phys. Rev. Lett. **84**, 232 (2000).

[22] R. Pasechnik, B. Z. Kopeliovich and I. K. Potashnikova, Phys. Rev. D **92**, no. 9, 094014 (2015).

[23] S. J. Brodsky, B. Kopeliovich, I. Schmidt and J. Soffer, Phys. Rev. D **73**, 113005 (2006).

[24] S. J. Brodsky, A. S. Goldhaber, B. Z. Kopeliovich and I. Schmidt, Nucl. Phys. B **807**, 334 (2009).

[25] M. Franz, M. V. Polyakov and K. Goeke, Phys. Rev. D **62**, 074024 (2000).

# Heavy flavors in nucleus-nucleus and proton-nucleus collisions

**Marzia Nardi**

Istituto Nazionale di Fisica Nucleare - Sezione di Torino
Via P. Giuria 1 - 10125 Torino (Italy)

**Abstract.**
A multi-step setup for heavy-flavor studies in high-energy nucleus-nucleus (AA) and proton-nucleus (pA) collisions is presented. The propagation of the heavy quarks in the medium is described in a framework provided by the relativistic Langevin equation, here solved using weak-coupling transport coefficients. Successively, the heavy quarks hadronize in the medium. We compute the nuclear modification factor and the elliptic flow parameter of the final $D$ mesons both in AA and in pA collisions and compare our results to experimental data.[1]

## 1   Introduction

The primary goal of the ongoing heavy-ion collision experiments at the Relativistic Heavy Ion Collider (RHIC) and at the Large Hadron Collider (LHC) is to create and study a new state of matter, the Quark-Gluon Plasma (QGP), where quarks and gluons are no longer confined, but can freely move over distances much larger than the typical hadronic size.

A nucleus-nucleus collision is a very complicated process undergoing several stages: right after the first interaction between the incident nuclei (or proton and nucleus) a dense system of partons is produced, which shortly reach a thermal equilibrium (at least locally) and form the QGP. It then expands, cools down and decades into a system of interacting hadrons. The hadronic interactions cease when the system, still expanding and cooling, is too dilute. The final hadrons (or their decay products) are then detected in the experimental apparatus.

Many observables has been proposed to study the properties of the QGP. Among them, the heavy quarks (charm and beauty) play a special role, for the following reasons:

- their mass $M$ is much larger than $\Lambda_{QCD}$: it is possible to compute cross sections and $p_T$ spectra with perturbative techiques from the QCD theory (next-to-lead order calculations are, presently, the "status of the art");

---

[1]Work done in collaboration with A. Beraudo, A. De Pace, M. Monteno and F. Prino (INFN, Torino)

- $M$ in also larger than the average temperature of the medium formed in the collision: their thermal production is expected to be negligible both in the plasma and, even more, in the hadronic phase;

- they are created at the very beginning of the collision between the two incident nuclei (or proton and nucleus) and witness all the subsequent evolution;

- $M \gg gT$, with $gT$ being the typical momentum exchange in the collision with the plasma particle: many soft scattering are needed to change significantly the momentum (and trajectory) of the heavy quark[2]; therefore heavy quarks do not thermalize with the medium in the later stage, they do not loose "memory" of their initial momentum and energy and carry precious information about the QGP phase.

In a series of papers [1, 2, 3, 4] over the last few years we developed a complete setup (referred to as POWLANG) for the study of heavy flavour observables in high-energy nucleus-nucleus (AA) collisions, describing the initial hard production of the $Q\overline{Q}$ pairs and the corresponding parton-shower stage through the POWHEG-BOX package [5, 6] and addressing the successive evolution in the plasma through the relativistic Langevin equation. Here, following Ref. [4], we supplement our numerical tool by modeling the hadronization of the heavy quarks accounting for the presence of a surrounding medium made of light thermal partons feeling the collective flow of the local fluid cell. Moreover, we present our first results for proton-nucleus (pA) collisions at LHC energies.

# 2   Heavy flavour in proton-proton collisions

Because of their large mass, the initial production of $c$ and $b$ quarks is a short-distance process involving a large-momentum transfer, described by perturbative QCD (pQCD). For this purpose we rely on a standard pQCD public tool, namely POWHEG-BOX, in which the hard $Q\overline{Q}$ event is interfaced with a shower stage described by PYTHIA [7], to include the effects of Initial- and Final-State Radiation [1, 2].

Experimental data obtained in proton-proton (pp) collisions can be exploited to validate the theoretical calculations used to simulate the initial hard $Q\overline{Q}$ production. In our setup, the heavy quarks are created in pairs by the POWHEG-BOX event generator. Their momenta are not back-to-back neither along the beam-axis, due to the different Bjorken-$x$ carried by the partons taking part in the hard event, nor in the azimuthal plane, due to the gluon radiation occurring during the hard process or the shower stage

---

[2]For realistic temperature $g \sim 2$, so the present condition, at least in the initial stage of the evolution, is only marginally fulfilled by charm quarks.
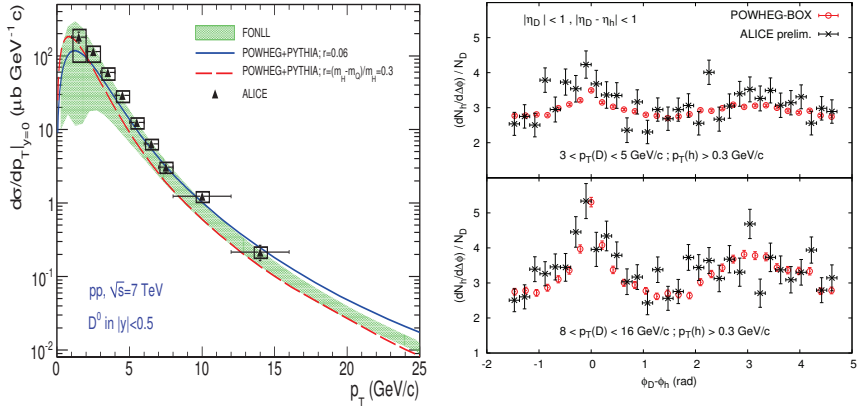
Figure 1: Results for *pp* collisions at $\sqrt{\underline{s}_{NN}} = 7$ TeV compared to experimental data by the ALICE Collab. [8, 10, 11]. Left: $p_T$ spectrum for $D^0$ mesons. Right: azimuthal $D-h$ correlations for different $p_T$-cuts.

and also to the intrinsic $k_T$-broadening one can include in the simulation. Eventually, heavy-quark hadronization and the final decays of the $D$ ($B$) mesons are simulated with PYTHIA, which is also used to describe the parton shower stage.

In Fig. 1 we show some results for *pp* collisions. In the left panel, the inclusive $p_T$ distribution of $D^0$ mesons [3] is compared to experimental data measured by the ALICE collaboration [8]. Also shown is the FONLL systematic uncertainty band [9]. The right panel shows $D-h$ azimuthal correlations compared to preliminary ALICE data [10, 11], for two different $p_T$-intervals of the charmed meson. In our simulation $D^0$, $\bar{D}^0$ and $D^\pm$ are used as trigger particles and the light hadrons are limited to charged pions and kaons, protons and antiprotons, excluding the weak decays of $\Lambda$ and $K^0$. Any $D$-meson is correlated with all the light hadrons (except its own decay products) created in the same event. The near-side peak takes contribution both from correlations present at the partonic level (from $Q\overline{Q}$ pairs arising from gluon splitting) and from hadrons coming from the fragmentation of the same string of the parent heavy quark. Our results include also the simulation of the Underlying Event due to Multiple Parton Interactions, performed with PYTHIA 6.4, which gives rise to the pedestal observed in Fig. 1.

The agreement between the results of POWHEG+PYTHIA event generator and the experimental data is quite good: this makes us confident that the production process is reasonably well described and can be used as a starting point for the simulation of AA and pA collisions.

# 3 Heavy flavour in pA and AA collisions: initial conditions

In nuclear collisions the $c\bar{c}$ or $b\bar{b}$ production given by the pQCD calculation must be modified in two ways: $i$) the nuclear parton distribution functions should be corrected for shadowing or antishadowing effects (we have adopted here the EPS09 scheme [12]); $ii$) the colliding partons acquire, on average, a larger transverse momentum during the crossing of the two nuclei (Cronin effect), which can be estimated by a Glauber calculation [2].

Moreover, their initial positions are distributed in the transverse plane according to the density of nucleon-nucleon collision, as computed in the (optical) Glauber model.

The heavy quarks created in nuclear collisions propagate in a strongly interacting and non-static medium, whose properties and evolution is described through hydrodynamical calculations, performed with the viscous 2+1 code of Ref. [13] (for the AA case), or with ECHO-QGP [14] (for the pA case, in 2+1 dimensions for simplicity). The assumption of longitudinal boost-invariance (implicit in the 2+1 description) restricts the validity of our calculation to a limited region around mid-rapidity.

While for the initial conditions in AA collisions one can adopt the smooth results provided by an optical-Glauber calculation, in a pA collision the event-by-event fluctuations in the initial state are extremely important, since they are the main source of anisotropic flow in the final state.

We assumed that each nucleon-nucleon collisions, occurring at the transverse coordinate $\mathbf{x}_i$ in a give initial distribution (the single nucleons being randomly located with a distribution probability given by a realistic nuclear density), deposit some entropy in the transverse plane, distributed according to a gaussian form centered around the scattering position and depending on the smearing parameter $\sigma$. For the numerical calculation we tested two values of $\sigma$ : 0.2 and 0.4 fm.

The total entropy distribution thus results in:

$$s(\mathbf{x}) = \frac{K}{2\pi\sigma^2} \sum_{i=1}^{N_{coll}} \exp\left[-\frac{(\mathbf{x} - \mathbf{x}_i)^2}{2\sigma^2}\right] \tag{1}$$

The multiplicative constant $K$ can be fixed, for instance, by matching the initial entropy density calculated with the Glauber Model in the optical approximation and in the Monte Carlo simulation. The initial eccentricity, which translate into a non-vanishing elliptic flow [15], can be then evaluated as (the brackets denote the average in the transverse plane, with the entropy density in Eq. 1 as a weight):

$$\epsilon_2 = \frac{\sqrt{\{y^2 - x^2\}^2 + 4\{xy\}^2}}{\{y^2 + x^2\}} \quad .$$
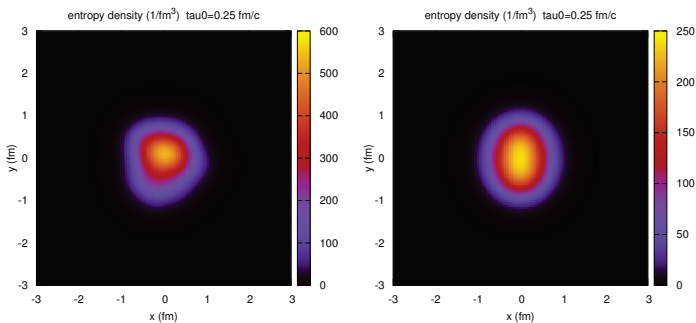
Figure 2: The initial entropy-density profile for a single p-Pb collision at $\sqrt{s_{NN}} = 5.02$ TeV (left panel) and the result of the weighted average of the 0-20% most central events (right panel).

Since a full event-by-event simulation with our hydro+transport setup would be really demanding, for the huge computing and storage resources required, we evaluate a realistic average background as follows: for a given centrality class we average over all the events of the considered percentile (based on the number of $N_{\text{part}}$); After rotating each of them by the event-plane angle $\psi_2$, we compute an average entropy-density distribution from which a realistic average eccentricity $\epsilon_2$ can be obtained. In Fig. 2 we shown an example of a single event (left) and the average distribution (right), for a p-Pb collision at $\sqrt{s_{NN}} = 5.02$ TeV.

# 4 Propagation of the Heavy Quarks through the medium

The time evolution of the heavy-quark phase-space distribution $f_Q(t, x, \boldsymbol{p})$ can be described by the Boltzmann equation:

$$\frac{\mathrm{d}}{\mathrm{d}t} f_Q(t, x, \boldsymbol{p}) = \mathcal{C}[f_Q] \ ; \tag{2}$$

$\mathcal{C}[f_Q]$ is the Boltzmann collision integral, taking into account losses and gains due to single-particle collisions [16]:

$$\mathcal{C}[f_Q] = \int \mathrm{d}\boldsymbol{k} \left[ w(\boldsymbol{p} + \boldsymbol{k}, \boldsymbol{k}) f_Q(\boldsymbol{p} + \boldsymbol{k}) - w(\boldsymbol{p}, \boldsymbol{k}) f_Q(\boldsymbol{p}) \right] \ ,$$

where $w(p, k)$ is the transition rate for a heavy quark changing its momentum from $\boldsymbol{p}$ to $\boldsymbol{p} - \boldsymbol{k}$.

Neglecting $x$- and mean field dependence of $f_Q$ and expanding the collision integral for small momentum exchange (Landau approximation [17]) the collision integral can be expressed as:

$$\mathcal{C}[f_Q] \simeq \quad \mathrm{d}\boldsymbol{k} \left[ k^i \frac{\partial}{\partial p^i} + \frac{1}{2} k^i k^j \frac{\partial^2}{\partial p^i \partial p^j} \right] [w(\boldsymbol{p}, \boldsymbol{k}) f_Q(t, \boldsymbol{p})] ;$$

the Boltzmann equation reduces to the Fokker-Planck equation:

$$\frac{\partial}{\partial t} f_Q(t, \boldsymbol{p}) = \frac{\partial}{\partial p^i} \left\{ A^i(\boldsymbol{p}) f_Q(t, \boldsymbol{p}) + \frac{\partial}{\partial p^j} [B^{ij}(\boldsymbol{p}) f_Q(t, \boldsymbol{p})] \right\}$$

where

$$A^i(\boldsymbol{p}) \quad = \quad \mathrm{d}\boldsymbol{k}\, k^i w(\boldsymbol{p}, \boldsymbol{k}) = A(p) p^i$$

$$B^{ij}(\boldsymbol{p}) \quad = \quad \frac{1}{2} \quad \mathrm{d}\boldsymbol{k}\, k^i k^j w(\boldsymbol{p}, \boldsymbol{k}) = B_0(p) + (\delta^{ij} - \hat{p}^i \hat{p}^j) B_1(p) .$$

The problem is reduced to the evaluation of three transport coefficients: a friction term $A(p)$ and two terms describing the momentum broadening $B_0(p)$ and $B_1(p)$.

The Fokker-Planck equation can be then recast into a form suitable to follow the dynamics of each individual quark: the Langevin equation

$$\frac{\Delta p^i}{\Delta t} = -\eta_D(p) p^i + \xi^i(t),$$

with the properties of the noise encoded in

$$\langle \xi^i(\boldsymbol{p}_t) \xi^j(\boldsymbol{p}_{t'}) \rangle = b^{ij}(\boldsymbol{p}_t) \frac{\delta_{tt'}}{\Delta t} \qquad b^{ij}(\boldsymbol{p}) = \kappa_{\parallel}(p) \hat{p}^i \hat{p}^j + \kappa_{\perp}(p)(\delta^{ij} - \hat{p}^i \hat{p}^j) .$$

The transport coefficients $\kappa_{\perp}$ and $\kappa_{\parallel}$ can be calculated within a weakly-coupled scenario: perturbative QCD and "Hard Thermal Loop" (HTL) approximation, as done in Ref. [1]. We note that the transport coefficients computed with pQCD+HTL have a strong dependence on the momentum $p$ of the heavy quark and on the temperature $T$ of the system.

The Langevin approach is a very convenient numerical tool and allows one to establish a link between observables and transport coefficients derived from QCD. However, it was derived starting from a soft-scattering expansion of the collision integral $\mathcal{C}[f]$ truncated at second order (friction and diffusion terms): in Ref. [16] it was found that this approximation is excellent for $b$-quarks for all the evolution of the system, while for $c$- quarks it is valid, in a short time interval of a few fm/c after the initial collision, only for small momenta.

Having all the ingredients, we can now procede to simulate the heavy-quark propagation in the medium. This occurs through several steps, repeated iteratively until hadronization:

1. a heavy quark with momentum $p$ is located in a position $\boldsymbol{x}$ at the time $t$: the hydrodynamical simulation tells us the conditions (temperature $T(\boldsymbol{x}, t)$, energy density $\varepsilon(\boldsymbol{x}, t)$, four-velocity $u^{\mu}(\boldsymbol{x}, t)$,...) of the surrounding fluid cell;

2. we perform a Lorentz boost in the local fluid rest-frame and set the transport coefficients using the temperature and the momentum $\tilde{p}$ of the quark (in this reference system);

3. we use the Langevin equation to compute the new quark momentum $\tilde{p}'$ and its new position $\tilde{\boldsymbol{x}}'$ at the time $t + \Delta t$;

4. we perform another Lorentz boost back to the laboratory frame; we check whether the surrounding fluid cell is in the QGP phase (i.e. its temperature is higher than the deconfining temperature $T_{dec}$: if so, we restart from step 1, otherwise the quark hadronizes.

The time step used in our simulation is $\Delta t = 0.02$ fm/c, for the deconfining temperature $T_{dec}$ we have tested two values: $T_{dec} = 155$ MeV (the value quoted in Lattice calculation for the QGP-hadron transition) and $T_{dec} = 170$ MeV, allowing the heavy quarks to form bound states with light quarks which may survive, in a small temperature range, in the deconfined phase [18].

# 5    Hadronizations of the Heavy Quarks

Finally, after the propagation through the dense medium, the heavy quarks decouple and hadronize. In the pp case, the hadronization is performed with PYTHIA, while for the nuclear collisions we introduce a new simple model to take into account the effect of the thermalized medium.

Once a heavy quark $Q$, during its stochastic propagation in the fireball, has reached a fluid cell below the decoupling temperature $T_{\text{dec}}$, it is forced to hadronize. One extracts then a light antiquark $\overline{q}$ (up, down or strange, with relative thermal abundances dictated by the ratio $m/T_{\text{dec}}$) from a thermal momentum distribution corresponding to the temperature $T_{\text{dec}}$ in the local rest frame of the fluid; the local fluid four-velocity $u^{\mu}$ allows one to boost the momentum of $\overline{q}$ to the laboratory frame. A string is then constructed joining the endpoints given by $Q$ and $\overline{q}$ and is then given to PYTHIA 6.4 to simulate its fragmentation into hadrons (and their final decays). In case the invariant mass of the string is not large enough to allow its decay into at least a pair of hadrons the event is resampled, extracting a new thermal parton to associate to the heavy quark.

With this hadronization scheme we can first of all provide a realistic estimate of the role of the thermal light quarks to explain peculiar features of the $D$ meson spectra at low and moderate $p_T$; secondly, the complete
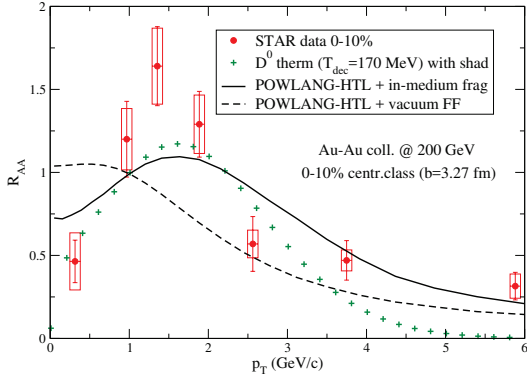
Figure 3: The $R_{AA}$ of $D^0$ mesons in central Au-Au collisions at $\sqrt{s_{NN}} = 200$ GeV. POWLANG results obtained with HTL transport coefficients and a decoupling temperature $T_{\text{dec}} = 170$ MeV are plotted. Also shown for comparison is the extreme case of full kinetic thermalization of $D$ mesons. Theory curves are compared to STAR data [STAR(2014)]

information on all the final state particles arising from the fragmentation of the strings allows us to provide theory predictions for observables like $D-h$, $e-h$, $e^+-e^-$... angular correlations to be compared to existing data and possibly used as a guidance to future measurements.

Notice that further possible interactions in the hadronic phase, which might enhance the elliptic flow, are here neglected: we plan to include them in our future work.

# 6    Results: AA collisions

In Fig. 3 we show some POWLANG outcomes for the $R_{AA}$ of $D^0$ mesons in central $(0-10\%)$ Au-Au collisions at $\sqrt{s_{NN}} = 200$ GeV. HTL transport coefficients are employed and the difference between the two hadronization schemes (here taken to occur at $T_{\text{dec}} = 170$ MeV, either with vacuum fragmentation or with in-medium string fragmentation, are clearly visible: in the second case the radial flow of the light thermal parton leads to the development of a bump around $p_T \sim 1.5$ GeV in qualitative agreement with the experimental data. Also shown for comparison is the result for the limiting scenario in which charmed particles reach full kinetic equilibrium with the medium [4]. Our results are compared to STAR data[STAR(2014)].

The ALICE Collaboration has released the data for the in-plane/out-of-plane nuclear modification factors of D mesons in semi-central (30- 50%) Pb-Pb collisions [19] displayed in Fig. 4 and compared to the transport
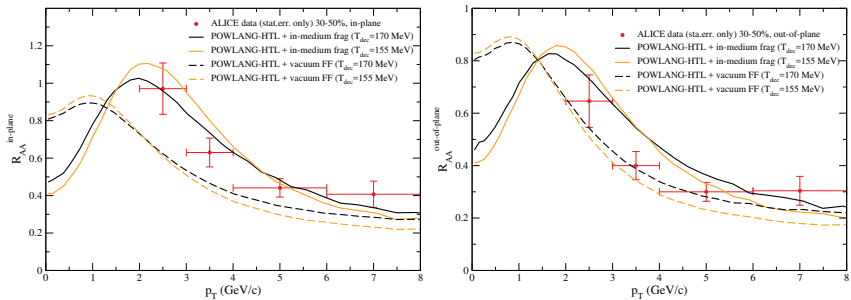
Figure 4: $R_{AA}$ in-plane (left) and out-of-plane (right) of $D$ mesons. AL-ICE data in the $30-50\%$ centrality class [19] are compared to POWLANG results obtained with different hadronization mechanisms (in-medium and vacuum fragmentation) and decoupling temperatures ($T_{\text{dec}} = 170$ MeV and 155 MeV).

predictions of the POWLANG setup: also in this case model results with in-medium fragmentation look in better agreement with the experimental data. The theoretical results are given for two different values of the deconfining temperature: we notice that the nuclear modification factor $R_{AA}$ is not very sensitive to the value of $T_{\text{dec}}$.

In Fig. 5 we address the $v_2$ of $D$ mesons in semicentral (30-50%) Pb-Pb collisions at $\sqrt{s_{NN}} = 2.76$ TeV at the LHC. The effect of the new procedure for in-medium hadronization through string fragmentation is clearly visible: while POWLANG outcome with standard in-vacuum fragmentation of charm largely underpredicts the observed $v_2$, the additional flow acquired from the light thermal partons move the theory curves with in-medium hadronization closer to the experimental data measured by the ALICE Collaboration [ALICE(2013)]. The value chosen for the decoupling temperature is $T_{\text{dec}} = 155$ MeV; we observed that $v_2$ is more sensitive to $T_{\text{dec}}$ than other observables, the lower value seeming to be preferred by the data: this agrees with the expectation that the elliptic flow needs more time to fully develop with respect to the quenching of the spectra. This plot also shows how a full kinetic thermalization up to large values of $p_T$ is disfavoured by the data.

Finally we address more differential observables like angular correlations between heavy flavour particles (or their decay products) and the charged hadrons produced in the same collision. In Fig. 6 we display our results for $D-h$ azimuthal correlations. All figures are obtained with weak-coupling HTL transport coefficients in the QGP phase. In general one observes a strong suppression of the away-side peak around $\Delta\phi = \pi$. Depending on the cuts imposed on the trigger particles ($D$-mesons) and on the associated hadrons this can be mostly due either to the energy loss (moving particles
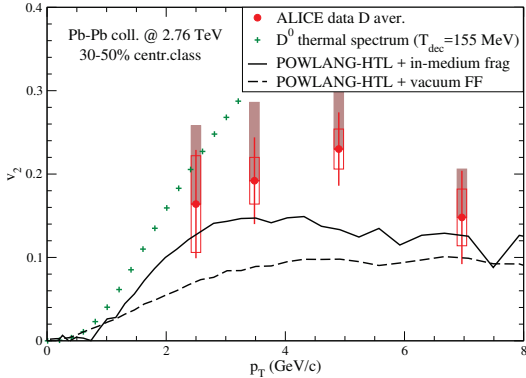
Figure 5: The $v_2$ of $D$ mesons in Pb-Pb collisions at $\sqrt{s_{NN}} = 2.76$ TeV. POWLANG results (with HTL transport coefficients) with in-vacuum and in-medium HQ fragmentation at the decoupling temperature $T_{\text{dec}} = 155$ MeV compared to ALICE data [ALICE(2013)] in the 30-50% centrality class and to the limit of kinetic thermalization.

below the $p_T$-cut) or to the angular decorrelation (moving particles away from $\Delta\phi = \pi$) of the parent heavy quark.

# 7    Results: pA collisions

For quite some time, it was commonly believed that in pA collision the formation of QGP can not occur, because the small size of the system does not allow to reach a sufficiently dense system in thermal equilibrium. Such measurements were considered just a benchmark to estimate cold nuclear-matter effects. However, the first experimental data on central p-Pb collisions at the LHC and d-Au (and $^3$He-Au) at RHIC may suggest the formation of a medium with collective behaviour even in such small systems.

It is therefore very important to make accurate simulations of these processes in order to give a correct interpretation of current experimental data.

We show some preliminary POWLANG results for $c$-quarks in p-Pb collisions at LHC. Work is still in progress to extend to calculation to the bottom quarks and to simulate d-Au collisions at RHIC.

In Fig. 7 we show how the formation of a hot deconfined medium in the p-Pb collision at $\sqrt{s_{NN}} = 5.02$ TeV affects the heavy quark and hadron spectra, by modifying their propagation and subsequent hadronization. The left panel shows the nuclear modification factor for $c$-quarks: the dashed line shows the result for the quarks produced by initial-state interaction,
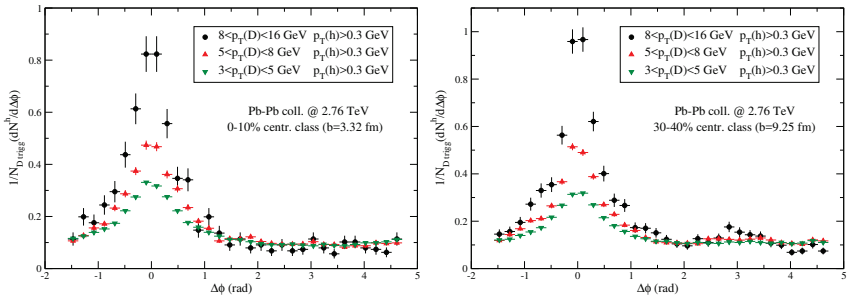
Figure 6: $D - h$ correlations in Pb-Pb collisions at $\sqrt{s_{\text{NN}}} = 2.76$ TeV for various $p_T$ cuts on the trigger particle and different centrality classes: 0–10% (left) and $30 - 40\%$ (right).

according to the EPS09 parton distribution functions (before the propagation in the expanding medium); the dotted and solid lines give the analogous result for the charm quarks after the propagation (both for central and minimum bias collisions, with two different choices of the smearing parameter od Eq. 1). The difference between the EPS09 curve and the other ones is a clear evidence of the effect of Langevin dynamics on the $c$-quark even in such a small system. In the right panel we show the result for the final $D$ meson, with the hadronization occurring in the medium as explained in Sec. 5. The peak at $p_T = 3 \div 4$ GeV/c (more pronounced for $\sigma = 0.2$ fm) is a consequence of the radial flow of light quarks inherited by the meson. The POWLANG result is compatible, within errorbars, with the experimental data measured by the ALICE Collaboration [20].

In Fig. 8 the elliptic flow coefficient $v_2$ is plotted, both for $c$-quarks (dotted lines) and for $D$ mesons, for a deconfining temperature of 155 MeV. Again, the contribution of the light-quark flow, inherited by the charmed meson in the hadronization process, is crucial to enhance the $v_2$.

# 8  CONCLUSIONS

The simple model to describe heavy quark hadronization in the presence of a hot deconfined medium (a Quark-Gluon Plasma) has considerably improved the agreement of the POWLANG results with the experimental data at RHIC and LHC energies. In particular, results for the nuclear modification factors and the elliptic flow of D mesons have been presented.

Recently, signatures of final-state medium effects were observed also in pA collisions: we have presented some preliminary results for p-Pb collisions at LHC energies, and we plan to continue this study in more detail in the
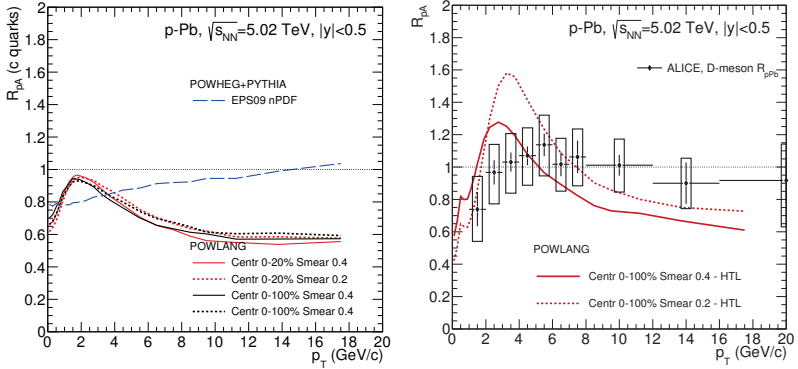
Figure 7: The nuclear modification factor of *c*-quarks (left) and for *D* mesons (right) in p-Pb collisions at $\sqrt{s_{NN}} = 5.02$ TeV. POWLANG results (with HTL transport coefficients) with in-medium heavy-quark fragmentation, for $\sigma = 0.2$ and 0.4 fm. Experimental data from Ref. [20]

next future.

# References

[1] A. Beraudo, A. De Pace, W.M. Alberico, A. Molinari, Nucl. Phys. A **831**, 59 (2009)

[2] W.M. Alberico, A. Beraudo, A. De Pace, A. Molinari, M. Monteno, M. Nardi, F. Prino, Eur. Phys. J. C **71**, 1666 (2011)

[3] W.M. Alberico, A. Beraudo, A. De Pace, A. Molinari, M. Monteno, M. Nardi, F. Prino, M. Sitta, Eur.Phys.J. **C73**, 2481 (2013)

[4] A. Beraudo, A. De Pace, M. Monteno, M. Nardi and F. Prino, Eur.Phys.J. **C75**, 121 (2015) 3

[5] S. Frixione, P. Nason, G. Ridolfi, JHEP 0709 (2007) 126.

[6] S. Alioli, P. Nason, C. Oleari and E. Re, JHEP 1006 (2010) 043.

[7] T. Sjostrand, S. Mrenna and P.Z. Skands, JHEP 0605 (2006) 026.

[8] ALICE Collaboration (B.I. Abelev et al.), J. High Energy Phys. **1201**, 128 (2012)

[9] M. Cacciari, M. Greco, P. Nason, J. High Energy Phys. **9805**, 007 (1998); J. High Energy Phys. **0103**, 006 (2001)
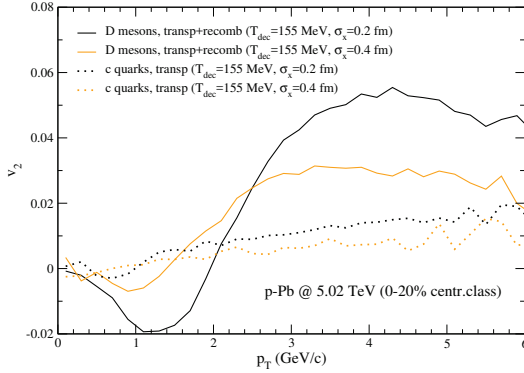
Figure 8: The $v_2$ of D mesons in p-Pb collisions at $\sqrt{s_{NN}} = 5.02$ TeV. POWLANG results (with HTL transport coefficients) with in-medium heavy-quark fragmentation, for $\sigma = 0.2$ and 0.4 fm. The $v_2$ coefficients for c-quarks alone are plotted for comparison.

[10] S. Bjelogrlić (ALICE Collab.), Nucl. Phys A **931**, 563 (2014)

[11] A. Rossi (ALICE Collab.), Nucl. Phys A **932**, 51 (2014)

[12] K.J. Eskola, H. Paukkunen, C.A. Salgado, J. High Energy Phys. **0904**, 065 (2009)

[13] P. Romatschke, U. Romatschke, Phys. Rev. Lett. **99**, 172301 (2007).

[14] ECHO-QGP project: `http://theory.fi.infn.it/echoqgp`

[15] H. Niemi, K. J. Eskola and R. Paatelainen, arXiv:1505.02677 [hep-ph].

[16] V. Greco et al., Phys. Rev. **C 90** (2014) 4, 044901

[17] B. Svetitsky Phys. Rev. **D 37**, 2484 (1988)

[18] W. M. Alberico et al. Phys. Rev. D **72** (2005) 114011.

[STAR(2014)] L.Adamczyk *et al.* (STAR Collab.), arXiv:1404.6185 [nucl-ex].

[19] ALICE Collaboration (B. Abelev *et al.*) 2014 *Phys. Rev.* C **90** 034904

[ALICE(2013)] B. Abelev (ALICE Collaboration), Phys. Rev. Lett. **111** (2013) 102301.

[20] B. B. Abelev (ALICE Collaboration), Phys. Rev. Lett. **113** (2014) 23, 232301.

# Highlights in elastic and inelastic diffraction at the LHC

László Jenkovszky[1], Rainer Schicker[2] and István Szanyi[3]

*[1]Bogolyubov Institute for Theoretical Physics (BITP), Ukrainian National Academy of Sciences, 14-b, Metrologicheskaya str., Kiev, 03680, UKRAINE; jenk@bitp.kiev.ua*

*[2]Physikalisches Institut, Im Neuenheimer Feld 226, Heidelberg University, 69120 Heidelberg, GERMANY; schicker@physi.uni-heidelberg.de*

*[3]Uzhgorod National University, 14, Universytets'ka str., Uzhgorod, 88000, UKRAINE; sz.istvan03@gmail.com*

Diffractive phenomena at the LHC are studied by several collaborations there. In this paper we present our recent results connected with the current and future studies at the LHC, namely the deviation of the exponential behaviour in elastic proton-proton scattering at low values of |t| and central exclusive resonance production. Although the above phenomena occur in different kinematical regions, they are related e.g. by Regge-factorization.

Deviation from the exponential behaviour of the diffraction cone observed near $t = -0.1 \text{ GeV}^2$ both at the ISR and the LHC (so-called break) follows from a two-pion loop in the $t$-channel imposed by unitarity. By using a simple Regge-pole model we extrapolate the "break" from the ISR energy region to that of the LHC. A model for Pomeron-Pomeron total cross section in the resonance region $\sqrt{M^2} \leq 5 \text{ GeV}$ is also presented.

Central production is treated in a Regge pole including the Pomeron and two different $f$ trajectories, as well as an isolated $f_0(500)$ resonance in the region $\sqrt{M^2} \lesssim 1 \text{ GeV}$. A slowly varying background is included. The presented Pomeron-Pomeron cross section is not directly measurable, but is an essential ingredient for calculating exclusive resonance production at the LHC.

## I. Introduction

Following TOTEM's impressive results [1] on the low-$t$ measurements of the $pp$ differential cross section at $8 \text{ TeV}$, and anticipating their new measurements at $13 \text{ TeV}$ announced recently we find it appropriate to remind of the physics behind the observed departure from the exponential behavior of the forward diffraction cone.

For the first time this phenomenon was observed in 1972 at the CERN ISR [2], a deflection from the exponential behaviour of the forward cone in proton-proton scattering around $-t = 0.1 \text{ GeV}^2$, detected at several energies.

Experimentalists [1,2] quantify the departure from the linear exponential by replacing

$$|A^N| = ae^{bt} \rightarrow |A^N| = ae^{b_1 t + b_2 t^2 + b_3 t^3 + \cdots} \tag{1}$$

with coefficients $b_i$ fitted to the data.

This effect can be well fitted [3] also by a relevant form factor (residue function) in the Regge-pole scattering amplitude. For a complete and up-to-date review see [4].

Soon after the ISR measurements, the phenomenon was interpreted [5] as manifestation of $t$-channel unitarity, producing a two-pion loop, as shown in Fig. 1, and resulting in a relevant threshold singularity in the Pomeron trajectory. This effect, for brevity called the "break", was confirmed by recent measurements by the TOTEM Collaboration at the CERN LHC, first at 8 TeV [1] and subsequently at 13 TeV.
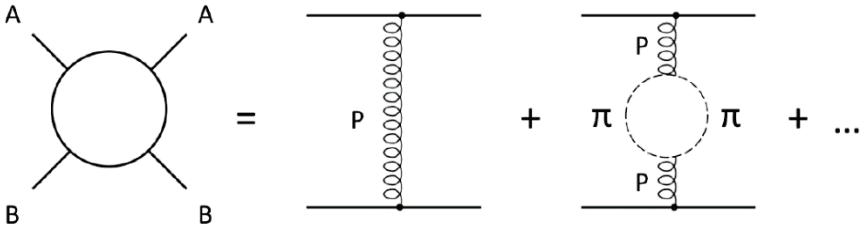


**Figure 1:** Feynman diagram for elastic scattering with a $t$-channel exchange containing a branch point at $t = 4m_\pi^2$.

The new LHC data from TOTEM at 8 TeV confirm the conclusions made [5] about the nature of the break and call for a more detailed analysis of the phenomenon. The new data triggered further theoretical work in this direction [6, 7], but many issues still remain open. Although the curvature, both at the ISR and the LHC is concave, convex cannot be excluded in other reactions and/or new energies. While the departure from a linear exponential was studied in details both at the ISR and LHC energies, an extra(inter)polation between the two is necessary to clarify the uniqueness of the phenomenon. This is a challenge for the theory, and it can be done within Regge-pole models. Below we do so by using a very simple one, with two Regge exchanges, a Pomeron and a secondary effective Reggeon. To test its viability, we first fit its parameters to the proton-proton total section data and calculate the $\rho$-parameter from this fit (Sec. II a).

Central production in proton-proton collisions has been studied in the energy range from the ISR at CERN up to the presently highest LHC energies [8]. Ongoing data analysis include data taken by the COMPASS collaboration at the SPS [9], the CDF collaboration at the TEVATRON [10], the STAR collaboration at RHIC [11], and the ALICE and LHCb collaborations at the LHC [12, 13]. The analysis of events recorded by the large and complex detector systems requires the simulation of such events to study the experimental acceptance and efficiency. Much larger data samples are expected in the next few years both at RHIC and at the LHC allowing the study of differential distributions with much improved

statistics. The purpose of the ongoing work presented here is the formulation of a Regge pole model for simulating such differential distributions.

In Sec. II we introduce a simple Regge-pole model, normalizing its energy dependence to $pp$ total, elastic, inelastic cross section data. By Regge-extrapolating the cross section from the ISR energy region to that of the ISR, we map the "break" fitted at the ISR to that seen at the LHC. Sec. III is dedicated to Pomeron-Pomeron scattering in central exclusive diffractive proton-proton scattering, based on the papers [14, 15]. These result should precede further studies including proton-proton scattering. Work in this direction is in progress.

## II. Low-|t| diffraction at the LHC

The basic premise behind our approach is the introduction of a two-pion loop contribution in the $t$-channel through Regge trajectories, that are non-linear complex functions. As shown by Barut and Zwanziger [16], $t$-channel unitarity constrains the Regge trajectories near the $t$-channel threshold, $t \rightarrow t_0$ by

$$\text{Im}\alpha(t) \sim (t - t_0)^{Re\alpha(t_0) + \frac{1}{2}}, \qquad (2)$$

where $t_0$ is the lightest threshold, $4m_\pi^2$ in the case of the vacuum quantum numbers (Pomeron or $f$ meson). Since $Re\alpha(t_0)$ is small, a square-root threshold is a reasonable approximation to the above constrain. Higher threshold, inevitable in the trajectory, may be approximated by their power expansion, i.e. by a linear term, as in Eqs. (5). This point is closely related also to the choice of the relevant interval in $t$ under study. Note that the threshold singularity is at positive $t = 4m_\pi^2$, while the "break" is observed at negative $t$, "symmetric" to $4m_\pi^2$. This reflection is a property of analytic functions. The concave departure from the linear exponential, observed in the interval $0 \lesssim |t| \lesssim 0.3 \text{ GeV}^2$ can be fitted by a single square-root threshold in the trajectory, but it would not reproduce the subsequent ($-t \gtrsim 0.3 \text{ GeV}^2$) linearity of the exponential cone, persistent up to the dip (t $\approx -1.4 \text{ GeV}^2$ at the ISR or $-0.6 \text{ GeV}^2$ at the LHC). Note also that we treat only the strong (nuclear) amplitude, separated from Coulombic forces.

Thus, the "break" (in fact a smooth deflection of the linear exponential) of the cone, has a relatively narrow location around $-t \approx 0.1 \pm 0.01 \text{ GeV}^2$, both at the ISR and the LHC energies, whereupon it recovers its exponential shape, followed by the dip, whose position is strongly energy-dependent.

In the present paper we study the "break" within a simple Regge-pole model, assuming the universality of this phenomenon in high-energy hadron scattering.

## II a.  A simpler Regge-pole model

For our purposes we use a simple Regge pole model with a supercritical Pomeron [17], its daughter and an effective Reggeon contributions, denoted by $A_f$, close (but not similar) to the $f$ Reggeon,

$$A(s,t) = A_P(s,t) + A_{P1}(s,t) + A_f(s,t), \tag{3}$$

where

$$A_P(s,t) = -a_P e^{b_P \alpha_P(t)} e^{-\frac{i\pi\alpha_P(t)}{2}} (s/s_{0P})^{\alpha_P(t)}, \tag{4.1}$$

$$A_{P1}(s,t) = -a_{P1} e^{b_P(\alpha_P(t)-1)} e^{-\frac{i\pi(\alpha_P(t)-1)}{2}} (s/s_{0P1})^{(\alpha_P(t)-1)}, \tag{4.2}$$

$$A_f(s,t) = -a_f e^{b_f \alpha_f(t)} e^{-\frac{i\pi\alpha_f(t)}{2}} (s/s_{0f})^{\alpha_f(t)}, \tag{4.3}$$

with the trajectories

$$\alpha_P(t) = \alpha_{0P} + \alpha'_P t - \alpha_{1P}\left(\sqrt{4m_\pi^2 - t} - 2m_\pi\right), \tag{5.1}$$

$$\alpha_f(t) = \alpha_{0f} + \alpha'_f t - \alpha_{1f}\left(\sqrt{4m_\pi^2 - t} - 2m_\pi\right). \tag{5.2}$$

We use the norm:

$$\sigma_{tot}(s) = \frac{4\pi}{s} Im A(s, t = 0), \tag{6.1}$$

$$\frac{d\sigma(s,t)}{dt} = \frac{\pi}{s^2}|A(s,t)|^2, \tag{6.2}$$

and

$$\sigma_{el}(s) = \int_{t_{min}}^{t_{max}} \frac{d\sigma(s,t)}{dt} dt, \tag{7.1}$$

$$\sigma_{inel}(s) = \sigma_{tot}(s) - \sigma_{el}(s), \tag{7.2}$$

$$\rho(s) = \frac{ReA(s, t = 0)}{ImA(s, t = 0)}. \tag{7.3}$$

The model contains 15 free parameters ($a_P(\sqrt{mbGeV^2})$, $b_P$ (dimensionless), $\alpha_{0P}$ (dimensionless), $\alpha'_P t$ (GeV$^{-2}$), $\alpha_{1P}$ (GeV$^{-1}$), $s_{0P}$ (GeV$^2$), $a_{P1}(\sqrt{mbGeV^2})$, $b_{P1}$ (dimensionless), $s_{0P1}$ (GeV$^2$), $a_f$ ($\sqrt{mbGeV^2}$), $b_f$ (dimensionless), $\alpha_{0f}$ (dimensionless), $\alpha'_f t$ (GeV$^{-2}$), $\alpha_{1f}$ (GeV$^{-1}$), $s_{0f}$ (GeV$^2$)) most of which are known a priori, needing only fine-tuning.

Anticipating detailed fits to the low-$|t|$ data, we start with a simple fit to the data on proton-proton total cross section starting from $10\,\text{GeV}$ then we calculate the $\rho$-parameter. All of our fits in this paper we fixed $s_{0P} = s_{0P1} = s_{0f} = 1\,\text{GeV}^2$. The results of fits are shown in Fig. 2 and values of fitted parameters are presented in Table I. Preliminary results were published in [18].
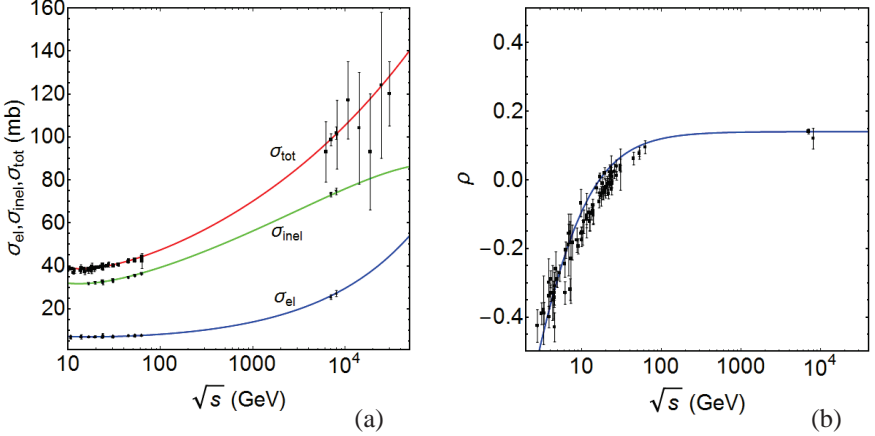


**Figure 2:** Results of fits (a) total, elastic, inelastic cross sections and (b) the $\rho$-parameter [19-22].

| $\alpha_{0P}$ | 1.0889 | $\alpha_{0f}$ | 0.5305 |
|---|---|---|---|
| $a_P$ | 1.497 | $a_f$ | 2.5426 |
| $b_P$ | 0.9553 | $b_f$ | 3.8115 |
| $\chi^2/dof$ | 13.261 | $a_{P1}$ | 5.2324 |
| $dof$ | 68 | $b_{P1}$ | 5.2946 |

**Table I:** Values of fitted parameters for total cross section.

## II b. Mapping the "low-energy" break upon that at the LHC

At the ISR the proton-proton differential cross section was measured at $\sqrt{s} = 23.5,\ 30.7,\ 44.7,\ 52.8$ and $62.5\,\text{GeV}$ [23], in the interval $0.01 < -t < 0.35\,\text{GeV}^2$. In all the above energy intervals the differential cross section changes its slope near $-t = 0.1\,\text{GeV}^2$ by about two units of $\text{GeV}^2$. By using a simple Regge pole model with two Regge exchanges - the Pomeron and an effective sub-leading trajectory we map the "break" fitted at the ISR onto the TOTEM 8 TeV data. The results are shown in Fig. 3 and the values of the fitted parameters are presented in Table II.

From these fits we calculate the relevant local slopes

$$B(s,t) = \frac{d}{dt} ln \frac{d\sigma}{dt} \tag{8}$$

and, anticipating the comparison with the LHC data, here we present the ISR data also in the normalized form, used by TOTEM [1] as

$$R(s,t) = \frac{d\sigma/dt - ref}{ref}, \tag{9}$$

where $ref = Ae^{Bt}$. The calculated local slopes are shown in Fig. 4 and R ratios are shown in Fig. 5 (for more details see [18]).
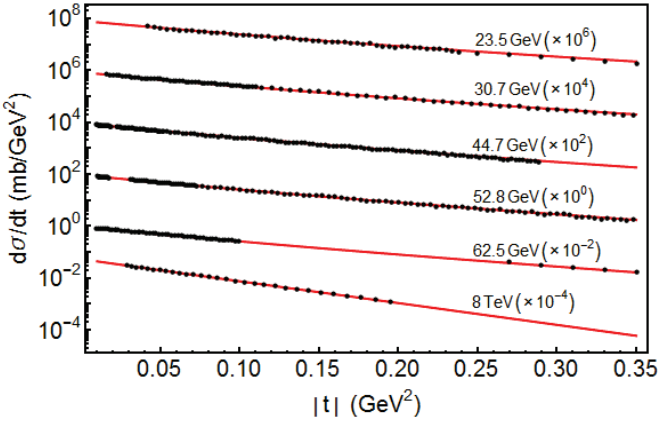


**Figure 3:** Result of our extrapolation form ISR to LHC.

| | | | |
|---|---|---|---|
| $\alpha_{0P}$ | 1.1242 | $\alpha_{0f}$ | 0.94147 |
| $\alpha'_P$ | 0.52929 | $\alpha'_f$ | 0.92396 |
| $\alpha_{1P}$ | -0.034649 | $\alpha_{1f}$ | -0.024453 |
| $a_P$ | 0.51963 | $a_f$ | 0.056968 |
| $b_P$ | 1.2248 | $b_f$ | 4.8092 |
| $\chi^2/dof$ | 0.4587 | $a_{P1}$ | 5.2324 (fixed) |
| $dof$ | 469 | $b_{P1}$ | 5.2946 (fixed) |

**Table II:** Values of fitted parameters in our extrapolation from ISR [23] to the LHC [1].

(a) ISR 52.8 GeV        (b) LHC 8 TeV (TOTEM)

**Fig. 4**: Local slopes.



(a) ISR 52.8 GeV        (b) LHC 8 TeV (TOTEM)
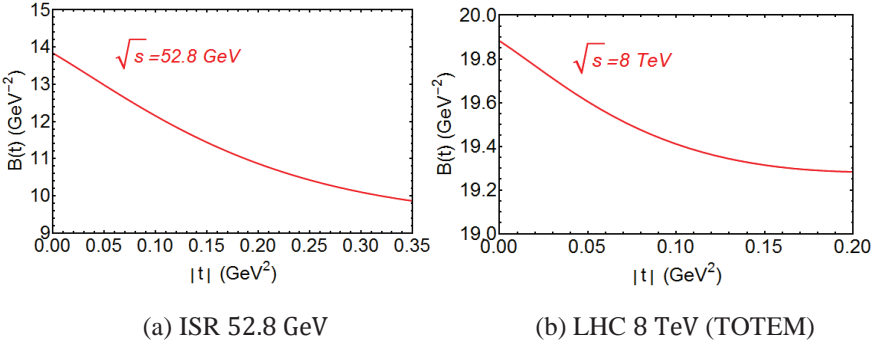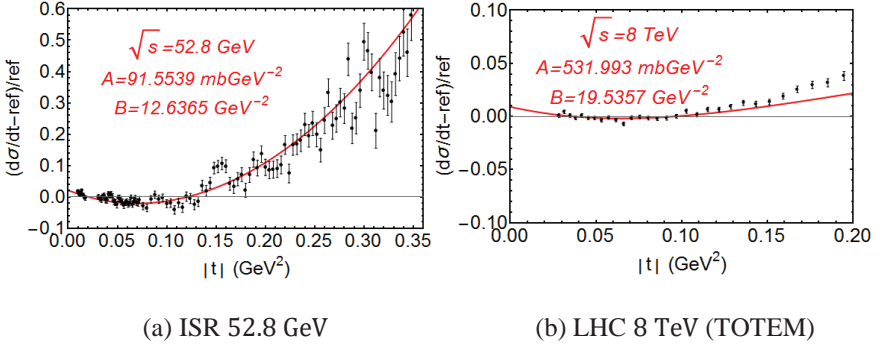
**Figure 5**: R ratios.

## III. Central production

The study of central production in hadron-hadron collisions is interesting for a variety of reasons. Such events are characterized by a hadronic system formed at mid-rapidity, and by the two very forward scattered protons, or remnants thereof. The rapidity gap between the mid-rapidity system and the forward scattered proton is a distinctive feature of such events. Central production events can hence be tagged by measuring the forward scattered protons and/or by identifying the existence of rapidity gaps. Central production is dominated at high energies by Pomeron-Pomeron exchange. The hadronization of this gluon-dominated environment is expected to produce with increased probability gluon-rich states, glueballs and hybrids. Of particular interest are states of exotic nature, such as tetra-quark ($q\bar{q} + \bar{q}q$) configurations, or gluonic hybrids ($q\bar{q} + gluon$).

The production of central events can take place with the protons remaining in the ground state, or with diffractive excitation of one or both of the outgoing protons.
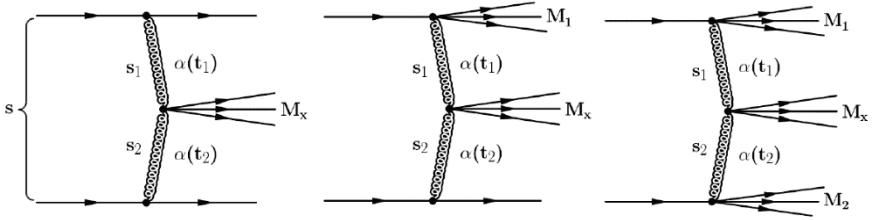


**Figure 6:** Central production event topologies.

The topologies of central production are shown in Fig. 6. This figure shows central production with the two protons in the ground state on the left, and with one and both protons getting diffractively excited in the middle and on the right, respectively. These reactions take place by the exchange of Regge trajectories $\alpha(t_1)$ and $\alpha(t_1)$ in the central region where a system of mass $M_x$ is produced. The total energy $s$ of the reaction is shared by the subenergies $s_1$ and $s_2$ associated to the trajectories $\alpha(t_1)$ and $\alpha(t_1)$, respectively. The LHC energies of $\sqrt{s} = 8$ and 13 TeV are large enough to provide Pomeron dominance. Reggeon exchanges can hence be neglected which was not the case at the energies of previous accelerators.

The main interest in the study presented here is the central part of the diagrams shown in Fig. 6, i.e. Pomeron-Pomeron ($PP$) scattering producing mesonic states of mass $M_x$. We isolate the Pomeron-Pomeron-meson vertex and calculate the PP total cross section as a function of the centrally produced system of mass $M_x$. The emphasis here is the behaviour in the low mass resonance region where perturbative QCD approaches are not applicable. Instead, similar to [24], we use the pole decomposition of a dual amplitude with relevant direct-channel trajectories $\alpha(M^2)$ for fixed values of Pomeron virtualities, $t_1 = t_2 = const$. Due to Regge factorization, the calculated Pomeron-Pomeron cross section is part of the measurable proton-proton cross section [25].

### III a. Dual resonance model of Pomeron-Pomeron scattering

Most of the existing studies on diffraction dissociation, single, double and central, are done within the framework of the triple Reggeon approach. This formalism is useful beyond the resonance region, but is not valid for the low mass region which is dominated by resonances. A formalism to account for production of resonances was formulated in Ref. [26]. This formalism is based on the idea of

duality with a limited number of resonances represented by nonlinear Regge trajectories.
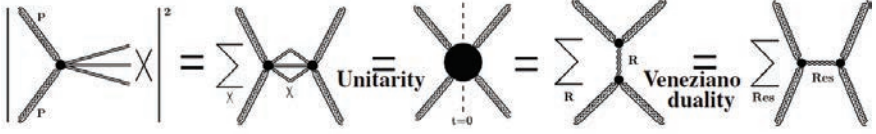


**Figure 7:** Connection, through unitarity (generalized optical theorem) and Veneziano-duality, between the Pomeron-Pomeron cross section and the sum of direct-channel resonances.

The motivation of this approach consists of using dual amplitudes with Mandelstam analyticity (DAMA), and is shown in Fig. 7. For $s \to \infty$ and fixed $t$ it is Regge-behaved. Contrary to the Veneziano model, DAMA not only allows for, but rather requires the use of nonlinear complex trajectories which provide the resonance widths via the imaginary part of the trajectory. A finite number of resonances is produced for limited real part of the trajectory.

For our study of central production, the direct-channel pole decomposition of the dual amplitude $A(M_X^2, t)$ is relevant. This amplitude receives contributions from different trajectories $\alpha_i(M_X^2)$, with $\alpha_i(M_X^2)$ a nonlinear, complex Regge trajectory in the Pomeron-Pomeron system,

$$A(M_X^2, t) = a \sum_{i=f,P} \sum_J \frac{[f_i(t)]^{J+2}}{J - \alpha_i(M_X^2)}. \tag{10}$$

The pole decomposition of the dual amplitude $A(M_X^2, t)$ is shown in Eq. (10), with $t$ the squared momentum transfer in the $PP \to PP$ reaction. The index $i$ sums over the trajectories which contribute to the amplitude. Within each trajectory, the second sum extends over the bound states of spin $J$. The prefactor $a$ in Eq. (10) is of numerical value $a = 1 \text{ GeV}^{-2} = 0.389 \text{ mb}$.

The imaginary part of the amplitude $A(M_X^2, t)$ given in Eq. (10) is defined by

$$ImA(M_X^2, t) = a \sum_{i=f,P} \sum_J \frac{[f_i(t)]^{J+2} Im\alpha_i(M_X^2)}{(J - Re\alpha_i(M_X^2))^2 + (Im\alpha_i(M_X^2))^2}. \tag{11}$$

For the $PP$ total cross section we use the norm

$$\sigma_t^{PP}(M_X^2) = ImA(M_X^2, t = 0). \tag{12}$$

The Pomeron-Pomeron channel, $PP \to M_X^2$, couples to the Pomeron and $f$ channels due to quantum number conservation. For calculating the $PP$ cross section, we therefore take into account the trajectories associated to the $f_0(980)$ and to the $f_2(1270)$ resonance, and the Pomeron trajectory.

223

## III b. Non-linear, complex meson Regge trajectories

Analytic models of Regge trajectories need to derive the imaginary part of the trajectory from the almost linearly increasing real part. We relate the nearly linear real part of the meson trajectory to its imaginary part by following Ref. [27],

$$Re\alpha(s) = \alpha(0) + \frac{s}{\pi} PV \int_0^{\infty} ds' \frac{Im\alpha(s')}{s'(s'-s)} \qquad (13)$$

In Eq. (13), the dispersion relation connecting the real and imaginary part is shown. The imaginary part of the trajectory is related to the decay width by

$$\Gamma(M_R) = \frac{Im\alpha(M_R^2)}{\alpha' M_R} \qquad (14)$$

Apart from the Pomeron trajectory, the direct-channel $f$ trajectory is essential in the $PP$ system. Guided by conservation of quantum numbers, we include two $f$ trajectories, labeled $f_1$ and $f_2$, with mesons lying on these trajectories as specified in Table III.

| | $I^G$ | $J^{PC}$ | traj. | $M$ (GeV) | $M^2$ (GeV$^2$) | $\Gamma$ (GeV) |
|---|---|---|---|---|---|---|
| f$_0$(980) | 0$^+$ | 0$^{++}$ | $f_1$ | 0.990±0.020 | 0.980±0.040 | 0.070±0.030 |
| f$_1$(1420) | 0$^+$ | 1$^{++}$ | $f_1$ | 1.426±0.001 | 2.035±0.003 | 0.055±0.003 |
| f$_2$(1810) | 0$^+$ | 2$^{++}$ | $f_1$ | 1.815±0.012 | 3.294±0.044 | 0.197±0.022 |
| f$_4$(2300) | 0$^+$ | 4$^{++}$ | $f_1$ | 2.320±0.060 | 5.382±0.278 | 0.250±0.080 |
| f$_2$(1270) | 0$^+$ | 2$^{++}$ | $f_2$ | 1.275±0.001 | 1.6256±0.003 | 0.185±0.003 |
| f$_4$(2050) | 0$^+$ | 4$^{++}$ | $f_2$ | 2.018±0.011 | 4.0723±0.044 | 0.237±0.018 |
| f$_6$(2510) | 0$^+$ | 6$^{++}$ | $f_2$ | 2.469±0.029 | 6.096±0.143 | 0.283±0.040 |

**Table III:** Parameters of resonances belonging to the $f_1$ and $f_2$ trajectories.

The real and imaginary part of the $f_1$ and $f_2$ trajectories can be derived from the parameters of the f-resonances listed in Table III, and have explicitly been derived in Ref. [14].

While ordinary meson trajectories can be fitted both in the resonance and scattering region corresponding to positive and negative values of the argument, the parameters of the Pomeron trajectory can only be determined in the scattering region $M^2 < 0$. A comprehensive fit to high-energy $pp$ and $p\bar{p}$ of the nonlinear Pomeron trajectory is discussed in Ref. [25]

$$\alpha_P(M^2) = 1 + \varepsilon + \alpha' M^2 - c\sqrt{s_0 - M^2}, \qquad (15)$$

with $\varepsilon = 0.08$, $\alpha' = 0.25$ GeV$^{-2}$, $s_0$ the two pion threshold $s_0 = 4m_\pi^2$, and $c = \alpha'/10 = 0.025$.

For consistency with the mesonic trajectories, the linear term in Eq. (15) is replaced by a heavy threshold mimicking linear behaviour in the mass region of interest ($M < 5$ GeV),

$$\alpha_P(M^2) = \alpha_0 + \alpha_1\left(2m_\pi - \sqrt{4m_\pi^2 - M^2}\right) + \alpha_2\left(\sqrt{M_H^2} - \sqrt{M_H^2 - M^2}\right), (16)$$

with $M_H$ an effective heavy threshold $M = 3.5$ GeV. The coefficients $\alpha_0$, $\alpha_1$ and $\alpha_2$ are chosen such that the Pomeron trajectory of Eq. (16) has a low energy behaviour as defined by Eq. (15).

### III c. The f₀ (500) resonance

The experimental data on central exclusive pion-pair production measured at the energies of the ISR, RHIC, TEVATRON and the LHC collider all show a broad continuum for pair masses $m_{\pi^+\pi^-} < 1$ GeV/c². The population of this mass region is attributed to the $f_0(500)$. This resonance $f_0(500)$ is of prime importance for the understanding of the attractive part of the nucleon-nucleon interaction, as well as for the mechanism of spontaneous breaking of chiral symmetry. In spite of the complexity of the $f_0(500)$ resonance, and the controversy on its interpretation and description, we take here the practical but simple-minded approach of a Breit-Wigner resonance [19]

$$A(M^2) = a\frac{-M_0\Gamma}{M^2 - M_0^2 + iM_0\Gamma}. \qquad (17)$$

The Breit-Wigner amplitude of Eq. (17) is used below for calculating the contribution of the $f_0(500)$ resonance to the Pomeron-Pomeron cross section.

### III d. Pomeron-Pomeron total cross section

The Pomeron-Pomeron cross section is calculated from the imaginary part of the amplitude by use of the optical theorem

$$\sigma_t^{PP}(M^2) = ImA(M^2, t = 0) =$$
$$= \sum_{i=f,P}\sum_J \frac{[f_i(0)]^{J+2}Im\alpha_i(M^2)}{(J - Re\alpha_i(M^2))^2 + (Im\alpha_i(M^2))^2}. \qquad (18)$$

In Eq. (18), the index $i$ sums over the trajectories which contribute to the cross section, in our case the $f_1$, $f_2$ and the Pomeron trajectory discussed above. Within each trajectory, the summation extends over the bound states of spin $J$ as expressed by the second summation sign. The value $f_i(0) = f_i(t)|_{t=0}$ is not known a priori. The analysis of relative strengths of the states of trajectory $i$ will, however, allow to extract a numerical value for $f_i(0)$ from the experimental data.

The Pomeron-Pomeron total cross section is calculated by summing over the contributions discussed above, and is shown in Fig. 8 by the solid black line.

The prominent structures seen in the total cross section are labeled by the resonances generating the peaks. The model presented here does not specify the relative strength of the different contributions shown in Fig. 8. A Partial Wave Analysis of experimental data on central production events will be able to extract the quantum numbers of these resonances, and will hence allow to associate each resonance to its trajectory. The relative strengths of the contributing trajectories need to be taken from the experimental data.
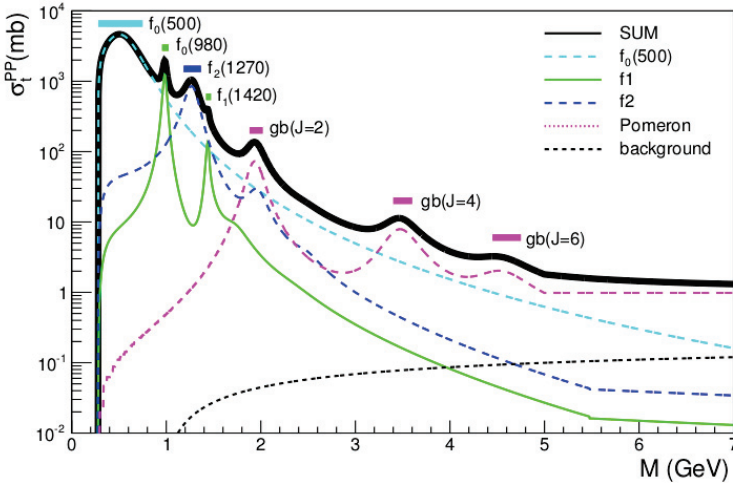


**Figure 8:** Contributions of the $f_0(500)$ resonance, the $f_1$, $f_2$ and the Pomeron trajectory, and of the background to $PP$ total cross section.

## IV. Conclusions

The successful fit to the proton-proton total cross section with a simple model, Fig. 2 shows the efficiency of Regge poles in reproducing energy dependence. Much more complicated is the parametrization of the $t$-dependence, containing irregularities, in particular the "break" under discussion. For a better comparison between the "break" as seen at ISR and that at the LHC, we have refitted the ISR data, normalizing to an exponential "test function" (Fig. 5) as done at the LHC [1, 22].

We have shown that the deviation from a linear exponential of the $pp$ diffraction cone as seen at the ISR, $20.3 \leq \sqrt{s} \leq 62.5$ GeV and at the LHC, $\sqrt{s} = 8$ and 13 TeV are of similar nature: they appear nearly at the same value of $t \approx -0.1$ GeV$^2$, have the same concave shape of comparable "size", $B(t) \approx 2 \div 4$ $GeV^{-2}$ and may be fitted by similar $t$-dependent function. Mapping this $t$-dependence through the tremendous energy span from the ISR to the LHC (almost

3 orders of magnitude) is a highly non-trivial task. We have done it within the simplest Regge pole model, with two trajectories: a leading one, the Pomeron and a sub-leading effective Reggeon. More advanced and refined Regge-type models may improve the fit and clarify details.

The threshold singularity in question should be present also in the $f$ trajectory, however it has secondary effect with respect to the Pomeron.

Note also that the low-$|t|$ structure of the diffraction cone was fitted also [3] by a relevant form factor (Regge residue).

The results presented in this paper leave open and raise also several questions, namely:

1) theoretical calculations of the relative weight of the loop contribution, second term in Fig. 1 relative to the first one ("Born term") are needed;

2) why is the "break" observed only in elastic $pp$ scattering, not in $p\bar{p}$, for example at the Tevatron? Once the Pomeron is universal, the effect should be present also in $p\bar{p}$. Non-observation of any convex or concave curvature in the diffraction cone at the Tevatron may be attributed to poor statistics of the relevant data (lacking Roman pots), preventing the observation of such a tiny effect.

To conclude, we expect more precise data in the low-$|t|$ region on elastic scattering and diffraction dissociation as well as further fits with improved phenomenological parametrizations. Theoretical calculations of the diagram (Fig. 1) may shed more light on the nature of the phenomenon. Needless to say, further attempts in this direction will be based on improved models for the scattering amplitude, with more details on individual Regge trajectories, including the Odderon.

Central exclusive production (CED) is an important ongoing program at the LHC. The present authors are now working on the extension of the model presented in this contribution to include full kinematics involving the "external" protons with their possible diffractive excitation.

### Acknowledgements

### References

[1] G. Antchev *et al.* (TOTEM Collaboration), Nucl. Phys. **B 899** (2015) 527-546, arXiv:1503.08111; T. Csörgő (for the TOTEM Collaboration), Evidence for Non-Exponential Differential Cross-Section of pp Elastic Scattering at Low |t| and $\sqrt{s} = 8$ TeV by TOTEM, arXiv:1602.00219.

[2] B. Barbiellini *et al.* Phys. Letters **B39** (1972) 663.

[3] D.A. Fagundes *et al.* Phys. Rev. **D88** (2013) 094019.

[4] G. Pancheri, Y. N. Srivastava, Introduction to the physics of the total cross-section at LHC: A Review of Data and Models, arXiv:1610.10038; to be published in the European Journal of Physics C.

[5] G. Cohen-Tannoudji *et al.* Lett. Nuov. Cim. **5** (1972) 957.

[6] L. Jenkovszky, A. Lengyel, Acta Phys. Pol. **B 46** (2015) 863; arXiv:1410.4106.

[7] D.A. Fagundes, L. Jenkovszky, E.Q. Miranda, G. Pancheri, P.V.R.G. Silva, Fine structure of the diffraction cone: from the ISR to the LHC, International Journal of Modern Physics A **31**, Nos. 28 & 29 (2016) 1645022, arXiv:1509.02197.

[8] M. Albrow, V. Khoze, Ch. Royon, Special Issue Int. J. Mod. Phys. **A29** (2014) 28.

[9] A. Austregesilo, for the COMPASS Coll., Proc.15th EDS Conference, Sept 2013, arXiv:1310.3190.

[10] M. Albrow, for the CDF Coll., Int. J. Mod.Phys. **A29** (2014) 28, 1446009, arXiv:1409.0462.

[11] L. Adamczyk, W. Guryn and J. Turnau, Int. J. Mod.Phys. **A29** (2014) 28, 1446010, arXiv:1410.5752.

[12] R. Schicker, Int.J.Mod.Phys. **A29** (2014) 28, 1446015, arXiv:1411.1283.

[13] R. McNulty, Int. J. Mod.Phys. **A29** (2014) 28, 1446003, arXiv:1409.8113.

[14] R. Fiore, L. Jenkovszky, R. Schicker, Eur.Phys.J. C76 (2016) no.1, 38, arXiv:1512.04977.

[15] R. Schicker, R. Fiore, L. Jenkovszky, arXiv:1607.04496.

[16] A.O. Barut, D.E. Zwanziger, Phys. Rev. **127** (1962) 974.

[17] S. Donnachie, G. Dosch, P. Landshoff , O. Nachtmann, Pomeron physics and QCD, Cambridge University Press (2002).

[18] L. Jenkovszky, I. Szanyi, Particles and Nuclei Letters, v. 14 (2017) No. 5, arXiv:1701.01269.

[19] K.A. Olive *et al.* (Particle Data Group), Chin. Phys. C, **38**, 090001 (2014).

[20] G. Antchev *et al.* (TOTEM Collaboration), Europhys. Lett. **101**, 21004 (2013).

[21] F. Nemes (for the TOTEM Collaboration), LHC optics and elastic scattering measured by the TOTEM experiment, arXiv:1602.06207;

[22] Antchev, G. et al. (TOTEM Collaboration), arXiv:1610.00603.

[23] http://durpdg.dur.ac.uk/review/pp2/exphtml/CERN-ISR.shtml

[24] L. Jenkovszky, O. Kuprash, J.W. Lamsa, V.K. Magas, and R.Orava, Phys.Rev.D **83** (2011) 056014, arXiv:1011.0664.

[25] L. Jenkovszky, Rivista Nuovo Cim., **10** (1987), p. N12.

[26] R. Fiore, A. Flachi, L. Jenkovszky, A. Lengyel and V. Magas, Phys. Rev. D **69** (2004), 014004, hep-ph/0308178.

[27] R. Fiore, L. Jenkovszky, V. Magas, F. Paccanoni, A. Papa, Eur.Phys.J. A10 (2001) 217-221, hep-ph/0011035.

# Numerical values of $f^F, f^D, f^S$ coefficients in SU(3) invariant interaction Lagrangian of vector-meson nonet with $1/2^+$ octet baryons

Cyril Adamuščín, Erik Bartoš, and Stanislav Dubnička
*Institute of Physics, Slovak Academy of Sciences, Bratislava, Slovakia*

Anna Zuzana Dubničková
*Department of Theoretical Physics,*
*Comenius University, Bratislava, Slovakia*
(Dated: March 13, 2017)

It is shown that experimental information on electric and magnetic nucleon form factors can be used to extract numerical values of $f^F$, $f^D$, $f^S$ coefficients in a SU(3) invariant interaction La-grangian of a vector-meson nonet with $1/2^+$ octet baryons.

## I. INTRODUCTION

The electromagnetic (EM) structure of the hyperons $(\Lambda^0, \Xi^0, \Xi^-, \Sigma^0, \Sigma^+, \Sigma^-)$ remains still largely unknown. However there are plans to measure the $e^+e^- \to \Lambda^0\bar{\Lambda}^0$ process and eventually similar processes for the other hyperons, which will allow to extract theirs time-like EM structure. In this paper we will show, that the link between EM structure of the hyperons and the nucleons exists and it can be used to predict the EM structure of the former.

The hyperons and nucleons together form $1/2^+$ octet of baryons. The strong interaction of such $1/2^+$ octet of baryons with the vector meson nonet can be described by the SU(3) invariant Lagrangian

$$L_{VB\bar{B}} = \frac{i}{\sqrt{2}} f^F [\bar{B}_\beta^\alpha \gamma_\mu B_\gamma^\beta - \bar{B}_\gamma^\beta \gamma_\mu B_\beta^\alpha](V_\mu)_\alpha^\gamma$$
$$+ \frac{i}{\sqrt{2}} f^D [\bar{B}_\gamma^\beta \gamma_\mu B_\beta^\alpha + \bar{B}_\beta^\alpha \gamma_\mu B_\gamma^\beta](V_\mu)_\alpha^\gamma + \frac{i}{\sqrt{2}} f^S \bar{B}_\beta^\alpha \gamma_\mu B_\alpha^\beta \omega_\mu^0, \quad (1)$$

where $f^F, f^D, f^S$ are coefficients of the Lagrangian, $\omega_\mu^0$ is a omega-meson singlet, $B, \bar{B}$ are baryon, anti-baryon octet matrices and $V$ is a vector-meson octet matrice defined as

$$B = \begin{pmatrix} \frac{\Sigma^0}{\sqrt{2}} + \frac{\Lambda^0}{\sqrt{6}} & \Sigma^+ & p \\ \Sigma^- & -\frac{\Sigma^0}{\sqrt{2}} + \frac{\Lambda^0}{\sqrt{6}} & n \\ \Xi^- & \Xi^0 & -\frac{2\Lambda^0}{\sqrt{6}} \end{pmatrix}, \quad (2)$$

$$V = \begin{pmatrix} \frac{\rho^0}{\sqrt{2}} + \frac{\omega_8}{\sqrt{6}} & \rho^+ & K^+ \\ \rho^- & -\frac{\rho^0}{\sqrt{2}} + \frac{\omega_8}{\sqrt{6}} & K^0 \\ K^- & \bar{K}^0 & -\frac{2\omega_8}{\sqrt{6}} \end{pmatrix}. \tag{3}$$

In order to determine numerical values of the $f^F, f^D, f^S$ coefficients, one need to analyze the experimental information on the interaction of the $1/2^+$ baryons with the vector-mesons. According to the vector meson dominance (VMD) hypothesis, the EM interaction between virtual photon and hadrons is mediated by the vector-mesons $\rho, \omega, \phi$, therefore electromagnetic structure of the $1/2^+$ octet of baryons contains sought information. Moreover the well known EM structure of the nucleons is sufficient for extraction of the $f^F, f^D, f^S$ coupling constants values, which can be later used to predict EM structure of hyperons.

## II.   CALCULATION OF THE $f^F, f^D, f^S$ COUPLING CONSTANTS

Considering the SU(3) invariant Lagrangian $L_{VB\bar{B}}$ (1) and $\omega - \phi$ mixing, we get relations between $f^F, f^D, f^S$ and the vector-meson to the nucleon coupling constants $f_{VNN}$ as

$$f_{\rho N\bar{N}} = \frac{1}{2}(f^D + f^F)$$
$$f_{\omega N\bar{N}} = \frac{1}{\sqrt{2}} f^S \cos\theta + \frac{1}{2\sqrt{3}}(3f^F - f^D)\sin\theta$$
$$f_{\phi N\bar{N}} = -\frac{1}{\sqrt{2}} f^S \sin\theta + \frac{1}{2\sqrt{3}}(3f^F - f^D)\cos\theta, \tag{4}$$

where $\theta = 39.1°$ is the $\omega - \phi$ mixing angle [1], which is defined as

$$\phi = \omega_8 \cos\theta - \omega_0 \sin\theta$$
$$\omega = \omega_8 \sin\theta + \omega_0 \cos\theta \tag{5}$$

in order do satisfy Gell-Mann-Okubo mass formula. The inverse relations can be derived for the ground and excited states of the vector mesons and

for both vector an tensor ((1),(2)) types

$$f_{(i)}^F = \frac{1}{2}\left[f_{\rho NN}^{(i)} + \sqrt{3}(f_{\phi NN}^{(i)}\cos\theta + f_{\omega NN}^{(i)}\sin\theta)\right]$$

$$f_{(i)}^D = \frac{1}{2}\left[3f_{\rho NN}^{(i)} - \sqrt{3}(f_{\phi NN}^{(i)}\cos\theta + f_{\omega NN}^{(i)}\sin\theta)\right]$$

$$f_{(i)}^S = \sqrt{2}\left(f_{\omega NN}^{(i)}\cos\theta - f_{\phi NN}^{(i)}\sin\theta\right)$$

$$f_{(i)}^{F'} = \frac{1}{2}\left[f_{\rho' NN}^{(i)} + \sqrt{3}(f_{\phi' NN}^{(i)}\cos\theta' + f_{\omega' NN}^{(i)}\sin\theta')\right]$$

$$f_{(i)}^{D'} = \frac{1}{2}\left[3f_{\rho' NN}^{(i)} - \sqrt{3}(f_{\phi' NN}^{(i)}\cos\theta' + f_{\omega' NN}^{(i)}\sin\theta')\right]$$

$$f_{(i)}^{S'} = \sqrt{2}\left(f_{\omega' NN}^{(i)}\cos\theta' - f_{\phi' NN}^{(i)}\sin\theta'\right), \tag{6}$$

where $i \in \{1, 2\}$. The mixing angle for the excited states $\rho', \omega', \phi'$ is $\theta' = 75.9°$. The values of the vector meson to the nucleon coupling constants $f_{VNN}$ will be extracted from the well known nucleon EM structure described within the U&A approach.

## III. UNITARY AND ANALYTIC APPROACH

We have analyzed known experimental data on the nucleon electromagnetic form factors using the advanced Unitary and Analytic (U&A) nucleon electromagnetic structure model. Such model is inspired by the VMD model saturated by nine vector meson resonances $\rho, \omega, \phi, \rho', \omega', \phi', \rho'', \omega'', \phi''$ and it contains some ratios of the coupling constants $f_{VNN}/f_V$ as free parameters of the model, while others can be fixed from the asymptotic conditions of the nucleon EM FFs. It allows to calculate isoscalar and isovector Dirac

and Pauli EM FFs of the nucleon as

$$
F_{1s}^N[V(t)] = \left(\frac{1-V^2}{1-V_N^2}\right)^4 \left\{ \frac{1}{2} H_{\omega''}(V)H_{\phi''}(V) + \right.
$$

$$
+ \left[ H_{\phi''}(V)H_{\omega'}(V)\frac{(C_{\phi''}^{1s}-C_{\omega'}^{1s})}{(C_{\phi''}^{1s}-C_{\omega''}^{1s})} + H_{\omega''}(V)H_{\omega'}(V)\frac{(C_{\omega''}^{1s}-C_{\omega'}^{1s})}{(C_{\omega''}^{1s}-C_{\phi''}^{1s})} - \right.
$$

$$
\left. - H_{\omega''}(V)H_{\phi''}(V) \right] (f_{\omega'NN}^{(1)}/f_{\omega'}) +
$$

$$
+ \left[ H_{\phi''}(V)H_{\phi'}(V)\frac{(C_{\phi''}^{1s}-C_{\phi'}^{1s})}{(C_{\phi''}^{1s}-C_{\omega''}^{1s})} + H_{\omega''}(V)H_{\phi'}(V)\frac{(C_{\omega''}^{1s}-C_{\phi'}^{1s})}{(C_{\omega''}^{1s}-C_{\phi''}^{1s})} - \right.
$$

$$
\left. - H_{\omega''}(V)H_{\phi''}(V) \right] (f_{\phi'NN}^{(1)}/f_{\phi'}) +
$$

$$
+ \left[ H_{\phi''}(V)L_{\omega}(V)\frac{(C_{\phi''}^{1s}-C_{\omega}^{1s})}{(C_{\phi''}^{1s}-C_{\omega''}^{1s})} + H_{\omega''}(V)L_{\omega}(V)\frac{(C_{\omega''}^{1s}-C_{\omega}^{1s})}{(C_{\omega''}^{1s}-C_{\phi''}^{1s})} - \right.
$$

$$
\left. - H_{\omega''}(V)H_{\phi''}(V) \right] (f_{\omega NN}^{(1)}/f_{\omega}) +
$$

$$
+ \left[ H_{\phi''}(V)L_{\phi}(V)\frac{(C_{\phi''}^{1s}-C_{\phi}^{1s})}{(C_{\phi''}^{1s}-C_{\omega''}^{1s})} + H_{\omega''}(V)L_{\phi}(V)\frac{(C_{\omega''}^{1s}-C_{\phi}^{1s})}{(C_{\omega''}^{1s}-C_{\phi''}^{1s})} - \right.
$$

$$
\left. - H_{\omega''}(V)H_{\phi''}(V) \right] (f_{\phi NN}^{(1)}/f_{\phi}) \right\} \tag{7}
$$

$$
F_{1v}^N[W(t)] = \left(\frac{1-W^2}{1-W_N^2}\right)^4 \left\{ \frac{1}{2} L_{\rho}(W)L_{\rho'}(W) + \right.
$$

$$
+ \left[ L_{\rho'}(W)L_{\rho''}(W)\frac{(C_{\rho'}^{1v}-C_{\rho''}^{1v})}{(C_{\rho'}^{1v}-C_{\rho}^{1v})} + L_{\rho}(W)L_{\rho''}(W)\frac{(C_{\rho}^{1v}-C_{\rho''}^{1v})}{(C_{\rho}^{1v}-C_{\rho'}^{1v})} - \right.
$$

$$
\left. - L_{\rho}(W)L_{\rho'}(W) \right] (f_{\rho NN}^{(1)}/f_{\rho}) \right\}, \tag{8}
$$

$$F_{2s}^N[U(t)] = \left.\frac{1-U^2}{1-U_N^2}\right)^6 \left\{ \frac{1}{2}(\mu_p + \mu_n - 1)H_{\omega''}(U)H_{\phi''}(U)H_{\omega'}(U) + \right.$$

$$+ \left[ H_{\phi''}(U)H_{\omega'}(U)H_{\phi'}(U)\frac{(C_{\phi''}^{2s} - C_{\phi'}^{2s})(C_{\omega'}^{2s} - C_{\phi'}^{2s})}{(C_{\phi''}^{2s} - C_{\omega''}^{2s})(C_{\omega'}^{2s} - C_{\omega''}^{2s})} + \right.$$

$$+ H_{\omega''}(U)H_{\omega'}(U)H_{\phi'}(U)\frac{(C_{\omega''}^{2s} - C_{\phi'}^{2s})(C_{\omega'}^{2s} - C_{\phi'}^{2s})}{(C_{\omega''}^{2s} - C_{\phi'}^{2s})(C_{\omega'}^{2s} - C_{\phi''}^{2s})} +$$

$$+ H_{\omega''}(U)H_{\phi''}(U)H_{\phi'}(U)\frac{(C_{\omega''}^{2s} - C_{\phi'}^{2s})(C_{\phi''}^{2s} - C_{\phi'}^{2s})}{(C_{\omega''}^{2s} - C_{\omega'}^{2s})(C_{\phi''}^{2s} - C_{\omega'}^{2s})} -$$

$$\left. - H_{\omega''}(U)H_{\phi''}(U)H_{\omega'}(U) \right](f_{\phi'NN}^{(2)}/f_{\phi'}) +$$

$$+ \left[ H_{\phi''}(U)H_{\omega'}(U)L_{\omega}(U)\frac{(C_{\phi''}^{2s} - C_{\omega}^{2s})(C_{\omega'}^{2s} - C_{\omega}^{2s})}{(C_{\phi''}^{2s} - C_{\omega''}^{2s})(C_{\omega'}^{2s} - C_{\omega''}^{2s})} + \right.$$

$$+ H_{\omega''}(U)H_{\omega'}(U)L_{\omega}(U)\frac{(C_{\omega''}^{2s} - C_{\omega}^{2s})(C_{\omega'}^{2s} - C_{\omega}^{2s})}{(C_{\omega''}^{2s} - C_{\phi'}^{2s})(C_{\omega'}^{2s} - C_{\phi''}^{2s})} +$$

$$+ H_{\omega''}(U)H_{\phi''}(U)L_{\omega}(U)\frac{(C_{\omega''}^{2s} - C_{\omega}^{2s})(C_{\phi'}^{2s} - C_{\omega}^{2s})}{(C_{\omega''}^{2s} - C_{\omega'}^{2s})(C_{\phi''}^{2s} - C_{\omega'}^{2s})} -$$

$$\left. - H_{\omega''}(U)H_{\phi''}(U)H_{\omega'}(U) \right](f_{\omega NN}^{(2)}/f_{\omega}) +$$

$$+ \left[ H_{\phi''}(U)H_{\omega'}(U)L_{\phi}(U)\frac{(C_{\phi''}^{2s} - C_{\phi}^{2s})(C_{\omega'}^{2s} - C_{\phi}^{2s})}{(C_{\phi''}^{2s} - C_{\omega''}^{2s})(C_{\omega'}^{2s} - C_{\omega''}^{2s})} + \right.$$

$$+ H_{\omega''}(U)H_{\omega'}(U)L_{\phi}(U)\frac{(C_{\omega''}^{2s} - C_{\phi}^{2s})(C_{\omega'}^{2s} - C_{\phi}^{2s})}{(C_{\omega''}^{2s} - C_{\phi''}^{2s})(C_{\omega'}^{2s} - C_{\phi''}^{2s})} +$$

$$+ H_{\omega''}(U)H_{\phi''}(U)L_{\phi}(U)\frac{(C_{\omega''}^{2s} - C_{\phi}^{2s})(C_{\phi''}^{2s} - C_{\phi}^{2s})}{(C_{\omega''}^{2s} - C_{\omega'}^{2s})(C_{\phi''}^{2s} - C_{\omega'}^{2s})} -$$

$$\left. - H_{\omega''}(U)H_{\phi''}(U)H_{\omega'}(U) \right](f_{\phi NN}^{(2)}/f_{\phi}) \right\}, \tag{9}$$

$$F_{2v}^N[X(t)] = \left(\frac{1-X^2}{X_N^2}\right)^6 \left( \frac{1}{2}(\mu_p - \mu_n - 1)L_{\rho}(X)L_{\rho'}(X)H_{\rho''}(X) \right), \tag{10}$$

where $V_N, V(t), W_N, W(t), U_N, Y(t), X_N, X(t), L_v, H_v, C_v^{ij}$ are functions defined within the U&A approach [2]. Then the nucleon Sachs form factors
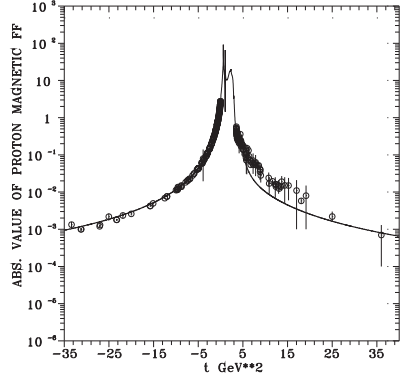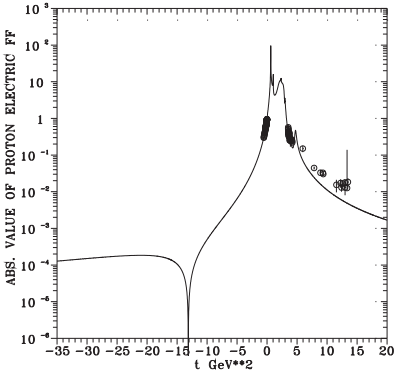
FIG. 1: The proton EM form factors behavior as predicted by the advanced U&A model of the nucleon.
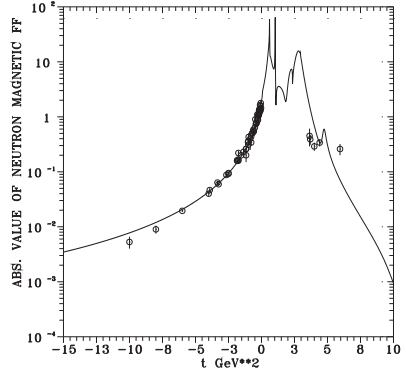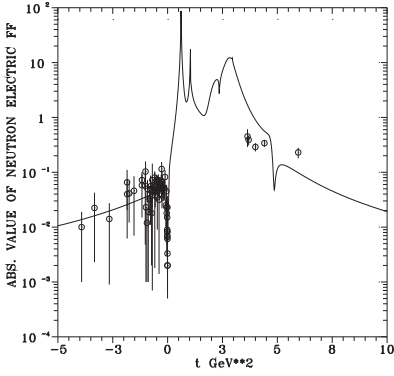


FIG. 2: The neutron EM form factors behavior as predicted by the advanced U&A model of the nucleon.

can be written as

$$G_E^p(t) = [F_{1s}^N(t) + F_{1v}^N(t)] + \frac{t}{4m_p^2}[F_{2s}^N(t) + F_{2v}^N(t)]$$

$$G_M^p(t) = [F_{1s}^N(t) + F_{1v}^N(t)] + 4m_p^2[F_{2s}^N(t) + F_{2v}^N(t)]$$

$$G_E^n(t) = [F_{1s}^N(t) - F_{1v}^N(t)] + \frac{t}{4m_n^2}[F_{2s}^N(t) - F_{2v}^N(t)]$$

$$G_M^n(t) = [F_{1s}^N(t) - F_{1v}^N(t)] + [F_{2s}^N(t) - F_{2v}^N(t)]. \tag{11}$$

The advanced U&A model of the nucleon has 12 free parameter – the effective inelastic thresholds $t_{in}^{1s}, t_{in}^{1v}, t_{in}^{2s}, t_{in}^{2v}$ and ratios of the coupling constants. The best description of the experimental data on the EM form factors of

nucleons can be obtained with following

$$\frac{f_{\omega NN}^{(1)}}{f_\omega} = (1.5717 \pm 0.0022) \qquad \frac{f_{\phi NN}^{(1)}}{f_\phi} = (-1.1247 \pm 0.0011)$$

$$\frac{f_{\omega' NN}^{(1)}}{f_{\omega'}} = (0.0418 \pm 0.0065) \qquad \frac{f_{\phi' NN}^{(1)}}{f_{\phi'}} = (0.1879 \pm 0.0010)$$

$$\frac{f_{\omega NN}^{(2)}}{f_\omega} = (-0.2096 \pm 0.0067) \qquad \frac{f_{\phi NN}^{(2)}}{f_\phi} = (0.2657 \pm 0.0067)$$

$$\frac{f_{\phi' NN}^{(2)}}{f_{\phi'}} = (0.1781 \pm 0.0029) \qquad \frac{f_{\rho NN}^{(1)}}{f_\rho} = (0.3747 \pm 0.0022) \qquad (12)$$

In order to calculate the $f^F, f^D, f^S$ coupling constants later, we need also numerical values of other coupling constant ratios $(f_{\rho' NN}^{(1)}/f_{\rho'}), (f_{\rho NN}^{(2)}/f_\rho), (f_{\rho' NN}^{(2)}/f_{\rho'}), (f_{\omega' NN}^{(2)}/f_{\omega'})$, which can be calculated within the advanced U&A model of the nucleon EM structure

$$\frac{f_{\rho' NN}^{(1)}}{f_{\rho'}} = \frac{1}{2}\frac{C_{\rho''}^{1v}}{C_{\rho''}^{1v} - C_{\rho'}^{1v}} - \frac{C_{\rho''}^{1v} - C_{\rho}^{1v}}{C_{\rho''}^{1v} - C_{\rho'}^{1v}}\frac{f_{\rho NN}^{(1)}}{f_\rho} = 0.7635$$

$$\frac{f_{\rho NN}^{(2)}}{f_\rho} = \frac{\mu_p - \mu_n - 1}{2}\frac{C_{\rho''}^{2v}C_{\rho'}^{2v}}{(C_{\rho'}^{2v} - C_{\rho}^{2v})(C_{\rho''}^{2v} - C_{\rho}^{2v})} = 2.8956$$

$$\frac{f_{\rho' NN}^{(2)}}{f_{\rho'}} = \frac{\mu_p - \mu_n - 1}{2}\frac{C_{\rho''}^{2v}C_{\rho}^{2v}}{(C_{\rho''}^{2v} - C_{\rho'}^{2v})(C_{\rho}^{2v} - C_{\rho'}^{2v})} = -1.3086 \qquad (13)$$

## IV.   UNIVERSAL VECTOR MESON COUPLING CONSTANTS $f_V$

As we are interested in the coupling constants between vector-meson and the nucleon (6), we need to eliminate the universal vector-meson photon coupling $f_V$ ($V \in \{\rho, \omega, \phi, \rho', \omega', \phi'\}$) from the coupling constant ratios obtained from the analysis of the nucleon EM form factors (12,13). The absolute values of the universal vector meson coupling constants $f_\rho, f_\omega, f_\phi$ can be calculated from the existing data on lepton width $\Gamma(V \to e^+ e^-)$ by means of relation

$$\Gamma(V \to e^+ e^-) = \frac{\alpha^2 m_V}{3}\left(\frac{f_V^2}{4\pi}\right)^{-1}. \qquad (14)$$

While the signs of the $f_\rho, f_\omega, f_\phi$ depends on the exact $\omega - \phi$ mixing form. In our case we get

$$f_\rho = 4.9582, \; f_\omega = 17.062, \; f_\phi = 13.4428 \qquad (15)$$

and the values of the coupling constants for the excited vector mesons can be calculated from the theoretical lepton width estimation

$$f_{\rho'} = 13.6491, \ f_{\omega'} = 47.6022, \ f_{\phi'} = 33.6598 \tag{16}$$

## V.   RESULTS

Inserting the values of the coupling constant ratios $(f_{VNN}/f_V)$ (12,13) and the values of the universal vector meson coupling constants $f_V$ (15,16) to the formulas for the Lagrangian $L_{VBB}$ coefficients we get following numerical values

$$
\begin{aligned}
&f^F_{(1)} = 5.414 && f^D_{(1)} = -1.699 && f^S_{(1)} = 42.916 \\
&f^F_{(2)} = 7.626 && f^D_{(2)} = 21.088 && f^S_{(2)} = -7.111 \\
&f^{F'}_{(1)} = 8.343 && f^{D'}_{(1)} = 12.498 && f^{S'}_{(1)} = -7.858 \\
&f^{F'}_{(2)} = -30.450 && f^{D'}_{(2)} = -5.271 && f^{S'}_{(2)} = -18.614.
\end{aligned}
\tag{17}
$$

## VI.   CONCLUSIONS

Using the U&A description of the nucleon electromagnetic structure we were able to extract the coupling constants of the vector mesons with nucleons $f_{VNN}$. These coupling constants were used to calculate the coefficients of the SU(3) Lagrangian $L_{VB\bar{B}} - f^F, f^D, f^S$. In the same manner $f^F, f^D, f^S$ can be used to express the coupling constants of the vector mesons with hyperons $\Lambda^0, \Sigma^0, \Sigma^+, \Sigma^-, \Xi^-, \Xi^0$. and the U&A model can be used to predict hyperons' electromagnetic structure without using any additional data.

## VII.   ACKNOWLEDGMENTS

[1] C. Patrignani *et al.* [Particle Data Group], Chin. Phys. C **40** (2016) no.10, 100001.

[2] S. Dubnicka and A. Z. Dubnickova, Acta Phys. Slov. **60** (2010) 1

# Proton charge radius and its consistency with the experiments

Cyril Adamuščín,[1, *] Erik Bartoš,[1, †]
Stanislav Dubnička,[1, ‡] and Anna Z. Dubničková[2, §]

[1]*Institute of Physics, Slovak Academy of Sciences,*
*Dúbravská cesta 9, 845 11 Bratislava, Slovak Republic*
[2]*Department of Theoretical Physiscs,*
*Faculty of Mathematics, Physics and Informatics,*
*Comenius University, Mlynská dolina, Bratislava, Slovakia*
(Dated: March 14, 2017)

In the work the new result for the value of proton charge root mean square radius in the framework of Unitary and Analytic model of proton electromagnetic structure is presented. The obtained result is compatible with the value obtained by spectroscopy of the muonic hydrogen target based on precision measurement of the Lamb shift and the resent results of low momentum transfer electron-proton scattering data analyzes.

## I.   INTRODUCTION

The problematic of the determination of the root mean square (rms) radius of the proton electric charge distribution attracts the attention in recent years. The precise measurements of the 2S–2P energy splitting in muonic hydrogen Lamb shift [1, 2] provided the value

$$r_{\mathrm{p}} = 0.84087(39)\,\mathrm{fm}, \tag{1}$$

which immediately focused view on the older CODATA value [3] received from standard analyses of electron-proton scattering data

$$r_{\mathrm{p}} = 0.8775(51)\,\mathrm{fm}. \tag{2}$$

Such large discrepancy between the values of $r_{\mathrm{p}}$ arises the question about the right value of rms radius of the proton and corresponding theory behind it [4]. Recently there was an attempt to determine the charge radius of the proton from the Mainz data [5, 6] by the polynomial expansions of the form factor [7–9], but Sick et al. [10] shown that their low values are not derived

––––––––

[*]Electronic address: cyril.adamuscin@savba.sk

[†]Electronic address: erik.bartos@savba.sk

[‡]Electronic address: stanislav.dubnicka@savba.sk

[§]Electronic address: dubnickova@fmph.uniba.sk

correctly. However the results also based on Mainz data using a dispersive framework [11] showed that such lower value of $r_\mathrm{p}$ is consistent with the measured value in Eq. (1).

In this paper we present the results received in the framework of Unitary and Analytic model of nucleon electromagnetic form factors and from the behaviour of electric proton form factor $G_\mathrm{E}^\mathrm{p}$ we determine the charge proton rms radius compatible with the value obtained from spectroscopy of the muonic hydrogen.

## II.  METHOD AND RESULTS

While the experimental information received from the precision spectroscopy of the muonic hydrogen sets the value of the charged rms radius of the proton with high accuracy, the data from elastic electron–proton scattering does not allow clearly determine the proton electric form factor $G_\mathrm{E}^\mathrm{p}$ which determine $r_\mathrm{p}$ by the fundamental formula

$$r_\mathrm{p} = \overline{\langle r_{\mathrm{Ep}}^2 \rangle} = 6 \frac{G_\mathrm{E}^\mathrm{p}(t)}{\mathrm{d}t} \bigg|_{t\to 0} . \tag{3}$$

The reason lays in two types of elastic scattering processes used to obtain the experimental information on $G_\mathrm{E}^\mathrm{p}$. First one is the unpolarized elastic scattering ep $\to$ ep, and the second one is the polarization transfer process $\vec{\mathrm{e}}\mathrm{p} \to \mathrm{e}\vec{\mathrm{p}}$ with longitudinally polarized electron beam.

**Unpolarized scattering.** The differential cross section of the process ep $\to$ ep

$$\left(\frac{\mathrm{d}\sigma}{\mathrm{d}\Omega}\right)_0 = \left(\frac{\mathrm{d}\sigma}{\mathrm{d}\Omega}\right)_\mathrm{Mott}\left[A(Q^2) + B(Q^2)\tan^2\frac{\theta}{2}\right] \tag{4}$$

is determined by the elastic structure functions

$$A(Q^2) = \frac{G_\mathrm{E}^{\mathrm{p}\,2}(Q^2) + \tau G_\mathrm{M}^{\mathrm{p}\,2}(Q^2)}{1+\tau}, \quad B(Q^2) = 2\tau G_\mathrm{M}^{\mathrm{p}\,2}(Q^2), \tag{5}$$

which are described by electric $G_\mathrm{E}^\mathrm{p}$ and magnetic $G_\mathrm{E}^\mathrm{p}$ proton form factors. By the Rosenbluth method one can determine both form factors from the ratio

$$\frac{\left(\frac{\mathrm{d}\sigma}{\mathrm{d}\Omega}\right)_0}{\left(\frac{\mathrm{d}\sigma}{\mathrm{d}\Omega}\right)_\mathrm{Mott}\frac{\varepsilon(1+\tau)}{\tau}} = \varepsilon\frac{1}{\tau}G_\mathrm{E}^{\mathrm{p}\,2}(Q^2) + G_\mathrm{M}^{\mathrm{p}\,2}(Q^2), \tag{6}$$

$$\tau = Q^2/(4m_\mathrm{p}^2), \quad \varepsilon = \left[1 + 2(1+\tau)\tan^2\frac{\theta}{2}\right]^{-1}, \tag{7}$$

when the slope and the intercept of the straight line Eq. (6) is gained from the fitting procedure. However, this method suffers to extract the correct electric proton form factor $G_{\mathrm{E}}^{\mathrm{p}\,2}(Q^2)$ for high $Q^2$. Recently was proposed new method [12], which allows one to reanalyze the Rosenbluth data in terms of the electric to magnetic form factor squared ratio $R$

$$\sigma_{\mathrm{red}} = G_{\mathrm{M}}^{\mathrm{p}\,2}(Q^2)(R^2\varepsilon + \tau), \quad R = G_{\mathrm{E}}^{\mathrm{p}}(Q^2)/G_{\mathrm{M}}^{\mathrm{p}}(Q^2). \tag{8}$$

**Polarization transfer process.** Up to now the most reliable experimental method of the determination of electromagnetic proton form factor is the measurement of the polarization $\vec{\mathbf{P}}$ of recoil proton in the process $\mathrm{e}\vec{\mathrm{p}} \to \mathrm{e}\vec{\mathrm{p}}$, namely its perpendicular $P_t$ and parallel $P_\ell$ component to the proton momentum in the scattering plane

$$P_t = -\frac{2h}{I_0}\sqrt{\tau(1+\tau)}G_{\mathrm{E}}^{\mathrm{p}}G_{\mathrm{M}}^{\mathrm{p}}\tan\frac{\theta}{2}, \tag{9}$$

$$P_\ell = \frac{h}{m_{\mathrm{p}}I_0}\left(E_e + E_{e'}\right)\sqrt{\tau(1+\tau)}G_{\mathrm{M}}^{\mathrm{p}\,2}\tan^2\frac{\theta}{2}, \tag{10}$$

where $h$ is the electron beam helicity and $I_0 = G_{\mathrm{E}}^{\mathrm{p}} + \frac{\tau}{\varepsilon}G_{\mathrm{M}}^{\mathrm{p}}$. The new data on ratio

$$\frac{G_{\mathrm{E}}^{\mathrm{p}}}{G_{\mathrm{M}}^{\mathrm{p}}} = -\frac{P_t}{P_\ell}\frac{\left(E_e + E_{e'}\right)}{2m_{\mathrm{p}}}\tan\frac{\theta}{2}. \tag{11}$$

have been obtained by the experimental groups in JLab [13–16].

**Unitary and analytic model.** For the determination of the rms radius of the proton one needs according Eq. (3) the model of electric proton form factor $G_{\mathrm{E}}^{\mathrm{p}}$. The exact functional form of proton as well as neutron electromagnetic form factors is unknown, there exists a plethora of models. In our group we developed unitary and analytic (U&A) model of electromagnetic structure of nucleons (see Section 4 in [17]) which allows us to analyze data for both sources of experimental data in space-like and time-like regions together.

The U&A model poses the known properties of nucleon electromagnetic form factors including

- The experimental fact of creation of unstable vector-meson resonances in the e$^+$ e$^-$ annihilation processes into hadrons.

- The analytic properties on the first (physical) sheet of the Riemann surface.

- The asymptotic behavior as predicted by QCD.

- The reality conditions and correct normalizations.

240

- The unitarization, i. e., the inclusion of the contributions of a continua and instability of vector-meson resonances.

**Results.** The received behaviour of the proton (neutron) electric and magnetic form factors is plotted in Fig. 1 and Fig. 2 by full lines. The dashed lines represent the results which include Rosenbluth space-like data for the comparison. Our model describes the JLab polarization data on the ration $\mu_{\mathrm{p}} G_{\mathrm{E}}^{\mathrm{p}}/G_{\mathrm{M}}^{\mathrm{p}}$ as one can see from Fig. 3, the charge distribution in the proton is presented on the right side of the plot. One can observe the non-dipole behavior of $G_{\mathrm{E}}^{\mathrm{p}}$ with the zero around around $Q^2 = 13\,\mathrm{GeV}^2$. From the behaviour of $G_{\mathrm{E}}^{\mathrm{p}}$ we have determined the value of rmd radius to be equal $r_{\mathrm{p}} = 0.8489(7)\,\mathrm{fm}$. The comparison of our received result with other values of $r_{\mathrm{p}}$ is presented in the Table I. It confirms the consistency between the electron–proton scattering and the muonic hydrogen spectroscopy experiments and it demonstrates the unreliability of Rosenbluth method in the determination of the values of $G_{\mathrm{E}}^{\mathrm{p}}$ in space-like region.
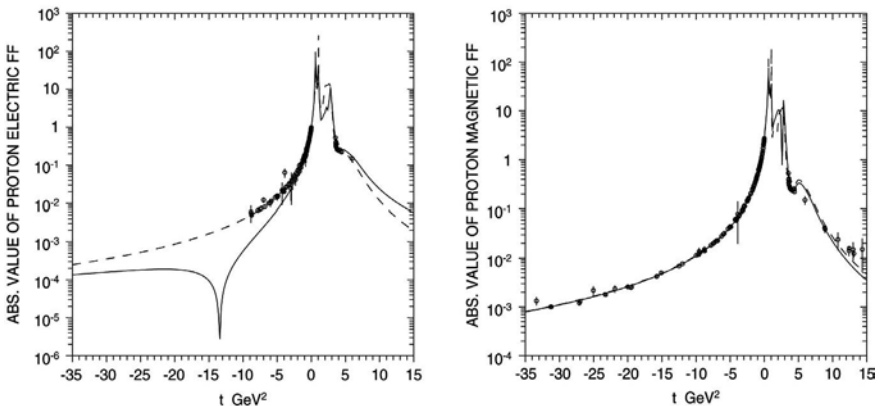


FIG. 1: Theoretical behavior of proton electric $G_{\mathrm{E}}^{\mathrm{p}}$ (left) and proton magnetic $G_{\mathrm{M}}^{\mathrm{p}}$ (right) form factors. The predicted behavior in $t < 0$ region depends on the fact if Rosenbluth technique data (dashed line) or JLab proton polarization data (full line) are used.

### III.   CONCLUSION

The Lamb shift measurement in muonic hydrogen exposed many theoretical attempts to find a solution of the proton charge radius puzzle. We have presented the method in the framework of our U&A model of nucleon electromagnetic structure how to determine the proton electromagnetic form
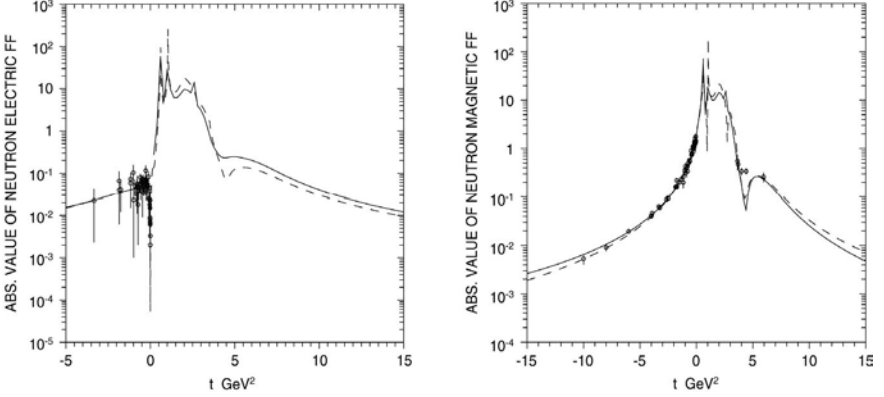
FIG. 2: Theoretical behavior of neutron electric $G_E^n$ (left) and neutron magnetic $G_M^n$ (right) form factors. The predicted behavior in $t < 0$ region depends on the fact if Rosenbluth technique data (dashed line) or JLab proton polarization data (full line) are used.
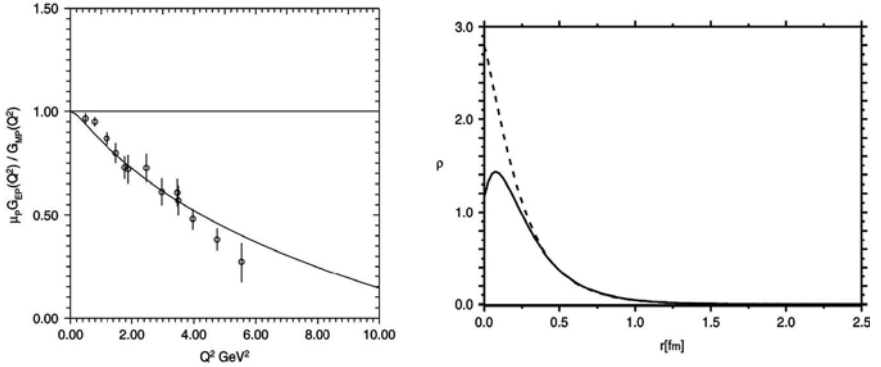


FIG. 3: JLab polarization data for the ratio $\mu_p G_E^p / G_M^p$ with U&A fit (left), charge distribution in the proton (right).

factors and with the help of the electric proton form factor $G_E^p$ we have determined the charge proton rms radius. We have performed global analysis of all existing nucleon electromagnetic form factor data by U&A model and we have found non-dipole behavior of $G_E^p$ with the zero around $Q^2 = 13\,\text{GeV}^2$. Such behaviour of $G_E^p$ has allowed us to determine the value $r_p = 0.8489(7)$ fm which corresponds to the value $r_p = 0.84087(39)$ fm obtained in the muonic hydrogen spectroscopy experiments. The understanding of proton structure and reanalyzes of scattering data will be of great importance

242

| result & source | $r_{\mathrm{p}}$ [fm] |
|---|---|
| ep scattering MAMI A1 [18] | 0.879(8) |
| hydrogen spectroscopy [19] | 0.8764(89) |
| continued fraction expansion [20] | 0.879(11) |
| conformal mapping technique [4] | 0.870(26) |
| dispersion analysis [11] | 0.840(10) |
| our U&A result | 0.8489(7) |
| muonic hydrogen [1] | 0.8418(7) |
| muonic hydrogen [2] | 0.8409(4) |

TABLE I: The comparison of different theoretical results, including our, determined from the electron-proton scattering data, with the obtained result from the measurement of the Lamb shift on muonic hydrogen.

for the explanation of the muonic experiment. We look forward for new experimental measurement to provide precise data.

### Acknowledgments

[1] R. Pohl, A. Antognini, F. Nez, F. Amaro, F. Biraben, J. Cardoso, D. Covita, A. Dax, S. Dhawan, L. Fernandes, et al., Nature **466**, 213 (2010).
[2] A. Antognini, F. Nez, K. Schuhmann, F. Amaro, F. Biraben, J. Cardoso, D. Covita, A. Dax, S. Dhawan, M. Diepold, et al., Science **339**, 417 (2013).
[3] P. J. Mohr, B. N. Taylor, and D. B. Newell, Rev. Mod. Phys. **84**, 1527 (2012).
[4] R. J. Hill and G. Paz, Phys. Rev. **D82**, 113005 (2010), 1008.4619.
[5] J. C. Bernauer et al. (A1), Phys. Rev. Lett. **105**, 242001 (2010).
[6] J. C. Bernauer, M. O. Distler, J. Friedrich, T. Walcher, P. Achenbach, C. Ayerbe Gayoso, R. Böhm, D. Bosnar, L. Debenjak, L. Doria, et al., Physical Review C - Nuclear Physics **90** (2014).
[7] K. Griffioen, C. Carlson, and S. Maddox, Phys. Rev. C **93**, 065207 (2016).
[8] D. W. Higinbotham, A. A. Kabir, V. Lin, D. Meekins, B. Norum, and B. Sawatzky, Phys. Rev. C **93**, 055207 (2016).
[9] M. Horbatsch and E. A. Hessels, Phys. Rev. C **93**, 015204 (2016).
[10] I. Sick and D. Trautmann, Phys. Rev. C **95**, 012501 (2017).
[11] I. T. Lorenz, H. W. Hammer, and U.-G. Meissner, Eur. Phys. J. **A48**, 151 (2012).

[12] S. Pacetti and E. Tomasi-Gustafsson, Phys. Rev. **C94**, 055202 (2016), 1604.02421.

[13] M. K. Jones et al. (Jefferson Lab Hall A), Phys. Rev. Lett. **84**, 1398 (2000).

[14] O. Gayou et al. (Jefferson Lab Hall A), Phys. Rev. Lett. **88**, 092301 (2002).

[15] V. Punjabi et al., Phys. Rev. **C71**, 055202 (2005).

[16] X. Zhan et al., Phys. Lett. **B705**, 59 (2011).

[17] S. Dubnicka and A. Z. Dubnickova, Acta Phys. Slov. **60**, 1 (2010), 1008.4490.

[18] J. C. Bernauer et al. (A1), Phys. Rev. **C90**, 015206 (2014).

[19] A. Beyer, J. Alnis, K. Khabarova, A. Matveev, C. G. Parthey, D. C. Yost, R. Pohl, T. Udem, T. W. Hänsch, and N. Kolachevsky, Annalen Phys. **525**, 671 (2013).

[20] J. Arrington and I. Sick, J. Phys. Chem. Ref. Data **44**, 031204 (2015).

# Helical turbulent Prandtl number in the $A$ model of passive vector advection: Two loop approximation

M. Hnatič[a,b,c], P. Zalom [c,d]

[a]*Faculty of Sciences, P.J. Safarik University, Košice, Slovakia*

[b]*Bogoliubov Laboratory of Theoretical Physics, Joint Institute for Nuclear Research, 141 980 Dubna, Moscow Region, Russian Federation*

[c]*RUDN University, 6 Miklukho-Maklaya St, Moscow, 117198, Russian Federation*

[d]*Institute of Experimental Physics, SAS, Watsonova 47, 040 01 Košice, Slovakia*

## Abstract

The application of the field theoretic renormalization group techniques as developed within high energy physics is demonstrated on a problem from the classical Newtonian physics. As an example, we consider the general $A$ model of passive vector advected by fully developed turbulent velocity field with violation of spatial parity introduced via the continuous parameter $\rho$. Values of $A$ represent a continuously adjustable parameter which governs the interaction structure of the model. In non-helical environments, we demonstrate that $A$ is restricted to the interval of approximately $-1.7 \leq A \leq 2.8$ in the two-loop order of the field theoretic model. However, when $\rho$ exceeds a threshold of around 0.75, the restrictions may be removed, which means that presence of helicity exerts a stabilizing effect onto the possible stationary regimes of the system. We demonstrate the RG techniques and show that interaction parameter $A$ exerts strong influence on advection diffusion processes in turbulent environments with broken spatial parity and identify internal structure of interactions given by the parameter $A$, and not the vector character of the admixture itself being the dominant factor influencing diffusion advection processes in the helical $A$ model.

# 1    Introduction

Systematic study of matter may roughly be divided into the physics of fundamental interactions among few particles at the most microscopic level and to the study of their macroscopic behavior when many body interactions are considered. The advances on the field of fundamental microscopic behavior are connected with the theoretical development of the Standard model of particle physics and its experimental verification that proceeds up to nowadays [1]. On the other hand, many-body physics is of coarse a field that encompasses very different systems which range from classical problems like the turbulent motion, over the theory of phase transitions up to inherently quantum systems studied, for example, within the modern condensed matter physics [2]. Although, seemingly unrelated the development of theoretical tools for the description of fundamental interactions as well as their macroscopic manifestations is inherently connected with the development of the ideas of Renormalization group as first given by Kenneth Wilson in the context of an Ising ferromagnet [3]. In this article, we are therefore considering a problem of turbulent motion and show how the tools of the Renormalization group in its form originally developed for Quantum Electrodynamics (QED) [4, 5] may be applied to this inherently classical problem [2]. As an example of a classical system, we discuss the $A$ model of passive advection in a fully developed turbulent flow. Our man goal here is to discuss basic and fundamental ideas underlying our study and give the technical details in hindsight of this purpose. Therefore, we focus on comparing the calculations within the $A$ model of passive advection with the approach commonly used in the high energy physics to solve the renormalization problem of QED for example. Thus, we will focus on similar as well as different aspects of RG analysis for such systems.

Let us start with a brief introduction to the problem of diffusion advection processes in turbulent environments. Although turbulence is basically a phenomenon of classical nature it still represents an unsolved problem [6, 7, 8, 9, 10]. In this respect, it is very important to note that analytic results on the field are notoriously difficult to obtain with theoretical results obtained within the Kolmogorov's theory being the most important, for details on the theory see Ref. [11]. Here, we just briefly state that its central idea is based around the notion of scaling invariance which is theoretically and experimentally well proven concept in the field of turbulence research and it originates back to the picture of the Richardson cascade. In more detail, the experimentally observed Fourier spectrum of three dimensional turbulence shows that an entire hierarchy of eddies develops in turbulent

flows even under small Reynolds numbers $Re$ [1]. The uppermost eddies coincide with the integral length $l_{max}$ which will be denoted as $1/m$ later in our field theoretical approach. Eddies of the successive generations are smaller but constrained by microscopic considerations. At scale $l_{min}$ corresponding to the smallest eddies energy dissipation takes place [11, 8]. The eddies however show a scaling behavior in the middle of the spectrum which is commonly referred to as the inertial interval. This is the crucial property for later application of the Renormalization group which will later also clearly emerge as the unifying description for such seemingly unrelated systems as interacting particles in high energy physics and turbulence. We also stress, that in the experimental as well as theoretical treatment of turbulence, scaling properties manifest itself more clearly the higher the Reynolds number $Re$ of the flow [2].

Furthermore, when admixtures are present in the turbulent flow we may compactly characterize the quantitative properties of flows under the study by using a well known parameter called Prandtl number [7, 8]. For all admixture types, it is defined as the dimensionless ratio of the coefficient of kinematic viscosity to the corresponding diffusion coefficient of a given admixture. For example, in the case of thermal diffusivity, the corresponding (scalar) Prandtl number equals the ratio of kinematic viscosity to the coefficient of molecular diffusivity [8]. Since both, the kinematic viscosity and the diffusion coefficient for the given admixture, are material and flow specific quantities, the resulting Prandtl numbers have always to be specified at distinct conditions required to characterize the flow and are thus often found in property tables alongside with other material specific properties [6, 7, 12, 13]. However, in the high Reynolds number limit with dominant scaling regime the state of fully developed turbulence manifests itself by reaching effective material and flow independent values for both the kinematic viscosity and the corresponding diffusion coefficient. We commonly refer to such effective values as the turbulent viscosity coefficient and turbulent diffusion coefficient [8, 9]. Consequently, in fully developed turbulent flows the resulting values of the Prandtl numbers are universal for a given admixture and do not depend either on microscopic or macroscopic properties of the flow under the consideration. Usually, we refer to them as the turbulent Prandtl numbers of given admixture type [6, 7, 14, 2].

In this respect, we show how fundamental the theory of Renormalization group is in connection to an asymmetric scenario with explicitly broken

---

[1] Reynolds number may be used as a measure of how much the flow exhibits turbulent behavior. it is given as $Re = LV/\nu$, where $L$ is a characteristic length at which turbulence is stirred, $V$ is the mean velocity before the obstacle and $\nu$ is the kinematic viscosity of the fluid.

spatial parity as observed usually in nature. [15, 16, 17, 18, 19]. Thus, in the section below we define a general model of vector admixture with a free parameter $A$ and is in the field of fully developed turbulence well known under the name $A$ model of passive advection. To avoid confusion, we stress that it should not be confused with the $A$ model according to the classification of Halperin and Hohenberg [20] or with the $A$ model of forced Navier-Stokes equation introduced in Refs. [21, 22]. The name of the present model is actually drawn from the commonly used notation for the parameter $A$ [23, 24, 25, 15, 16, 17, 18, 19] which appears in its definition (see Sec. 2 for more details). The parameter $A$ plays actually a central role in an appropriate definition of a unified description of a wide variety of vector admixture models. Moreover, even scalar admixtures embedded within a flow of distinct spatially anisotropic properties may under some conditions be modeled as having a vectorial nature with respect to diffusion-advection processes in an otherwise anisotropic flow. The parameter $A$ is thus a quantity which determines specific interactions between the admixture and the flow itself. In this respect, the well known case of a sufficiently weak magnetic fluid corresponds to a special choice of $A = 1$ [2]. Other distinct choices as $A = 0$ and $A = -1$ have been studied frequently as separate models, see Ref. [25] for more details. Consequently, the general $A$ model represents a tool to unite several distinct but physically important cases into one single model.

To perform the investigations discussed above, we use the well established tools of the field renormalization group (RG) technique, as presented, for example, in Refs.[2, 26, 27]. Such techniques are very well known in the field of high energy physics where they developed first. Nevertheless, we show how it may successfully be used for problems of fully developed turbulence with admixtures. We also stress that it has previously been successfully applied also to fully developed problems without admixtures [28, 29, 30, 31, 32, 33, 34] as well as for advection diffusion processes of several admixtures including passive scalar admixture [35, 19, 36, 37, 40, 38, 39], magnetic admixtures [41, 42, 43, 44] and also vector admixtures [15, 16, 17, 18, 25, 45, 47, 46, 48]. The two-loop techniques for calculation of the turbulent Prandtl number within the $A$ model used here are similar to those of Ref. [19]. The resulting helical values of turbulent Prandtl number are then analyzed to finally investigate the hypothesis raised in Ref. [15]. The goal of this paper is to represent the similarities of the present analysis to that commonly employed, for example, within QED or other high energy physics models.

# 2 Model $A$ of passive vector advection with spatial parity violation

We consider a passive solenoidal vector field $\mathbf{b} \equiv \mathbf{b}(x)$ driven by a helical turbulent environment given by an incompressible velocity field $\mathbf{v} \equiv \mathbf{v}(x)$ where $x \equiv (t, \mathbf{x})$ with $t$ denoting the time variable and $\mathbf{x}$ the $d$ dimensional spatial position (later $d = 3$ strictly). Apparently, $\mathbf{v}$ and $\mathbf{b}$ are the divergence free vector fields satisfying $\partial \,.\, \mathbf{b} = \partial \,.\, \mathbf{v} = 0$. Additionally, within the general $A$ model of passive advection the following system of stochastic equations is required:

$$\partial_t \mathbf{b} = \nu_0 u_0 \triangle \mathbf{b} - (\mathbf{v} \cdot \partial)\mathbf{b} + A(\mathbf{b} \cdot \partial)\mathbf{v} - \partial P + \mathbf{f}^b, \qquad (1)$$

$$\partial_t \mathbf{v} = \nu_0 \triangle \mathbf{v} - (\mathbf{v} \cdot \partial)\mathbf{v} - \partial Q + \mathbf{f}^v, \qquad (2)$$

where $\partial_t \equiv \partial/\partial_t$, $\partial_i \equiv \partial/\partial_{x_i}$, $\Delta \equiv \partial^2$ is the Laplace operator, $\nu_0$ is the bare viscosity coefficient, $u_0$ is the bare reciprocal Prandtl number, $P \equiv P(x)$ and $Q \equiv Q(x)$ represent the pressure fields while the stochastic terms $\mathbf{f}^v$, $\mathbf{f}^b$ and the parameter $A$ are discussed later in this section. The subscript 0 denotes unrenormalized quantities in what follows (see Sec. **??** for more details).

Let us now briefly review the physical meaning of $A$. We require $A$ to be real with $A \in -1, 0, 1$ representing various physically important models [18, 45, 25, 47]. For $A = 1$ the kinematic MHD model is recovered, the $A = 0$ case leads to passive advection of a vector field in turbulent environments and finally $A = -1$ represents the model of the linearized Navier-Stokes equations [25]. The parameter $A$ stands in front of the so called stretching term [45] and due to its continuous nature it represents a measure of specific interactions allowed by Galilean symmetry. Varying $A$ allows therefore to investigate a variety of passively advected vector admixtures with different interaction properties[2]. Although $A$ may take any real values, it is frequently discussed only in the smallest possible continuous interval encompassing the three special cases $A \in \{-1, 0, 1\}$. Contrary, we extend the analysis to all physically allowed values of $A$ (see Sec. **??** for more details) which allows a straightforward discussion of the influence of interactions on advection diffusion processes. The previously undefined stochastic terms $\mathbf{f}^v$ and $\mathbf{f}^b$ introduced in Eqs. (1) and (2) represent sources of fluctuations for $\mathbf{v}$ and $\mathbf{b}$. For energy injection of $\mathbf{b}$ we assume transverse Gaussian random

---

[2]As already discussed above, even scalar admixtures in turbulent environments with anisotropic properties may under some conditions be modeled as vectorial admixtures in isotropic flows. Especially, when only advection-diffusion properties are of interest.

noise $\mathbf{f^b} = \mathbf{f^b}(x)$ with zero mean via the following correlator:

$$D_{ij}^b(x;0) \equiv \langle f_i^b(x)f_j^b(0)\rangle = \delta(t)C_{ij}(|\mathbf{x}|/L), \quad (3)$$

where $L$ is an integral scale related to the corresponding stirring of $\mathbf{b}$ while $C_{ij}$ is required to be finite in the limit $L \to \infty$ and for $|x| \gg L$ it should rapidly decrease, but remains otherwise unspecified in what follows. Contrary, the transverse random force per unit mass $\mathbf{f^v} = \mathbf{f^v}(x)$ simulates the injection of kinetic energy into the turbulent system on large scales and must suit the description of real infrared (IR) energy pumping. To allow the later application of the RG technique, we shall assume a specific, power-like form of injection as usual for fully developed turbulence within the RG approach (for more details see Refs. [2, 26, 32]). Nevertheless, although a specific form is used, universality of fully developed turbulence ensures that the results obtained here may easily be extended to all fully developed turbulent flows. Additionally, it allows easy generalization to environments with broken spatial parity by defining suitable tensorial properties of the correlator of $\mathbf{f^v}$. For this purpose, we prescribe the following pair correlation function with Gaussian statistics:

$$D_{ij}^v(x;0) \equiv \langle f_i^v(x)f_j^v(0)\rangle = \delta(t) \int \frac{d^d\mathbf{k}}{(2\pi)^d} D_0 k^{4-d-2\varepsilon} R_{ij}(\mathbf{k})e^{i\mathbf{k}\cdot\mathbf{x}}. \quad (4)$$

Here, $d$ denotes the spatial dimension of the system, $\mathbf{k}$ is the wave number with $k = |k|$ and $D_0 \equiv g_0\nu_0^3 > 0$ is the positive amplitude with $g_0$ being the coupling constant of the present model related to the characteristic ultraviolet (UV) momentum scale $\Lambda$ by the relation $g_0 \simeq \Lambda^{2\varepsilon}$. The term $R_{ij}(k)$ appearing in Eq. (4) encodes the spatial parity violation of the underlying turbulent environment and its detailed structure is discussed separately in the text below. Finally, the parameter $\varepsilon$ is related to the exact form of energy injection at large scales and assumes value of 2 for physically relevant infrared energy injection. However, as usual in the RG approach to the theory of critical behavior, we treat $\varepsilon$ formally as a small parameter throughout the whole RG calculations and only in the final step its physical value of 2 is inserted [2, 27].

Further, in Eq. (4), we encounter typical momentum integrations which lead to two troublesome regions, namely the IR region of low momenta and the UV region of high momenta as discussed in detail in Refs. [2, 26]. Frequently, these troublesome integration regions are avoided by directly prescribing all relevant micro- and macroscopic properties of the flow. Here however, we use the universality of fully developed turbulent flows to avoid unnecessary specifications. Thus, we only demand real IR energy injection of energy via Eq. (4) and neglect the exact macroscopic structure of the

flow by introducing a sharp IR cut-off $k \geq m$ for integrations over $\mathbf{k}$ with $L$ assumed to be much bigger than $1/m$. Using sharp cut-off, IR divergences like those in Eq. (4) are avoided. As already done for Eq. (4), the IR cut-off is understood implicitly in the whole paper and we shall stress its presence only at the most crucial stages of the calculation. Contrary, UV divergences and their renormalization play the central role in calculations presented here.

Finally, let us now turn our attention to the projector $R_{ij}$ in Eq. (4) which controls all of the properties of the spatial parity violation in the present model. In the case of fully symmetric isotropic incompressible turbulent environments the projector $R_{ij}(k)$ assumes the usual form of the ordinary transverse projector

$$P_{ij}(\mathbf{k}) = \delta_{ij} - k_i k_j / k^2, \tag{5}$$

as explained in Ref. [2] in more details. In the case of helical flows with spatial parity violation, Eq. (4) is specified in the form of a mixture of a tensor and a pseudotensor as $R_{ij}(k) = P_{ij}(k) + H_{ij}(k)$ where $H_{ij}(k)$ respects the transversality of the present fields. The ordinary non-helical transverse projector $P_{ij}$ is thus shifted by a helical contribution

$$H_{ij}(\mathbf{k}) = i\rho\, \varepsilon_{ijl} k_l / k. \tag{6}$$

Here, $\epsilon_{ijl}$ is the Levi-Civita tensor of rank 3, and the real valued helicity parameter $\rho$ satisfies $|\rho| \leq 1$ due to the requirement of positive definiteness of the correlation function 4. Obviously, $\rho = 0$ corresponds to the fully symmetric (non-helical) case whereas $\rho = 1$ means that spatial parity is fully broken.

We finally conclude the section by discussing the structure of interactions in Eqs. (1) and (2). Obviously, according to Eq. (2), the admixture field $\mathbf{b}$ does not disturb evolution of the velocity field $\mathbf{v}$. In other words, the velocity field $\mathbf{v}$ is completely detached from the influence of admixtures, as required by demanding passive advection. Of course, real problems usually involve at least some small amount of mutual interaction between the flow and its admixtures. However, even in the case of active admixtures there exist regimes which correspond to the passive advection problem, as seen, for example, in the case of the MHD problem with an active magnetic admixture which has the so-called kinetic regime controlled by the kinematic fixed point of the RG equations (see, e.g., Ref. [41]). Such a situation corresponds to the passive advection obtained within the present model when $A = 1$ in Eqs. (1) and (2). Therefore, the present picture of passive advection within the $A$ model represents a highly interesting physical scenario.

$$\langle v_i v_j \rangle_0 \; = \; \text{-------------------}$$

$$\langle v_i' v_j \rangle_0 \; = \; \text{-|----------------}$$

$$\langle b_i b_j \rangle_0 \; = \; \text{————————————}$$

$$\langle b_i' b_j \rangle_0 \; = \; \text{+————————————}$$

Figure 1: Propagators of the general $A$ model. Dashed lines corresponds to fields $\mathbf{v}$ and $\mathbf{v}'$ while full lines denote fields $\mathbf{b}$ and $\mathbf{b}'$. Slash denotes auxiliary fields $\mathbf{v}'$ and $\mathbf{b}'$.

# 3 Field theoretic formulation of the model

According to the Martin-Sigia-Rose theorem [49], the system of stochastic differential Eqs. (1) and (2) is equivalent to a field theoretic model of the double set of fields $\Phi = \{\mathbf{v}, \mathbf{b}, \mathbf{v}', \mathbf{b}'\}$ where primed fields are the auxiliary response fields [2]. The field theoretic model is then defined via the Dominicis-Janssen action functional

$$
\begin{aligned}
S(\Phi) \;=\; & \frac{1}{2} \int dt_1 \, d^d\mathbf{x}_1 \, dt_2 \, d^d\mathbf{x}_2 [v_i'(x_1) D_{ij}^v(x_1; x_2) v_j'(x_2) \\
+ \; & b_i'(x_1) D_{ij}^b(x_1; x_2) b_j'(x_2)] + \int dt \, d^d\mathbf{x} \{\mathbf{v}'[-\partial_t \\
+ \; & \nu_0 \triangle - (\mathbf{v} \cdot \partial)]\mathbf{v} + \mathbf{b}'[-\partial_t \mathbf{b} + \nu_0 u_0 \triangle \mathbf{b} - (\mathbf{v} \cdot \partial)\mathbf{b} \\
+ \; & A(\mathbf{b} \cdot \partial)\mathbf{v}]\},
\end{aligned}
\tag{7}
$$

where $x_l \equiv (t_l, \mathbf{x}_l)$ with $l = 1, 2$, $D_{ij}^b$ and $D_{ij}^v$ are given in Eqs. (3) and (4), respectively, and the required summations over dummy indices $i, j \in 1, 2, 3$ are implicitly assumed. The auxiliary fields and their original counterparts $\mathbf{v}, \mathbf{b}$ share the same tensor properties, which means that all fields appearing in the present model are transverse. The pressure terms $\partial Q$ and $\partial P$ from Eqs. (1) and (2), respectively, do not appear in action (7) because transversality of the auxiliary fields $\mathbf{v}'(x)$ and $\mathbf{b}'(x)$ allows one to integrate these out of the action (7) by using the method of partial integration. In the frequency-momentum representation the following set of bare propagators is obtained:

$$\langle b_i' b_j \rangle_0 = \langle b_i b_j' \rangle_0^* \;=\; \frac{P_{ij}(\mathbf{k})}{i\omega + \nu_0 u_0 k^2}, \tag{8}$$

$$\langle v_i' v_j \rangle_0 = \langle v_i v_j' \rangle_0^* \;=\; \frac{P_{ij}(\mathbf{k})}{i\omega + \nu_0 k^2}, \tag{9}$$

$$\langle b_i b_j \rangle_0 \;=\; \frac{C_{ij}(\mathbf{k})}{|-i\omega + \nu_0 u_0 k^2|^2}, \tag{10}$$

$$\langle v_i v_j \rangle_0 \quad = \quad \frac{g_0 \nu_0^3 k^{4-d-2\varepsilon} R_{ij}(\mathbf{k})}{|-i\omega + \nu_0 k^2|^2}, \tag{11}$$

with helical effects already appearing in the propagator (11) via $R_{ij}(\mathbf{k})$. The function $C_{ij}(k)$ is the Fourier transform of $C_{ij}(r/L)$ from Eq. (3), but remains arbitrary in the calculations that follow. The propagators are represented as usual by the dashed and full lines, where the dashed lines involve the velocity type of fields and full lines represent the vector admixture type fields. The auxiliary fields are denoted using a slash in the corresponding propagators as shown in Fig. 1. The field theoretic formulation of the $A$ model contains also two different triple interaction vertices, namely $b_i'(-v_j\partial_j b_i + Ab_j\partial_j v_i) = b_i' v_j V_{ijl} b_l$ and $-v_i' v_j \partial_j v_i = v_i' v_j W_{ijl} v_l/2$. In the momentum-frequency representation, $V_{ijl} = i(k_j\delta_{il} - Ak_l\delta_{ij})$ while $W_{ijl} = i(k_l\delta_{ij} + k_j\delta_{il})$. In both cases, momentum $\mathbf{k}$ is flowing into the vertices via the auxiliary fields $\mathbf{b}'$ and $\mathbf{v}'$, respectively. In the end, let us also briefly remind that the formulation of the stochastic problem given by Eqs. (1)-(2) through the field theoretic model with the action functional (7) allows one to use the well-defined field theoretic means, e.g., the RG technique, to analyze the problem [2, 50]. However, even at first look we notice several important differences to problems which are treated within the usual high energy physics of fundamental interactions. First, time and space in Eq. (7) are obviously treated separately and do not form a four-vector as required in relativistic theories. Consequently, the Fourier image of space and time yields two independent quantities $\omega$ and $\vec{k}$. This is a distinct property of many problems of critical dynamics and the corresponding models are often referred to as two scale models [2]. Such a two scaled nature of the problem is already clearly visible in the propagators of our theory. Looking at the denominator of the propagators above, we notice their form which is a linear combination of $\omega$ and $k^2$. In other words, $\omega$ and $k^2$ do not appear in the same power in the denominator and are both completely independent. This is of coarse just the consequence of non-relativistic nature of the problem but leads later to very important differences to the usual relativistic models of high energy physics. From the more technical point of view, it is also important to note that denominators of propagators involve parameters $u_0$ and $nu_0$ which as later shown are actually flowing quantities with respect to RG analysis. Moreover, the present theory is clearly massless which as very well known also in high energy physics makes the analysis technically more demanding.
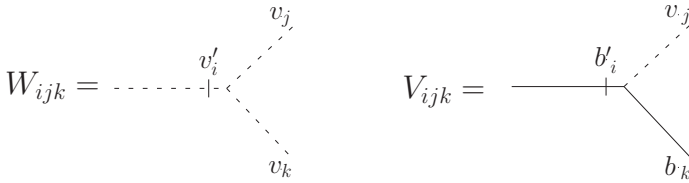
Figure 2: The interaction vertices of the $A$ model. The vertex $W_{ijk} = i(k_k\delta_{ij} + k_j\delta_{ik})$ involves the fields $\mathbf{v}$ and $\mathbf{v}'$ while $V_{ijk}$ is the only diagrammatic object of the present Feynman rules which contains $A$ dependent contribution in the form of $V_{ijk} = i(k_j\delta_{ik} - Ak_k\delta_{ij})$.

# 4 Renormalization group analysis

To determine all relevant UV divergences in the present model, we employ the analysis of canonical dimensions and identify all objects (graphs) containing the so called superficial UV divergences which turn out to be the only relevant divergences left for the subsequent RG analysis performed here, for details, see Refs. [2, 26, 27]. Since the present $A$ model belongs to the class of the so called two scale models [2, 26, 32], an arbitrary quantity $Q$ has a canonical dimension $d_Q = d_Q^k + d_Q^\omega$, where $d_Q^k$ corresponds to the canonical dimension in the momentum scale while $d_Q^\omega$ corresponds to the frequency scale. A straightforward calculation shows that for the helical parameter $\rho$ one obtains $d_\rho^k = d_\rho^\omega = 0$ while all the other quantities possess canonical dimensions according to Ref. [18]. Consequently, the helical $A$ model possess dimensionless coupling constant $g_0$ at $\varepsilon = 0$.

The present model is thus logarithmic at $\varepsilon = 0$ which in the framework of the minimal subtraction (MS) scheme, as used here, means that all possible UV divergences are of the form of poles in $\varepsilon$ [27, 50]. Using now the general expression for the total canonical dimension of an arbitrary 1-irreducible Green's function $\langle\Phi\ldots\Phi\rangle_{1-ir}$ and the symmetry properties of the model, one finds that for $d = 3$ the superficial UV divergences are present only in the 1-irreducible Green functions $\langle v_i' v_j\rangle_{1-ir}$ and $\langle b_i' b_j\rangle_{1-ir}$. Thus, all divergences can be removed by the counterterms of the form $\mathbf{v}'\Delta\mathbf{v}$ or $\mathbf{b}'\Delta\mathbf{b}$ which leads to the multiplicative renormalization of $g_0$, $u_0$, and $\nu_0$ via

$$\nu_0 = \nu Z_\nu, \quad g_0 = g\mu^{2\varepsilon}Z_g, \quad u_0 = uZ_u, \tag{12}$$

where the dimensionless parameters $g, u$, and $\nu$ are the renormalized counterparts of the corresponding bare ones and $\mu$ is the renormalization mass required for the dimensional regularization, as used in the present paper. The quantities $Z_i = Z_i(g, u; d, \rho; \varepsilon)$ contain poles in $\varepsilon$.

Furthermore, we stress that $A$ is a free parameter in the model and is not

renormalized as opposed to the charges listed in Eq. (12). This feature was already observed in Ref. [18] where a non-helical equivalent of our model is investigated. On the other hand, when the correlations of the velocity field **v** are prescribed synthetically, as done for example in Refs. [23, 24], parameter $A$ cannot be freely adjusted. In such models, $A$ becomes a charge of the model which for incompressible flows leads to only three allowed renormalized values of $1, 0, -1$ [24]. Moreover, when compressibility is present, the parameter $A$ is renormalized only to a non-zero values of $1, -1, \alpha$ where $\alpha$ is a parameter describing compressibility (for details see Eq. (2.5) in Ref. [24]). However, such consequences are attributed to **v** being prescribed synthetically by its two point correlator. We avoided such synthetic definitions by using stochastic Navier-Stokes equation to describe the evolution of **v**. This scenario is not only more physical but additionally, it has the benefit of $A$ being a free parameter of the present model.

Before going further, we briefly address also the issue of additional divergences present in the analyzed model. These divergences appear only in the helical model and are linear in $\rho$, for details see Ref. [55]. Nevertheless, as shown in detail in Ref. [55], they have no impact on the form of beta functions nor do they change the fixed points and their stability in the present model. Furthermore, we are only interested in the values of the effective inverse turbulent Prandtl number $u_{eff}$ given according to the definitions of Ref. [19] where it is defined as the ratio of the response functions $\langle v'v \rangle$ and $\langle b'b \rangle$. However, asymptotic behaviour of the response function $\langle b'b \rangle$ is not affected by the presence of linear divergences which may completely be removed from the physical analysis after the inclusion of the Lorentz-like terms into the Eq. 2 which is then called as the full model or the general $A$ model of active vector admixture. Consequently, the presence of the linear divergences is artificial here and may completely be removed in a full problem which as discussed in Ref. [55] has a kinematic mode as a solution of RG equations which then corresponds to the present physical case. Thereby, linear divergences play no significance for the present paper and we only concentrate on the problem of the existence and stability of the IR scaling regime, which can be studied without considering the linear divergences discussed above. Bearing the problem of linear $\rho$ divergences in mind we write down the renormalized action functional as

$$
\begin{aligned}
S(\Phi) \quad = \quad & \frac{1}{2} \int dt_1 \, d^d\mathbf{x}_1 \, dt_2 \, d^d\mathbf{x}_2 \\
& [v_i'(x_1) D_{ij}^v(x_1; x_2) v_j'(x_2) + b_i'(x_1) D_{ij}^b(x_1; x_2) b_j'(x_2)] \\
& + \int dt \, d^d\mathbf{x} \{ \mathbf{v}'[-\partial_t + \nu Z_1 \triangle - (\mathbf{v} \cdot \partial)] \mathbf{v}
\end{aligned}
$$

255

$$+ \mathbf{b}'[-\partial_t \mathbf{b} + \nu u Z_2 \triangle \mathbf{b} - (\mathbf{v} \cdot \partial)\mathbf{b} + A(\mathbf{b} \cdot \partial)\mathbf{v}]\},$$

$$(13)$$

with $Z_1$ and $Z_2$ being the renormalization constants connected with the previously defined renormalization constants $Z_i = Z_i(g, u; d, \rho; \varepsilon)$ with $i \in \nu, g, \mu$ via the equations

$$Z_\nu = Z_1, \quad Z_g = Z_1^{-3}, \quad Z_u = Z_2 Z_1^{-1}. \qquad (14)$$

Each of the renormalization constants $Z_1$ and $Z_2$ corresponds to a different class of Feynman diagrams (as discussed below) but they share an analogous structure within the MS scheme: the $n$-th order of perturbation theory corresponds to the $n$-th power of $g$ with the corresponding expansion coefficient containing a pole in $\varepsilon$ of multiplicity $n$ and less. I. e.:

$$Z_1(g; d, \rho; \varepsilon) \;=\; 1 + \sum_{n=1}^{\infty} g^n \sum_{j=1}^{n} \frac{z_{nj}^{(1)}(d, \rho)}{\varepsilon^j}, \qquad (15)$$

$$Z_2(g, u; d, \rho; \varepsilon) \;=\; 1 + \sum_{n=1}^{\infty} g^n \sum_{j=1}^{n} \frac{z_{nj}^{(2)}(u, d, \rho)}{\varepsilon^j}, \qquad (16)$$

where $z_{nj}^{(1)}(d, \rho)$ and $z_{nj}^{(2)}(u, d, \rho)$ are free of the parameter $\varepsilon$. Using the last expressions with renormalized variables inserted leads to divergence free 1-irreducible Green's functions $\langle v_i' v_j \rangle_{1-ir}$ and $\langle b_i' b_j \rangle_{1-ir}$. Moreover, 1-irreducible Green's functions $\langle v_i' v_j \rangle_{1-ir}$ and $\langle b_i' b_j \rangle_{1-ir}$ are associated with the corresponding self-energy operators $\Sigma^{v'v}$ and $\Sigma^{b'b}$ by the Dyson equations which in the frequency-momentum representation read

$$\langle v_i' v_j \rangle_{1-ir} \;=\; [\; i\omega \; - \nu_0 p^2 + \Sigma^{v'v}(\omega, \mathbf{p})]P_{ij}(\mathbf{p}), \qquad (17)$$

$$\langle b_i' b_j \rangle_{1-ir} \;=\; [i\omega - \nu_0 u_0 p^2 + \Sigma^{b'b}(\omega, \mathbf{p})]P_{ij}(\mathbf{p}). \qquad (18)$$

Thus, substitution of $e_0 = e\mu^{d_e} Z_e$ for $e = \{g, u, \nu\}$ is required to lead to UV convergent Eqs. (17) and (18) which in turn determine the renormalization constants $Z_1$ and $Z_2$ up to an UV finite contribution. The employed MS scheme fixes then the renormalization constants in the form of $1 + $ poles in $\varepsilon$ and the coefficients $z_{nj}^{(i)}$, $i = 1, 2$ are then fully prescribed in the corresponding order of perturbation theory.

The aim of the present paper consists of deriving the two-loop perturbative results for the $A$ model with helical effects included via proper definition of Eq. (4). Since in the limit $\rho \to 0$ the less general non-helical model of Ref. [18] is recovered, all non-helical results of Ref. [18] have to be reproduced here. Moreover, all quantities depending exclusively on velocity field

**v** follow only from stochastic Navier-Stokes equation (2) and the correlator (4). In Refs. [15, 31], exactly the same conditions were imposed on the velocity type of the fields **v** and **v**′ in the two-loop calculations of the given model. Consequently, the corresponding quantities depending exclusively on the velocity type of fields in the present model have to equal those obtained in Refs. [15, 31]. Taking together, $Z_1$ in the present model must be the same as in Ref. [31] while non-helical values of $Z_2$ in the generalized helical $A$ model must reproduce results of Ref. [18]. Thus, before generalizing the approach of Refs. [18, 19] to the more general $A$ model with helical contributions we review results of Refs. [15, 18, 19] which are relevant for the present paper.

Let us start with the coefficients related to **v** and **v**′ which comprise the renormalization coefficient $Z_1$. As stated above, the present model and the model under study in Refs. [15, 31] have the same renormalization constant $Z_1$ and the expansion coefficient $z_{11}^{(1)}$ is therefore given as

$$z_{11}^{(1)} = -\frac{S_d}{(2\pi)^d}\frac{(d-1)}{8(d+2)},\tag{19}$$

where $S_d$ is the surface area of the $d$-dimensional unit sphere defined as $S_d \equiv 2\pi^{d/2}/\Gamma(d/2)$ with $\Gamma(x)$ being the standard Euler Gamma function. Thus, no helical contributions at the one-loop level emerge for quantities involving only the velocity type of the fields **v** and **v**′. In Ref. [31], the two-loop order coefficient $z_{22}^{(1)}$ is shown to satisfy

$$z_{22}^{(1)} = -\left(z_{11}^{(1)}\right)^2.\tag{20}$$

Consequently, $z_{22}^{(1)}$ is also $\rho$ independent and only the remaining coefficient $z_{21}^{(1)}$ contains helical contributions to $Z_1$. Since the corresponding expression from Ref. [15] is rather huge we shall not reprint it here.

Let us now turn our attention to $Z_2$ which requires to analyze the structure of the self-energy operator $\Sigma^{b'b}$ in the Dyson equation (18). In the two-loop order, $\Sigma^{b'b}$ equals the sum of singular parts of nine one-irreducible Feynman diagrams as shown in Fig. 3. Using the notation of Ref. [18] for the sake of easier comparison, we write down the two-loop approximation of $\Sigma^{b'b}$ as

$$\Sigma^{b'b} = \Gamma^{(1)} + \Gamma^{(2)} = \Gamma^{(1)} + \sum_{l=1}^{8} s_l \Gamma_l^{(2)},\tag{21}$$

where $\Gamma^{(1)}$ represents the single one-loop diagram shown in Fig. 3 and $\Gamma^{(2)}$ represents the sum of the eight two-loop diagrams shown in Fig. 3. The
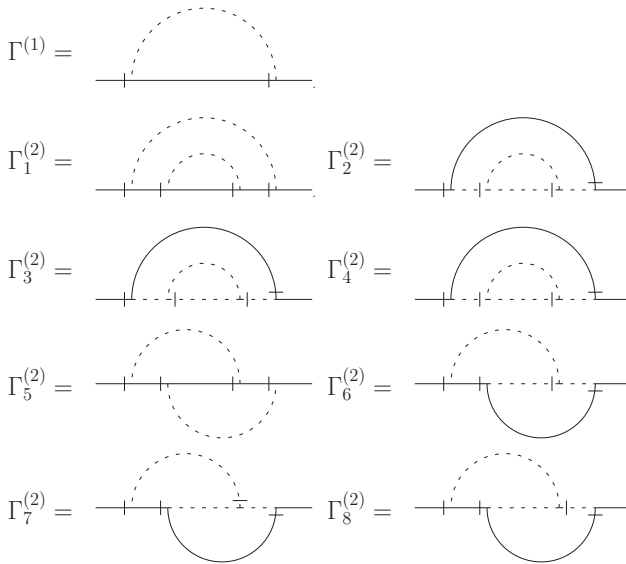
Figure 3: One-loop and two-loop diagrams that contribute to the self-energy operator $\Sigma^{b'b}(\omega, p)$ in Eq. (18).

258

terms $s_l$, $l = 1, \ldots, 8$ denote the corresponding symmetry factors which equal 1 for all diagrams except for the fourth with $s_4 = 1/2$.

The single one-loop diagram of Fig. 3 apparently does not include the propagator $\langle v_i v_j \rangle_0$ which is the only diagrammatic object that contains helical contributions. The corresponding coefficient $z_{11}^{(2)}$ that follows from the $\Gamma^{(1)}$ contribution is thus actually also $\rho$ independent. Since all non-helical quantities in the present helical $A$ model must reproduce the corresponding values of Ref. [18], the following $z_{11}^{(2)}$ expansion coefficient must be obtained (as verified also by direct calculation):

$$
\begin{aligned}
z_{11}^{(2)} &= -\frac{S_d}{(2\pi)^d} \\
&\times \frac{(d^2 - 3)(u + 1) + A\,[d + u(d - 2)] + A^2(1 + 3u)}{4d(d + 2)u(u + 1)^2}.
\end{aligned}
\tag{22}
$$

The contributions to $\Gamma^{(2)}$ which determine $z_{22}^{(2)}(d, \rho)$ and $z_{21}^{(2)}(d, \rho)$ are given by the eight two-loop diagrams of Fig. 3. After a quick inspection we notice that each of the diagrams contains two $\langle v_i v_j \rangle_0$ propagators which are linearly dependent on the helicity parameter $\rho$. Thus, all two-loop diagrams can depend only quadratically on $\rho$ (linear dependences are not relevant for the present calculations and are dropped systematically). Thus, using the notation equivalent to that of Ref. [18] we can write the divergent part of $\Gamma^{(2)}$ in the following form:

$$
\begin{aligned}
\Gamma^{(2)} &= \frac{g^2 \nu \, p^2 \, S_d}{16(2\pi)^{2d}} \left(\frac{\mu}{m}\right)^{4\varepsilon} \frac{1}{\varepsilon} \\
&\times \left\{ \frac{S_d}{\varepsilon} C^\rho + B^{(0)} + \rho^2 \delta_{3d} B^{(\rho)} \right\},
\end{aligned}
\tag{23}
$$

where $C^\rho$, $B^{(0)}$ and $B^{(\rho)}$ are for now undetermined. The $d, g, p, \mu, u, m$ dependent factors in Eq. (23) could principally by absorbed into $C^\rho$, $B^{(0)}$ and $B^{(\rho)}$, but are kept in order to comply with notation of Ref. [18]. By definition $B^{(0)}$ encodes non-helical contributions of the corresponding diagrams and for $\rho \to 0$ must yield the same expressions as shown in Ref. [18]. Since, $B^{(0)}$ was not explicitly introduced in Ref. [18] we define it via

$$
B^{(0)} = S_{d-1} \int_0^1 dx \, (1 - x^2)^{(d-1)/2} \, B,
\tag{24}
$$

where the variable $x$ denotes the cosine of the angle between two independent loop momenta $\mathbf{k}$ and $\mathbf{q}$ of the two-loop diagrams, i.e., $x = \mathbf{k}.\mathbf{q}/|k|/|q|$.

The function $B$ is obtained in the same form as in Ref. [18] but is rather huge and shall not be reproduced here. We merely notice that within the scope of the present calculations we have determined $B^{(0)}$ directly by the methods discussed later in connection with the helical contributions in the present model. Furthermore, the expression $C^\rho$ is directly related to the second order pole coefficient of $Z_2$, namely to $z_{11}^{(2)}(d, \rho)$. Although, we denoted this contribution by superscript $\rho$, in reality it must be independent of helical contributions because of the one-loop order of the present generalized $A$ model which is completely free of any helical effects. Consequently, second order $\varepsilon$ pole contributions to $\Gamma^{(2)}$ have to remain also $\rho$ independent and the superscript $\rho$ in $C^\rho$ may be dropped, i. e., $C^\rho \equiv C$. Due to helical independence of $C$ it assumes the same form as in Ref. [18] yielding thus the corresponding $z_{22}^{(2)}(d, \rho)$ as

$$z_{22}^{(2)}(d, \rho) = z_{22}^{(2)}(d) = -\frac{S_d^2}{(2\pi)^{2d}}\frac{C}{16u}. \tag{25}$$

At this place, we only briefly note that $C$ is a polynomial of fourth order in $A$ and postpone the details to later on. Eqs. (19)-(25) thus briefly summarize the results common to the present model and the models of Refs. [19, 15, 18]. Passing to our generalized helical $A$ model requires now an explicit calculation of helical contributions to $\Gamma^{(2)}$ . We once again stress that although $B^{(\rho)}$ is calculated with the explicit $d$ dependence, the helical contributions make sense only for $d = 3$ as indicated by the insertion of the Kronecker delta $\delta_{d3}$ into Eq. (23).

Before going further let us now explain the general character of the $A$ dependences in the expressions $C^\rho \equiv C$, $B^{(0)}$ and $B^{(\rho)}$ without considering the details of the corresponding calculations. According to Fig. 3 and Eqs.(21) and (23), all of the discussed expressions are given by the diagrams $\Gamma^{(1)}$ or $\Gamma_l^{(2)}$ with $l = 1, \ldots 8$. Noting now that the parameter $A$ appears only in the $V_{ijl}$ type vertex as a linear function we may gain direct insights into the structure of the $A$ dependences of the given diagrams. To this end, imagine a diagram with only two vertices of the $V_{ijl}$ type. Since each of the vertices contains only a linear function of $A$ when necessary summations on dummy field indices are performed, we get an overall dependence which may include the most a quadratical term in $A$ as a result of two linear terms in $A$ being multiplied together. In other words, the resulting diagram may therefore be only a polynomial in $A$ of order 2 the most. The same reasoning extends also to the case when four $V_{ijl}$ type vertices appear simultaneously in given diagram. Here, the resulting polynomial must be of an order of 4 in $A$. Of coarse, since $V_{ijl}$ type vertices are of tensorial nature, summation over field indices in a given diagram may lower the actual order of the polynomials in

$A$ while some polynomial coefficients may also vanish completely. However, under any circumstances higher powers of $A$ may not emerge in the graphs. The diagrams $\Gamma_l$ with $l = 1, \ldots 8$ contain two or four $V_{ijl}$ type vertices and their sum $\Gamma^{(2)}$ must consequently be a polynomial in $A$ of an order of 4 the most. Additionally, $C^\rho \equiv C$ is proportional to the second order pole in $\varepsilon$ of $\Gamma^{(2)}$ and must therefore also be a polynomial of an order of 4 the most. The parameters $B^{(0)}$ and $B^{(\rho)}$ are proportional to the corresponding parts of $\Gamma^{(2)}$ and are therefore polynomials in $A$ with order of 4 the most.

Although the previous discussions determine the structure of the diagrams, only a direct calculation may give us the needed coefficients of the resulting polynomials in $A$. Thus, we have to perform the calculation of the coefficients $z_{21}^{(2)}(u, d, \rho)$ and $z_{22}^{(2)}(d, \rho)$ directly. On the other hand, since all helical properties of the generalized helical $A$ model are encoded by the term $B^{(\rho)}$ and linear $\rho$ divergences are left out in the present model, we note that $z_{21}^{(2)}(u, d, \rho)$ contains a quadratic term in $\rho$ as the only $\rho$ dependent part. However, to correctly determine the exact term proportional to $\rho^2$ we are required to calculate $B^{(\rho)}$. For this purpose, we use the Dyson equation (18), the relation (21), and the structure of $\Gamma^{(2)}$, as given by Eq. (23). Finally, $z_{21}^{(2)}(u, d, \rho)$ is found as (once again notation of Ref. [18] is used)

$$z_{21}^{(2)}(u, d, \rho) = \frac{S_d}{16u(2\pi)^{2d}} \left( B^{(0)} + \rho^2 \delta_{d3} B^{(\rho)} \right), \qquad (26)$$

where $B^{(0)}$ and $B^{(\rho)}$ are defined via Eqs. (23) and (24), respectively. According to Eq. (26), $B^{(\rho)}$ is given by the two-loop diagrams of Fig. 3 and is written in close analogy with Eq. (24) in the following form:

$$B^{(\rho)} = S_{d-1} \int_0^1 dx \, (1 - x^2)^{(d-1)/2} \sum_{l=1}^{8} s_l B_l^{(\rho)} \qquad (27)$$

and thus define $B_l^{(\rho)}$ as the corresponding helical parts of the $\Gamma_l^{(2)}$ diagrams. Thus, as already discussed, when the limit $\rho \to 0$ is imposed on Eq. (26) the resulting value gives the $B^{(0)}$ coefficient which in turn complies with its corresponding counterpart of Ref. [18]. On the other hand, for $\rho \neq 0$ the eight two-loop graphs contain nonzero terms which via $B^{(\rho)}$ encode all of the helical effects investigated here. In other words, the result of Ref. [18] is only a special case of the present calculations when appropriate limits are taken while for $0 < |\rho| \leq 1$ the corresponding expressions are completely unknown and require to be calculated here. For this purpose, for the diagrams $\Gamma_l^{(2)}$ with $l = 2, \ldots 8$, we utilize the derivative technique outlined in Ref. [19] whose prerequisites are fulfilled for selected diagrams
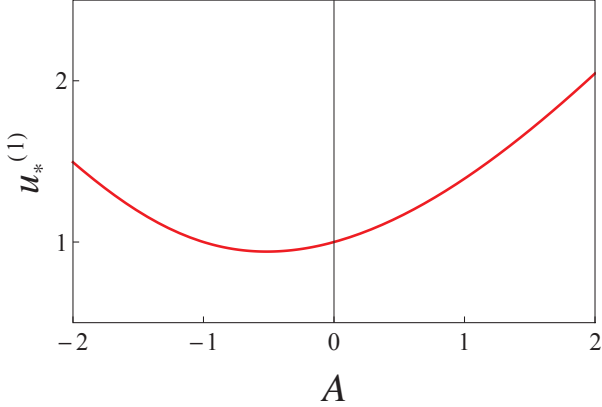
Figure 4: (Color online) Dependence of the one-loop inverse turbulent Prandtl number $u_*^{(1)}$ on the parameter $A$ in the region $-2 \leq A \leq 2$. Note that for $A = -1$ one obtains $u_*^{(1)} = 1$. Apparently, one-loop values of $u_*^{(1)}$ are always positive ($u_*^{(1)} \to \infty$ for $A \to \pm\infty$) and therefore physical for all arbitrary real $A$.

with $l = 2, \ldots 8$. However, in the case of diagram $\Gamma_1^{(2)}$, only its non-helical value, a special case of the model considered here, can by evaluated using the derivative technique of Ref. [19]. Therefore, the well established techniques outlined, for example, in Ref. [2] are used for the graph $\Gamma_1^{(2)}$. Nevertheless, calculations for all graphs are quite straightforward; however, they result in complicated lengthy expression.

In the end, we have to reexamine the influence of helicity on the properties of the IR scaling regime and its stability. First, since the fields $\mathbf{v}$, $\mathbf{v}'$, $\mathbf{b}$, and $\mathbf{b}'$ are not renormalized, the following simple relation holds:

$$W^R(g, u, \nu, \mu, \cdots) = W(g_0, u_0, \nu_0, \cdots). \tag{28}$$

It states that the renormalized connected correlation functions $W^R = \langle \Phi \ldots \Phi \rangle^R$ differ from their unrenormalized counterparts $W = \langle \Phi \ldots \Phi \rangle$ only by the choice of variables (renormalized or unrenormalized) and in the corresponding perturbation expansion (in $g$ or $g_0$), where the dots stand for arguments untouched by the renormalization [2, 26, 50]. This means that unrenormalized correlation functions are independent of the scale-setting parameter $\mu$ of dimensional regularization. Thus, applying the differential

operator $\mu\partial_\mu$ at fixed unrenormalized parameters on both sides of Eq. (28) gives the basic differential RG equation of the following form [2, 26]:

$$[\mu\partial_\mu + \beta_g\partial_g + \beta_u\partial_u - \gamma_\nu\nu\partial_\nu]W^R(g, u, \nu, \mu, \cdots) = 0, \tag{29}$$

where the so-called RG functions (the $\beta$ and $\gamma$ functions) are given as follows:

$$\beta_g \equiv \mu\partial_\mu g = g(-2\varepsilon + 3\gamma_1), \tag{30}$$

$$\beta_u \equiv \mu\partial_\mu u = u(\gamma_1 - \gamma_2), \tag{31}$$

$$\gamma_i \equiv \mu\partial_\mu \ln Z_i, \quad i = 1, 2, \tag{32}$$

and are based on relations among the renormalization constants (14) together with the explicit expressions of $Z_1$ and $Z_2$ given by (15) and (16), respectively. Here, it should be noticed that $\beta$ functions are calculated up to the given order and their exact (non-perturbative) expansion in terms of $\varepsilon$ is unknown as usual in high energy physics. However, due to Galileo invariance, both functions $\gamma_1$ and $\gamma_2$ are exact and equal $2\varepsilon/3$. In other words, they do not obtain contributions from higher loop orders and are already given at one loop order. For details see Ref. [2]. To obtain the IR asymptotic behavior of the correlation functions deep inside of the inertial interval, we need to identify the coordinates $(g_*, u_*)$ of the corresponding IR stable fixed point where $\beta_g$ and $\beta_u$ vanish since they establish the required Kolmogorov regime. We demand

$$\beta_g(g_*) = 0, \quad \beta_u(g_*, u_*) = 0, \tag{33}$$

where $g_* \neq 0$ and $u_* \neq 0$ in the two-loop approximation are required to have the form

$$g_* = g_*^{(1)}\varepsilon + g_*^{(2)}\varepsilon^2 + O(\varepsilon^3), \tag{34}$$

$$u_* = u_*^{(1)} + u_*^{(2)}\varepsilon + O(\varepsilon^2). \tag{35}$$

It may be verified by a direct calculation that at non-trivial fixed points the following expressions hold:

$$g_*^{(1)} = \frac{(2\pi)^d}{S_d}\frac{8(d+2)}{3(d-1)}, \tag{36}$$

$$g_*^{(2)} = \frac{(2\pi)^d}{S_d}\frac{8(d+2)}{3(d-1)}\lambda, \tag{37}$$

$$u_*^{(1)} = \frac{1}{3a_2}\left(-2a_2 - \frac{\sqrt[3]{2}b_1}{\sqrt[3]{b_2+b_3}} + \frac{\sqrt[3]{b_2+b_3}}{\sqrt[3]{2}}\right), \tag{38}$$

$$u_*^{(2)} = \frac{2(d+2)}{d[1+2u_*^{(1)}]}\left[\lambda - \frac{128(d+2)^2}{3(d-1)^2}\mathcal{B}(u_*^{(1)})\right], \tag{39}$$

263

where $\lambda$ is related to the coefficient $z_{21}^{(1)}$ in Eq. (15) as

$$\lambda = \frac{2}{3} \frac{(2\pi)^{2d}}{S_d^2} \left[ \frac{8(d+2)}{d-1} \right]^2 z_{21}^{(1)}. \tag{40}$$

The coefficient $\mathcal{B}(u_*^{(1)})$ will be discussed in the text below. Let us now give the explicit expressions for $a_i$ with $i \in 0, 1, 2$ and $b_i$ with $i \in 1, 2, 3$. They read:

$$
\begin{align}
b_1 &= a_2 \left( 3a_1 - 4a_2 \right) \tag{41}\\
b_2 &= a_2^2 \left( -27a_0 + 18a_1 - 16a_2 \right) \tag{42}\\
b_3 &= \sqrt{4b_1^3 + b_2^2} \tag{43}\\
a_0 &= -2 \left[ d^2 - 3 + A(A+d) \right] \tag{44}\\
a_1 &= 6(1 - A^2) - 2A(d-2) - d(d+1) \tag{45}\\
a_2 &= d(d-1) \tag{46}
\end{align}
$$

The value of the coefficient $a_1$ differs from that presented in Ref. [18] where most probably a typesetting error occurred since for $\rho \to 0$ our present result reproduce the less general non-helical model of Ref. [18]. Moreover, $a_1$ from Ref. [18] takes the same form as the current one when the (probably misplaced) brackets are corrected.

As already mentioned, one-loop results given by Eqs. (36) and (38) are free of helical contributions. Furthermore, $g_*^{(2)}$ depends exclusively on the properties of the underlying velocity field which means that it is common within a class of models with passively advected admixtures, as discussed, for example, in Ref. [15]. In more detail, $g_*^{(2)}$ is completely determined by $\lambda$ from Eq. (40). However, $u_*^{(2)}$ is model specific and known only for special choices of $A \in 0, 1$ [15]. Here, it is expected to contain helical contributions via the quantity $\mathcal{B}(u_*^{(1)})$ which in turn is completely given by the coefficient $z_{21}^{(2)}$ in Eq. (26) and it obtains the following value at $u = u_*^{(1)}$ :

$$\mathcal{B}(u_*^{(1)}, \rho) = \frac{(2\pi)^{2d}}{S_d^2} z_{21}^{(2)}(u_*^{(1)}, \rho) \tag{47}$$

We retained the $d$ dependencies for notation purpose. However, only spatial dimension $d = 3$ is physically meaningful when helical effects are considered. The IR behavior of the fixed point is determined by the matrix of the first derivatives which is given as

$$\Omega_{ij} = \begin{pmatrix} \partial\beta_g/\partial g & \partial\beta_g/\partial u \\ \partial\beta_u/\partial g & \partial\beta_u/\partial u \end{pmatrix} \tag{48}$$
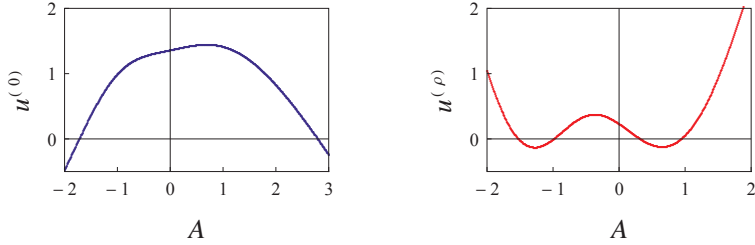
Figure 5: (Color online) Dependence of $u^{(0)}$ and $u^{(\rho)}$ on parameter $A$ shown in regions $-2 \leq A \leq 3$ and $-2 \leq A \leq 2$ respectively. Quantity $u^{(0)}$ corresponds to non-helical value of inverse turbulent Prandtl number, while $u^{(\rho)}$ represents helical contribution to the inverse turbulent Prandtl number. Points represent numerical values obtained from Eq. (50).

and is evaluated for given $(g_*, u_*)$. The present matrix is triangular since $\beta_g$ is independent of $u$. Consequently, $\partial \beta_g / \partial u = 0$ and diagonal elements $\partial \beta_g / \partial g$ and $\partial \beta_u / \partial u$ correspond directly to the eigenvalues of the present matrix. Using numerical analysis one can show that the real parts of the diagonal elements are positive for all values of $A$ in the vicinity of $\epsilon = 0$. Furthermore, we have also shown that including spatial parity violation shifts the values of the present matrix even further to positive values. In the end, we stress the well-known fact that $\beta$ functions of the present model are exactly given even at the one-loop order since all higher order terms cancel mutually, which means that the anomalous dimensions $\gamma_1^* = \gamma_2^*$ equal exactly $2\varepsilon/3$ at the IR stable fixed point.

# 5   Helicity and the turbulent Prandtl number

Once the crucial RG analysis is finished all of the physical quantities as measured by experiments may be obtained. As this is a very specific calculation and our aim was to discuss the RG approach in the specified classical model we only give a brief overview of the results. An interested reader may find the details in Refs. [55, 19]. We now merely stress that all helical properties specific for the given admixture type described by Eq. (1) are in the two-loop order of perturbation theory of the corresponding field theoretic model completely encoded by the two-loop Feynman graphs of Fig. 3. According to

Ref. [19], the resulting two-loop expression for the inverse turbulent Prandtl number reads as

$$u_{eff} = u_*^{(1)}\left(1 + \varepsilon\left\{\frac{1 + u_*^{(1)}}{1 + 2u_*^{(1)}}\left[\lambda - \frac{128(d+2)^2}{3(d-1)^2}\mathcal{B}(u_*^{(1)})\right]\right.\right.$$
$$\left.\left. + \frac{(2\pi)^d}{S_d}\frac{8(d+2)}{3(d-1)}\left[a_v - a_b(u_*^{(1)})\right]\right\}\right), \tag{49}$$

where $\varepsilon$ and the dimension $d$ are taken to their physical values of $\varepsilon = 2$ and $d = 3$, the one-loop value of the inverse turbulent Prandtl number $u_*^{(1)}$ is given in Eq. (38), $\mathcal{B}(u_*^{(1)})$ is defined in Eq. (47) and $\lambda$ is shown in Eq. (40). The following numerical value corresponds to $\lambda$ in $d = 3$ as considered here for helical environments: $\lambda = -1.0994$. The remaining parameters $a_v$ and $a_b$ which enter into Eq. (49) are quite complicated and correspond to the finite parts of one-loop diagrams with two external velocity type fields $\mathbf{v}$, $\mathbf{v}'$ and two admixture type fields $\mathbf{b}$, $\mathbf{b}'$, respectively. We omit the details here and refer the reader to Ref. [55]. For further discussion it is convenient to split $u_{eff}(A)$ into its non-helical part $u^{(0)}(A)$ and its corresponding helical contribution $\rho^2 u^{(\rho)}(A)$ via

$$u_{eff}(A) = u^{(0)}(A) + \rho^2 u^{(\rho)}(A). \tag{50}$$

Note that both $u^{(0)}(A)$ and $u^{(\rho)}(A)$ are defined to be independent of $\rho$. Nevertheless, $u^{(\rho)}(A)$ stands in front of the helical contribution in Eq. (50) and thus encodes all helical effects of the present model. Both $u^{(0)}(A)$ and $u^{(\rho)}(A)$ are analytic functions but we shall not reproduce the corresponding expressions here and merely show their graphical representation given in Fig. 5.

Considering $u^{(0)}(A)$ we note that at $A = -1.723$ and $A = 2.800$ (numerical values rounded to 3 decimal places) the zero points of $u^{(0)}$ would cause the turbulent Prandtl numbers to grow infinitely which would be unphysical. Consequently, in the non-helical case values of $A$ are restricted to $A \in \langle-1.723, 2.800\rangle$. However, we note that constraints for non-helical environments arise only in connection with the two-loop order calculation used here and are therefore inherently given by the structure of perturbation theory of the $A$ model. In other words, such constraints are not inherent in values of $A$ outside of the usually studied region $-1 \leq A \leq 1$ and represent only an artifact of the perturbative approach.

However, when symmetry breaking is taken into account as done by $u^{(\rho)}$ we note that restrictions imposed on $A$ are lifted off. This is shown as before graphically via Fig. 6 where inverse turbulent Prandtl number is
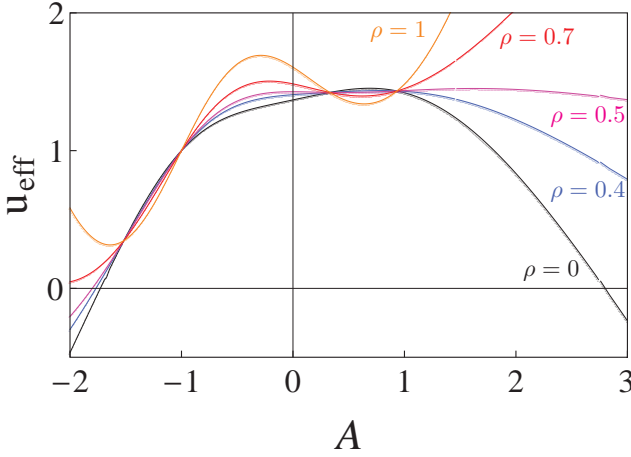
Figure 6: (Color online) Inverse turbulent Prandtl number $u_{eff}$ as a function of $A$ shown for fixed values of $\rho$ in the range of $-2 \leq A \leq 3$. On the right side of the graph, in the region of approximately $A > 1$, the dependences for selected values of $\rho$ are stacked one above the other with $\rho = 1$ (orange) being on the top while the remaining dependences follow in the successive order of $\rho = 0.7$ (red), $\rho = 0.5$ (magenta), $\rho = 0.4$ (blue) and $\rho = 0$ (black). Note that for $\rho = 1$ the function is apparently bound from below but unbound from above which is a behaviour observed for all $\rho > 0.749$ which represents a threshold value of helicity above which the stationary regimes of the system are fully stabilized.

depicted as a function of $A$ for selected values of $\rho$. Clearly, there exist some critical value of the helicity parameter $\rho$ for which the corresponding inverse turbulent Prandtl number $u_{eff} = u^{(0)} + \rho^2 u^{(\rho)}$ gets positive for all values of $A$. In other words, when spatial parity violation is strong enough, the resulting inverse turbulent Prandtl number obtains always positive values.

Summing up, we have shown that the impact of the interactions as given via the parameter value of $A$ has a highly non-trivial impact on diffusion-advection processes when helical environments are considered. The resulting dependences are truly complicated functions of $A$ and lead to non-trivial effects in connection with the helicity parameter $\rho$. Therefore, instead of the tensorial nature of the admixture itself we have clearly identified the tensorial structure of interactions to be a more dominant factor which effectively alters the advection diffusion process in fully developed turbulent environ-

ments. Thus, assertions made by the authors of Ref. [15] must partially be revided at least for the case of vector admixtures advected passively in turbulent environments, and a greater than expected impact of interactions on the actual advection diffusion processes must be recognized. Additionally, we once again stress that present calculations clearly demonstrate that helical effects exert stabilizing effect on diffusion advection processes.

# 6    Conclusion

Using the field theoretic renormalization group technique in the two-loop approximation, we have obtained analytic expressions for the turbulent Prandtl number within the general $A$ model of passively advected vector impurity by techniques which are well known in high energy physics but obtain considerable modifications due to the two scaled nature of the problem as a consequence of non-relativistic properties of the classical model under the consideration. In the two-loop order we noticed the importance of additional restrictions on $A$ to obtain physically well defined values of turbulent Prandtl numbers. However, these are most probably only an artifact of the two-loop order perturbative calculations. Additionally, the stability of stationary regimes when a critical threshold of $\rho \approx 0.75$ is exceeded resembles helicity effects already observed in the framework of the specific models of developed turbulence [56, 57, 58].

# 7    Acknowledgement

# References

[1] M. E. Peskin, and D. V. Schroeder, An Introduction to Quantum Field Theory, The Advanced Book Program, Perseus Books (Reading, Massachusetts), 1995.

[2] A. N. Vasilev, *Quantum-Field Renormalization Group in the Theory of Critical Phenomena and Stochastic Dynamics* (Chapman & Hall/CRC, Boca Raton, 2004).

[3] K. G. Wilson, Renormalization Group and Critical Phenomena. I. Renormalization Group and the Kadanoff Scaling Picture, Physical Review B, vol. 4, Issue 9, pp. 3174-3183 (1971); K. G. Wilson, Renormalization Group and Critical Phenomena. II. Phase-Space Cell Analysis of Critical Behavior, Physical Review B, vol. 4, Issue 9, pp. 3184-3205 (1971).

[4] E. Stueckelberg, and A. Petermann La normalization des constantes dans la theorie des quanta, Helvetica Physica Acta, Vol.26, 1953, p.499.

[5] M. Gell-Mann, and F. E. Low, Phys. Rev. 95, 1300 (1954).

[6] A. Yoshizawa, S. I. Itoh, and K. Itoh, *Plasma and Fluid Turbulence: Theory and Modelling* (IoP, Bristol and Philadelphia, 2003).

[7] D. Biskamp, *Magnetohydrodynamic Turbulence* (CUP, Cambridge, 2003).

[8] A. S. Monin and A. M. Yaglom, *Statistical Fluid Mechanics* (MIT Press, Cambridge, MA, 1975), Vol. 2.

[9] W. D. McComb, *The Physics of Fluid Turbulence* (Clarendon, Oxford, 1990).

[10] B. I. Shraiman and E. D. Siggia, Review Nature **405**, 639-646 (2000)

[11] U. Frisch, The Legacy of A. N. Kolmogorov, Cambridge University Press (1995).

[12] J. M. Coulson, J. F. Richardson, *Chemical Engineering* (Elsevier, 1999), Vol.1.

[13] L. P. Chua and R. A. Antonia, Int. J. Heat Mass Transf. **33**, 331 (1990).

[14] L. P. Chang and E. A. Cowen, J. Eng. Mech. **128**, 1082 (2002).

[15] E. Jurčišinová, M. Jurčišin, and P. Zalom, Phys. Rev. E **89**, 043023 (2014).

[16] N. V. Antonov and N. M. Gulitskiy, Phys. Rev. E **91**, 013002 (2015)

[17] N. V. Antonov and N. M. Gulitskiy, Phys. Rev. E **92**, 043018 (2015)

[18] E. Jurčišinová, M. Jurčišin, and R. Remecký, Phys. Rev. E **93**, 033106 (2016).

[19] L. Ts. Adzhemyan, J. Honkonen, T. L. Kim, and L. Sladkoff, Phys. Rev. E **71**, 056311 (2005).

[20] P. C. Hohenberg and B. I. Halperin, Rev. Mod. Phys. **49**, 435 (1977).

[21] D. Forster, D. R. Nelson, and M. J. Stephen, Phys. Rev. Lett. **36**, 867 (1976).

[22] D. Forster, D. R. Nelson, and M. J. Stephen, Phys. Rev. A **16**, 732 (1977).

[23] L. Ts. Adzhemyan, N. V. Antonov, A. Mazzino, P. Muratore-Ginanneschi and A. V. Runov, Europhys. Lett. **55**, 801 (2001).

[24] N. V. Antonov, M. Hnatich, J. Honkonen and M. Jurčišin, Phys. Rev. E **68**, 046306 (2003).

[25] H. Arponen, Phys. Rev. E **79**, 056303 (2009).

[26] L. Ts. Adzhemyan, N. V. Antonov, and A. N.Vasilev, *The Field Theoretic Renormalization Group in Fully Developed Turbulence* (Gordon & Breach, London, 1999).

[27] J. Zinn-Justin, Quantum Field Theory and Critical Phenomena (Clarendon, Oxford, 1989).

[28] L. Ts. Adzhemyan, A. N. Vasilev, and Yu. M. Pismak, Theor. Math. Phys. **57**, 1131 (1983).

[29] L. Ts. Adzhemyan, N. V. Antonov, M. V. Kompaniets, and A. N. Vasilev, Int. J. Mod. Phys. B **17**, 2137 (2003).

[30] L. Ts. Adzhemyan, J. Honkonen, M. V. Kompaniets, and A. N. Vasilev, Phys. Rev. E **68**, 055302(R) (2003).

[31] L. Ts. Adzhemyan, A. N. Vasilev and M. Gnatich, Theor. Math. Phys. **74**, 180-191 (1988).

[32] L. Ts. Adzhemyan, N. V. Antonov, and A. N. Vasilev, Usp. Fiz. Nauk **166**, 1257 (1996) [Phys. Usp. 39, 1193 (1996)].

[33] L. Ts. Adzhemyan, J. Honkonen, M. V. Kompaniets, and A. N. Vasilev, Phys. Rev. **E** 71, 036305 (2005).

[34] L. Ts. Adzhemyan, J. Honkonen, T. L. Kim, M. V. Kompaniets, L. Sladkoff, and A. N. Vasil'ev, J. Phys. A: Math. Gen. **39** 7789 (2006).

[35] L. Ts. Adzhemyan, A. N. Vasilev, and M. Gnatich, Theor. Math. Phys. **58**, (1983).

[36] L. Ts. Adzhemyan, N. V. Antonov and A. N. Vasilev, Phys. Rev. E **58**, 1823 (1998)

[37] L. Ts. Adzhemyan, N. V. Antonov, V. A. Barinov, Yu. S. Kabrits, and A. N. Vasilev, Phys. Rev. **E** 63, 025303(R) (2001); L. Ts. Adzhemyan, N. V. Antonov, V. A. Barinov, Yu. S. Kabrits, and A. N. Vasilev Phys. Rev. **E** 64, 019901 (2001).

[38] S. V. Novikov, Theor. Math. Phys. 136, 936 (2003)

[39] N. V. Antonov and M. M. Kostenko, Phys. Rev. E **90**, 063016 (2014).

[40] C. Pagani, Phys. Rev. **E** 92, 033016 (2015).

[41] L. Ts. Adzhemyan, A. N. Vasilev, and M. Gnatich, Theor. Math. Phys. **64**, 777 (1985).

[42] L. Ts. Adzhemyan, A. N. Vasilev, and M. Hnatich, Theor. Math. Phys. **72**, 940 (1987).

[43] N. V. Antonov and M. M. Kostenko, Phys. Rev. E **92**, 053013 (2015).

[44] E. Jurčišinová, M. Jurčišin, R. Remecký, and P. Zalom, Phys. Rev. E **87**, 043010 (2013)

[45] L. Ts. Adzhemyan, N. V. Antonov, P. B. Goldin, and M. V. Kompaniets, J. Phys. A: Math. Theor. **46**, 135002 (2013); N. V. Antonov and N. M. Gulitskiy, Theor. Math. Phys. **176**, 851 (2013).

[46] S. V. Novikov, J. Phys. A: Math. Gen. **39** 8133 (2006).

[47] H. Arponen, Phys. Rev. E **81**, 036325 (2010).

[48] E. Jurčišinová, M. Jurčišin, and R. Remecký, Phys. Rev. E **88**, 011002(R) (2013).

[49] P. C. Martin, E. D. Siggia, and H. A. Rose, Phys. Rev. A **8**, 423 (1973); C. De Dominicis, J. Phys. (Paris), Colloq. 37, C1-247 (1976); H. K. Janssen, Z. Phys. B **23**, 377 (1976); R. Bausch, H. K. Janssen, and H. Wagner, ibid. **24**, 113 (1976).

[50] J. C. Collins, *Renormalization: An Introduction to Renormalization, the Renormalization Group and the Operator-Product Expansion*, (Cambridge University Press, Cambridge 1986).

[51] S. S. Moiseev, R. Z. Sagdeev, A. V. Tur, G. A. Khomenko and V. V. Yanovskii, Zh. Eksp. Teor. Fiz., **85**, 1979 (1983).

[52] A. Pouquet, J. D. Fournier and P. L. Sulem, J. Phys. Lett. (Paris), 39L, 199 (1978).

[53] S. I. Vainshtein, Ya. B. Zel'dovich and A. A. Ruzmaikin, The Turbulent Dynamo in Astrophysics [in Russian], Nauka, Moscow (1980); S. I. Vainshtein, Magnetic Fields in Space [in Russian], Nauka, Moscow (1983).

[54] H. K. Moffat, Magnetic Field Generation in Electrically Conducting Fluids, C.U.P., Cambridge (1978).

[55] M. Hnatič, and P. Zalom, Phys. Rev. E **94**, 053113 (2016)

[56] A. A. Migdal, Mod. Phys. Lett. A, **06**, 1023 (1991).

[57] L. Ts. Adzhemyan, M. Hnatich, and M. Stehlik, J. Phys. II (France), 5, 10771092 (1995).

[58] L. Ts. Adzhemyan, M. Hnatich and M. V. Kompaniets, Theor. Math. Phys., 176(1): 835842 (2013).

# SECTION "NEW COLLIDERS, FACILITIES, DETECTORS, COMPUTING AND DATA ANALYSES TECHNIQUES"
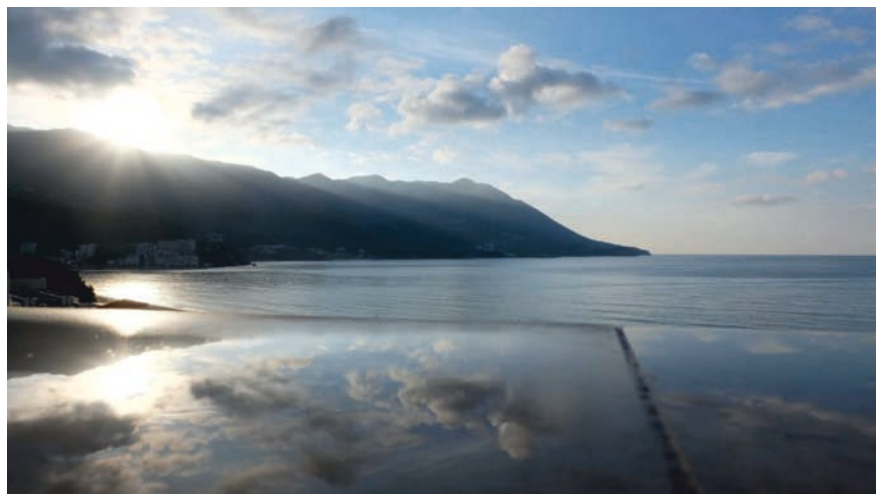
# The increase of the light collection from scintillation strip with hole for WLS fiber using various types of fillers

A. Simonenko[1], A. Artikov[1,2], V. Baranov[1], J. Budagov[1], D. Chokheli[1,3], Yu. Davydov[1], V. Glagolev[1], Yu. Kharzheev[1], V. Kolomoetz[1], A. Shalyugin[1], V. Tereschenko[1]

[1]Joint Institute for Nuclear Research, Russia, Dubna, Joliot-Curie 6, 141980
[2]NPL, Samarkand State University, Uzbekistan, Samarkand, University Boulevard 15, 703004
[3]IHEP, Tbilisi State University, Georgia, Tbilisi, University str. 9, 0186

**Abstract**

The light collection of the extruded scintillator strip samples with WLS fibers placed in the longitudinal hole in the plates was measured. The holes were filled with various liquid fillers. Measurements were carried out under irradiation by cosmic muons. The method of pumping liquid filler with viscosity more than 10 Pa*s in the strip's hole with WLS fiber inside was designed and successfully tested.

**Introduction**

Currently, detectors based on extruded plastic scintillators are an integral part of most physical experiments in particle physics. One of their advantages is the fast rise time of the signal $\tau_{rise}$ equal to a few nanoseconds. Another important fact - this is a relatively low cost material. Such scintillators are made, usually in the form of long (several meters) plates [1, 2]. The light usually occurs via WLS fibers, which absorb the light emitted by the scintillator's material, and re-emit it in the range close to the maximum spectral sensitivity of the photo-detector. Often WLS fiber is fixed with optic adhesive on one face over the entire length of the scintillator [3].

However, the more technological solution for the placement of fibers is to provide extruded scintillators with holes passing inside the scintillator along its entire length [4, 5]. Typically, the hole diameter of 2-3 times higher than the fiber diameter. In such scintillators WLS fibers are inserted into the holes and the light from the scintillator is captured by them through an air gap.

When using a fairly long strips with WLS fibers inserted in the holes may not be sufficient amount of light entering to the photodetector. An adhesion the fibers into the inner hole may increase the light collection [4]. However, the high viscosity and limited time use of a two-component adhesive make the task of filling holes difficult. Decision in such a situation can be filling holes by suitable liquids with low viscosity or the use of optical adhesives without hardener, which eliminates the condition of time (speed) injection. In this paper we present the results of tests with different fillers. Four types of fillers were selected: distilled water, an aqueous solution of glycerol, UV glue with ultra-low viscosity "Spectrum-K-59-EN" [6] and a low molecular weight rubber "SKTN-MED" mark E [7].

Their characteristics are shown in Table 1. It should be noted that at this stage of research the fillers haven't be checked on their radiation resistance and possible chemical influence to the scintillator.

**Table 1**. Characteristics of the fillers

| Name | distilled water | aqueous solution of glycerol | UV glue «Spectrum-K-59-EN» | low molecular weight rubber "SKTN-MED" mark E |
|---|---|---|---|---|
| refractive index. $(20C^0)$ | 1.333 | 1.388 | 1.460 | 1.606 |
| dynamic viscosity, mPa*c | 1 | 20 | 20 | 10000 |
| comments | | 43% solution | | hardener not used |

**Apparatus and materials**

Tests were carried out with triangular samples of scintillation strips (33mm base, height 17 mm), 50 cm long, with longitudinal holes diameter 2.6 mm, produced in the ISMA (Kharkiv, Ukraine). The strips are made by extrusion of polystyrene with additives 2% PTP and 0.03% POPOP. The sample surface was covered with a reflective layer of titanium oxide (TiO2). The sample ends were polished and covered with a layer of mirrored Mylar. WLS fiber cladding

Kuraray Y11 (200) [8] 1.2 mm diameter was used, which was fixed in the hole from both ends of the scintillator with glue. Holes with thread and plastic plugs for injection of fillers on the surface (base) strips were made (Figure 1).
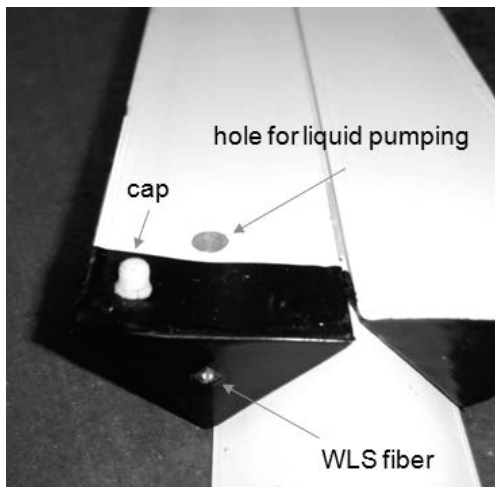


**Figure 1.** Scintillation strip samples.

We used PMT EMI 9814B as a photodetector with photocathode diameter - 51 mm. Trigger counters are based on SiPM SensL 3x3 $mm^2$ with a scintillator dimensions 20*20*20 $mm^3$ (Figure 2). These counters have the output signals in analog and digital formats.



**Figure 2.** Trigger counter based on SiPM SensL.

## Test conditions

Measurements were carried out by comparing the light collection of the same strips dry and filled with a certain filler when passing through them cosmic-ray muons. Light came only from fibers which had optical contact with PMT window through the optical lubricant. There used 2 pair of trigger counters, i.e. spectra were recruited at two points simultaneously (Figure 3). Scintillators trigger counters were adjusted in the center across the strip, thus blocking 20*20 mm$^2$ area of the test strip. Fillers pumped into the hole in two ways: liquid (water, glycerol, and the UV glue) - manually with a syringe; viscous rubber - with compressor and fluid dispenser (see below).
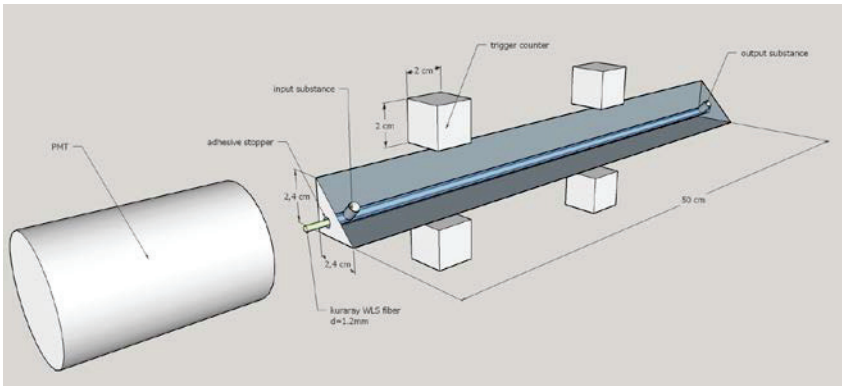


**Figure 3.** The layout of the elements.

An absolute calibration method was applied to calculate the light collection into photoelectrons [9]. Because the running distance of the muons in the triangular scintillator varies greatly (from 4 mm to 24 mm in leg size for normally incident muons), the range of output signals looks wider compared with in the rectangular strip (see. Fig.4).
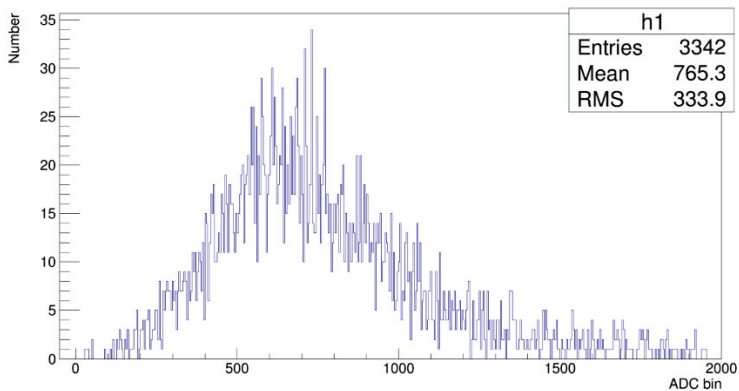
**Figure 4.** Typical spectrum of the cosmic-ray muons for a triangular strip sample.

The data acquisition system (Figure 5) was implemented in the following way. The signals from the two pairs of trigger counters after passing the discriminator, and then pairwise coincidence unit, summed and fed to the input of the gate generator. That, in turn, generate a gate signal with a specific duration (strobe) to the input of the charge-to-digital converter (LeCroy 2249W), thereby starting the processing of the signal coming from the main PMT. At the same time generated an inhibit signal for all input trigger signals. The digitized signals from ADC were read by PC, the input register showed which pair of trigger counter worked at that time moment.
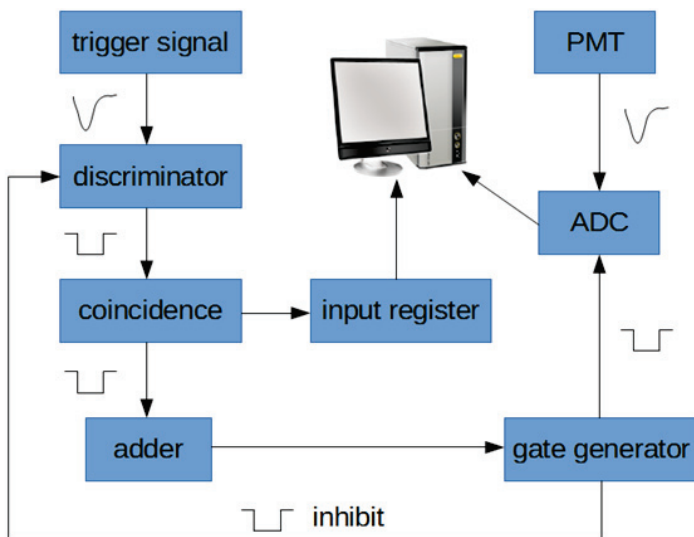
**Figure 5.** Block-diagram of the data acquisition system.

## Methods of injection fillers

As mentioned above, we used a conventional syringe and a transparent tube  for water, glycerin and UV glue injection to strip scintillation sample. A syringe was attached to the first hole and the tube inserted into the second hole and we squeezed until the contents began to flow out from the tube. The process continued until all air bubbles come out. At the end of the process both holes tightened by the plastic plugs.

In the case of viscous rubber used commercial compressor for supplying air to the dispenser «Fisnar» [10] and then  into a vessel with rubber. Empirically, it was picked up excess pressure in the dispenser at 0.2 atm. The rubber under the influence of such a small constant pressure slowly squeezed into a tube connected to the first hole of the scintillation strips. For filling holes strip 50 cm long it took 30 minutes. We have conducted preliminary experiments with strip samples without TiO2 layer. Results showed good filling holes with absence of air bubbles. Sealing holes after injection of rubber was carried out by adding of a small amount of hardener in both holes.

## Results

Final results about increasing light collections for each filler are shown in Table 2. The measurements were made in four fixed positions 13, 23, 33 and 43 cm from the surface of the PMT window. For each position was got the spectrum of signals and then was defined the average value of the photoelectrons by absolute calibration. The measurement results are shown in Figure 6. The obtained data were fitted by a function $f(x) = exp^{p0+p1*x}$.

The unfilled data marked with round symbols, the data with the appropriate filler - square symbols. Priority scheduling is as follows (left - right, top - down): distilled water, an aqueous solution of glycerol, UV glue and low molecular weight rubber.
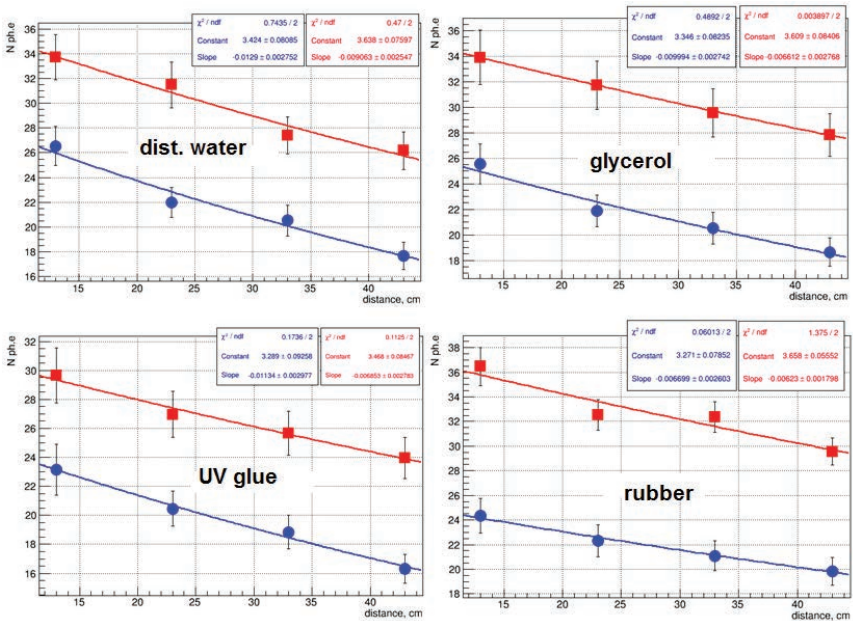


**Figure 6.** Light collection from strips for a variety of filler options. Round symbols - no filler, squares - with the filler.

**Table 2**. The total increase in light collection for each filler.

| filler | distil. water | aq. solution of glycerol | UV glue SPECTRUM | rubber SKTN |
|---|---|---|---|---|
| light collection's increase,% | 38 ± 6 | 43 ± 6 | 36 ± 6 | 50 ± 5 |

As a result, all four fluids given increase of the light collection in the range 36-50%. The greatest increase in light collection demonstrated a low molecular weight rubber "SKTN-MED" mark E (round symbols).

**Conclusions**

The samples of extruded scintillator strips with slotted holes and inserted into the WLS fibers for increasing the light collection using various optical fillers were tested.

Four sorts of the fillers have been investigated: distilled water, an aqueous solution of glycerol, UV glue ultra-low viscosity "Spectrum-to-59-EN" and a low molecular weight rubber "SKTN-MED" mark E.

The method of filler injection with viscosity greater than 10 Pa*s in the hole with a 2.6 mm diameter of the strips after placing into them the WLS fibers with a 1.2 mm diameter developed and tested. Filling time was 30 minutes for a sample strip 50 cm long.

Filling optical liquids having a low viscosity and viscous adhesives without hardener (for example in the case of rubber "SKTN-MED" mark E) in order to increase the light collection is a good alternative gluing of fibers, which is particularly problematic for the long scintillator strips.

It is shown that the use of various liquid fillers between the surface of WLS fibers and the scintillator's material enables the increase of light collection in the range of 36-50% in comparison with the samples using an air gap.

**References**

1.   *Thevenin J.C., Allemand L., Locci E., Micolon P., Palanque S., Spiro M*. Extruded polystyrene, a new scintillator, NIM. 1980. V. 169. P. 53-56

2. *Ananiev V.K., Bazilevski A.V., Durum A.A., Diachkov A.I., Kochetkov V.I., Mayatsky V.A., Semenov V.K., Soldatov A.P.* New Extruded Scintillator from Commercial Polystyrene: IHEP Preprint 97-1. – Protvino, 1997. – p. 11, figs. 9, refs.: 25.

3. *Kudenko Yu.G., Littenberg L.S., Mayatski V.A., Mineev O.V., Yershov N.V.* Extruded plastic counters with WLS fiber readout, NIM.A. 2001. V. 469. P. 340-346

4. *Anna Pla-Dalmau, Alan D. Bross, Kerry L. Mellott.* Low cost Extruded Plastic Scintillator, NIM.A. 2001. V. 466. P. 482-491

**5.** *Aliaga L. et al.*, Design, Calibration, and Performance of the MINERvA Detector, NIM.A . 2014. V.743. P. 130-159

6. Research and Production Group "SPECTRUM", Nizhny Novgorod, Russia, <http://www.nipg.ru>

7. Research and Production Group "SUREL", St. Petersburg, Russia, <http://www.surel.ru>

8. Kuraray Corp, 3-10, Nihonashi, 2 chrome, Chou-Ku, Tokio, Japan

9. *Bellamy E.T., Bellettini G., Budagov J., Cervelli F., Chirikov-Zorin I., Incagli M., Lucchesi D., Pagliarone C., Tokar S., Zetti F..* Absolute calibration and monitoring of a spectrometric channel using a photomultiplier, NIM.A. 1994. V. 339. P. 468-476

10. Fisnar Inc.19C Chapin Rd., Suite 307, Pine Brook, NJ 07058, USA, <www.fisnar.com>

# High Technology Application to Modernization of International Electron-Positron Linear Collider (ILC)

*B.Sabirov[1], A.Basti[3], F.Bedeschi[3], A.Bryzgalin[2], J.Budagov[1], P.Fabbricatore[3], E.Harms[5], S.Illarionov[2], S.Nagaitsev[5], E.Pekar[2], V.Rybakov[4], Ju. Samarokov[4], G.Shirkov[1], W.Soyars[5], Yu.Taran[1]*

1 - JINR, Dubna, Russia

2 - PWI, Kiev, Ukraine

3 - INFN, Pisa/Genova, Italy

4 – VNIIEF, Sarov, Russia

5 – FNAL, USA

### Introduction

The past few years, we have made a great deal of progress in developing and demonstrating the enabling technology needed for a linear collider for the modernization of the cryomodule for the International Linear Collider (ILC) in the frame of collaboration JINR (Dubna, Russia), INFN (Pisa/Genova, Italy), *PWI ( Kiiv, Ukraine), FNAL (USA) and VNIIEF (Sarov, Russia)* [1-4] .

Based on our experience, the collaboration got down to creating a transition specimens between the steel shell of the cryomodule vessel and the niobium cavity [Fig.1]. Trimetallic Nb+Ti+SS specimens were produced using the explosion welding and successfully tested at liquid nitrogen and liquid helium temperatures. This version deserves special attention for its manufacturability, simpler design, guaranteed strength and reliability of the joint and above all for an appreciably lower cost. It is a promising new transition joint technology based on cladding side surfaces of a steel flange by titanium using explosion bonding and welding a Nb pipe to titanium by EBW.
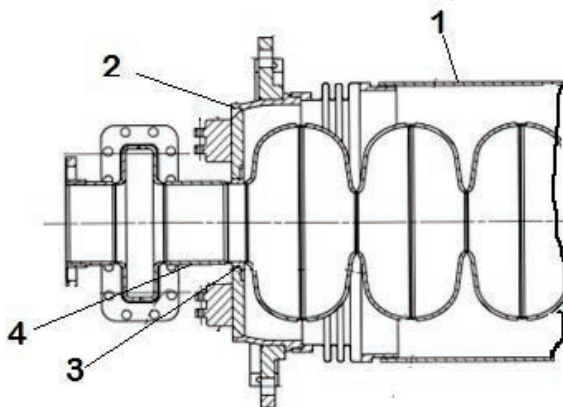
**Fig.1** *Scheme of combined adapter connection with a cryogenic module: 1 – steel shell; 2 - electron beam welding or argon arc welding connection of shell with steel flange of adapter; 3 - steel flange; 4 - niobium tube;*

## Problem Definition

It is known that welding of similar materials gives the best results. The adapter should consist of at least two metals, niobium and stainless steel. No fusion welding, including electron beam welding is suitable for joining niobium and stainless steel because it results in formation of intermetallic compounds like $Nb_xFe_y$, which do not allow the required adapter tightness to be obtained. In addition, this compound does not withstand the thermal load at cryogenic temperatures and fails.

Earlier experiments showed that electron beam welding of niobium and titanium did not result in formation of intermetallic compounds and ensured the required helium and vacuum tightness. In this connection the following adapter manufacture procedure was proposed [5]. First, the stainless steel disc is clad with titanium on both sided by explosion welding, the resulting trimetal is shaped as required (by planishing and turning to the size), and a hole is cut for the niobium pipe. The pipe is inserted in the hole and electron-beam welded to titanium (Fig. 2).

Advantages of this adapter manufacture procedure are as follows:

- electron beam welding of niobium and titanium did not result in formation of intermetallic compounds and ensured the required helium and vacuum tightness;
- possible formation of intermetallic compounds in the explosion weld steel–titanium joint does not affect helium tightness;
- explosion welding of flat pieces is technologically much simpler than welding of pipes and allows joints with quality as much stable as possible;
- expenditure of steel and niobium decreases.
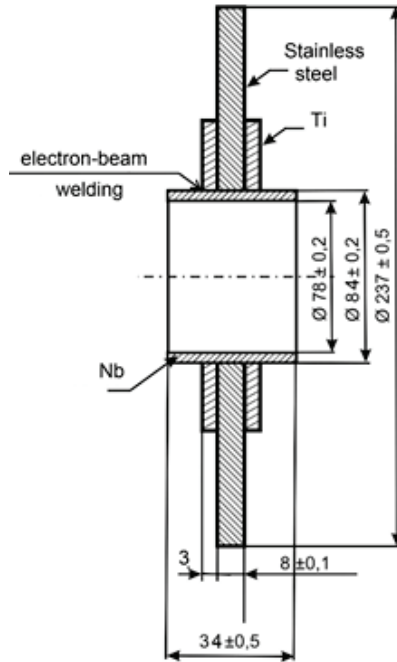
**Fig.2.** *The design of the adapter, ensuring the absence of niobium intermetallic formations during welding.*

**Explosion welding of metals and its main parameters**

Explosion welding is a process of making a permanent joint through metallic bonding [6]. It does not require a heat source because the energy comes to the joint area from the collision of the plates (Fig. 3). In optimum explosion welding regimes the heat-affected zone is very small, as is the existence time of high temperature.
The surfaces of the metals to be joined suffer plastic deformation creating a wave pattern bond line. An increase in the welding energy (collision energy of plates) increases wave parameters.

Since explosion welding is a complicated and high-velocity process, there is so far no universal mathematical model capable of precisely describing all its details.
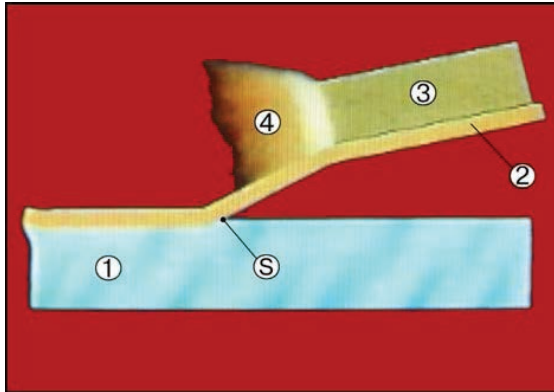
**Fig.3.** *Principal schemes of explosion welding process   with an angle between metal sheets   1 - base plate; 2 –cladding plate; 3 - explosive; 4 - detonation products; S - point (line) of contact of surfaces during welding*

It is worth noting that titanium forms intermetallic compounds with almost all metals except niobium, tantalum, and vanadium

Explosion welding regimes for fabricating the titanium–steel–titanium trimetal were selected experimentally. The titanium was 3 mm thick and the steel was 8 mm thick. Plates with dimensions 250x250 mm (Ti) and 300x700 mm (SS) were welded. After the explosion and after the fabrication of the trimetal    the planishing was performed on an industrial rolling mill to eliminate local deformation to make the billet flat.

Discs 237 mm in diameter with a central hole 84 mm in diameter for the niobium pipe were cut and electron beam welding (EBW) process of niobium tube with titanium clad  occurs in a high-vacuum chamber in the deepest penetration regime (Fig.4).

287

**Fig. 4.** *Appearance of combined adapter.*

The Vickers microindentation test was performed. The results of measuring microhardness at a load of 100 g are presented in Fig.5
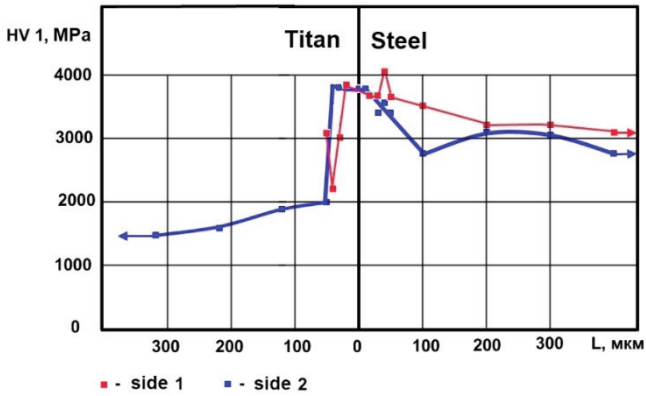


**Fig.5.** *The microhardness of the steel-titanium*
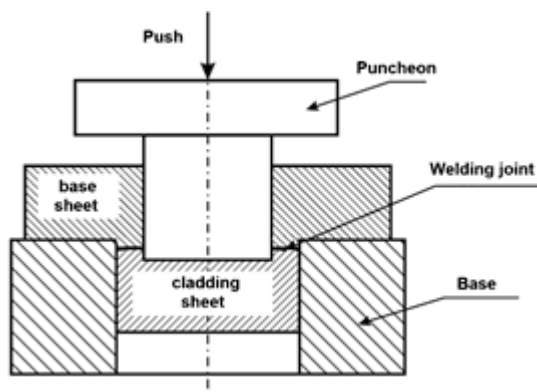
**Fig.6.** *The scheme of layer tear test boundary after explosion welding*

The layer shear tests (Fig. 6) showed the strength at a level of 350 MPa considered satisfactory.

Obtained test results are rather optimistic and encouraged : the joining density characterized by absence of leak at background leak rate ~$4.7 \cdot 10^{-9}$mbar·l/sec, measured at variety extreme conditions: thermocycles at temperature 77K and 2K, at pressure 6.5 atm; test at high temperature thermoload, exposure to ultrasonic radiation.

The next test is **main crusial** one: for imitation of use transition sample in real working position, connected with Nb cavity, Nb rings were joint with Nb pipe of samples by EBW. The welded joint experienced various internal stresses, first, due to the explosion welding, then due to the thermal load from the electron beam welding (niobium melting point is 2460°C), and ultimately due to the thermal load at an extreme low helium temperature of 4°K. Superposition of all these residual stresses may result plastic deformation, failure of welds, and consequently occurrence of a leak. Test result ussued absence of leak at background leak rate ≈$0.5 \cdot 10^{-10}$atm·cc/sec.

We have measured residual stresses in Ti+SS joint using the neutron diffraction method. Measurements were carried out with the POLDI stress diffractometer on the neutron beam from the ISIS reactor of the Paul Scherrer Institute (Switzerland) [4]
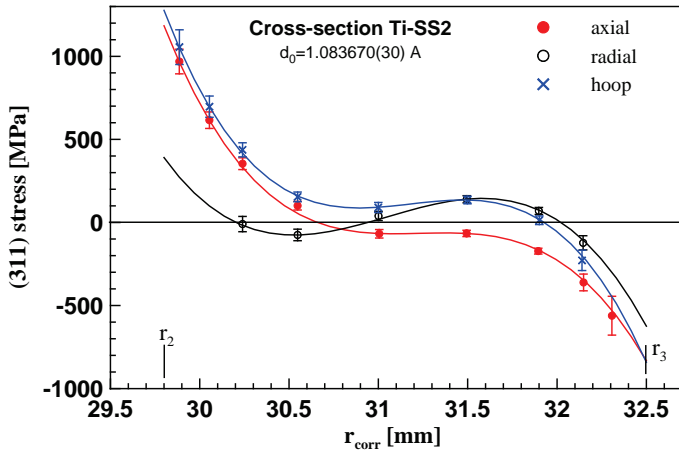


**Fig.7.** *Measured (points) and fitted (curves) radial dependence of the stress .*
*tensor components obtained for the peak (311) in the Ti+SS cross section*

Measured (points) and fitted (curves) radial dependences of the stress tensor components obtained for the peak (311) in the Ti+SS cross section ultimate result of residual stress measurements in the bimetallic Ti+SS joint in the process of scanning the titanium-to-stainless steel joint (Fig.7). As is evident from the plot, the residual stress is quite considerable, amounting to ≈1000 MPa. Considering that foregoing residual internal stresses superposition can make titanium turn into the state which corresponds to the deep plastic region. This may cause local microcracks in the Ti+SS (or Nb+SS) joint, which in turn may adversely affect tightness of the transition element when it is used in the cryomodule.

**CONCLUSION**

The adapter is designed which is suitable for manufacturing a linear collider cryomodule and eliminates the necessity to weld niobium to steel.

  An explosion welding technology is developed that allows a trimetallic billet for manufacturing an adapter to be made such that the niobium–titanium bond is free of intermetallic compounds and the effect of the difference in the linear expansion coefficients of the ensemble components is eliminated. Regimes for EBW of steel to niobium and titanium are chosen which tentatively meet the adapter operation requirements.

The results showed the full eligibility of suggested design Nb+Ti+SS transition sample not for only Linear Collider, but for any cryogenic systems [7,8].

**REFERENCES**

1. Sabirov B. *"Explosion welding: New Design of the ILC Cryomodule"*. JINR NEWS, 3/2010, p.16, Dubna,2010.
2. "*Electric welding technology of metalls and alloys by melting*"(rus) By edition of B.E.Paton. Moscow: "Mashinostroenije", 1974.
3. B.Sabirov et al., *"Recent Advances in Ti and Nb explosion welding with stainless steel for 2K operating (ILC Program)"*, Proceedings of the International Workshop on Future Linear Colliders (LCWS11), Spain, Granada, 26-30 September, 2011, arXiv:1201.3472.
4. B.Sabirov, J.Budagov, G.Shirkov *"First samples of Ti and Nb tubes explosion welding joint with stainless steel for ILC 1.8K Cryomodule"*, PARTICLE&NUCLEI, **44**, part 4, p.1388, Dubna, 2013
5. Taran Yu.V. et al. Residual Stresses in an Explosion Welding Titanium-Steel Bilayer Pipe by Neutron Diffraction // JINR News. 2011. No.4. P.16.
6. B.Sabirov et al.,*"Modernisation of the ILC Cryomodule using High-Tech Technology — Explosion Welding*", XXIV Russian Particle Accelerator Conference (RuPAC'2014), Obninsk, Russia, 6-10 October, 2014
7. Lisak V.I., Kuzmin S.V. *"Explosion welding*" (rus). Moscow, "Mashinostroenie", 2005, 511 p.
8. Basti A.,…Sabirov B., et al., *"Optimization of ILC Cryomodule Design Using Explosion Welding Technology"*, International Particle Accelerator Conference (IPAC'15), Richmond, Virginia ,3-8 May, 2015

# Solar-blind photodetectors with AlGaN photocathodes for light registration in UVC range

N.V. Atanov[1], V.V. Tereshchenko[1],

S.I. Ivanov[2], V.N. Jmerik[2], D.V. Nechaev[2]

1) Joint Institute for Nuclear research, Dubna, Russia;
2) Ioffe Institute, St. Petersburg, Russia

Experiment Mu2e is divided into 2 phases. During each phase different particle intensity and radioactive background will take place: up to 100 krad for first phase and up to 200 Mrad for second one. To meet these requirements collaboration suggests to use $BaF_2$ scintillation crystals for electromagnetic calorimeter construction in second phase of Mu2e experiment. Emission spectrum of $BaF_2$ scintillator consist of fast and slow components in UVC light range. Fast component has decay time ~0.8 ns and wavelengths shorter than 260 nm; slow component lies above 260 nm, has emission peak at 310 nm and decay time about 600 ns. To meet timing requirement for Mu2e electromagnetic calorimeter we should use only fast emission component.

To select only fast component of $BaF_2$ emission one can use photocathodes with p-type semiconductor AlGaN:Mg top layer. These cathodes show negative electron affinity after $Cs/O_2$ activation, and this property gives higher electron emission from semiconductor after an electron-hole couples generation under influence of an UV light. In this report solar-blind AlGaN UV photocathodes development results are described. These cathodes are based on AlGaN heterostructures that were grown with plasma activated molecular-beam epitaxy method (MBE) using different methods of threading dislocations density decreasing and polarizing p-doping of top AlGaN:Mg layers with linear variation of Al.

Heterostructures were grown on $c$-$Al_2O_3$ substrates (fig. 1). On the first stage of grown initial 65-nm thick AlN layers with improved atoms mobility were grown. Then ~1.5 µm buffer layers with two ultra-thin GaN layers (3.5 nm) were grown using metal-modulated epitaxy method. GaN layers are used to decrease threading dislocation density in the top active layers of heterostructures. AlN layers we grown with a constant substrate temperature $T_S$=780°C. On the second stage (metal-modulated epitaxy) it was decreased to $T_S$=700°C, and this allowed to control Al mass fraction with simple equation x= $F_{Al}/F_N$. At last in the case of photocathodes structures single AlGaN 100 nm-thick layer was grown, which was doped with Mg molecular beam. One should note that structures were grown with

constant Al mass fraction x=0.4 in the top AlGaN:Mg layer and with variable Al fraction with $\Delta x=-0.25$ for 40 nm deep.



*Fig.1. After manufacturing UV-photocathode heterostructure is activated with Cs/O₂ to get negative electron affinity.*

Manufacturing of the photocathodes with negative electron affinity based on AlGaN/AlN heterostructures includes additional technological operations: final surface polish and $Cs/O_2$ activation (Fig.1).

We used double beam spectrophotometer to measure spectrum of light passed through structure, thereby we can estimate optical properties of grown heterostructures. Thin titan layers was added on the bottom of structure, on sapphire substrate side. The light from deuterium light source passes through structure, reflects from titan layer at the bottom of structure, passes again through active layer (Fig. 2). Then it is collected on detector and is compared with direct beam (Fig. 2,3). By this, we can measure absorption in active layer. In this method light pass twice through structure, and absorption is more evidence, than in simple transition without titan layer.
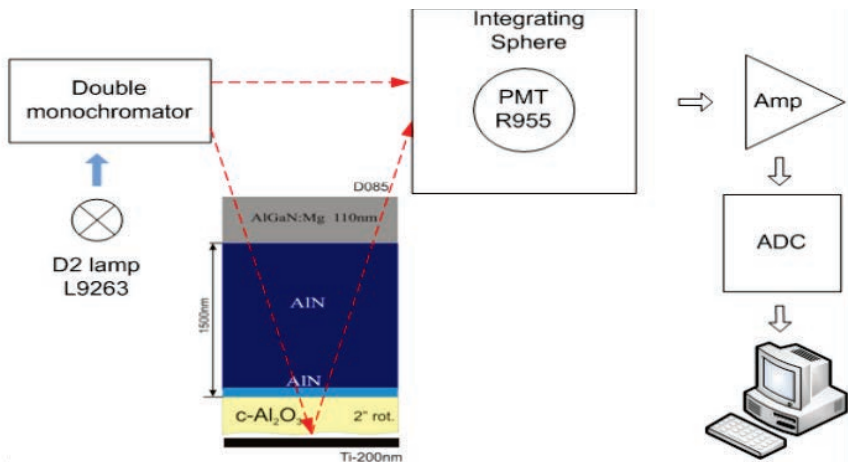
*Fig.2. Light absorption in the photocathode heterustructure measuring scheme.*
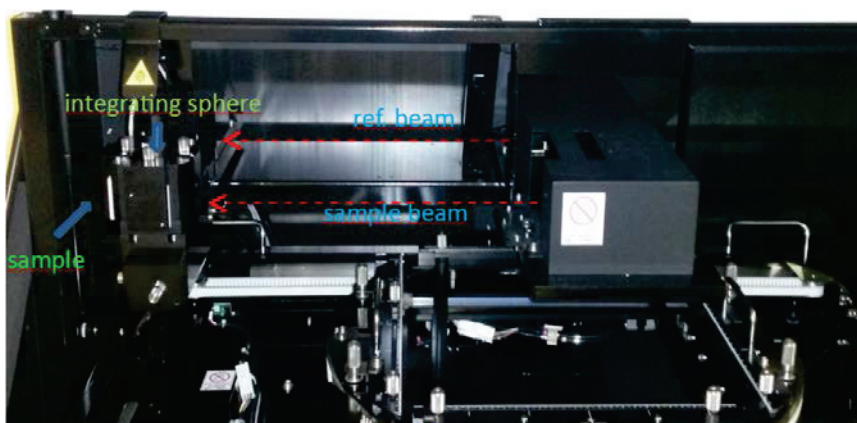


*Fig.3. To measure UV light absorption in a sample we used double-beam spectrophotometer. Light passed twice through the sample is compared with direct reference beam.*

Reflection from the bottom titan layer spectrum measurements are presented on Fig.4 for two heterostructures with different Al mass fraction in a $Al_xGa_{1-x}N$ alloy (x>0.4). The long-wavelength edge of absorption spectrum is

succesfully controlled by changing Al mass fraction in AlGaN alloy. Wavelength decreases when Al fraction is grown.
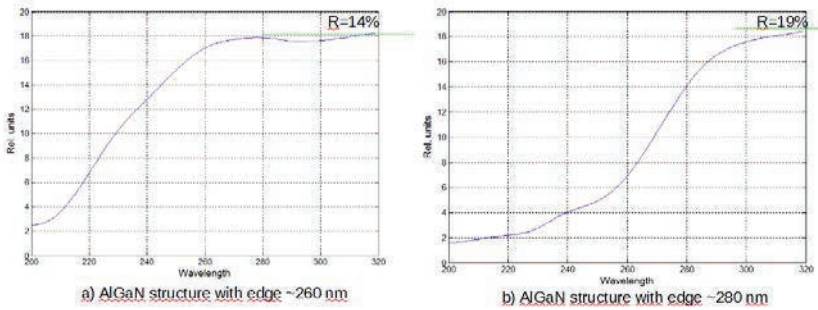


Fig.4. Measurement of long-wavelength edge for the AlGaN photocathode heterostructure. Wavelength decreases when Al fraction is grown.

To get complete photodetecting device, which can be used for our purposes, we build Photomultiplier based on microchannel plate (MCP). MCP consists of a two-dimensional periodic array of very-small diameter glass capillaries (channels) fused together and sliced in a thin plate (Fig.5). A single incident particle enters a channel and emits an electron from the channel wall and so on. By this we have got high multiplication. Using MCP allow us to get compact devices with high internal multiplication.
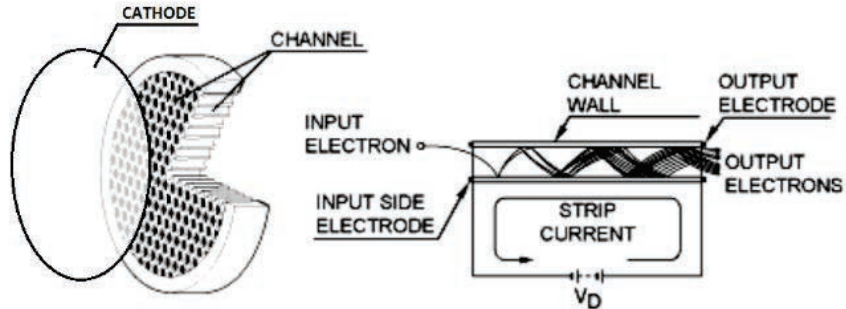


Fig.5. Microchannel plate (MCP). A single incident particle enters a channel and emits an electrons from the channel wall by multiple reflection.

AlGaN photocathode with Al mass fraction x=0,3 was combined with MCP in a

single device with 18 mm window diameter, which characteristics are presented on Fig.6.



| PMT with MCP amplifier | |
|---|---|
| **Base parameters** | |
| Window material | sapphire |
| Photocathod material | $Ga_xN/Al_{1-x}N$ |
| Catod diameter ⌀ | 18mm |
| Case | metalloceramics |
| Amplifier | mcp |
| Number of MCP | 2-stage |
| Diameter with HV | 43mm |
| Diameter w/o HV | 31mm |
| Height | 22.5mm |
| Mass | 60g |
| **Light parameters** | |
| Spectral range $(Ga_{0.7}N/Al_{1-0.7}N)$ | 200-400nm |
| Photocathod sensitivity $\lambda=275$nm | 40 mA/W |
| Anode sensitivity | 100 mA/mkW |
| Gain | $(1.5-3)10^6$ |
| Anode dark current for anode sensitivity 100mA | $10^{-12}$A |
| Pulsed peak current | 300 mA |
| Supply voltage | 3V |
| Supply current | 25mA |

*Fig. 6. Size and characteristics of the photomultiplier based on AlGaN photocathode with MCP.*

To estimate photodetector efficiency a simple experiment was proceeded (Fig. 7). We used small BaF2 scintillator to measure a gamma radiation spectrum of weak radioactive Co60 source. Light from BaF2 crystal goes to our photomultiplier. The signal from high impedance output of photomultiplier is connected through buffer amplifier and coaxial 50-Om cable to the DRS4 digitizer. Then we in offline mode integrate digital signal to get charge and draw this on the plot in PC. Trigger is generated inside digitizer on the constant level excess (self-running trigger). For $Al_xGa_{1-x}N$ photocathode with x=0.3 fast component level of BaF2 scintillations is still high so we need to use 2 ns get, when we integrate charge in autonomous mode.
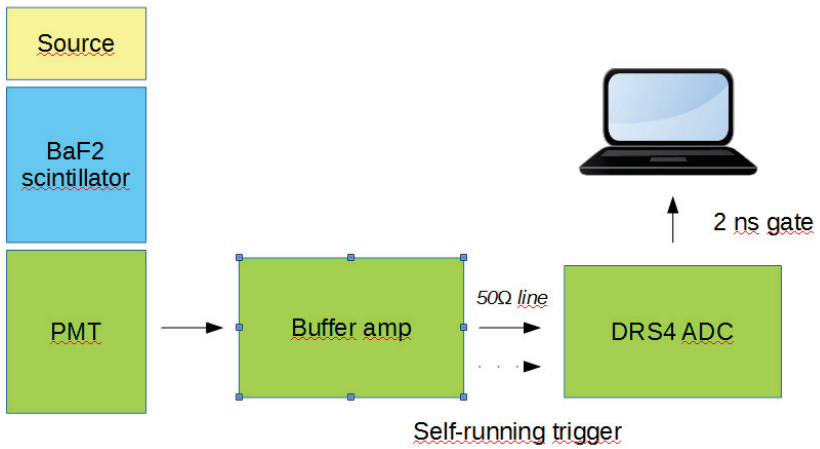


*Fig.7. Experimental setup scheme to measure Co60 gamma-radiation spectrum.*

We used buffer transimpedance amplifier to balance 50 Om line that connect photomultiplier to an ADC. The ADC is DRS4 chip based board with bandwidth of 700 MHz and sampling speed 5 GSPS (Fig. 8).
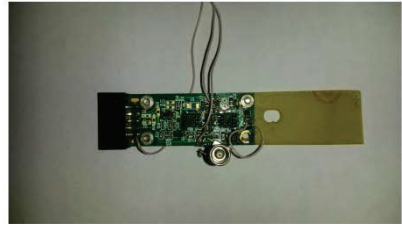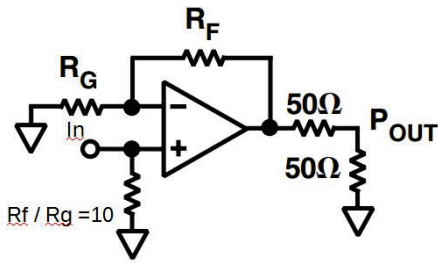
*Fig.8. Buffer transimpedance amplifier to balance 50 Om line that connect photomultiplier to an ADC.*

The result of Co60 radioactive source gamma radiation spectrum measurement is presented on Fig.9. In current configuarion we can obtain energy resolution ~10% FWHM
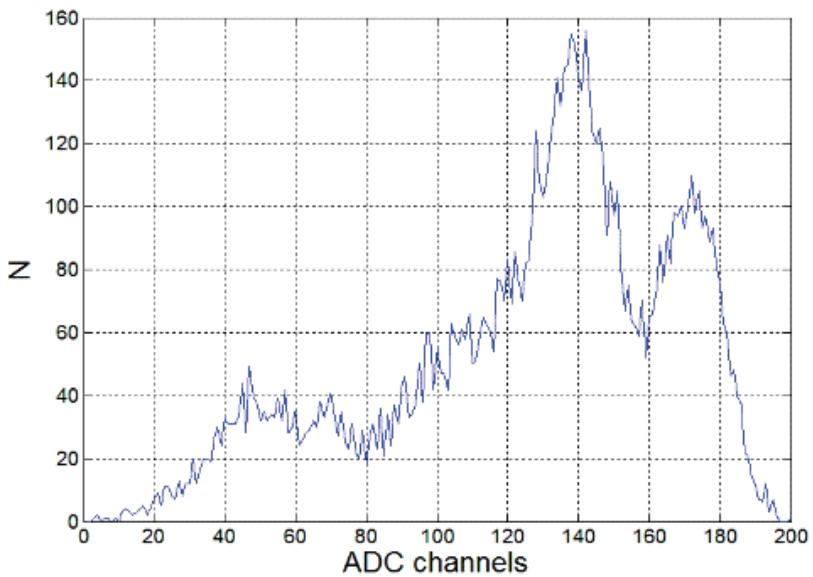


*Fig. 9. Co60 radioactive source radiation spectrum.*

# CLIC Physics Potential

## Mila Pandurović[1]

On behalf of the CLICdp Collaboration

Vinca Institute of Nuclear Sciences, Mihajla Petrovica Alasa 12-14.
Belgrade, Serbia

**Abstract**. The CLICdp is an international collaboration that investigates the physics potential of the Compact Linear Collider (CLIC) and performs research and development of the CLIC detector. CLIC is a future multi-TeV linear electron-positron collider, designed to cover a physics program of the Standard model physics, with the emphasis on Higgs and top as well as to address the wide range of open questions of the phenomena beyond the Standard model with high precision. The CLIC is designed to be build and operated at three discrete energy stages, $\sqrt{s}$= 380 GeV, 1.5 and 3.0 TeV, which are optimized for the foreseen physics program. In this talk the CLIC accelerator, detector and experimental environment of CLIC will be presented, as well as, the number of the full-simulation measurements in the Higgs, top and beyond Standard model sector, presenting the capabilities of CLIC for high precision measurements.

## 1. Introduction

The Compact Linear Collider (CLIC) [1] is one of the most mature options for a future linear electron-positron collider. The clean environment in comparison to hadron colliders provides the possibility for precision measurements, in the first place, of Standard Model (SM) Higgs and top physics, while showing high sensitivity for the measurements of physics beyond the SM. This talk describes shortly the staged scenario of CLIC with the overview of the physics motivation for the staged approach. This is followed by the accelerator, description of beam induced backgrounds and the detector requirements set by the physics benchmark processes. To show the capability of CLIC for the precise measurements, a comprehensive set of full simulation studies have been carried out within the CLICdp collaboration. In this talk the results of the full simulation studies, in Higgs, top and beyond the Standard model physics have been presented, demonstrating the high precision potential of CLIC.

[1] email: milap@vinca.rs

## 2. CLIC accelerator

The particle acceleration at CLIC is based on a new, two-beam acceleration technique, operating at room temperature, where the high intensity beam is used to generate RF power for the acceleration of particles of the colliding electron/positron beams. The feasibility of the two-beam concept, with the maximal accelerating gradient of 100 MV/m foreseen for the highest energy stage of $\sqrt{s}$=3 TeV, has been demonstrated at the CLIC CTF3 test facility. The transverse beam sizes of $(\sigma_x, \sigma_y) = (40 \text{ nm}, 1 \text{ nm})$, have been optimized to increase the luminosity while minimizing beam-induced background, delivering an instantaneous luminosity of $6 \cdot 10^{34}$ cm$^{-2}$ s$^{-1}$. Dense trains of 312 bunches separated by 20 ms allow for power pulsing in the detector and a trigger-less readout.

### 2.1. CLIC staged physics program

The CLIC is designed to be built and operated as an energy-staged machine, with the stages projected to maximize the physics potential of the machine and provide an early start of physics [1]. Recently, a comprehensive set of measurements, at the first place in the top and Higgs physics sector, have led to the optimization of the energy stages [2]. The first of three energy stage evolved from $\sqrt{s}$ =350 to 380 GeV, while the 1.4 was optimized to 1.5 TeV. Also, the possibility of extending the energy reach of CLIC even further has been considered. The results presented in this talk were obtained for the previous staging scenario.

The first stage of CLIC operation, $\sqrt{s}$=380 GeV, with the predicted integrated luminosity of 500 fb$^{-1}$, is primarily devoted to the precision Standard model Higgs physics, with the emphasis on the model independent measurement of the Higgs coupling. Also at this energy stage, a dedicated run of 100 fb$^{-1}$ is foreseen for the exploration of the top physics in a $t\bar{t}$ threshold scan. The search for phenomena beyond the Standard Model, either through direct observation or indirect precision measurements, is one of the main motivations for the high-energy stages of CLIC. The projected luminosities reach 1.5 ab$^{-1}$ and 3.0 ab$^{-1}$, respectively. These energy stages provide the sensitivity to many BSM models and deliver higher statistics for the measurement of the rare Higgs decay processes, including the Higgs self-coupling and quartic Higgs coupling. Also, measurements at this energy stage improve the precision obtained at previous energy stages.

### 2.2 Beam induced background

At a linear e$^+$e$^-$ collider high luminosity is achieved using high bunch population, o $(10^9)$, and by tight beam focusing. However, the beam focusing is limited by the energy loss of a type of radiation, beamstrahlung, which is produced in electromagnetic interaction of the opposite beams. The emission of this type of radiation has several consequences. Firstly, it degrades the luminosity spectrum, especially at the highest energy stage, where around 35% of events preserve the nominal center of mass energy within less than a percent energy loss. However, it

has been shown that the systematic uncertainty of this effect can be controlled at a per mille level in the peak region above 80% of the nominal center of mass energies [3]. Other consequences concern conversion of beamstrahlung photons into electron-positron pairs, which are produced under very low polar angles, depositing severe amount of energy in the forward region calorimeters (~10mG/y). Also, the beamstrahlung photons can interact and produce hadrons in the final state, which deposit around 20 TeV of energy per bunch train in the central calorimeters. This influences the event reconstruction in the central tracker, especially at the highest energy stage, where there is an average of 3.2 events per bunch crossing. This type of background is rejected using the transverse momentum and timing cuts, which drives challenging requirements on detector timing capabilities.

## 3. Detector model

The goal to reach high precision of the measurements is driven by the physics processes of interest which put demands on certain sub-detector systems:

- jet energy resolution of high energy jets (E >100 GeV) of 3.5 - 5%;
- track momentum resolution $\sigma_{p_T}/p_T \sim 10^{-5}$ GeV$^{-1}$;
- impact parameter resolution in a transverse plane, $\delta_{r\varphi} = 5 \oplus \frac{15}{p \cdot sin^{3/2}(\theta)}$ [$\mu m$].

The high jet energy resolution is needed to distinguish between jets coming from W, Z or Higgs boson decays. This is particularly challenging at the highest energy stage where the boosted topology of the main Higgs production channel, WW-fusion, could lead to jet merging. The precision limit on the resolution of the tracker is driven by the benchmark study for the measurement of absolute Higgs boson couplings, the recoil mass analysis, which will be discussed in detail in section 4. Besides, rare Higgs decay, $H \to \mu^+\mu^-$, also rely on the excellent track momentum resolution. The resolution of the vertex detector is the essential part of the flavor separation like in the measurement of the Higgs couplings to beauty and charm. Other constrains include detector hermeticity, with the very forward calorimeters covering the acceptance down to ~ 1 mrad. This is essential in many beyond/and Standard model processes with missing energy signatures. It has been shown that the current polar angle coverage of the forward calorimeters allows an electron tagging down to 10 mrad with high lepton identification efficiency [6].

The CLIC detector has emerged from two ILC detector concepts, ILD and SiD, which were adapted for higher center-of-mass energies foreseen at CLIC. The main difference between these two models lays in the principal of operation of a tracker: the CLIC_ILD detector model assumes a gaseous tracking (TPC), while the CLIC_SiD is designed for a silicon tracker. The other subdetector systems are similar and contain a low mass pixel vertex detector, finely segmented electronic and hadronic calorimeters designed to perform particle flow analysis, a strong solenoidal field of 4 T, an instrumented return yoke and a complex forward region

including final focusing magnets and additional calorimeters. Recently, the optimized detector model, CLICdet [2], based on silicon tracking, is adopted.

## 4. CLIC physics program

Three most important tasks of the CLIC physics program are high-precision physics measurements in the Higgs and top sector as well as beyond the Standard Model (BSM) searches through direct and indirect measurements.

### 4.1. Higgs physics at CLIC

The priority of CLIC operation would be studying of the properties of the newly discovered Higgs boson. The high luminosity of CLIC will lead to more than $10^6$ Higgs decays including all energy stages, conservatively assuming 4 years of running with 50% efficiency. The low background environment and the high statistics makes CLIC an excellent machine for precision measurements of the Higgs properties.

Energy staging at CLIC allows access to the different Higgs production channels. Figure 1 shows the evolution of the Higgs production cross section for various production channels, with the center of mass energy. The leading Higgs production channels are the Higgsstrahlung process (HZ) which is dominant at the lowest energy stage $\sqrt{s}$=380 GeV and the WW-fusion dominating at higher energies. Also, ZZ-fusion gives non-negligible contribution to the Higgs production at high energies.
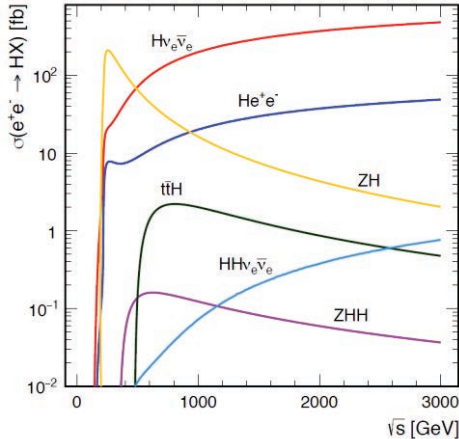


**Figure 1** Evolution of the Higgs production cross sections, for various Higgs production channels, with the center of mass energies available at CLIC. The distributions are given for unpolarized beams and do not include initial state radiation and beamstrahlung.

The corresponding Feynman diagrams of the dominant Higgs production channels are given in Figure 2.
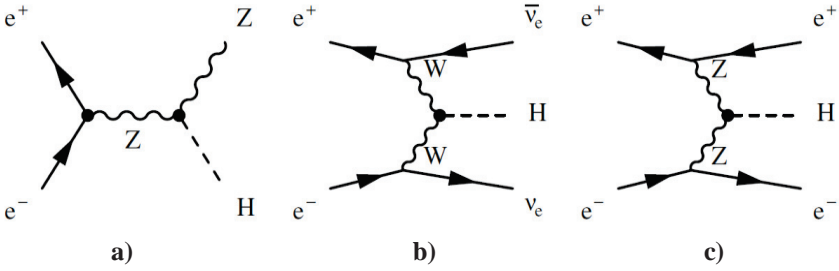


**Figure 2** The Feynman diagram of the dominant Higgs production channels a) Higgsstrahlung (ZH)    b) WW-fusion ($H\nu_e\bar{\nu}_e$)    and    c) ZZ-fusion ($He^+e^-$).

Expected number of events of Higgs bosons produced per energy stage[2], with unpolarised beams, is given in Table 2.

| $\sqrt{s}$ | 350 GeV | 1.4 TeV | 3.0 TeV |
|---|---|---|---|
| Integrated luminosity | 500 fb$^{-1}$ | 1.5 ab$^{-1}$ | 2.0 ab$^{-1}$ |
| #HZ events | 68000 | 20000 | 11000 |
| #WW-fusion events | 17000 | 370000 | 830000 |
| #Z-fusion events | 3700 | 37000 | 84000 |

**Table 1** Number of expected events in the dominant Higgs production channels. The effects of the initial state radiation and luminosity spectrum are included. The numbers are given for unpolarized beams.

With maximal electron polarization -80%, the cross-section of the WW-fusion process can be increased up to 80%, while the Higgsstrahlung cross-sections could be raised by 12%.

## 4.2. Model independent Higgs boson measurements at linear collider

A unique feature of lepton colliders is a model independent measurement of the absolute couplings of Higgs to Z boson, $g_{HZZ}$. This is performed using a recoil mass analysis which enables the measurement of the total cross-section of the Higgsstrahlung (HZ) process (Figure 2 a), to be determined independently of the Higgs decay mode. The total HZ cross-section is proportional to the absolute coupling of the Higgs to Z boson and it is the starting point for the determination of all other absolute Higgs couplings. The identification of the Higgsstrahlung process goes as follows: the Z boson from the HZ process is identified by a pair of leptons ($e^+e^-$ or $\mu^+\mu^-$) with the invariant mass of dilepton pair, $m_{ll}$, consistent

---

[2]Number of events are given for CLIC staging scenario that was used for the analysis presented in this talk

with the Z mass ($m_{ll} \sim m_Z$). The Higgs boson is identified using the recoil mass ($m_{rec} \sim m_H$) distribution, which is consistent with the mass of the Higgs boson.

The distribution of the recoil mass is constructed using only the properties of the di-lepton pair and the center of mass energy, $m_{rec}^2 = s + m_Z^2 - 2E_Z\sqrt{s}$. The left side of Figure 3 shows the distribution of the recoil mass, constructed for $\sqrt{s}$=350 GeV and a Z decay to a pair of muons. The figure features a clear peak at the invariant mass of a Higgs boson. The high energy tail is due to emission of beamstrahlung and initial state radiation. The obtained relative statistical uncertainty of the total cross-section of the Higgsstrahlung process, $\delta\sigma_{HZ}/\sigma_{HZ}$, is determined by counting the number of events in the peak. For the combined muonic and electronic Z-decays channels it amounts to 4%, with the resulting absolute coupling of Higgs to Z boson of 2% [4]. The absolute statistical uncertainty of the invariant mass of the Higgs boson obtained in the recoil mass analysis with the Z→μ+μ− decay, at 350 GeV center of mass energy, is 120 MeV.
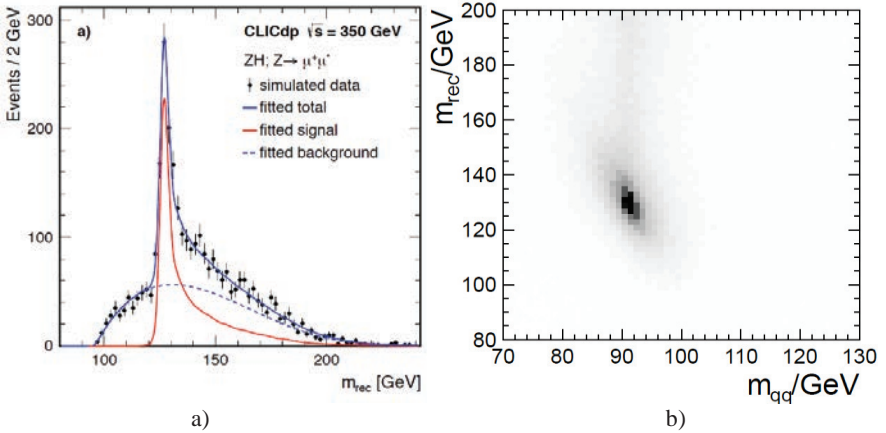


**Figure 3** a) The recoil mass distribution constructed using Z→μ+μ- at a center of mass energy of 350 GeV, for an integrated luminosity of 500 fb$^{-1}$ b) The distribution of the recoil mass vs. the invariant mass of the di-jet pair obtained using $Z \to q\bar{q}$ decay in Higgsstrahlung process, at the same center of mass energy and integrated luminosity.

The leptonic Z-decays, in the first place Z→ μ⁺μ⁻, give a clear tag of the Higgsstrahlung process, so the selection efficiency is independent of the Higgs decay mode. However, the limiting factor of leptonic recoil mass analysis is the low branching fraction BR(Z→l⁺l⁻) of 3%. It has been shown that the hadronic Z decay channel, which has a high branching fraction, BR(Z→ qq ≈ 69%), can be used to improve the relative statistical uncertainty of the absolute Higgs to Z-couplings. Even though the hadronic Z reconstruction depends on the Higgs decay mode, it has been shown that certain selection criteria can be chosen to ensure almost model independence [5]. The clearest separation between signal and background is obtained from $m_{qq}$ and the recoil mass $m_{rec}$, as shown in Figure 3b.

The signal is clearly peaked at $m_{qq} \to m_Z$ and $m_{rec} \to m_H$. By combining the hadronic with the leptonic channel, the relative statistical error is improved to 0.8%.

## 4.3. The measurements of cross-sections of specific Higgs decays

Besides these model independent measurements, the first stage of CLIC operation enables Higgs cross-section × branching fraction measurements, making use of the high capabilities of the designed detector. One example is the measurement of the Higgs couplings to b, c quarks and gluons which is particularly challenging at the hadron colliders. It was shown that using simultaneous analysis of the H → $b\bar{b}, c\bar{c}, gg$ decays, the relative statistical uncertainties on the charm and gluon channel could be kept at the level of a few percent, while for the b channel the reached precision at below percent. This analysis shows the excellent capability of CLIC for efficient flavor separation.

At the higher energy stages, the high cross-section of the WW-fusion process and high luminosity, besides improving the results obtained at the lowest energy stage, allow the measurement of the rarer Higgs decays $H \to \mu^+\mu^-$, or indirect couplings of $H \to \gamma\gamma$ and $H \to Z\gamma$. The branching fractions of these processes are at the order/below per mile.

It was shown that the statistical precision of $\sigma(H\nu_e\nu_e) \times BR(H \to \mu^+\mu^-)$ that can be achieved is 29% (16%) at the 1.4TeV (3 TeV) CLIC [6].

The measurement of indirect couplings of Higgs to γ, is highly sensitive to BSM physic processes, which modify the effective H→γγ branching ratio. In the SM, this decay is induced via loop diagrams, dominated by heavy charged particles, mostly W bosons and t quarks. It has been shown that a statistical uncertainty of 15% can be obtained at the 1.4 TeV energy stage [7]. Also, simulation studies of the H→γZ decay give a precision of the Higgs production cross-section times branching ratio of 42% at 1.4 TeV [7].

At the energy stage of 1.4 TeV, measurement of the top-Yukawa coupling is possible using the $t\bar{t}H$ process. This process is studied using the most favorable Higgs decay, $H \to b\bar{b}$. Two types of final states were studied, semileptonic and hadronic. These complex final states, with six and eight jets including four b-jets, are an excellent detector benchmark processes, testing jet reconstruction, flavor tagging, lepton identification, and reconstruction of missing energy. The achieved combined precision is 8.1% resulting in a precision on the top-Yukawa coupling of 4.3% [8].

The shape of the Higgs potential can be accessed through the measurement of the trilinear Higgs self-coupling. It was shown that a precision of 32% can be achieved at $\sqrt{s}$ =1.4 TeV and 16% at 3 TeV [4].

The measurement of the quartic coupling $g_{HHWW}$ is also possible at higher energy stages. The simulation studies have shown that, using the HH→$b\bar{b}b\bar{b}$, the quartic coupling can be measured with a statistical uncertainty of 7% at $\sqrt{s}$ = 1.4 TeV and 3% at 3 TeV, including a $P_e$=80% polarization [9].

## 4.4. Combined Higgs Fit

To reach the ultimate precision on the Higgs couplings and decay width at CLIC, results from all three energy stages are combined using a simultaneous fit. The starting point of two types of fits that are employed at CLIC, is the model independent measurement of the coupling of Higgs to Z boson, $g_{HZZ}$.

For the model independent, fit the uncertainties of the couplings as well as the total Higgs decay width enter as free parameters of the fit, ten parameters in total. For each production and decay channel, the measured observable $\sigma$xBR is related to the corresponding relative coupling, $\frac{g_{HWW}^2 \cdot g_{Hxx}^2}{\Gamma_H}$. These relative couplings correspond to the particular combination of Higgs production channel ($g_{Hvv}$, V=Z,W for Higgsstrahlung and WW-fusion respectively) and Higgs decay channel ($g_{Hxx}$) where x denotes x=c, b, t, $\mu$, $\tau$, $\gamma$, W, Z. The relative couplings are used in the fit to construct the chi-squared distribution:

$$\chi^2 = \sum_i \frac{(C_i/C_i^{SM} - 1)^2}{\delta F_i^2},$$

where the $C_i$ are measured relative couplings of the certain process, the $C_i^{SM}$ are the Standard model expectation value and the $\delta F_i$ are the statistical uncertainties of the measurement of the considered process. The obtained overall relative statistical precision of the measurement of Higgs couplings to the SM particles is shown in Figure 4 a) [4]. It has been shown that the relative statistical uncertainties can reach a percent level. The Higgs width is extracted with a 3.5 % precision.
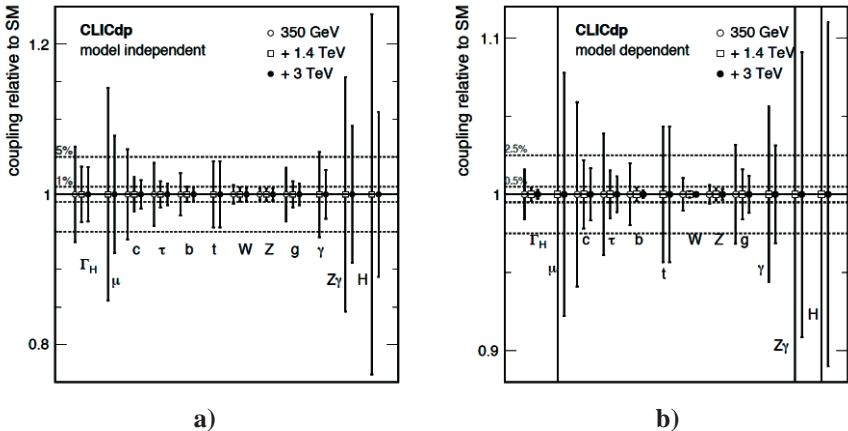


**Figure 4** Illustration of the precision of the Higgs couplings and total Higgs decay width obtained in the fit using all three energy stages. The results for a) model independent fit, b) model dependent fit. The impact of electron polarization of -80% at $\sqrt{s} = 1.4$ and $\sqrt{s}$=3.0 TeV are included as a scaling factor.

The obtained results can be improved using the model dependent fit, which assumes that the total Higgs decay width is constrained by the Standard model. The free parameters of the fit are relative partial widths of the Higgs decays with respect to corresponding SM values, $\kappa_i^2 = \Gamma_i / \Gamma_i^{SM}$. The uncertainty of the total Higgs decay width does not enter the fit, but is calculated using the uncertainties of the partial widths obtained in the fit. The relative statistical uncertainty obtained by this method improves and reaches per mille level for most of the measurements. The exceptions are rare Higgs decays, like H→γγ or H→μμ. However, the results of this fit are model dependent. The results of the model-dependent fit are shown in Figure 4 b).

## 5. Top Physics

The second important part of the CLIC physics program is dedicated to the top quark. The emphasis of the studies are the determination of the mass of top quark, with very high precision, as well as the top couplings. The mass of the foremost heaviest of all Standard model particles, the top quark, suggests that it may play a special role in the mechanism of the electroweak symmetry breaking. Also, due to its mass it provides leading contributions in higher order corrections to many processes and may provide high sensitivity to physics beyond the SM. Moreover, the analyses concerning the nature of the vacuum stability, rely on the uncertainties of the masses of the Higgs boson and the top quark [10]. With the current precision of the Higgs mass (LHC), the uncertainty of the top mass is the leading uncertainty in this evaluation. Thus the improvements in the measurement of the top quark mass that can be achieved at a linear collider could substantially reduce these uncertainty.

### 5.1. Top Quark Mass Measurements at CLIC

The CLIC proposes two ways of measuring the top quark mass. The first one is by direct reconstruction of the invariant mass of the decay products, and the second one is a scan of the cross-section around the top-pair production threshold. The shape of the cross-section is sensitive to the properties of the top quark and the parameters of the used theoretical model. Thus by scanning the cross-section the values of the top quark mass $m_t$, top width $\Gamma_t$, top-Yukawa coupling $Y_t$ and the strong coupling constant $\alpha_S$ can be obtained.

The scan requires a dedicated run of the CLIC collider at several closely spaced energies around the pair production threshold. It has been shown that a precise top quark mass measurement could be performed using ten scan points each with 10 fb$^{-1}$ of integrated luminosity results in a total statistical uncertainty of ~ 50 MeV [11]. The direct reconstruction on the top invariant mass gives competitive precision of ~80 MeV at the center of mass energy of 500 GeV, with the same integrated luminosity [11]. However, the main difference between these two approaches of top mass measurements, is the theoretical interpretation of these measurements. In the top threshold scan, the top mass is well defined from a

theoretical point of view, while the direct reconstruction bears significant theoretical uncertainties when converting the obtained mass into a particular mass scheme.

## 5.2. Electroweak couplings

The measurement of the top pair production above the threshold is sensitive to the top electroweak couplings. These couplings are precisely determined in the Standard model but may be enhanced due to the presence of corrections, originating from one of the scenarios of the physics beyond Standard model. The top quark coupling at the vertices ttZ and ttγ can be described using eight form-factors, where only three of them are contributing to the Standard model $t\bar{t}$ production. The measurement of the total cross section of forward backward and left-right asymmetry and helicity angle, using polarized beams, provides the sufficient information to constrain these form-factors with very high precision [13]. It has been shown that with an integrated luminosity of 500 fb$^{-1}$, form factors could be constrained to the percent level, which is an order of magnitude better than the ones projected for the High Luminosity LHC (HL-LHC).

## 5.3. Top-Yukawa coupling

At e$^+$e$^-$ colliders the top Yukawa coupling can be determined, as mentioned, in the top threshold scan, while at the high energies in the process where a Higgs boson is produces in association with the top-quark pair ($e^+e^- \to t\bar{t}H$, mentioned in 2.3). Using the former method the coupling can be extracted with a statistical uncertainty of ~6% using the proposed integrated luminosity of 100 fb$^{-1}$, assuming the value of the strong coupling constant is constrained independently from other measurement. The corresponding theoretical uncertainties are of the order of 20%.

## 6. Beyond Standard model physics at CLIC

Higher energy stages of CLIC provide excellent sensitivity to search for physics beyond the Standard Model (BSM). The clean environment and the low level of background provided by lepton collisions will allow to improve the precision on many measurements beyond the LHC reach and to explore additional processes and production mechanisms, extending and complementing the LHC program.

Two approaches have been foreseen at CLIC for studying phenomena of physics beyond standard model, depending on the nature of the processes involved.

Direct searches for possible new particles profit from the high center of mass energy available at CLIC, and can extend to the kinematic limit of $\sqrt{s}/2$~1.5 TeV. Much higher mass scales can be reached through the indirect searches, where we compare theoretically well-known observables, like the cross-sections of the

sensitive process, to the expected Standard model predictions. Signal of 'new' physics is expected to arise in the deviations of these precision observables. By indirect searches, CLIC could probe BSM theories up to tens of TeV, well beyond the spectra of particles that could be directly produced. However, as mentioned, these searches are model dependent.

## 6.1. Direct searches

Out of all theories that extend the Standard model, Supersymety (SUSY) is the natural extension of the symmetry principle that founded the Standard model. It offers a plausible solution to many of the unsolved questions of particles physics, like the hierarchy problem or supplying the dark matter candidate. However, until now the existence of sypersymmetry has not been confirmed, with very high exclusion limits [12]. Nevertheless, to demonstrate the capability of CLIC for the precision measurements in the direct searches of the BSM sector, CLIC has focused on several benchmark studies in the SUSY sector, which probe energy limit and the key aspects of detector performance. Three SUSY models have been chosen [1] which contain sparticles within the kinematic reach of CLIC and which challenge key aspects of the detector performance.

The spectra of particles for these models include sleptons, squarks and heavy Higgses. Naturally, given the wide range of mass and spin for the predicted particles, the validity of these studies can be extended from SUSY to any other theory interpretation that predicts particles with the same quantum numbers. If any new particle is discovered, either at LHC or at CLIC itself, CLIC could provide precise measurements of the properties of such a particle, like mass, couplings and spin.

For example, to test a jet energy resolution in the high energetic, multijet environment a study has been performed on the chargino and neutralino pair production processes, $e^+e^- \rightarrow \tilde{\chi}_1^+ \tilde{\chi}_1^- \rightarrow \tilde{\chi}_1^0 \tilde{\chi}_1^0 W^+ W^-$ , $e^+e^- \rightarrow \tilde{\chi}_2^0 \tilde{\chi}_2^0 \rightarrow \tilde{\chi}_1^0 \tilde{\chi}_1^0 Z^0/h\ Z^0/h$, at the highest energy stage of CLIC. The signature of the signal is the pair of bosons and a missing energy. The result after the jet reconstruction and pairing to form W, Z or Higgs boson is shown in Figure 5. The relative statistical uncertainties of the measured gaugino masses are of the order of 1%, for gaugino masses of ~640 GeV (1).
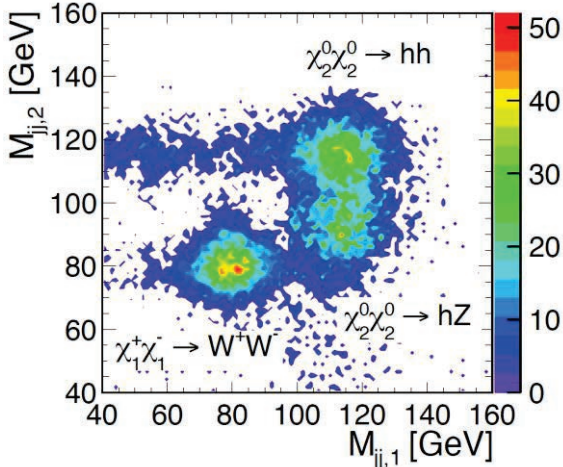
**Figure 5** Reconstructed di-jet masses from gaugino decay.

To demonstrate the capabilities of finely granulated calorimeters, the complex final state involving heavy Higgs bosons, the Two-Higgs-Doublet model is studied. A measurement of the mass of the four heavier Higgs bosons, $H^{\pm}$, A and H, which are almost degenerate in mass, is performed by reconstruction of their complex final states $e^+e^- \rightarrow H^0A \rightarrow b\bar{b}b\bar{b}$, Figure 6 a) and $e^+e^- \rightarrow H^+H^- \rightarrow b\bar{t}t\bar{b}$, Figure 6 b). This requires precise jet clustering and efficient flavor tagging. As illustrated in Figure 6, CLIC has the ability to measure these masses to a percent level and to distinguish the mass splitting among all of these states.



a)



b)
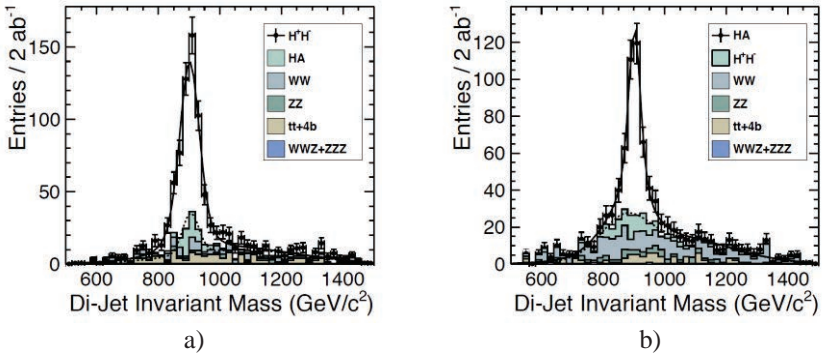
**Figure 6** Heavy Higgs bosons produced at the highest energy stage of CLIC, $\sqrt{s}$= 3 TeV, which are nearly degenerate in mass.

In all studied SUSY models the relative statistical uncertainty on the mass measurement of different sparticles using different channels is found to be at the order of one percent.

310

## 6.2. Indirect searches

Beyond the kinematic reach of CLIC, new physics can be found by their effects on the precisely known observables. Observables like the cross-section, left-right or forward-backward asymmetry provide the discovery reach up to several tens of TeV, depending on the underling model, assuming ±80% electron polarization. Several theories have been tested, and one of the examples concerns extended gauge theories, with associated new gauge boson, Z′. This gauge boson couples to leptons, therefore the two fermion production, eg. $e^+e^- \to \mu^+\mu^-$, can be used to probe the higher order corrections coming from the extended gauge theories. Using the cross-section and measurement of asymmetries for the different polarization combinations it was found that in some regions of parameter space, mass reach is several tens of TeV. Figure 7 shows the discovery limit of 5 σ of the mass of the Z′ boson as a function of integrated luminosity as a function of different coupling parameter combinations. The results from two highest CLIC energy stages are combined [14].
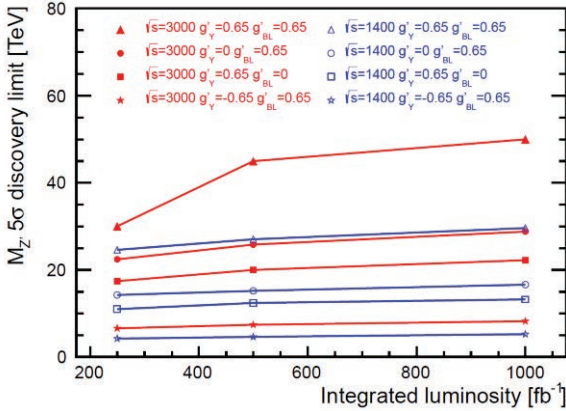


**Figure 7** The discovery limit of the new gauge boson, Z′, as a function of integrated luminosity, for different values of couplings $g'_Y$ and $g'_{BL}$.

Another indirect measurement concerns the models of compositeness, in which the Higgs boson is viewed, not as a fundamental scalar, but as a bound state of fermions, with the compositeness scale of the order of TeV. In this case, every sensitive observable is corrected with the $\xi = (v/f)^2$, where $v = 246$ GeV is the vacuum expectation value and $4\pi f$ is the scale of compositeness. Figure 8 summarizes the current constraints and prospects form LHC and CLIC. The ρ stands for the vector resonance of the composite theory. Using the combined fit of single and double Higgs production, with 2 ab$^{-1}$ of data at 3 TeV CLIC, it should be possible to exclude coupling values down to relative compositeness scale of $\xi = 0.002$. That corresponds to the scale of compositeness of 70 TeV [4].

311
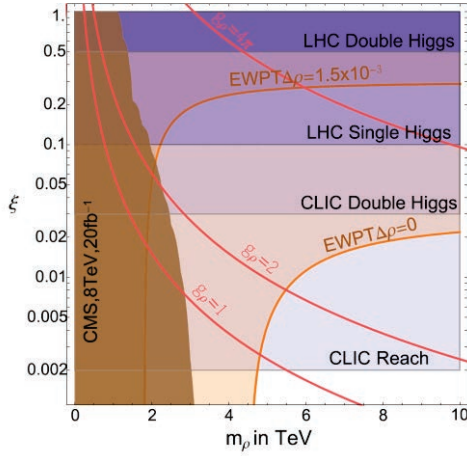
**Figure 8** Summary plot on the current constraints and prospects on the Higgs compositeness from CLIC and LHC. 300 fb⁻¹ of integrated luminosity is assumed for double (single) Higgs production at LHC. The 'CLIC Double Higgs' band corresponds to a double Higgs production alone, at 3 TeV CLIC with 1 ab⁻¹ of integrated luminosity. The final CLIC reach includes also the single Higgs production.

## 7. Conclusion

In this talk, the motivation for a linear e⁺e⁻ collider as a next generation facility in high energy physics is given. One of the possible options is the Compact linear collider CLIC. CLIC is a staged machine operating at three center of mass energies, 380 GeV, 1.5 TeV and 3.0 TeV, which are optimized for the physics program, from precision studies of the Higgs and top sector to BSM probes.

The results of comprehensive studies in the Higgs physics program have been presented. Precise measurements of many Higgs couplings and branching ratios can already be made at the lowest energy stage of $\sqrt{s}$=380 GeV. The measurement of the top mass and couplings are also foreseen. Higher energy stages give access to rarer Higgs decay modes, $t\bar{t}H$ and double-Higgs production. All Higgs measurements are combined in a model-independent simultaneous fit, with sub-percent level precision on many measurements.

Top physics is also accessible, in particular using the threshold scan to achieve unprecedented precision on the top quark mass. Above the threshold the measurement of electroweak couplings and top mass are foreseen.

The Beyond the Standard Model physics can be accessed through direct and indirect searches. Direct observation of SUSY particles production allows for determination of their masses at a percent level, in most of the available scenarios. The indirect searches can extend the energy scale far beyond the kinematic reach of the machine, as far as few tens of TeV for some of the studied scenarios.

# References

1. L. Linssen et al. (editors), Physics and Detectors at CLIC: CLIC Conceptual Design Report, CERN-2012-003, CERN, (2012).
2. M.J. Boland et al., CLIC, CLICdp Collaborations, Updated baseline for a staged Compact Linear Collider, CERN Publishing, DOI: http://dx.doi.org/10.5170/CERN-2016-004, (2016)
3. S. Lukic, I. Bozovic-Jelisavcic, M. Pandurovic, I. Smiljanic, JINST 8 P05008, (2013).
4. H. Abramowicz et al. [CLICdp Collaboration], Physics at the CLIC e⁺e Linear Collider Input to the Snowmass Process 2013, (2013), arXiv:1307.5288.
5. M. A. Thomson, Model-Independent measurement of the e⁺e⁻ →HZ cross section at a future e⁺e⁻ linear collider using hadronic Z decays, (2015). arXiv:1509.02853.
6. G. Milutinovic-Dumbelovic, I. Bozovic-Jelisavcic, C. Grefe, G. Kacarevic, S. Lukic, M. Pandurovic, P. Roloff, I. Smiljanic, Physics potential for the measurement of $\sigma(e^+e^- \to H\nu_e\overline{\nu}_e) \times BR(H \to \mu^-\mu^+)$ at the 1.4 TeV CLIC collider, Eur. Phys. J. C75, (2015) 515.
7. C. Grefe and E. Sicking, Physics potential of the $\sigma(e^+e^- \to H\nu_e\overline{\nu}_e) \times BR(H \to Z\gamma)$ measurement at a 1.4 TeV Compact Linear Collider, CLICdp-Note-2014-003, (2014).
8. S. Redford, P. Roloff and M. Vogel, Physics potential of the top Yukawa coupling measurement at a 1.4 TeV Compact Linear Collider using the CLIC SiD detector, CLICdp-Note-2014-001, (2014).
9. S. Redford [on behalf of the CLICdp Collaboration], Higgs and BSM physics at CLIC, European Physical Society Conference on High Energy Physics 2015, 22-29 July 2015, Viena, Austria, CLICdp-Conf-2015-007.
10. G. Degrassi, S. Di Vita, J. Elias-Miro, J. R. Espinosa, G. F. Giudice, G. Isidori and A. Strumia, Higgs mass and vacuum stability in the Standard Model at NNLO, JHEP 1208, (2012)098.
doi:10.1007/JHEP08(2012)098, arXiv:1205.6497
11. K. Seidel, F. Simon, M. Tesar, S. Poss, Top quark mass measurements at and above threshold at CLIC, Eur. Phys. J. C 73, (2013) 2530.
12. M. Klute [on behalf of the ATLAS and CMS collaborations], Highlights of LHC Run I and first 13 TeV results, LCWS15 6-10 November, Whistler, Canada, (2015).
13. M. Amjad et al., A precise characterisation of the top quark electro-weak vertices at the ILC, Eur. Phys. J. C75, (2015) 512.
14. J.-J. Blaising and J. D. Wells, Physics performances for Z searches at 3 TeV and 1.5 TeV CLIC, LCD-NOTE-2012-009, (2012). arXiv:1208.1148

# PHENIX results on leading particles and jets measured in Cu+Au collisions at RHIC

Ya.Berdnikov[1,2], A.Berdnikov[1], S.Zharko[1], D.Kotov[1,2]

[1]Peter the Great Saint-Petersburg Polytechnic University
[2]Petersburg Nuclear Physics Institute, NRC KI

## 1.   INTRODUCTION

Jet quenching is one of the evidences of quark-gluon plasma (QGP) formation in central heavy ion collisions [1]. Experimentally jet-quenching at RHIC and LHC is observed as suppression of leading particles such as $\pi^0$-mesons and jets, which are directly associated with partons, formed in the medium. RHIC results from Au+Au and Cu+Cu collisions showed suppression of high $p_T$ particles as expected from parton energy loss in a hot and dense medium. An additional insight into the mechanism of particle production and parton energy loss can be gained from interactions of asymmetric Cu+Au collisions. Configuration of two different nuclei – Cu and Au - opens an opportunity to study particle production in different initial collision geometries. Fig.1 presents schematic view of heavy ion collision: one showing Au+Au, and one showing Cu+Au at the same number of nucleons participating in interaction. Despite the fact that number of nucleons participating in interaction is similar for both cases, the shape of overlap region is different, which can influence particle production. In 2012 RHIC delivered successful Cu+Au run at 200 GeV.
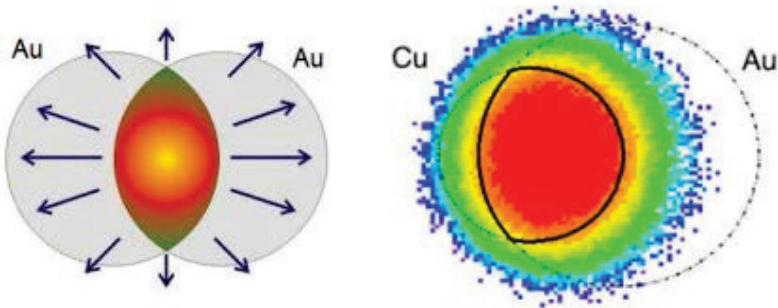


Fig.1. Schematic view of the overlap region in Au+Au and Cu+Au collisions.

Relativistic Heavy Ion Collider (RHIC) at Brookhaven National Laboratory is one of the biggest operating particle accelerators designed to study heavy ion collisions at high energies [2]. RHIC is a flexible and reliable accelerator complex with an extensive experimental program. A lot of operational time is devoted to beam energy scan and switching between colliding nuclei. In total

RHIC delivered 9 combinations of nuclei and 11 energies and beam luminosity is being continuously increased from to run to run.

## 2. EXPERIMENTAL SETUP

PHENIX experimental setup is presented on Fig.2. It consists of central and forward arms (not shown on the picture). Rapidity and phi coverage is 0.35 and 90 degrees for each central arm (east and west), and from 1.2 to 2.2 in rapidity and 360 degrees in phi for each forward arms, (north and south).

Charged particle track reconstruction in PHENIX is performed with drift and three layers of pad chambers which have high momentum and spatial resolution. Main purpose of electromagnetical calorimeter (EMCal) is to measure energy and coordinates of photons and electrons originating from interaction region. Two time of flight systems (TOF) in east and west central arms of the PHENIX spectrometer are used for particle identification at the low and intermediate transverse momentum region. Particle identification can also be performed with EMCal, although with a timing resolution and as good as for the TOF. PHENIX also provides excellent capabilities for muon measurements at forward rapidities. Main detectors responsible for muon registration are Muon Trackers and MuID.
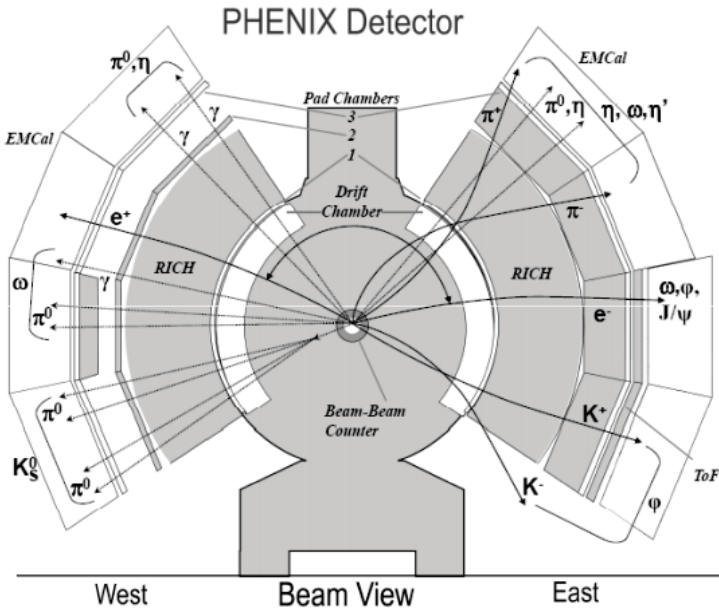

Fig.2. Schematic view of PHENIX central arms.

Physics program of PHENIX experiment is mostly devoted to the study of QCD matter under extreme energy densities and temperatures: system where quarks and gluons are dominating degrees of freedom. All results presented in this proceeding were obtained with PHENIX experiment at RHIC.

## 3. RESULTS

Neutral pions ($\pi^0$) are reconstructed in gamma-gamma decay channel using EMCal for gamma clusters measurement. $\pi^0$-meson yields are extracted in different transverse momentum ($p_T$) and centrality bins from invariant mass gamma-gamma distributions. Good signal to background ratio and lots of statistics allows to measure $\pi^0$-meson yields up to high $p_T$.

Jet reconstruction is done with drift and pad chambers for charged tracks and EMCal for neutral clusters. Anti-$k_T$ algorithm is used with radius parameter 0.3 for jet reconstruction in proton-proton collisions and 0.2 in Cu+Au collisions due to larger contribution of underlying event [3].

Fig.3 presents results from p+p collisions obtained at 200 GeV in PHENIX central arms: invariant transverse momentum spectra for $\pi^0$-mesons and reconstructed jets measured in a wide $p_T$ range up to 20 GeV/c for $\pi^0$-mesons and 50 GeV/c for jets. From this figure and so on vertical bars represent statistical uncertainties and boxes around markers represent systematic uncertainties. In some cases, statistical uncertainties can be not visible if their size is smaller than the marker size.

Presented spectra agree with next to leading order pQCD calculations, which validates $\pi^0$-meson and jet reconstruction procedure in PHENIX and explains $\pi^0$-meson and jet production in elementary p+p collisions. Obtained spectra are used as a baseline to compare with more complex and heavy colliding systems, such as p+A and A+A.
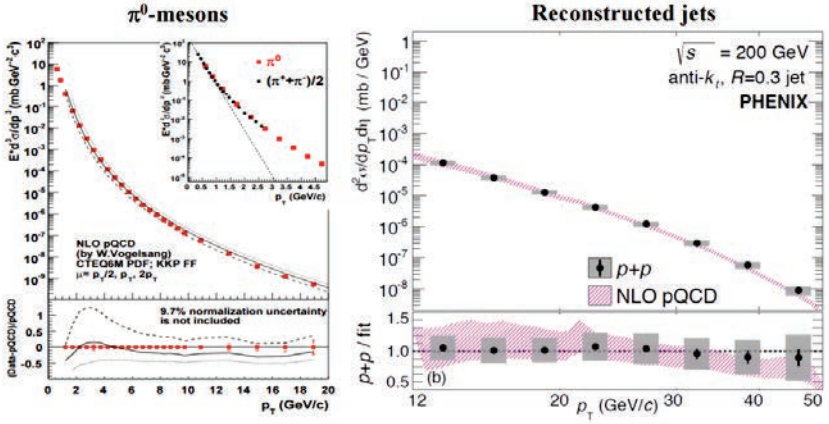
Fig.3. $\pi^0$-mesons and reconstructed jets invariant transverse momentum spectra obtained in p+p collisions at 200 GeV by PHENIX experiment.

Fig.4 presents invariant transverse momentum production spectra for $\pi^0$-mesons measured in Cu+Au collisions at 200 GeV by PHENIX experiment. Spectra were obtained in a wide $p_T$ ranges up to 20 GeV/c with high precision with no centrality selection as well as for 5 different centralities. These spectra are used to calculate $\pi^0$-mesons nuclear modification factors $R_{AA}$ for heavy ion colliding systems.
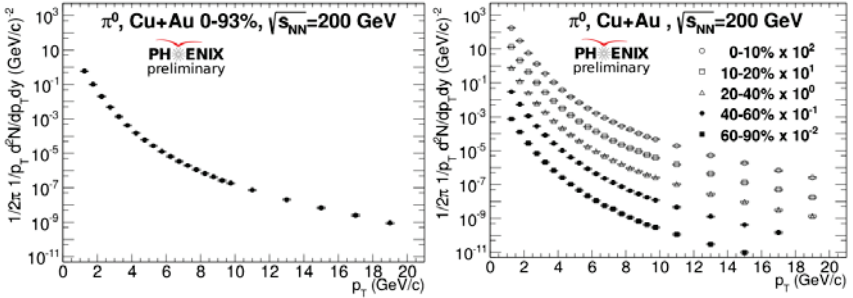


Fig.4. Invariant transverse momentum spectra measured for $\pi^0$-mesons with no centrality selection and for 5 centrality classes in Cu+Au collisons at 200 GeV.

At high $p_T$ region particle production is governed by fragmentation of hard-scattered partons. Hard processes are characterized by small cross section and large value of transferred momentum. This fact allows us to describe hard processes in heavy ion collisions as an independent superposition of nucleon nucleon interactions. Such processes can be compared with p+p collisions when scaled by number of binary collisions – $N_{coll}$.

The difference between heavy ion collisions and simple superposition of nucleon nucleon interactions lies in presence of collective effects. These effects are often being studied with so called nuclear modification factor $R_{AA}$ which is calculated as the ratio of particle yield in heavy ion collision to yield of same particles in p+p collisions scaled by number of binary collisions - $N_{coll}$.

Different $p_T$ dependence of $R_{AA}$ includes enhancement of the particle yields at the intermediate $p_T$ which is a chraracteristic of Cronin effect ($R_{AA} > 1$) and is often explained as multiple parton scaterring in the initial state [4], suppression of particle yields ($R_{AA} < 1$) which is called jet-quenching and is explained by parton energy loss before fragmentation, and also the case when collective effects are absent ($R_{AA} = 1$).

Fig.5 shows nuclear modification factors obtained for $\pi^0$-mesons in Cu+Au collisions at 200 GeV in PHENIX central arms. Nuclear modification factors $R_{AA}$ are measured in a wide $p_T$ range up to 20 GeV/c. In central Cu+Au collisions production of $\pi^0$-mesons is suppressed. Suppression gradually disappears with centrality and in peripheral collisions one can say that there's a hint of enhancement of $\pi^0$-mesons production.
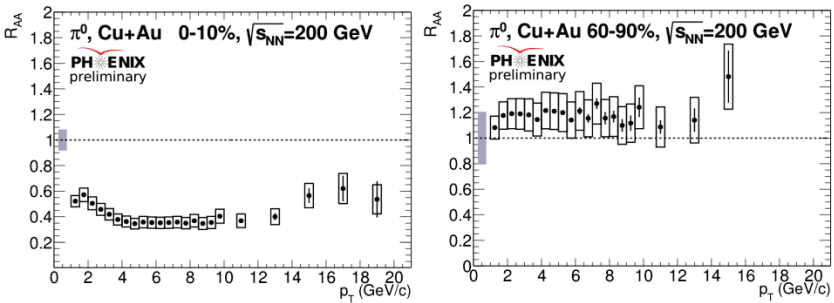


Fig.5. Nuclear modification factors $R_{AA}$ obtained for $\pi^0$-mesons central and peripheral Cu+Au collisions at 200 GeV.

Fig.6 presents nuclear modification factors $R_{AA}$ for reconstructed jets obtained in Cu+Au collisions at 200 GeV by PHENIX experiment. Jets are suppressed by a factor of 2 in central Cu+Au collisions. Suppression shows no $p_T$ dependence. A similar trend has been seen from LHC experiments in Pb+Pb collisions at much higher energies [5]. One can see that observed suppression gradually disappears with centrality suggesting a hint of enhancement in peripheral collisions. $\pi^0$-mesons results and jet measurement in Cu+Au collisions seem to show the consistent trend: suppressed in central collisions and non-zero enhanced in peripheral collisions.

318
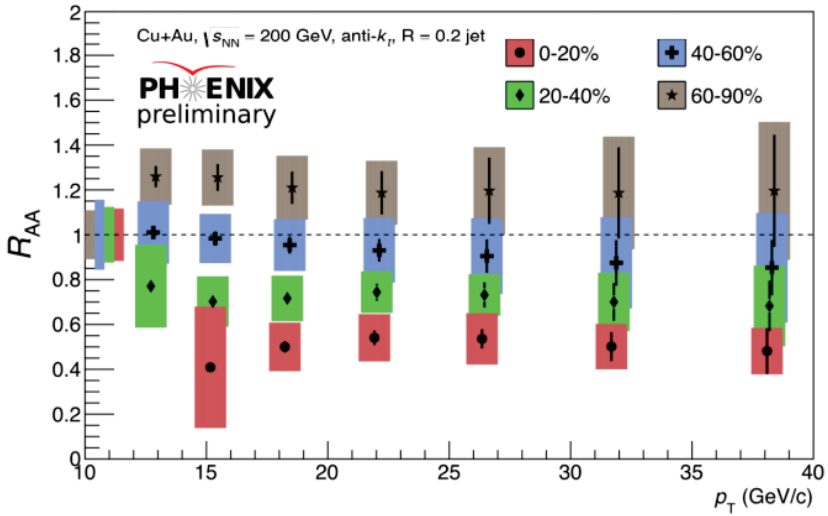
Fig.6. Nuclear modification factors $R_{AA}$ obtained for reconstructed jets in central and peripheral Cu+Au collisons at 200 GeV.

Fig.7 shows the comparison of nuclear modification factors obtained for $\pi^0$-mesons by PHENIX experiment in Cu+Cu, Au+Au and Cu+Au collisions at 200 GeV. The comparison is done for the similar number of nucleons participating in interaction – $N_{part}$. In central and semi central Cu+Au collisions $\pi^0$ yields are suppressed similar to Cu+Cu and Au+Au collisions which means that the level of suppression depends on number of participants $N_{part}$ but not on the collision system. In other words, $\pi^0$ production depends on the size of the nuclear overlap, but not on its shape. In peripheral Cu+Au collisions $\pi^0$ yields show a hint of enhancement, while they are suppressed in Au+Au with Cu+Cu lying in the middle between Cu+Au and Au+Au.
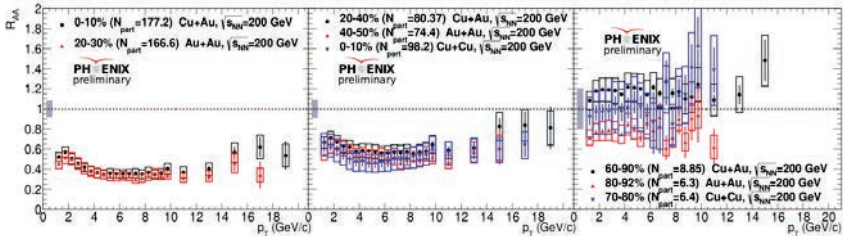


Fig.7. Nuclear modification factors $R_{AA}$ obtained for $\pi^0$-mesons by PHENIX experiment in Cu+Cu, Au+Au and Cu+Au collisions at 200 GeV.

Fig.8 presents $p_T$ integrated nuclear modification factors for $\pi^0$-mesons and reconstructed jets respectively in Cu+Au collisions at 200 GeV. $\pi^0$-meson

suppression pattern is similar in Cu+Au and Au+Au collisions for $N_{part}$ values larger than 50. At $N_{part}$ values smaller than 50 (peripheral collisions) $\pi^0$-mesons are less suppressed in Cu+Au than in Au+Au. Both $\pi^0$-mesons and jets show a hint of enhancement in peripheral Cu+Au collisions at 200 GeV.
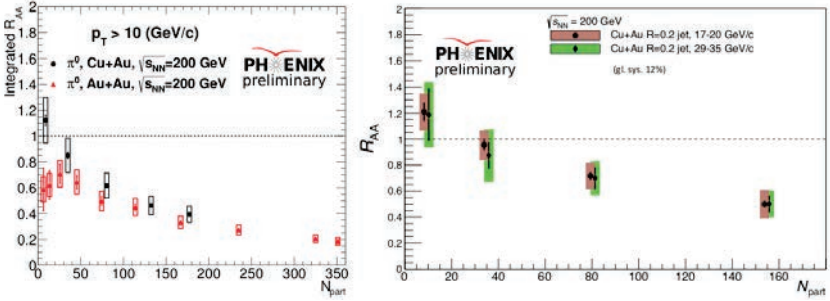


Fig.8 Transverse momentum integrated nuclear modification factors $R_{AA}$ for $\pi^0$-mesons and reconstructed jets obtained in Cu+Au collisions at 200 GeV.

Fig.9 shows SCET model [6] predictions (red and black lines) for reconstructed jets nuclear modification factors $R_{AA}$ obtained in central 0-20% and 40-60% centrality bins in Cu+Au collisions. The model uses coupling between jet and the medium as an input parameter, the calculations were done for two values of this parameter: 2.0 and 2.2. As seen from the figures, model predictions quantitatively agree with experimental results. So far, there are no predictions for $\pi^0$-mesons results yet.
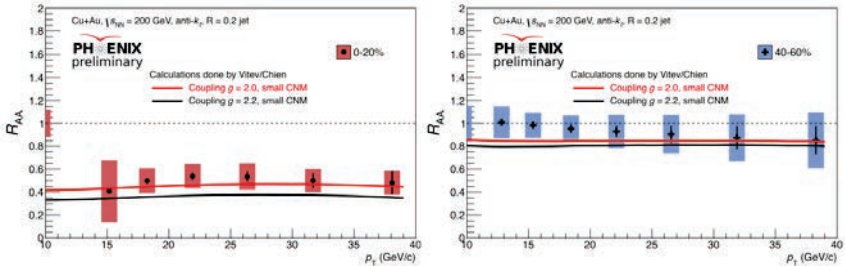


Fig.9. SCET model predictions for jets nuclear modification factors obtained in central 0-20% and 40-60% centrality bins in Cu+Au collisions at 200 GeV.

## 4. CONCLUSIONS

PHENIX experiment at RHIC has measured nuclear modification factors for $\pi^0$-mesons and reconstructed jets in Cu+Au collisions at 200 GeV. $\pi^0$-mesons production is suppressed in central Cu+Au collisions like in Au+Au and Cu+Cu collisions at similar $N_{part}$, which suggests that suppression level depends on nuclei overlap size and not on its geometry. In peripheral collisions there is a hint of $\pi^0$

and jet production enhancement. Jet nuclear modification factors are in agreement with SCET model calculations but there are no predictions for $\pi^0$-mesons nuclear modifications available yet. We acknowledge support from Ministry of Education and Science, Russia, project 3.1498.2017.

## REFERENCES

1. Adcox K. et al. // Nucl. Phys. A, 2005. V.757, issues 1–2 P.184.
2. Baym G. // Nucl. Phys. A, 2002. V.698, issues 1–4, P.23.
3. Adare A. et al. // Phys. Rev. Lett., 2016, V.116, P.122301.
4. Adare A. et al. // Phys. Rev. C., 2013, V.88, P.024906.
5. Adam J. et al. // Phys. Rev. B., 2015, V.746, P.1–14.
6. Chien Y., Vitev, I. // J. High Energ. Phys., 2016:23.